ORGANIZATION OF NANOPARTICLES AND POLYMERS IN HEXAGONAL LIQUID CRYSTALLINE PHASES OF C_nE_m/WATER SYSTEMS

THESIS

Submitted To The

UNIVERSITY OF PUNE

For The Degree Of

DOCTOR OF PHILOSOPHY

In

CHEMISTRY

By

KAMENDRA P. SHARMA

Research Supervisor

Dr. GURUSWAMY KUMARASWAMY

DIVISION OF POLYMER SCIENCE & ENGG.
NATIONAL CHEMICAL LABORATORY
PUNE – 411008

March 2011

DECLARATION

I, hereby declare that all the experiments embodies in this thesis entitled, "**ORGANIZATION OF NANOPARTICLES AND POLYMERS IN HEXAGONAL LIQUID CRYSTALLINE PHASES OF C_nE_m/WATER SYSTEMS**" submitted for the degree of Doctor of Philosophy in Chemistry, to the University of Pune have been carried out by me at the Polymer Science and Engineering Division, National Chemical laboratory, Pune, India, under the supervision of Dr. Guruswamy Kumaraswamy. The work is original and has not been submitted in part or full by me, for any degree or diploma to this or to any other University.

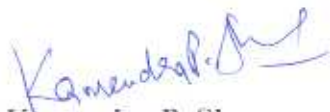

Kamendra P. Sharma

Date: 11th March 2011

Polymer Science and Engineering Division,

National Chemical laboratory, Pune-411008

India

राष्ट्रीय रासायनिक प्रयोगशाला
(वैज्ञानिक तथा औद्योगिक अनुसंधान परिषद)
डॉ. होमी भाभा मार्ग पुणे - 411 008. भारत
NATIONAL CHEMICAL LABORATORY
(Council of Scientific & Industrial Research)
Dr. Homi Bhabha Road, Pune - 411 008. India.

CERTIFICATE

This is to certify that the work incorporated in the thesis entitled, "**ORGANIZATION OF NANOPARTICLES AND POLYMERS IN HEXAGONAL LIQUID CRYSTALLINE PHASES OF C_nE_m/WATER SYSTEMS**" submitted by Mr. Kamendra P. Sharma, has been carried out by him under my supervision at the Polymer Science and Engineering Division, National Chemical laboratory, Pune. All the materials from other sources have been duly acknowledged in the thesis.

Research Guide

(Dr. Guruswamy Kumaraswamy)

Date: 11th March 2011

Place: Pune

Communication Channels
NCL Level DID : 2590
NCL Board No. : +91-20-25902000
EPABX : +91-20-25893300
+91-20-25893400
FAX
Director's Office : +91-20-25902601
COA's Office : +91-20-25902660
COS&P's Office : +91-20-25902664
WEBSITE
www.ncl-india.org

Acknowledgements

In the journey of my thesis, many people have contributed significantly to help me reach this level through their constant support and encouragement. Thus, without acknowledging their effort, this thesis is incomplete. I reserve the first and best part of it to my research guide and mentor Dr. **Guruswamy Kumaraswamy** (NCL, Pune), whose noble principles and whole hearted dedication to science has gained my unassailable respect. He has been highly supportive and his constructive criticism has helped me a lot during my thesis work. I absolutely admire his ethics, his desire to perform high quality science and instilling the thirst for science in not only his students but in all whom he comes across and I wish I could imbibe some of those qualities and exercise them for the rest of my life. I believe that the essential habits he cultivated in me such as attending seminars, group meetings, yearly resolutions and planning will give me the confidence to start an independent scientific career.

I would also like to thank my Ph.D. research committee members, Dr. Ashish Lele (NCL, Pune) and Dr. Ranjini Bandyopadhyay (RRI, Bangalore), for their valuable comments and suggestions. I would also thank Prof. Olivier Mondain-Monval and Isabelle Ly (both CRPP, Bordeaux, France) for helping me in performing Freeze Fracture TEM studies. Special thanks are due to Dr. Sayam Sen Gupta, Dr. Sudip Roy, Dr. B. L. V. Prasad, Dr. P. R. Rajamohanan with whom I had collaborated during the course of my Ph.D thesis. I would take this opportunity to thank Dr. Suresh Bhat for helping me perform light scattering and confocal microscopy experiments at NCL, Pune. I am also grateful to Mrs. Anuya Nisal and Mr. Ketan who helped me in electron microscopy experiments. I would also like to appreciate efforts of Dr. Vinod Aswal and Dr. Debasis Sen in helping me carrying out neutron scattering experiments

at BARC, Mumbai. I would also like to thank Dr. V. Premnath who has been there when i needed his help.

My special thanks to friends especially, Prof. Ashok Kumar Das Mahapatra (IIT, Guwahati), Dr. Kishore Bharadwaj, Dr. Amit Patwa, Ekta and Aashka for their constant support throughout my research work at both personal and professional fronts. Some of my colleagues and friends whom I would like to thank for helping me during my research work are Anal Kr. Ganai, E. Venugopal, Chandan Kr. Choudhary, Virginia D'Britto, V. J. Jijo, R. Kannan, Siva Swaroop, Rajendra Reddy, Manasi Kasture, K. Sreenivas, S. Prathap Chandran and all my labmates. I sincerely acknowledge the financial support from CSIR (New Delhi), NCL (Pune), Department of Science & Technology (DST) and French Embassy in India. My extended thanks are due to the former and present Directors, Dr. S. Sivaram and Dr. Sourav Pal respectively.

A big thankyou goes to my beloved grand-mother (bibi) from the bottom of my heart who had envisaged a vision for me. Without her love, blessings and constant support my efforts could have never come in the form this thesis. I would also thank my wife (Trupti) for her support and love. I would also like to thank Aai and Papa for their blessings and well-wishes. Thanks are due to my dear Maj. Rajendra who has taught me how to smile in hard phases of the life. Thanks to Mahendra Kulkarni and family for their support and care.

Kamendra P. Sharma

Abstract

Surfactant molecules organize to form micellar structures in aqueous solutions. At high surfactant concentrations, liquid crystalline mesophases may form, for example, by organization of surfactants into cylinders that arrange in a hexagonal packing to form the H_1 phase. In such systems, the matrix microstructure could influence the localization or assembly of particles or particles dispersed in it, especially when the particle size is comparable to the length scale that characterizes the matrix. In this thesis, we present a detailed investigation of the organization of nanoparticles and polymers incorporated in a hexagonal mesophase (H_1) formed by a nonionic surfactant, $C_{12}E_9$ and water.

We begin with an introduction to the process of self-assembly, and a description of surfactants and their phase behaviour, and thus provide the context for this work. Then, we present the results of our investigations into the self-assembly of silica particles in a hexagonal mesophase of $C_{12}E_9$ and water. The structure of the H_1 phase comprises of cylindrical micelles arranged hexagonally, with a center to center spacing of 5.7 nm. We disperse preformed, narrowly dispersed silica particles, with sizes from 1-3 nm to 500 nm, in the H_1 phase. When cage-like silsesquioxanes with a size of 1-3 nm (that are analogues of silica particles) are incorporated in the H_1 phase, they swell the space between cylindrical micelles and behave like a solvent. Silica particles comparable to the characteristic hexagonal spacing, partition between the hexagonal phase and into strand-like particulate aggregates. Nanoparticles having a diameter >10 nm phase separate from the surfactant phase and aggregate at the boundaries of H_1 domains, to form particulate strands that organize into a network that strongly scatters visible light. The silica particles nucleate the formation of the H_1

phase and increase the transition temperature for the isotropic to H_1 transition, relative to the neat H_1 phase. As the H_1 domains grow, the particles are concentrated in the isotropic domain, and when the H_1 domains impinge, the particles aggregate at the domain boundaries, to form particulate strands. We observe that the formation of aggregated particulate network is thermoreversible i.e. the particles redisperse on heating the particle-H_1 composite into the isotropic micellar phase, and reaggregate as the composite is cooled into the hexagonal phase. This reversible aggregation is unusual for charge-stabilized silica nanoparticles, since aqueous dispersions are irreversibly destabilized by addition of salt or change in pH. We show, using SAXS and external contrast matching SANS measurements, reversible aggregation of silica particles in the surfactant system is a result of adsorption of surfactant onto the silica particle surface. We demonstrate that the structure of surfactant/particle system can be modeled as adsorbed micelles of surfactant on the surface of the silica particles Surfactant adsorption gives rise to short range inter particle repulsions so that the interparticle interactions can be modeled using a hard sphere potential. This surfactant-induced short range repulsion between the silica particles renders particle aggregation reversible. We have also show that adsorption of polyethyleneimine on the surface of the silica particles prevents adsorption of surfactant micelles on the particle surface.

When PEI coated silica particles organize into particulate networks in the H_1 phase, the PEI can be crosslinked to obtain a self standing macroporous scaffold after surfactant removal. Phase separation of the particles from the H_1 phase is independent of particle chemistry, and dispersed nanoparticles (> 10 nm) assemble into networks, when the surfactant matrix cools into the hexagonal phase. We demonstrate assembly

of inorganic, polymeric and bionanoparticles into networks. As our technique involves near ambient temperatures, and a benign water wash for template removal, it is suitable for bionanoparticles that cannot tolerate extreme temperatures or harsh methods of template removal. We also demonstrate that the network mesh size can be varied from the sub-micron to tens of microns by controlling the cooling rate. Particle networks can be flow-oriented prior to crosslinking, and interpenetrating networks can also be formed.

We have also investigated the dispersion of a pH responsive polymer, polyethylenimine, PEI, in the $C_{12}E_9/H_2O$ hexagonal (H_1) mesophase, at pH ranging from basic (pH = 12.8) to acidic (pH = 1). While the $C_{12}E_9/H_2O$ phase behavior is independent of pH, we demonstrate that changing the pH influences PEI-$C_{12}E_9$ interactions, and thus, influences the isotropic-H_1 phase transition. With decrease in pH, there is increasing protonation of the PEI chain, and consequently, the chain extends. We show, using a combination of SAXS and optical microscopy, that the inclusion of PEI in a 1:1 surfactant-water mixture, lowers the hexagonal-isotropic transition temperature, T_{HI}. At higher pH = 12.8, T_{HI} shows a pronounced decrease from 45^{o}C to 13^{o}C on addition of PEI, and the PEI/$C_{12}E_9/H_2O$ system forms a transparent gel. At pH = 1, we observe qualitatively different behavior and an opaque gel forms below T_{HI} = 25^{o}C. The isotropic-H_1 transition influences the phase separation of PEI chains from the $C_{12}E_9/H_2O$ system. 2D NMR ROESY data provides evidence that there are strong surfactant-PEI interactions at high pH, that significantly reduce at lower pH. The NMR data is in accord with molecular dynamics simulations, that show that surfactants strongly aggregate with fully protonated PEI chains, but not with unprotonated chains. Thus, in this system, the pH controls a cascade of

microstructural organization: increasing pH decreases chain protonation, and increases polymer-surfactant interactions; this results in suppressing the transition to an H_1 phase to lower temperatures, which influences the phase separation of the PEI chains from the surfactant/water system.

In the last part of the thesis we investigate the effect of particle anisotropy on their organization in the H_1 phase. We report preliminary results on the assembly of anisotropic particles i.e. Au nanorods (Au NRs) and micron-sized polystyrene ellipsoids (PSe) in the H_1 phase of the $C_{12}E_9$/water system. Using a combination of UV-Vis and ultra small angle neutron scattering experiments, we show that Au NRs assemble in an end-to-end fashion at the domain boundaries of the H_1 phase. Our data indicates a wide distribution in the number of Au NRs that form the aggregates. This linear assembly of AuNRs is not a result of chemical functionalization of the Au NRs, but is mediated by particle assembly in the surfactant phase. We also report confocal and optical microscopy of the assembly of larger (micron sized) PSe of two different aspect ratios and show that they predominantly aggregate into end-to-end structures.

Contents

List of Figures

List of Tables

Chapter 1

Introduction and Literature

1.1. Introduction

The organization and phase behaviour of nanoparticles and polymers dispersed in a matrix, are strongly governed by their interactions with the matrix. In *microstructured* matrices, viz., in matrices where molecular organization results in supramolecular assemblies and/or where the matrix exhibits inherent anisotropy, the matrix microstructure is important in determining its interactions with dispersed entities. In this thesis, we describe the behaviour of nanoparticles and polymers that are dispersed in aqueous phases of non-ionic surfactants. We set the stage for the thesis in this chapter, by introducing the concept of self-assembly, the methods used for assembly of colloidal particles, and the various templates/matrices used for colloidal assembly. We then describe the organization of amphiphilic surfactant molecules that comprise the matrix in our investigations, and finally outline the motivation for our work, and the objectives of this thesis.

1.2. Organization or Self-assembly

Self-assembly of building blocks such as, for example, molecules, colloids, polymers, etc. results in formation of structures over larger length scale as compared to the "monomeric" building blocks. Self assembled structures can form through either equilibrium or non-equilibrium routes.[1] At equilibrium, self assembled systems are characterized by a minimum in free energy. Common examples of these include inorganic and organic crystals, as well as several surfactant and block copolymer microphase separated structures.[1] In contrast, dynamically self-assembled systems, such as cytoskeletal machinery (from polymerization and depolymerization of actin filaments), formation of structures by bacterial colonies based on change in the food environment, replication of DNA, etc., are far from equilibrium.[1] Self-assembly is possible

at all length scales i.e. starting from molecules to colloids and even larger particles. According to Whitesides et. al.[1] self-assembly of molecules can happen through covalent interactions or through non-covalent forces such as van der Waals, electrostatic, hydrogen bonding and hydrophobic interactions. For the assembly of larger particles (meso or macroscopic objects), several other interactions for e.g. capillarity and external fields (for example electric, magnetic and gravitational fields), play an important role. These forces are typically insignificant when compared with the forces for covalent bonding in molecules.[1] In this thesis we describe the organization of polymers and colloids and will, therefore, restrict ourselves to literature appropriate to these systems.

1.3. Organization or Self-assembly of colloids

According to Whitesides et. al.,[1] the organization of colloids can be achieved by (a) tuning the chemical interactions between the colloids, (b) applying external fields (e.g. electrical, magnetic or flow) or (c) matrix mediated interactions: confinement or templating. We now examine the process of colloidal organization in the context of applications where colloidal organization is important.

Organization of colloids yields *structures* that find applications in photonic, sensing, electronics and drug delivery applications.[2-5] The organization of colloids provides an elegant bottom-up process of fabricating *structured* materials with desired characteristics. For example various methods like sedimentation,[6,7] evaporation,[8] epitaxial crystallization,[9] electric/magnetic fields, flow, etc. or a combination of these[10-16], can be used to produce three dimensionally ordered colloidal crystals that possess optical properties useful for photonic applications. For other applications like, filtration, catalysis, sensing, drug delivery, tissue engineering etc., highly porous structures are required. These porous structures can be fabricated so as to have micropores (< 2

nm), mesopores (2-50 nm) or macropores (>50 nm) and, are in some cases, comprised of highly ordered colloidal structures. In the next section, we discuss the methods used for colloidal organization, in detail.

1.3.1. Colloidal assembly by tuning interparticle interactions:

As mentioned above, colloids can be organized by changing interparticle chemical interactions. For e.g., colloids grafted with environment sensitive surface moieties, such as DNA, proteins, or specific ligands, can be organized by change in solvent polarity,[17] pH,[18-20] by initiating redox reactions,[21] using light[22-27] or temperature.[28,29] Environment sensitive intermolecular forces that may be used to control colloidal organization include, hydrogen bonding, π- π stacking, hydrophobic and dipole-dipole interactions. Control of environment mediated interparticle interactions has been applied for the assembly of spherical gold and silver particles,[30,31] rod-like gold particles[32] and carbon nanotubes.[33] Nanoparticles may also be assembled using sol-gel chemistry.[34] For example., Arachchige et, al. demonstrated that a concentrated dispersion of metal chalcogenide nanoparticles can be assembled into a porous gel by surface grafting the nanoparticles with thiolate groups and their subsequent oxidiation and polymerization. Lin et. al.,[35] showed how controlled 1D assembly of citrate stabilized Au particles can be obtained by ligand exchange using 2-mercapto ethanol. However, relying on changes in interparticle interactions to organize colloids, typically involves complicated chemistry to graft stimuli responsive moieties on the surface of nanoparticles.

1.3.2. Colloidal organization by templating or confinement:

One of the most common methods for organizing colloids is the use of templates. Template-assisted self assembly involves use of 1D, 2D or 3D substrates having sites for colloidal particle localization. Templated assembly thus gives rise to complex structures decided by the shape of the tempate.[36] The typical process of formation of *structured* materials using templates can be summarized as follows: (a) colloidal particles/precursor solution are mixed with the template, (b) the former occupies the empty spaces/voids or the surface of these templates and organize to form an inverse structure and, (c) the templates are finally removed after fixation, for example, by chemical crosslinking, of the colloidal structure. Typically, templates can be classified as soft and hard templates. Soft templates can generally be removed by heat treatment or by mild dissolution conditions and are usually organic molecules, for e.g., surfactant micelles, polymers or biological molecules like DNA, virus, proteins etc.[37] Hard templates, for e.g., porous alumina membranes, microporous zeolites, mesoporous silica materials like MCM- 41, MCM-48, SBA-15, and SBA-16 are mostly removed by using harsh acid or alkali leaching processes and are usually used for fabrication of highly ordered inverse structures.[37b] The different methods/strategies that have been used for organizing colloids using templates include, spray drying,[38] dynamic templating using breath figures,[39] polymerization induced phase separation,[40] adsorption on an interface or substrate(layer by layer, LbL, technique),[41] etc.. The various types of templates used for assembling nanoparticles include emulsion droplets,[42] bubbles,[43] colloidal crystals,[44-49] polymer foams,[50] membranes,[51] polymer gels, [52,53] biopolymers,[54] biological templates.[55-65] etc. Colloidal crystals, for example, have been used to make exact replicas of the template as shown in Figure 1.1. Pre-

organized larger colloidal spheres template the organization of smaller nanoparticles, that fill the cavities of the 3D structure (Figure 1.1 a). In another case, colloidal spheres can be coated with nanoparticles and the former can then be organized by various methodologies as discussed in section 1.3. (Figure 1.1 b). Removal of template in these cases leads to formation of three-dimensionally ordered macroporous (3DOM) materials or hollow sphere array of nanoparticles, respectively. Biological matter, for example, sponges, leaves and wood cellulose from natural plants,[55-61] bacterial structures,[62] rod like virus molecules,[63] insect wings,[64] and pollen grains[65] also provide beautiful and inexpensive templates that can be used to form inverse inorganic structures having different morphologies.

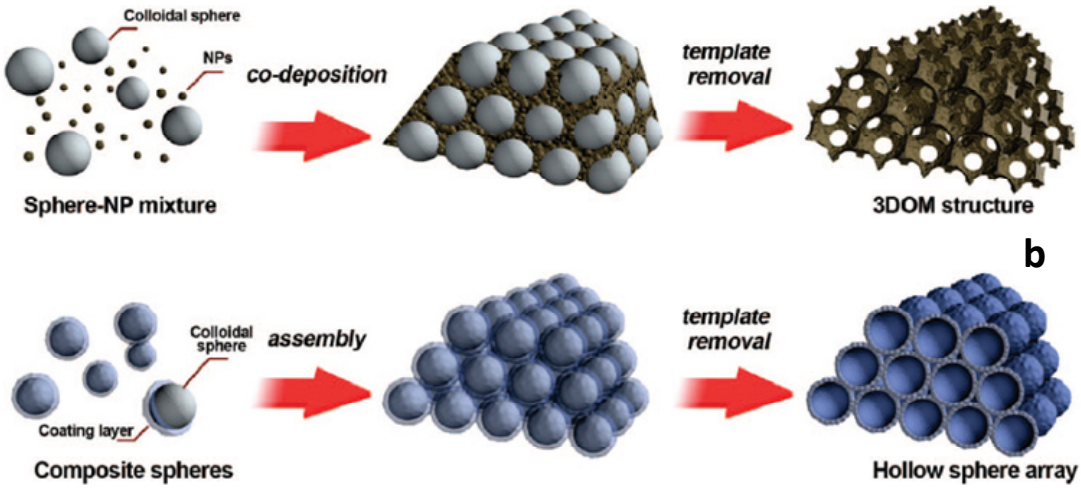

Figure 1.1: Different methodologies for fabrication of three-dimensionally ordered macroporous (3DOM) materials by colloidal crystal templating (Figure adapted from ref. 44 with permission).

The aforementioned templates, in combination with organized block copolymer/surfactant micelles, have been used to form hierarchical bimodal mesoporous-macroporous materials from colloidal organization. The micelles along with the small colloidal particles infiltrate the cavities of the template (colloidal crystals, polymer foams, membranes, bio-cellulose, emulsion, etc.) and, the surfactant micelles, in turn, act as a templating structure for the colloidal particles. Thus a colloidal structure is obtained by using a template within a template.[39c,66-69]

A recent method used for colloidal organization to prepare macroporous materials, is the dynamic templating of ice crystals.[70] This method has been be used to generate porous structures made of polymer–inorganic nanocomposites, aligned gold microwires and microwire networks, silica microhoneycombs, aligned silica fibers and porous composite microfibres.[70]

Block copolymer molecules have also been used as templates as they spontaneously self assemble by segregation of chemically different blocks into a range of morphologies, for e.g., spherical, vesicles, cylindrical, lamellae, gyroid, etc.[71] The spacing between microdomains in block copolymers can be controlled by changing the molecular weight of the polymers or by blending with homopolymers.[71] Therefore block copolymers can be used for tuning the spatial organization of colloids by either using different morphologies or copolymer compositions.[72] For e.g., cylindrical or lamellar morphologies of polystyrene-*b*-poly(methyl methacrylate) films have been used to organize CdSe nanorods on the surface of poly(methyl methacrylate) domains.[73] This makes block copolymers ideal templates for assembling the colloidal particles into different morphologies, for applications ranging from sensors to magnetic storage

devices.[74] Thus, templates provide a versatile route to synthesize inorganic, organic, or composite mesoporous and macroporous materials.

1.3.3. Matrix assisted colloidal assembly using liquid crystals:

Liquid crystals (LCs) are interesting matrices for directing the assembly of colloidal particles. Liquid crystals possess order that is intermediate to a liquid and a solid. A molecule that shows a liquid crystalline behavior should be anisotropic and rigid. In the LC state, the axes of the molecules are, on average, oriented in a specific direction, termed as the *director*. Liquid crystals can be broadly classified as thermotropic; viz. that exhibit temperature dependent phase behaviour, and lyotropics, viz. that exhibit concentration dependent phase behavior.[75] Among the most well studied liquid crystal phases is the nematic phase, since nematics find application for making widely used display devices. Liquid crystal displays (LCDs) are ubiquitously used in televisions, watches, calculators, mobile phones, laptop computer screens, and for instrumentation display panels in the automobile industry. In general, their utility relies on the fact that the orientation of the molecules in a nematic liquid crystal can be altered by applying an external electric field, and that liquid crystalline phases have anisotropic optical properties. Polymer dispersed liquid crystals (PDLC's)[76] which are formed by immersing liquid crystal droplets in a polymer matrix find applications as optical switching devices, reflection gratings, holography, optical displays and fiber optic elements.[77,78]

Researchers have also tried to exploit the long range orientational order of nematic liquid crystals for organizing colloidal particles. In orientationally ordered nematics, dispersion of colloids results in topological defects that arise from having to simultaneously satisfy boundary conditions for director orientation at the surface of

the colloid and in the bulk i.e. away from the surface of the colloid. The nature of these defects depends on two factors: the elastic cost associated with distortion of the director field given by KR (where K is the elastic constant characterizing the liquid crystal and R is the radius of the colloidal particle) and, the anchoring energy of liquid crystal molecules on the colloid surface given by WR^2 (where W is the surface energy term corresponding to the strength of anchoring). The topological defects associated with colloidal particles in nematics result in long-range anisotropic interactions between colloidal particles, originating from the elasticity of the liquid crystalline matrix.[79-84] These inter-particle interactions result in self-assembly of the particles in the liquid crystalline matrix. Loudet et. al.[85] reported the formation of chain-like linear arrays of colloidal silicone droplets with inter-droplet dipolar interactions, in the nematic matrix. Two-dimensional crystals of colloids with quadrupolar interactions have also been reported recently.[86] Investigations of large particles doped in cholesteric nematics[87] and lamellar smectic phases,[88] show that large colloidal particles tend to phase separate to the defect nodes and stabilize a network of defects that link these nodes, and thereby result in an increase of the storage moduli (G') of the composite. Depending on the chemistry and size of the particle included in the liquid crystal and cooling kinetics from the isotropic to the nematic phase, many different phase separated textures like root-like, striped or cellular have been reported.[89-94]

Surfactants are also known to form liquid crystalline phases, typically at high concentrations. However, in contrast to nematics, here the liquid crystalline behavior arises due to collective orientation of ordered surfactant aggregates in a specific direction. These surfactant aggregates that form the liquid crystalline structures are characterized by a length scale that is much larger than the size of surfactant molecules. Be-

fore discussing liquid crystals formed by surfactants and their use as templates, we first describe surfactants, in detail.

1.4. Surfactants

Surfactants are amphiphilic molecules that possess a hydrophilic polar head group and a non-polar hydrophobic tail. Surfactants are surface active agents and have a tendency to adsorb at interfaces, to reduce interfacial tension.

1.4.1. Classification of surfactants:

Surfactants are found in Nature, and can also be synthetically prepared. The polar lipids that are abundantly present in all living organisms in Nature are surfactants. The most important example of such natural surfactants are phospholipids, that pack in bilayers, to constitute cell membranes.[95] Further, bile salts contain many polar lipids that solubilise hydrophobic components in the blood. Other common examples of polar lipids found in Nature are fatty acid salts, acylglycerols (monoglyceride, diglyceride and glycolipids), lecithin, trehalose lipids, etc.[95] Synthetic surfactants are also used widely, and are classified as oleochemical or petrochemical, depending on the starting materials for their synthesis. Surfactants based on oleochemicals are derived from renewable materials like vegetable oils while petrochemically derived surfactants are prepared from monomers that are derived from crude oil.

Surfactants can also be classified according to the type of charge borne by the polar head group. The different classes include anionic, cationic, non-ionic and zwitterionic. Zwitterionic surfactants have both anionic and cationic groups. The physicochemical properties of ionic surfactants are influenced by the type of counter-ion associated with the polar head group. Anionic surfactants are the most widely used and contribute to 60% of the total production of synthetic surfactants.[95] Typically, the head

groups are carboxylate, sulphate, sulphonate or phosphate while the hydrophobic groups are alkyl or alkylaryl. The most common counter-ion for an anionic surfactant is Na^+; but other ions like Li^+, K^+, Ca^{2+}, Mg^{2+} and $-NH_3^+$ are also used in specific surfactants. The largest volume application of anionic surfactant is for soaps, prepared by saponification of natural oils and fats. Soaps are sodium salts of carboxylic acid of triglycerides found in animal fats or vegetable oils. Soaps are very sensitive to salts and tend to lose their ability to solubilise oils in hard water. Detergents are anionic surfactants that can overcome this disadvantage of soaps. The most widely used detergents in household and industrial applications are alkylbenzene sulphonates. These are synthesized by sulphonation of linear alkyl benzene with either sulphur trioxide or oleum.[95] The other category of ionic surfactant, viz. cationics are mainly based on amine and quaternary ammonium head groups. Cationic surfactants with other head groups like phosphonium, sulphonium, sulphoxonium are also used industrially, but in smaller volumes. The most common class of cationics include fatty amine salts, fatty diamine salts, alkyl *quat* (*quat* refers to the quaternary ammonium group), dialkyl *quat* and ester *quat*. The main use of cationic surfactants is in the form of adsorbed layers on metals, minerals, plastics, fibres, cell membranes, and other surfaces that are mainly charged. For e.g., cationic surfactants are used as anticorrosion agents for steels, floatation collectors for mineral ores, antistatic agents for plastics and fibres, and anticaking agents in the fertilizer industry.[95]

The second most highly used class of surfactants, after anionics, are non-ionics. In these, the polar head group is uncharged and contains hydrophilic groups like polyoxyethers or polyhydroxyls. The polyoxyethers are synthesized by ethoxylation of an alcohol, viz. polymerization of *m* ethylene oxide units, where *m* typically

varies from 2-20, starting from the alcohol. The most common among the polyoxyether surfactants are fatty alcohol ethoxylates also referred to as C_nE_m, where *C* represents the hydrophobic carbon chain and *E* is the polyoxyethylene hydrophilic part (*n* is generally above 5 while *m* typically varies between 2-20). Examples of polyhydroxy based surfactants include sucrose esters, sorbitan esters and alkyl glucosides. The most important characteristic of non-ionic surfactants that distinguishes them from ionics is that they are unaffected by the presence of electrolytes or change in pH. The physico-chemical properties of non-ionics are temperature and concentration dependent. At higher temperature, ethoxylated non-ionics are less soluble in water while sugar based non-ionics (polyhydroxyl) show increased water solubility. However, non-ionics are typically more expensive than ionic surfactants and form foams that are less stable when compared with anionic surfactants.

1.4.2. Self-assembly of surfactant molecules:

One of the fundamental properties of surfactants is that monomers in solution form aggregates, known as micelles, above a critical concentration called the critical micelle concentration (c.m.c.). The micelle size and shape depends on various parameters, for example, temperature, pH, salt and type and concentration of co-surfactant. The c.m.c. of non-ionic surfactants is typically lower than that of ionics having a similar number of C-atoms. As the number of C-atoms in the hydrophobic chain increases, the c.m.c. decreases. Temperature and salt also can alter the c.m.c. of the ionic surfactants, but for non-ionic surfactants there is no pronounced effect of added salt. The size of the micelle depends on the length of the hydrocarbon chain while shape is determined by the molecular packing to form the aggregate or micelle.

Israelachvili et. al.[96] proposed the concept of a molecular packing parameter which can be used to determine the equilibrium size and shape of surfactant aggregates. In this model, the shape of surfactant micelles is given by a packing parameter, $N_s=v/al$, where v and l are the volume and length of the surfactant tail within the hydrophobic core of the aggregate and a is the effective area occupied by each surfactant head group at the surface of the aggregate. This parameter is also referred to as the critical packing parameter or surfactant number. It gives an idea of the preferred curvature of a micellar aggregate on the basis of the surfactant molecular properties. Smaller value of N_s suggests higher curvature, and as its value increases, the surface reduces its curvature to form planar structures. As the value of N_s (shown in Table 1.1) varies from 0-1/3, 1/3-1/2, 1/2-1 or >1, the favoured aggregate morphology in solution changes from spherical, to cylindrical, to flat bilayers, and to the corresponding inverse structures, respectively, as shown in the Table and in Figure 1.2. Values >1 indicate inverse, i.e. water in oil aggregated structures. The surfactant aggregate morphology can be altered by a number of external variables. The addition of electrolyte to ionic surfactant solutions reduces electrostatic repulsive forces between head groups, whereas incorporation of *n*-alcohols causes the hydrophobic component of the aggregate to swell, and both effects cause a reduction in aggregate curvature and hence influence the micellar morphology. It is to be emphasized here that spherical micelles do not form at all for many surfactants and, for others, such micelles occur in a limited range of concentration and temperature.

Value of N_s	Micellar morphology
0-0.33	Spherical micelles
0.33-0.5	Cylindrical micelles
0.5-1	Flat bilayers or Lamellar micelles
>1	Inverted spherical or cylindrical micelles

Table 1.1. Values of N_s and the resultant surfactant aggregate morphologies.

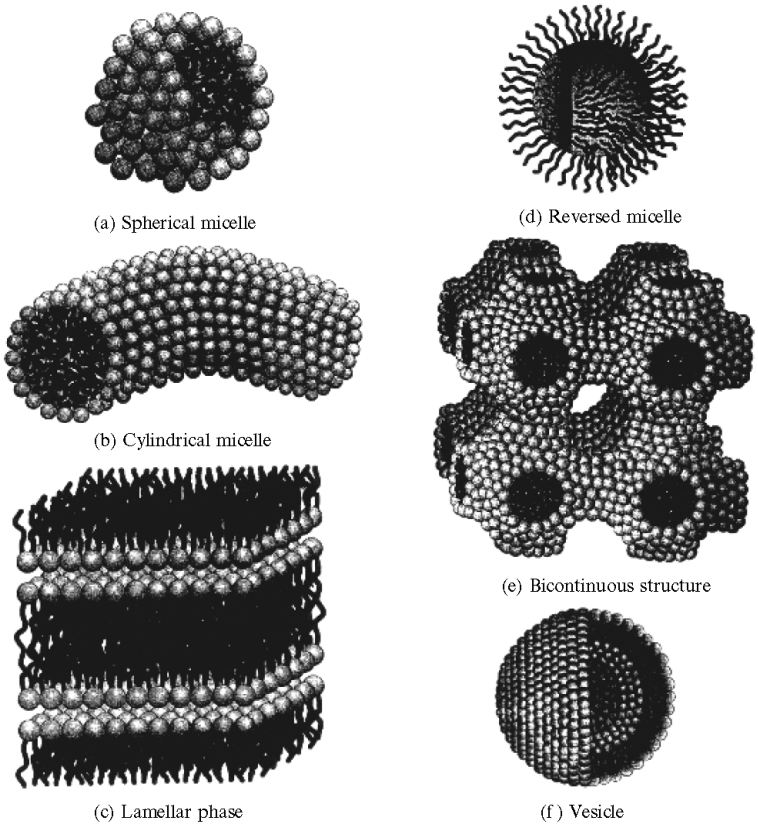

Figure 1.2. Different structures formed by surfactants by change of temperature and concentration (Figure adapted from ref. 95 with permission).

The value of N_s is also a function of surfactant concentration. With increase in surfactant concentration, micelles often transform from spherical aggregates to other geometries, for example, long rod- or thread-like micelles, or into bilayers. The relation of the molecular packing parameter with the micellar aggregate architecture and the resultant mesophase structure is shown in Figure 1.3.[95] Surfactant aggregates can further pack into ordered lattices – for example, cylindrical micelles can pack to form ordered hexagonal structure having *p6mm* symmetry, while bilayers pack into one-dimensional lamellar stacks. These ordered assemblies, however, possess fluidity since the surfactant chains within each aggregate are mobile and disordered. Therefore, such lamellar and hexagonal assemblies exhibit liquid crystalline properties. The characteristic length scale in these liquid crystals is given by the average micellar spacing and spans from 1nm -100 nm. Therefore, such states are also termed as mesophases.

The temperature and concentration dependent changes in the surfactant aggregate morphology constitute the phase diagram of the surfactant. This phase diagram can be constructed by characterizing the different structures, using a combination of scattering and optical microscopy. These phase diagrams[97] are used as a guiding tool to study the use of these different surfactant structures for various applications; as nanoreactors or nanotemplates.

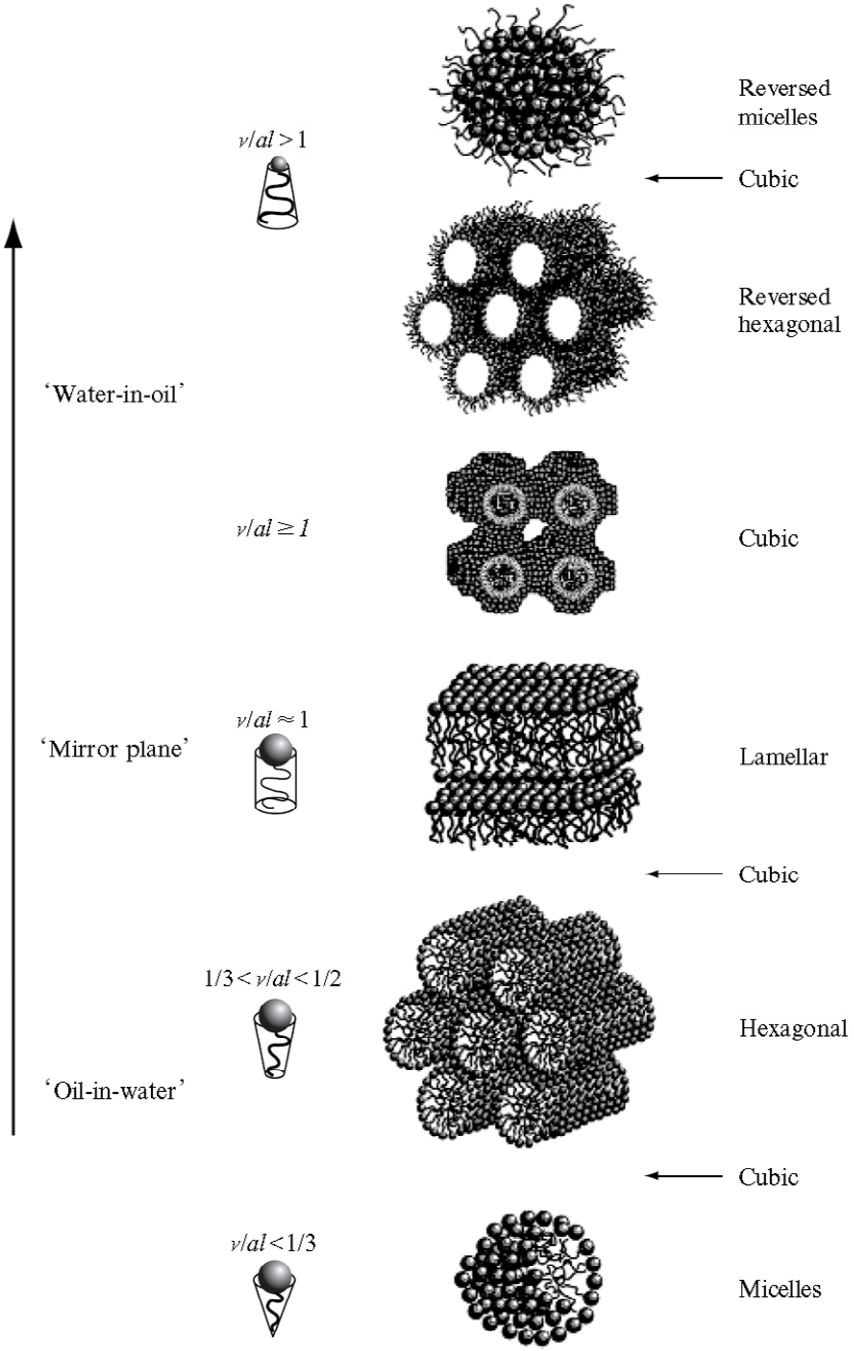

Figure 1.3. Different types of mesophases formed by changing the value of N_s by varying temperature or concentration of surfactant (Figure adapted from ref. 95 with permission).

1.4.3. Surfactants as nanoreactors and nanotemplates for performing chemistry:

The first investigation[98] that demonstrated the use of surfactants for making mesostructured materials was by researchers at Mobil in 1992, when they used dilute surfactant solutions of CTAB for co-precipitation of aluminosilicate precursors to form meosporous silica with uniform cylindrical pores, organized in a hexagonal array. They further showed that the pore size could be varied from 1.6 nm to 10 nm by changing the surfactant.

Surfactant mesophases can also be used as nanoreactors to confine reactants within nanometer-sized domains. The liquid crystalline mesophase partitions space into hydrophilic and hydrophobic regions, and allows for segregation of hydrophilic and hydrophobic reactants. For the first time, Attard et al.[99] showed the use of non-ionic surfactant mesophases to template the formation of silica by the condensation of tetramethyl orthosilicate (TMOS). A mixture of $C_{12}E_8/H_2O$/TMOS was used to form a hexagonal mesophase (H_1), and the TMOS hydrolyzed and condensed within this, to form silica under acidic conditions. This composite was calcined to result in an ordered hexagonal silica structure having pores size of ~3nm. Similarly ordered silica structures could be formed by using lamellar (L_α) phase of another surfactant, $C_{16}E_8$. The silica mesostructures thus formed, were a nanocast or a negative print of the organic phase and formed as a result of liquid crystal templating, where the silica formed inorganic walls in an ordered surfactant mesophase. Since then, there have been significant advances in using lyotropic liquid crystals for nanocasting silica, metal oxides and metals.[100]

Non-ionic surfactant mesophases have also been employed for the formation of lattices of semiconducting sulphides, such as, for example, CdS, CdSe and ZnS.[101] It has been proposed that the mineralization process of metallic salts in the organic mesophase depends on the interactions of the inorganic ions with the surfactant. For example, mineralized sulphides of Cd and Zn showed strong interactions with organic moieties in the surfactant and therefore, the structures formed were a direct template of the organic mesophase. However, for Cu^{2+}, Ag^{+}, Pb^{2+} and Hg^{2+} ions that did not interact with the surfactants, the structure of the sulphides formed was not a cast of the organic template.

The ability of surfactant liquid crystals to direct and cast inorganics into desired morphologies led researchers to investigate their utility in controlling the pore microstructure, when in-situ polymerization was conducted in a mesophase. Hentze et al.[102] used inverse hexagonal liquid crystalline phase of anionic surfactant, bis(2-ethylhexyl) sulfosuccinate sodium salt (AOT), for free radical polymerization of divinylbenzene and styrene. However they found that the final morphology of the polymer was not a replica of the surfactant template. They speculated that the polymer phase separated from the mesophase to form the observed structure. For polymers with moderate to large degree of polymerization, N, the enthalpic free energy cost of staying dispersed in the surfactant phase (= χN, where χ is the Flory interaction parameter) grows with N. There is also an entropic free energy penalty for confinement in the mesophase domains.[103] Thus, it has been suggested that the mesophase template only acts as a point of nucleation for the polymeric structure and, as polymerization propagates and large N chains form, phase separation occurs. Hentze et al.,[102] have suggested that polymerization in an inverse hexagonal phase results in polymer particles

that interact as in a nematic, and that these interactions guide the final microstructure of the polymer. However Lester et al.[104] have demonstrated that, rapid polymerization, for example, in the case of photopolymerization of acrylamides in lyotropic crystalline phases of non-ionic surfactants, yield structures that replicate the template. In recent work,[105] polycondensation reaction of different silanes has been reported; whereby phase separation can be controlled to result in crosslinked silicone particles that are rod-like when polymerized in a hexagonal mesophase and sheet-like in a lamellar phase. The mechanism of formation of these structures is still unclear.

Bouchama et al.[106] reported the formation and confinement of ~1-2 nm metal nanoclusters in the hexagonal mesophase (H_1) of AOT/water mixture by in-situ reduction of metallic salts. The complexes formed by surfactant mesophases and biopolymers for e.g. DNA and proteins have also been demonstrated. There has been recent interest in understanding the transfection of mammalian cells by different liquid crystalline structures of cationic liposome complexed with DNA.[107] It has been observed that the hexagonal mesophase formed by such complexes showed superior transfection of mammalian cells as compared to a lamellar complex. This was explained as a result of instability of hexagonal complexes which bound inefficiently to the cell membrane as compared to the lamellar complexes. Another example where surfactant mesophase have been used as templates for organizing structures is the crystallization of membrane proteins.[108]

1.5. Motivation and objective of the Present Thesis

The above critical review of current research activities on self assembly techniques and methods to form materials at larger length scales suggest an opportunity to explore the capability of lyotropic liquid crystals to control colloidal organization and form hierarchically organized materials. Since lyotropic liquid crystals form morphologically different phases by changing the concentration, or temperature, it is possible that inclusion of colloidal particles into them can provide routes to a variety of organized structures obtained from one single starting template. Also, since, we can vary the characteristic length scales for lyotropic liquid crystals (1~100 nm) while those for thermotropics are restricted to molecular sizes (~few Å), there are more opportunities to tailor matrix mediated interactions in lyotropics. This pathway of using lyotropics to assemble particles could provide a simple and benign method to form structured materials.

The lyotropic liquid crystals formed by surfactants are easy to handle and only require water for phase formation. Therefore we use a system comprising of non-ionic surfactant (insensitive to pH and ionic strength change) and water for the mesophase formation. Till now there has been no report of particle size effects in the lyotropic liquid crystals and the resultant structures formed by the particles. There is also scope to extend the current understanding of particle-particle interactions in such matrices and the changes that occur as a function of particle chemistry and geometry.

The broad objective of the present thesis is to examine the phenomena and materials that result when we disperse colloids in surfactant mesophases. Specifically, this thesis describes the organization of colloidal particles (of different size, chemistry

and geometry) and polymers, when dispersed in a hexagonal mesophase (H_1) formed by non-ionic surfactant, $C_{12}E_9$ and water system.

1.6. Organization of Thesis

After a focused introduction to the self assembly procedures for colloids in Chapter 1, we describe self assembly of silica nanospheres in the hexagonal mesophase (H_1) of the non-ionic surfactant $C_{12}E_9$/water systems in Chapter 2. We also describe the size dependence on the localization of silica particles in the H_1 phase. Chapter 3 describes the surfactant structure and interparticle interactions for dispersion of silica nanospheres in H_1 phase. In this chapter we use a combination of small angle X-ray scattering (SAXS) and contrast matched small angle neutron scattering (SANS) to investigate interparticle interactions and microstructure in dispersions of silica particles in aqueous non-ionic surfactant solutions.

Assembly of nanoparticles into free-standing macroporous materials has implications for a wide range of applications. In Chapter 4, we describe dynamic templating of surfactant hexagonal domains, a facile general technique to organize nanoparticles into a network of particulate strands and obtain self-standing structures.

Chapter 5 describes the behaviour of pH responsive polymer polyethylenimine, PEI, in the H_1 phase. Chapter 6 investigates the effect of anisotropy on the phase separation driven self assembly of particles at the domain boundaries of H_1 phase. The particles used for the study are anisotropic Au nanorods and their behaviour in the H_1 phase has been monitored using UV-Vis spectroscopy, SANS and microscopy techniques. We also show some preliminary results on micron sized polystyrene ellipsoids dispersed in the H_1 phase.

A summary of the major conclusions of the present study with respect to preparation, characterization, properties and potential applications of these self assembled structures by using phase separation induced self assembly in H_1 phase is presented in Chapter 7. This chapter also outlines some of the future investigations that can be carried out using this methodology.

1.7. References

1.(a) Grzybowski, B. A.; Wilmer, C. E.; Kim, J.; Browne, K. P.; Bishop, K. J. M., **2009,** *5*, (6), 1110-1128. (b) Whitesides, G. M.; Grzybowski, B. A. *Science*, **2002**, *295*, 2418**.**

2. Braun, P. V.; Wiltzius, P. *Nature* **1999,** *402*, (6762), 603-604.

3.Velev, O. D.; Kaler, E. W. *Adv. Mater.* **2000,** *12*, (7), 531-534.

4.Vlasov, Y. A.; Bo, X.-Z.; Sturm, J. C.; Norris, D. J. *Nature* **2001,** *414*, (6861), 289-293.

5.Wang, W.; Shi, X.; Kariuki, N. N.; Schadt, M.; Wang, G. R.; Rendeng, Q.; Choi, J.; Luo, J.; Lu, S.; Zhong, C.-J., *J. Am. Chem. Soc.* **2007,** *129*, (7), 2161-2170.

6.Davis, K. E.; Russel, W. B.; Glantschnig, W. J., *Science* **1989,** *245*, (4917), 507-510.

7. Zhu, J.; Li, M.; Rogers, R.; Meyer, W.; Ottewill, R. H.; STS-73 Space Shuttle Crew; Russel, W. B.; Chaikin, P. M., *Nature* **1997,** *387*, (6636), 883-885.

8.(a) Denkov, N.; Velev, O.; Kralchevski, P.; Ivanov, I.; Yoshimura, H.; Nagayama, K.*Langmuir* **1992,** *8*, (12), 3183-3190. (b) Jiang, P.; Bertone, J. F.; Hwang, K. S.; Colvin, V. L. *Chem. Mater.* **1999,** *11*, (8), 2132-2140.

9.(a) Blaaderen, A. V.; Ruel R.; Wiltzius, P. *Nature* **1997**, *385*, 321. (b) Lin, K.-H.; Crocker, J. C.; Prasad, V.; Schofield, A.; Weitz, D. A.; Lubensky, T. C.; Yodh A. G. *Phys. Rev. Lett.* **2000**, *85*, 1770. (c) Yin, Y.; Xia, Y. *J. Am. Chem. Soc.* **2003**, 125, 2048. (d) Schaak, R. E.; Cable, R. E.; Leonard, B. M.; Norris, B. C. *Langmuir* **2004**, *20*, 7293.

10. Trau, M.; Saville, D. A.; Aksay, I. A. *Langmuir* **1997,** *13*, (24), 6375-6381.

11. Gong, T.; Marr, D. W. M. *Langmuir* **2001,** *17*, (8), 2301-2304.

12. (a) Lumsdon, S. O.; Kaler, E. W.; Velev, O. D. *Langmuir* **2004,** *20*, (6), 2108-2116. (b) Lumsdon, S. O.; Kaler, E. W.; Williams, J. P.; Velev, O. D. *Appl. Phys. Lett.* **2003**, *82*, 949.

13. Yan, Y. D.; Dhont, J. K. G.; Smits, C.; Lekkerkerker, H. N. W. *Physica A: Statistical Mechanics and its Applications* **1994,** *202*, (1-2), 68-80.

14. Fraden, S.; Hurd, A. J.; Meyer, R. B. *Phys. Rev. Lett.* **1989**, *63*, 2373.

15. Dassanayake, U.; Fraden, S.; van Blaaderen, A. *J. Chem. Phys.* **2000**, *112*, 3851.

16. Hynninen, A.; Dijkstra, M. *Phys. Rev. Lett.* **2005**, *94*, 138303.

17. Yamada, M.; Shen, Z.; Miyake, M. *Chem. Commun.* **2006**, (24), 2569-2571.

18. Lim, I. S.; Mott, D.; Ip, W.; Njoki, P. N.; Pan, Y.; Zhou, S.; Zhong, C. *Langmuir* **2008**, *24*, 8857–8863.

19. Sun, Z.; Ni, W.; Yang, Z.; Kou, X.; Li, L.; Wang, J *Small* **2008**, *4*, 1287–1292.

20. Ni, W.; Mosquera, R. A.; Perez-Juste, J.; Liz-Marzan, L. M. *J. Chem. Phys. Lett.* **2010**, *1*, 1181–1185.

21. Olson, M. A.; Coskun, A.; Klajn, R.; Fang, L.; Dey, S. K.; Browne, K. P.; Grzybowski, B. A.; Stoddart, J. F., *Nano Lett.* **2009,** *9*, (9), 3185-3190.

22. Klajn, R.; Bishop, K. J. M.; Grzybowski, B. A., *PNAS* **2007,** *104*, (25), 10305-10309.

23. Alivisatos, A. P.; Johnsson, K. P.; Peng, X.; Wilson, T. E.; Loweth, C. J.; Bruchez, M. P.; Schultz, P. G., *Nature* **1996,** *382*, (6592), 609-611.

24. Fialkowski, M.; Bishop, K. J. M.; Klajn, R.; Smoukov, S. K.; Campbell, C. J.; Grzybowski, B. A. *J. Phys. Chem. B* **2006,** *110*, (6), 2482-2496.

25. Ipe, B. I.; Mahima, S.; Thomas, K. G. *J. Am. Chem. Soc.* **2003,** *125*, (24), 7174-7175.

26. Sidhaye, D. S.; Kashyap, S.; Sastry, M.; Hotha, S.; Prasad, B. L. V. *Langmuir* **2005,** *21*, (17), 7979-7984.

27. Ahonen, P. A. i.; Schiffrin, D. J.; Paprotny, J.; Kontturi, K. *Phys. Chem. Chem. Phys.* **2007,** *9*, (5), 651-658.)

28. Park, S. Y.; Lytton-Jean, A. K. R.; Lee, B.; Weigand, S.; Schatz, G. C.; Mirkin, C. A., *Nature* **2008,** *451*, (7178), 553-556.

29. Nykypanchuk, D.; Maye, M. M.; van der Lelie, D.; Gang, O., *Nature* **2008,** *451*, 549-552.

30. Kim, J.; Lee, J. *Nano Lett.* **2009**, *9*, 4564–4569.

31. Pal, S.; Sharma, J.; Yan, H.; Liu, Y. *Chem. Commun.* **2009**, 6059–6061.

32. Dujardin, E.; Mann, S.; Hsin, L.; Wang, C. R. C. *Chem. Commun.* **2001**, 1264–1265.

33. Chen, Y.; Liu, H.; Ye, T.; Kim, J.; Mao, C. *J. Am. Chem. Soc.* **2007**, *129*, 8696–8697.

34. Arachchige, I. U.; Brock, S. L. *Acc. Chem. Res.* **2007**, *40*, 801-810.

35. Lin, S.; Li, M.; Dujardin, E.; Girard, C.; Mann, S. *Adv. Mater.* **2005**, *17*, 2553-2559.

36. Grzelczak, M.; Vermant, J.; Furst, E. M.; Liz-Marzan, L. M. *Nano* **2010**, *7*, 3591-3605.

37. Yuan, Z. –Y.; Su, B.,-L. *J. Mater. Chem.* **2006**, *16*, 663–677.

38. Iskandar, F.; Mikrajuddin; Okuyama, K. *Nano Lett.* **2001**, *1*, 231-234.

39. (a) Böker, A.; Lin, Y.; Chiapperini, K.; Horowitz, R.; Thompson, M.; Carreon, V.; Xu, T.; Abetz, C.; Skaff, H.; Dinsmore, A. D.; Emrick, T.; Russell, T. P. *Nature Mater.* **2004**, *3*, 302-306. (b) Bunz, U. H. F. *Adv. Mater.* **2006**, *18*, 973-989. (c)

Sakatani, Y.; Boissière, C.; Grosso, D.; Nicole, L.; Soler-Illia, G. J. A. A.; Sanchez, C. *Chem. Mater.* **2007**, *20*, 1049-1056. (d) Shah, P. S.; Sigman, M. B. Jr.; Stowell, C. A.; Lim, K. T.; Johnston, K. P.; Korgel, B. A. *Adv. Mater.* **2003**, *15*, 971-974.

40. Amatani, T.; Nakanishi, K.; Hirao, K.; Kodaira, T. *Chem. Mater.* **2005**, *17*, 2114-2119. (b) Nakanishi, K.; Kobayashi, Y.; Amatani, T.; Hirao, K.; Kodaira, T. *Chem. Mater.* **2004**, *16*, 3652-3658.
41. (a) Boker, A.; He, J.; Emrick, T.; Russell, T. P. *Soft Matter* **2007**, *3*, 1231–1248. (b) Kinge, S.; Crego-Calama, M.; Reinhoudt, D. N. *Chem. Phys. Chem.* **2008**, *9*, 20–42. (c) Tao, A. R.; Huang, J. X.; Yang, P. D. *Acc. Chem. Res.* **2008**, *41*, 1662–1673. (d) Collier, C. P.; Saykally, R. J.; Shiang, J. J.; Henrichs, S. E.; Heath, J. R. *Science* **1997**, *277*, 1978–1981. (e) Tao, A.; Sinsermsuksakul, P.; Yang, P. *Nature Nanotech.* **2007**, *2*, 435–440. (f) Lin, Y.; Skaff, H.; Emrick, T.; Dinsmore, A. D.; Russell, T. P. *Science*, **2003**, *299*, 226–229.
42. Imhof, A.; Pine, D. J. *Nature* **1997**, *389*, 948.
43. (a) Carn, F.; Colin, A.; Achard, M. F.; Deleuze, H.; Saadi, Z.; Backov, R. *Adv. Mater.* **2004**, *16*, 140; (b) Carn, F.; Colin, A.; Achard, M. F.; Deleuze, H.; Saadi, Z.; Sanchez, C; Backov, R. *Adv. Mater.*, **2005**, *17*, 62. (c) Suzuki, K.; Ikari, K.; Imai, H. *J. Mater. Chem.*, **2003**, *13*, 1812.
44. (a) Vlasov, Y. A.; Yao, N.; Norris, D. J. *Adv. Mater.* **1999**, *11*, 165-169. (b) Holland, B. T.; Blanford, C. F.; Do, T.; Stein, A. *Chem. Mater.*, **1999**, *11*, 795.
45. Velev, O. D.; Kaler, E. W. *Adv. Mater.* **2000**, *12*, 531-534.
46. Davis, S. A.; Breulmann, M.; Rhodes, K. H.; Zhang, B.; Mann, S. *Chem. Mater.* **2001**, *13*, 3218-3226.

47. Rhodes, K. H.; Davis, S. A.; Caruso, F.; Zhang, B.; Mann, S. *Chem. Mater.* **2000**, *12*, 2832-2834.

48. Stein, A.; Li, F.; Denny, N. R. *Chem. Mater.* **2008**, *20*, 649-666.

49. Nie, Z.; Petukhova, A.; Kumacheva, E. *Nature Nanotech.* **2009**, *5*, 15-25.

50. (a) Huerta, L.; Guillem, C.; Latorre, J.; Beltrán, A.; Beltrán, D.; Amorós, P. *Chem. Commun.* **2003**, 1448-1449. (b) Zhang, Y.; Zha, S.; Liu, M. *Adv. Mater.* **2005**, *17*, 487-491.

51. (a) Caruso, R. A.; Antonietti, M. *Chem. Mater.* **2001**, *13*, 3272-3282. (b)Wang, Y.; Tang, Y.; Dong, A.; Wang, X.; Ren, N.; Shan, W.; Gao, Z. *Adv. Mater.* **2002**, *14*, 994-997.

52. Breulmann, M.; Davis, S. A.; Mann, S.; Hentze, H. P.; Antonietti, M. *Adv. Mater.* **2000**, *12*, 502-507.

53. Caruso, R. A.; Giersig, M.; Willig, F.; Antonietti, M. *Langmuir* **1998**, *14*, 6333-6336.

54. (a) Ogasawara, W.; Shenton, W.; Davis. S. A.; Mann, S. *Chem. Mater.*, **2000**, *12*, 2835. (b) Zhang, B.; Davis, S. A.; Mann, S. *Chem. Mater.*, **2002**, *14*, 1369. (c) Walsh, D.; Arcelli, L.; Toshiyuki, I.; Tanaka, J.; Mann, S. *Nat. Mater.*, **2003**, *2*, 386.

55. Valtchev, V.; Smaihi, M.; Faust, A. C.; Vidal, L. *Angew. Chem., Int. Ed.*, **2003**, *42*, 2782.

56. Valtchev, V.; Smaihi, M.; Faust, A. C.; Vidal, L. *Chem. Mater.*, **2003**, *16*, 1350.

57. Dong, A.; Wang, Y.; Tang, Y.; Ren, N.; Zhang, Y.; Yue, Y.; Gao, Z. *Adv. Mater.*, **2002**, *14*, 926.

58. Shin, Y.; Liu, J.; Chang, J. H.; Nie, Z.; Exarhos, G. J. *Adv. Mater.*, **2001**, *13*, 728.

59. Shin, Y.; Wang, L. Q.; Chang, J. H.; Samuels, W. D.; Exarhos, G. J.; *Stud. Surf. Sci. Catal*., **2003**, *146*, 447.

60. Wang, L. Q.; Shin, Y.; Samuels, W. D.; Exarhos, G. J.; Moudrakovski, I. L.; Terskikh, V. V.; Ripmeester, J. A. *J. Phys. Chem. B*, **2003**, *107*, 13793.

61. Li, X.; Jiang, J.; Wang, Y.; Nie, X.; Qu, F. *J. Sol-Gel Sci. Technol.* **2010**, *56*, 75–81.

62. (a) Davis, S. A.; Patel, H. M.; Mayes, E. L.; Mendelson, N. H.; Franco, G.; Mann, S. *Chem. Mater.* **1998**, *10*, 2516-2524. (b) B.-J. Zhang, S. A. Davis, N. H. Mendelson and S. Mann, *Chem. Commun.*, **2000**, 781.

63. (a) Fowler, C. E.; Shenton, W.; Stubbs, G.; Mann, S. *Adv. Mater.*, **2001**, *13*, 1266; (b) Lee, S. W.; Lee, S. K.; Belcher, A. M. *Adv. Mater.*, **2003**, *15*, 689.

64. Cook, G.; Timms, P. L.; Goeltner-Spickermann, C. *Angew. Chem., Int. Ed.*, **2003**, *42*, 557.

65. . Hall, S. R.; Bolger, H.; Mann, S. *Chem. Commun.*, **2003**, 2784.

66. Zhou, Y.; Antonietti, M. *Chem. Commun.*, **2003**, 2564.

67. Zhang, H. F.; Hardy, G. C.; Rosseinsky, M. J.; Cooper, A. I. *Adv. Mater.*, **2003**, *15*, 78.

68. Maekawa, H.; Esquena, J.; Bishop, S.; Solans, C.; Chmelka, B. F. *Adv. Mater.*, **2003**, *15*, 591.

69. Iwasaki, M.; Davis, S. A.; Mann S. *J. Sol-Gel Sci. Technol.*, **2004**, *32*, 99.

70. (a) Nishihara, H.; Mukai, S. R.; Yamashita, D.; Tamon, H. *Chem. Mater.*, **2005**, *17*, 683. (b) Zhang, H.; Hussain, I.; Brust, M.; Butler, M. F.; Rannard, S. P.; Cooper, A. I. *Nature Mater.* **2005**, *4*, 787-793. (c) Munch, E.; Launey, M. E.; Alsem, D. H.; Saiz, E.; Tomsia, A. P.; Ritchie, R. O. *Science* **2008**, *322*, 1516-1520. (d) De-

ville, S.; Saiz, E.; Nalla, R. K.; Tomsia, A. P. *Science* **2006**, *311*, 515-518. (e) Vickery, J. L.; Patil, A. J.; Mann, S. *Adv. Mater.* **2009**, *21*, 2180-2184.

71. (a) Bates, F. S. *Science* **1991,** 251, (4996), 898-905; Matsen, M. W.; Schick, M., *Current Opinion in Colloid & Interface Science* **1996,** 1, (3), 329-336. (b) Cheng, J. Y.; Ross, C. A.; Smith, H. I.; Thomas, E. L. *Advanced Materials*, **2006,** ***18***, 2505-2521. (c) Zhang, L. F.; Eisenberg, A. *Science* **1995**, *268*, 1728–1731.
72. Wang, H. *J. Am. Chem. Soc.* **2007***,129***,** 12924–12925.
73. Zhang, Q. L.; Gupta, S.; Emrick, T.; Russell, T. P. *J. Am. Chem. Soc.*, **2006**, *128*, 3898–3899.
74. Park, S.; Lee, D. H.; Xu, J.; Kim, B.; Hong, S. W.; Jeong, U.; Xu, T.; Russell, T. P. *Science* **2009,** *323*, (5917), 1030-1033.
75. DeGennes P.G.; Prost, J. *The Physics of Liquid Crystals*, 2nd ed. and Chandrashekhar, S. *Liquid Crystals*, 2nd ed. Cambridge University Press, New York 1992.
76. Coates, D. *J. Mater. Chem.* **1995,** *5*, (12), 2063-2072.
77. Natarajan, L. V.; Shepherd, C. K.; Brandelik, D. M.; Sutherland, R. L.; Chandra, S.; Tondiglia, V. P.; Tomlin, D.; Bunning, T. J. *Chem. Mater.* **2003,** *15*, (12), 2477-2484.
78. Maschke, U.; Coqueret, X.; Benmouna, M. *Macromolecular Rapid Communications* **2002,** *23*, (3), 159-170.
79. Poulin, P.; Raghunathan, V. A.; Richetti, P.; Roux, D. *J. Phys. II France* **1994**, *4*, 1557.
80. Poulin, P.; Stark, H.; Lubensky, T. C.; Weitz, D. A. *Science* **1997**, *275*, 1770.
81. Poulin, P.; Weitz, D.A. *Phys. Rev. E* **1998**, *57*, 626.

82. Mondain-Monval, O.; Dedieu, J. C.; Gulik-Krzywicki, T.; Poulin, P. *Eur. Phys. J. B* **1999**, *12*, 167.

83. Ramaswamy, S.; Nityananda, R.; Raghunathan, V. A.; Prost, J. *Mol. Cryst. Liq. Cryst.* **1998**, *288*, 175.

84. Völtz, C.; Maeda, Y.; Tabe, Y.; Yokoyama, H. *Phys. Rev. Lett.* **2006**, *97*, 227801.

85. Loudet, J. C.; Barois, P.; Poulin, P. *Nature* **2000**, *407*, 611 ; Loudet, J. C.; Barois, P.; Auroy, P.; Keller, P.; Richard, H.; Poulin, P. *Langmuir* **2004**, *20*, 11336.

86. Musevic, I.; Skarabot, M.; Tkalec, U.; Ravnik, M.; Zumer, S. *Science* **2006**, *313*, 954.

87. Zapotocky, M.; Ramos, L.; Poulin, P.; Lubensky, T. C.; Weitz. D. A. *Science* **1999**, *283*, 209.

88. Basappa, G.; Suneel; Kumaran, V.; Nott, P. R.; Ramaswamy, S.; Naik, V. M.; Rout, D. *Eur. Phys. J. B* **1999**, *12*, 269.; Shouche, S. V.; Chokappa, D. K.; Naik, V. M.; Khakhar, D. V. *J. Rheol*. **1994**, *38*, 1871.

89. Meeker, S. P.; Poon, W. C. K.; Crain, J.; Terentjev, E. M. *Phys. Rev. E* **2000**, *61*, R6093.

90. Anderson, V. J.; Terentjev, E. M.; Meeker, S. P.; Crain, J.; Poon, W. C. K. *Eur. Phys. J. E* **2001**, *4*, 11.

91. Petrov, P. G.; Terentjev, E. M. *Langmuir* **2001**, 17, 2942.

92. Cleaver, J.; Vollmer, D.; Crain, J.; Poon, W. C. K. *Mol. Cryst. Liq. Cryst.* **2004**, *409*, 59.

93. Vollmer, D.; Hinze, G.; Poon, W. C. K.; Cleaver, J.; Cates, M. E. *J. Phys. Cond. Matt.* **2004**, *16*, L227.

94. West, J. L.; Glushchenko A. ; Liao G.; Reznikov Y.; Andrienko D.; Allen M. P. *Phys. Rev. E* **2002**, *66*, 012702.

95. Holmberg, K.; Jönsson, B.; Kronberg, B.; Lindman, B.; *Surfactants and Polymers in Aqueous Solution*; 2nd ed. John Wiley & Sons: West Sussex, U.K., 2003.

96. Israelachvili, J. N. *Intermolecular and Surface Forces* **1992** 2nd ed., Academic Press Limited, London.

97. (a) Kunieda, H.; Ozawa, K.; Huang, K.-L. *J. Phys. Chem. B* **1998,** *102*, 831.; (b) Kunieda, H.; Shigeta, K.; Ozawa, K. *J. Phys. Chem. B* **1997,** *101,* 7952-7957.

98. Kresge, C. T.; Leonowicz, M. E.; Roth, W. J.; Vartuli, J. C.; Beck, J. S. *Nature* **1992,** *359*, (6397), 710-712.

99. Attard, G. S.; Glyde, J. C.; Goltner, C. G., *Nature* **1995,** *378*, (6555), 366-368.

100. (a) Polarz, S.; Antonietti, M. *Chem. Commun.* **2002**, *22*, 2593-2604. (b) Antonietti, M. *Current Opinion in Colloid & Interface Science* **2001,** *6*, (3), 244-248. (c) Goltner, C. G.; Antonietti, M. *Adv. Mater.* **1997,** *9*, (5), 431. (d) Goltner, C. G.; Henke, S.; Weissenberger, M. C.; Antonietti, M. *Angew. Chem. Int. Ed.* **1998,** *37*, (5), 613-616. (e) Thomas, A.; Schlaad, H.; Smarsly, B.; Antonietti, M. *Langmuir* **2003,** *19*, (10), 4455-4459. (f) Weissenberger, M. C.; Goltner, C. G.; Antonietti, M. *Phys. Chem. Chem. Phys.* **1997,** *101*, (11), 1679-1682. (g) Attard, G. S.; Goltner, C. G.; Corker, J. M.; Henke, S.; Templer, R. H., *Angew. Chem. Int. Ed.* **1997,** *36*, (12), 1315-1317. (h) Kim, J. U.; Cha, S. H.; Shin, K.; Jho, J. Y.; Lee, J. C. *Adv. Mater.* **2004,** *16*, (5), 459-464.

101. Braun, P. V.; Osenar, P.; Tohver, V.; Kennedy, S. B.; Stupp, S. I., *J. Am. Chem. Soc.* **1999,** *121*, (32), 7302-7309.

102. Hentze, H.-P.; Kaler, E. W. *Chem. Mater.* **2003**, *15*, 708; Antonietti, M.; Goeltner, C. G.; Hentze, H.-P. *Langmuir* **1998**, *14*, 2670.

103. DeGennes, P. G. *Scaling Concepts in Polymer Physics*; Cornell University Press: Ithaca, NY, **1979**; p 49.

104. Lester, C. L.; Smith, S. M.; Jarrett, W. L.; Guymon, C. A. *Langmuir* **2003,** *19*, (22), 9466-9472.; Lester, C. L.; Smith, S. M.; Guymon, C. A. *Macromolecules* **2001,** *34*, (25), 8587-8589.

105. (a) Wadekar, M. N.; Pasricha, R.; Gaikwad, A. B.; Kumaraswamy, G. *Chem. Mate*r. **2005**, *17*, 2460. (b) Guruswamy, K.; Wadekar, M. N.; Agrawal, V. V.; Pasricha R. *Polymer*, **2005**, *46*, 7961–7968.

106. Bouchama, F.; Thathagar, M. B.; Rothenberg,G.; Turkenburg, D. H.; Eiser, E. *Langmuir* **2004**, *20*, 477-483.

107. (a) Koltover, I.; Salditt, T.; Radler, J. O.; Safinya, C. R. *Science* **1998,** *281*, (5373), 78-81*;* Radler, J. O.; Koltover, I.; Salditt, T.; Safinya, C. R. *Science* **1997,** *275*, (5301), 810-814; (b) Safinya, C. R.; Ewert, K.; Ahmad, A.; Evans, H. M.; Raviv, U.; Needleman, D. J.; Lin, A. J.; Slack, N. L.; George, C.; Samuel, C. E., *Philosophical Transactions of the Royal Society A: Mathematical, Physical and Engineering Sciences* **2006,** *364*, (1847), 2573-2596.

108. Caffrey, M. *Current Opinion in Structural Biology* **2000**, *10*, 486–497.

Chapter 2

Assembly of Silica Nanospheres in Surfactant Hexagonal (H_1) Mesophase

2.1. Introduction

When colloids are dispersed in an ordered matrix, they self-assemble, driven by their interactions with the matrix, and by matrix-mediated particle-particle interactions. Materials with self-assembled particulate phases are found in many applications such as cosmetics, food, pharmacy or catalysis. Increasingly, it has been realized that control over spatial localization and assembly of particles in ordered block-copolymers[1,2] or in liquid crystals has important implications for novel functional materials, such as, negative refractive index "metamaterials"[3], etc.

In orientationally ordered nematics, dispersion of colloids results in long-range, anisotropic inter-particle interactions originating from the elasticity of the liquid crystalline matrix.[4-6] These inter-particle interactions result in self-assembly of the particles in the liquid crystalline matrix. For example, chain-like linear arrays of colloidal silicone drops with dipolar interactions, mediated by a nematic matrix, have been reported[7]; as well as two-dimensional crystals of colloids with quadrupolar interactions.[8] Other morphologies have also been reported: in cholesteric nematic[9] and lamellar smectic phases,[10, 11] where large colloidal inclusions phase separate to defect nodes and stabilize a disclination network, resulting in increased solid moduli. Further, kinetically determined cellular, striped or "root-like" structures have been shown to form by particles excluded from the nematic phase.[12-14] Purely geometrically driven localization of particles in one of the contiguous fluid regions in sponge phases has also been reported.[15,16]

Most of the literature on interparticle interactions in liquid crystals focus on colloidal entities with typical size scales, R ~ O(100 nm – 1 μm), dispersed in a thermotropic nematic such as 5-cyanobiphenyl (5CB). In such nematics, the orientational

elasticity is characterized by three elastic constants, K_1 (splay), K_2 (twist) and K_3 (bend). In most cases, it is assumed that $K_1 \sim K_2 \sim K_3 \sim K \sim O(10\ pN)$. Thus, the free energy cost of accommodating the colloidal particles in the liquid crystal, KR is several hundred to several thousand times the thermal energy k_BT and thermal motion is strongly reduced. Inclusion of colloids in an orientationally ordered fluid results in topological defects that satisfy boundary conditions for director orientation at the surface of, and far from the colloid. Thus, the nature of interparticle interactions are determined by the ratio between WR^2 (where W is the anchoring energy at the surface) and KR.

Here, we focus on the organization of particles in lyotropic hexagonal surfactant-water systems. It has been reported that addition of nanoparticles to even relatively simple surfactant micellar systems results in rich phase behavior since preferential adsorption of the surfactant onto the particles could open up a ternary region in the surfactant-water-particle phase diagram.[17] In hexagonal phases (H_1), cylindrical micelles of surfactants are packed in a hexagonal array in water. For such phases, typical repeat spacings are between 5 to 10 nm, about ten times larger than the mesogen size in thermotropic nematics, and the elastic constants are estimated to be $K \sim O(1\ pN)$[18], viz. about a tenth of those for thermotropic nematics. Thus, for particles with a size, R, comparable with the hexagonal phase repeat distance, KR is on the order of a few k_BT. Thus, as particle size changes in this range, one would imagine a qualitative change in particle organization. It has been reported that nanoparticles smaller than the characteristic size of the hexagonal mesophase are included in and therefore, *template* the mesophase[19, 20] while larger particles are expelled from the cylindrical micelles.[19, 21] A mean field description[22] of large particles (viz. much larger than the characteristic me-

sophase repeat spacing) in a hexagonal columnar phase indicates that the particles align at some finite angle, θ (< 90^o) with the cylinder axis. This has, however, not been experimentally verified. Thus, there is currently no detailed understanding of the structures formed when particles assemble in hexagonal surfactant mesophases, the processes by which these structures form and their dependence on particle size. We address these issues in this chapter.

2.2. Experimental

2.2.1. Materials:

Non ionic surfactant nonaethylene glycol dodecyl ether ($C_{12}E_9$) was obtained from Sigma Aldrich and was used as received (HPLC previously reported[23]). Distilled deionized water (resistivity = 18.2 MΩ.cm) from a Millipore MilliQ unit was used to prepare the surfactant mesophases.

Polysilsesquioxane hydrate-Octakis tetramethylammonium substituted (a cage-like molecule with the molecular formula $C_{32}H_{96}O_{20}Si_8 \cdot 60H_2O$, termed Sil, for convenience, in this chapter) was obtained from Sigma Aldrich and used as received. The structure of Sil is shown in Figure 2.1. Sil is soluble in water and is reported to be stable at the experimental conditions used here. Data from the supplier states that Sil has a size of between 1.5 and 3 nm. The silica nanoparticles, Ludox FM, SM, LS and TM were obtained as electrostatically-stabilized concentrated dispersions (between 15 and 50 weight %) from Sigma Aldrich and were used as received. Larger silica particles, synthesized using the Stöber process were generously prepared for us by a collaborator (by Dr. B. L. V. Prasad's group in the Physical Chemistry Division, NCL, Pune) and supplied in the form of a dispersion.

2.2.2. Characterization Tools:

SAXS was performed on a Bruker Nanostar, equipped with a rotating (copper) anode generator operating at 45kV and 100mA (λ= 1.54 Å). The X-rays are collimated through a 3 pin-hole system and data is acquired using a 2-D gas filled Hi-Star® detector over a *q*-range of 0.011 to 0.2Å^{-1}. The detector was calibrated using a silver behenate sample. Samples were sealed in quartz capillaries having an outer diameter of 2 mm and wall thickness of ≈ 10 μm, and temperature control was via the Bruker hot stage. We calibrated the hot stage using the isotropic-nematic phase transition of 5CB. The capillary filled with gel sample after proper sealing was heated to 50^{o}C and held there for 5 minutes so as to remove any shearing history. Later it was cooled back to room temperature at 5^{o}C/min. The collimation tubes and flight path to the detector were evacuated, but the sample chamber was maintained at ambient pressure. Data was corrected for background scattering (including solvent scattering and air scattering). The 2D data were reduced to 1D by circularly averaging, using the software provided with the instrument.

Polarized optical microscopy (POM) was performed on an Olympus BX-50, equipped with a Mettler hot stage (calibrated using the phase transition of 5CB). To perform freeze fracture transmission electron microscopy (FFTEM), a small drop of the sample was cooled on a gold planchette that was subsequently vitrified by plunging into liquid propane (liquefied using liquid nitrogen). This vitrified drop was then fractured inside an evacuated chamber kept at -150°C. The fractured surface was coated by evaporating 3 to 4 nm of platinum at an angle of 45°, followed by 30 nm of carbon to reinforce the metal coating. The Pt-C replica was treated with a dilute (10%) solution of HF for 12 hours to remove all the silica particles and then washed repeat-

edly with a methanol/water mixture before it was dried for TEM imaging. TEM imaging was performed on a 100 kV Hitachi H600.

2.2.3. Preparation of particle/H_1 phase composites:

The particle dispersions or Sil were sonicated in a bath for 30 minutes and, were then added to the $C_{12}E_9$/water mixture at 50°C, above the isotropic-H_1 transition temperature. The ratio of the surfactant to water in the final composite was maintained as 1, by accounting for the water in the particle dispersions during addition. We have estimated the change in surfactant to water ratio for adsorption of surfactant on the particle surface for the highest particle loadings and for the smallest particles used in our experiments, and find that this change is small. The composite mixture was thoroughly vortexed to ensure homogeneous mixing and was subsequently allowed to cool to ambient temperature. The approximate cooling rate in our experiments was 5^oC/min.

2.3. Results

2.3.1. Particle characterization:

We characterized the size distribution for Ludox particles using TEM (by averaging over about 200 particles); by fitting the form factor from small angle X-ray scattering (SAXS) on dilute solutions and, by using dynamic light scattering (DLS). We obtain the form factor, $F^2(q)$, from SAXS on 1 weight % (≈ 0.5 volume %) solutions of particles, containing 25 mM NaCl to screen long range interparticle electrostatic interactions. We fit the SAXS data assuming that the particles are spherical with a normal distribution of particle diameters and, obtain good fits with diameters of 7.6±1.9 nm, 10.7±1.9 nm, 14.8±1.8 nm and 25.6±3.2 nm for Ludox FM, SM, LS and

TM respectively (Figure 2.2 a). The DLS gives decay of the intensity autocorrelation function, $[g^2(t, a) – 1]$ for dilute solutions (0.5% by weight) for particles with radius, a. The solid lines represent fits to the DLS data assuming spherical particles with a normal distribution of diameters. The inset shows the fitted particle size distribution (volume fractions). Fitting yields mean diameters/standard deviations of 8/3.4nm, 10.2/2nm, 14.8/2.5 and 27/2.1nm for Ludox FM, SM, LS and TM particles respectively (Figure 2.2 b). The average particle sizes from the SAXS measurements accord well with those estimated from DLS. Therefore, we term the Ludox FM, SM, LS and TM particles as S8, S11, S15 and S26 respectively. The particle sizes from SAXS/DLS are higher than those specified by the manufacturer: 5 nm, 7 nm, 12 nm and 22 nm for Ludox FM, SM, LS and TM respectively. Our TEM measurements (averaged over images of around 200 particles) on Ludox LS and TM indicate a particle size of 12.1±1 nm and 22.4±1.7 nm respectively, in accord with the manufacturer specifications (Figure 2.2 c, d). Therefore, we believe that drying of the particles during preparation for electron microscopy results in a shrinkage in the size of the particles, in accord with previous reports.[25] TEM measurements showed that the larger silica particles, synthesized using the Stöber process were 500 nm in diameter, hence we term them S500.

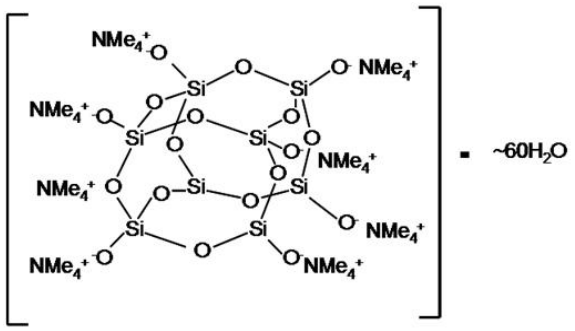

Figure 2.1. Schematic of the molecular structure of Sil (Polysilsesquioxane; molecular analogue of silica nanoparticle).

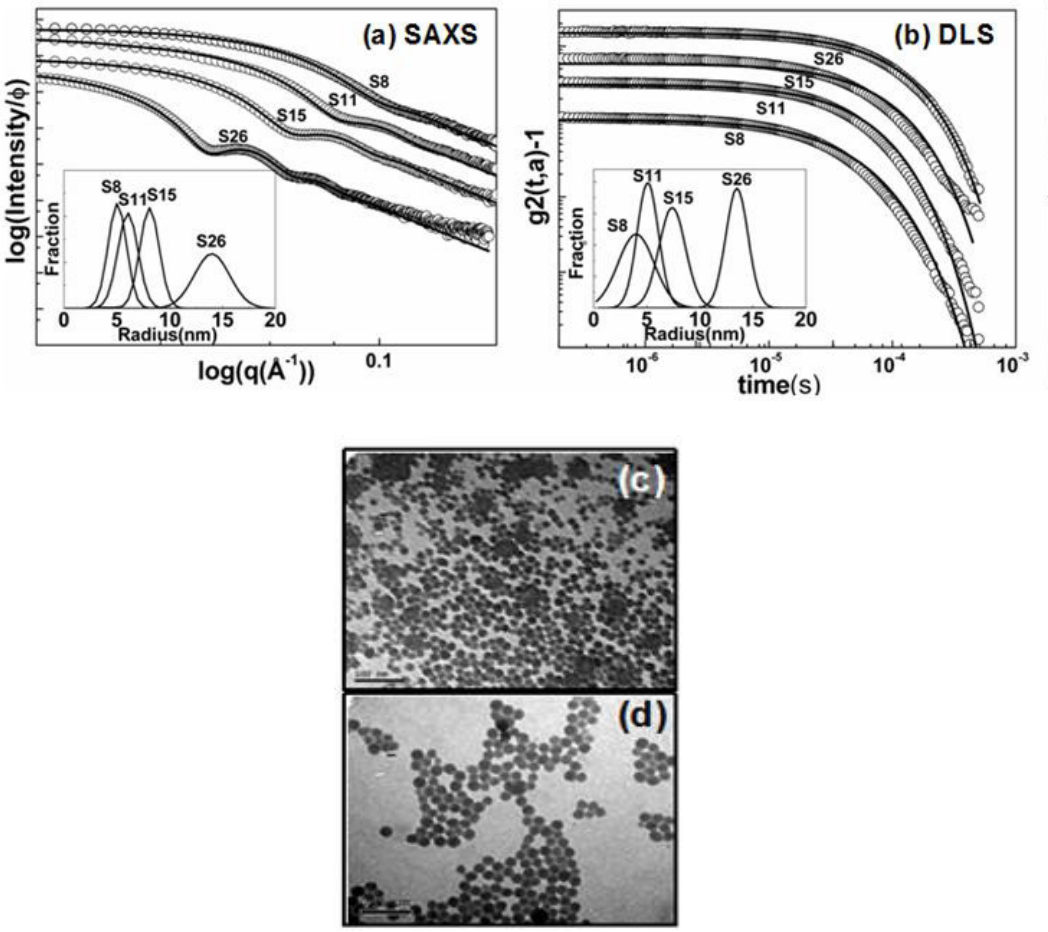

Figure 2.2. Characterization of the particle size distribution for the silica particles. (a) SAXS, (b) DLS, (c) and (d) TEM measurements. The scale bar in both TEM images represents 100 nm.

2.3.2. Effect of particle size:

The $C_{12}E_9$-water system organizes into a hexagonal phase (H_1) at surfactant concentrations between about 35-70% by weight, at room temperature.[26] In all the compositions described in this chapter, we maintain a surfactant to water weight ratio of 1, viz. our compositions are roughly in the middle of the H_1 phase concentration window. This system transitions from H_1 to an isotropic micellar phase at a temperature $T_{HI} \approx 40°C$. Accordingly, at $T < T_{HI}$, we see the SAXS signature for a H_1 phase (Figure 2.3, top), with a primary peak at $q_1 = 0.11$ Å^{-1} and a secondary peak at $q_2 = 0.189$ Å^{-1} ($q_2/q_1 \approx \sqrt{3}$; characteristic center-to-center cylinder distance = $2\pi/q_1 \approx 5.7$ nm), and observe the formation of a characteristic fan-shaped texture between crossed polarizers (see, for example, Figure 2.5 a).

Organization of the surfactant into a H_1 phase is preserved in composites containing 5% by weight of Sil or of the silica particles, as indicated by the characteristic SAXS signatures (primary and secondary peaks such that $q_2/q_1 \approx \sqrt{3}$; Figure 2.3). For the H_1-Sil composite, we observe a shift in q_1 to lower q (= 0.104 Å^{-1}) indicating an increase in the surfactant cylinder center-to-center distance to 6.1 nm. This suggests that Sil enters the space between cylinders and swells the H_1 phase. For composites containing the silica particles, there is a shift in q_1 for S8 ($q_1 = 0.107$ Å^{-1}) and for S11 ($q_1 = 0.108$ Å^{-1}) – however, for the larger particles (S15, S26 and S500), there is no shift in q_1 relative to the neat H_1 phase (Figure 2.3).

For composites containing silica particles, we observe additional features in the SAXS intensity at low q ($q < 0.1$ Å^{-1}, lower than the H_1 phase primary peak). These features are not observed for the neat H_1 phase or for the H_1-Sil composite, and clearly arise due to scattering from the silica particles. We compare the scattering for

the H_I-silica composites at $q < 0.1$ Å^{-1} to the scattered intensities from dilute solutions of the particles (particle weight fraction = 1%, viz. volume fraction ≈ 0.5% ; scattered intensity shown in dotted lines next to that from the corresponding composite). Scattering from dilute solutions of the particles is dominated by the particle form factor, $F^2(q)$ – we confirm this by examining the scattered intensity from particle solutions at lower concentrations (particle weight fraction = 0.5%) and noting that shape of the SAXS intensity is unchanged. With increase in particle size, the scattered intensity due to $F^2(q)$ shifts to lower q, and for S500, we observe only the tail of the scattering from particle $F^2(q)$. As our data at low q is limited by the beamstop (at $q = 0.011$ Å^{-1}, corresponding to a d-spacing of around 55 nm), SAXS does not give us much information about the H_I-S500 composite. However, for H_I-S8, H_I-S11, H_I-S15 and H_I-S26, we notice that scattering at $q < 0.1$ Å^{-1} exhibit peaks (indicated by arrows in Figure 2.3) that are not present in the corresponding particle $F^2(q)$, indicating the influence of particle-particle correlations in the composites. We obtain a "pseudo" structure factor by normalizing the scattered intensity from the composites for $q < 0.1$ Å^{-1}, by the corresponding particle $F^2(q)$. The pseudo structure factors for the composites all show a prominent peak at q values of 0.07 Å^{-1}, 0.055 Å^{-1}, 0.04 Å^{-1} and 0.024 Å^{-1} for H_I-S8, H_I-S11, H_I-S15 and H_I-S26 respectively. It is interesting to compare the d-spacings obtained from these structure factor peaks, viz. 9 nm, 11.4 nm, 15.8 nm and 26.2 nm respectively for H_I-S8, H_I-S11, H_I-S15 and H_I-S26, with the average particle diameter for these particles, 7.6 nm, 10.7 nm, 14.8 nm and 25.6 nm (section 2.3.1). This suggests that in all the H_I-particle composites examined here, there is particle aggregation.

For surfactant H_1 mesophases, the typical elastic constant, K ~ O(1 pN). Therefore, while the free energy penalty for inclusion of the particles in the mesophase is a few kT for a particle diameter of 8 nm, this increases to O(100 kT) for particles with a diameter of 500 nm. Accordingly, we observe that there is swelling of the mesophase (viz. increased spacing between surfactant cylinders) for H_1-Sil and for the H_1-S8 and H_1-S11 composites. At the same time, we observe clear evidence for particle aggregation from the structure factor peaks for H_1-S8, H_1-S11, H_1-S15 and H_1-S26. Thus, our data suggests that Sil (that we consider a molecular analog of a water soluble silica particle, and that is around 1.5 to 3 nm in size), and at least some fraction of the smaller silica particles (S8 and S11) partition to the H_1 phase and are located in the aqueous regions between surfactant cylinders. For composites with S15 and larger particles, there is no evidence for swelling of the H_1 phase. Further, for all silica particles larger than Sil, we observe particle aggregation. Thus, there appears to be a systematic change in the structure of the H_1 composites with the size of the added particles – particles smaller than the characteristic mesophase repeat distance (Sil) swell the mesophase; particles with a size comparable to the mesophase repeat distance (S8 and S11) partition between dispersed and particle-particle aggregated phases, while larger particles (S15 and larger) organize into a particle-aggregate phase.

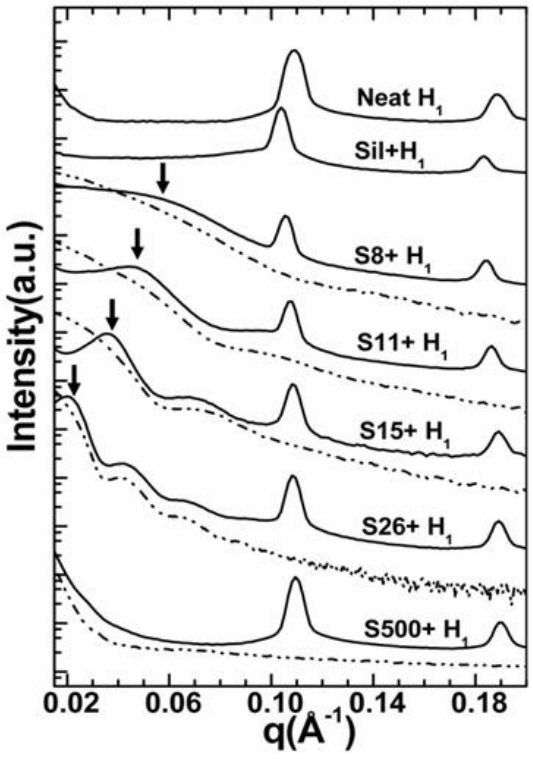

Figure 2.3. SAXS for neat H_1 phase (top) and for composites containing 5% (by weight) of Sil, S8, S11, S15, S26 and S500 (from top to bottom). The dilute solution form factor, $F^2(q)$ is indicated by dashed lines next to the SAXS from the corresponding composite. Arrows indicate the peak in the pseudo- structure factor due to particle aggregation. Data are plotted on the same scale and are vertically shifted for clarity.

2.3.3. Effect of particle concentration:

We now focus on the effect of particle concentration on particle organization and the structure of the hexagonal phase. We observe that for H_1-Sil composites, the swelling of the H_1 phase increases systematically with increased Sil loading up to just above 5% (Data not presented). Beyond 5%, the hexagonal phase is no longer stable and transforms into a low-viscosity micellar phase. This data suggests that, due to the small size of Sil relative to the surfactant structure, Sil behaves like a solvent, and

changes the molecular curvature of the surfactant micelles.[27] All other composites (H_I-S8, H_I-S11, H_I-S15, H_I-S26 and H_I-S500) retained the hexagonal phase even at particle loadings close to 20% by weight. Further, all these composites exhibited qualitatively similar behavior – therefore, we exemplify their behavior by focusing only on the H_I-S15 composites in the rest of this chapter.

We observe that, even at particle loadings as small as 1% (by weight), particle aggregates form, as evidenced by the peak in the pseudo structure factor at low q (Figure 2.4 a). With increase in particle loading from 1% to 17.6%, there is no change in the peak positions for either the particle structure factor, or for the H_I phase. However, increasing the particle loading leads to broadening of the H_I phase peaks. We use the Debye-Scherrer relation to obtain an estimate of the coherence length for hexagonal order, $d_c = 2\pi/\Delta q_1$ where Δq_1 is the full width at half maximum for the q_1 peak. The coherence length, d_c decreases monotonically from 81 nm for the neat H_I phase to 59 nm for 17.6% by weight of the particles. As mentioned earlier, the qualitative behavior described here is observed for all the H_I-particle composites – viz. there is no change in the position of either the particle aggregation peak or the H_I phase peaks with particle loading (from the lowest examined loading of 1% by weight to around 20% by weight). Further, there is a decrease in the SAXS coherence length for H_I order and, the coherence length decreases with the particle loading by approximately the same extent for H_I-S8, H_I-S11, H_I-S15 and H_I-S26 (Figure 2.4 b). The decrease in coherence length with increased particle loading in our work is similar to observations of reduced short-range order in small molecule smectic-A phases with increased loadings of silica aerosils.[28] While silica aerosils are fused aggregates of silica nanoparticles, in our work, the silica particles form aggregates on dispersion in the hexagonal phase. It

is interesting that in both cases, a decrease in the coherence length for liquid crystalline order is observed with increased particle loading.

We observe the texture of the mesophase as a function of particle loading using polarized light microscopy (POM, Figure 2.5). For the neat H_1 phase, we can clearly observe a fan-like structure that is typical for the H_1 phase (Figure 2.5 a). There is no qualitative change in the fan-like texture as particle loading is increased from 1% to 15% by weight for the H_1-S15 composites (Figures 2.5 b-d) – however, there is a decrease in the length scale that characterizes this texture. While the POM length scale is orders of magnitude larger than d_c, it appears qualitatively meaningful that both lengths decrease with increasing particle loading (Figures 2.4 b, 2.5).

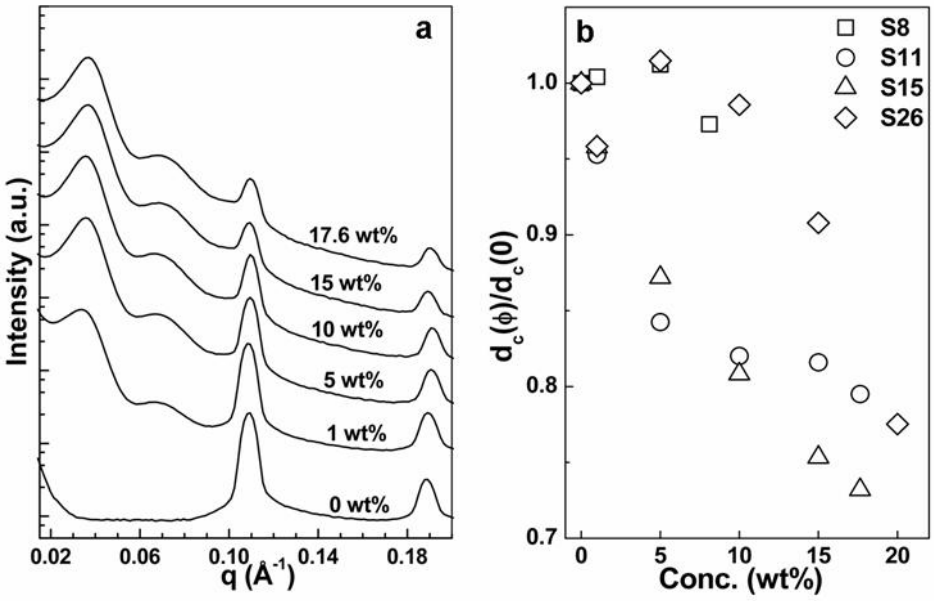

Figure 2.4. (a) SAXS for S15-H_1 composites at particle concentrations (percent, by weight) of 0, 1, 5 , 10, 15 and 17.6 (bottom to top). (b) Decrease in the Debye-Scherrer length, d_c, obtained from the primary H_1 peak (normalized to 1 for the neat H_1 phase) with increase in particle concentration for composites with S8, S11, S15 and S26.

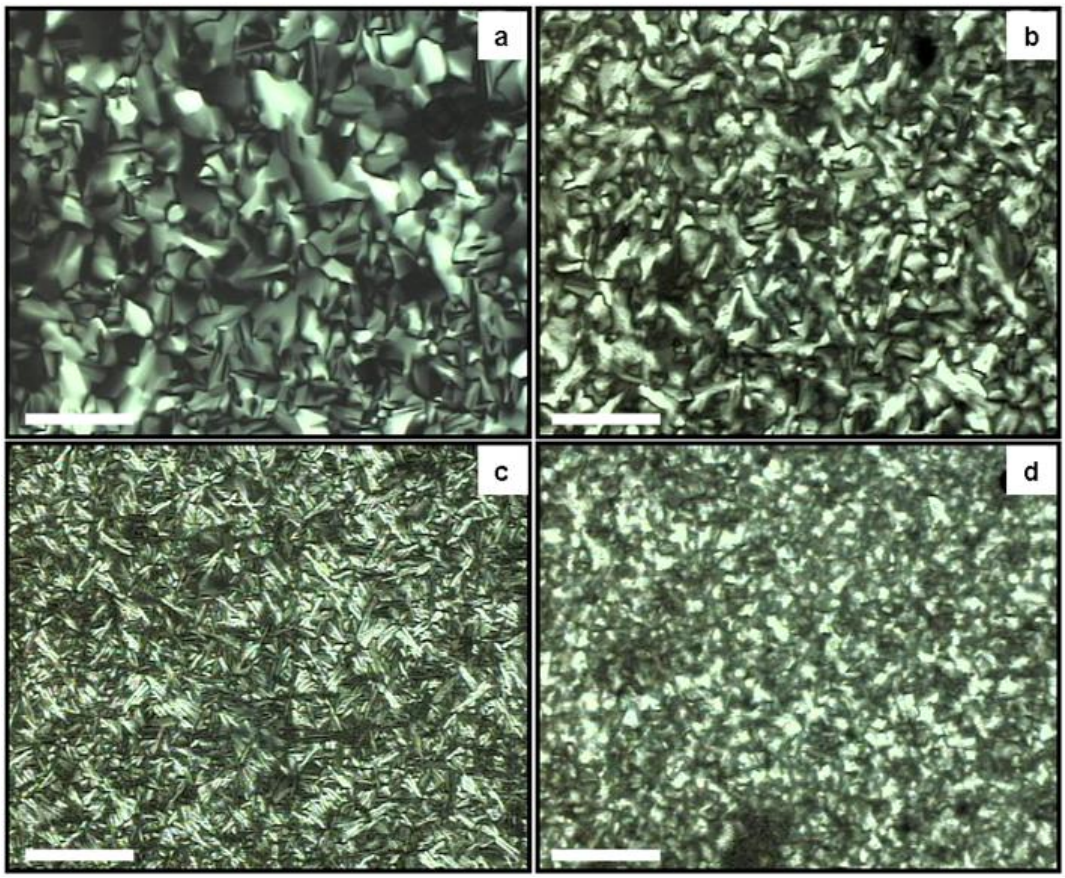

Figure 2.5. Optical micrographs between crossed polarizers for S15-H_1 composites at a particle concentration (by weight) of (a) 0%; (b) 1%; (c) 5% and (d) 15%. The scale bar corresponds to 200µm.

2.3.4. Structure formed by particle aggregation:

It is difficult to quantify the length scale of hexagonal domains from POM; neither is it possible to comment on the organization of nanoparticles in the mesophase. Therefore, we use freeze fracture TEM (FFTEM) to investigate nanoparticle organization in the mesophase. The replica sample preparation protocol adopted in our work allows us to observe only the particles and not the surfactant structures in the H_1 phase around the particles. FFTEM of a 5% (by weight) H_1-S15 composite reveals that the silica particles organize into a network structure, with strands comprised of ≈ 4-5

particles (viz. ≈ 90 nm thick) forming a network with a mesh size (viz. strand separation) of around 500 nm (Figure 2.6 a). FFTEM of composites prepared with 5 weight % of S11 (Figure 2.6 b) and S26 (Figure 2.6 c) reveal the formation of similar strands as for H_1-S15. We did not attempt FFTEM to image the H_1-S8 composites due to difficulties associated with replicating and imaging the small silica particles using our sample preparation protocol. Interestingly, in the H_1-S11 composite, we are able to identify several isolated particles (arrows in Figure 2.6 b) – however, for H_1-S15 and H_1-S26 composites, particles were almost always observed in strand-like aggregates. It is possible that the isolated particles imaged in the H_1-S11 composite represent the fraction that is partitioned into and swells the H_1 phase.

Thus, the combination of SAXS and real space imaging suggests that the silica particles phase separate from the H_1 phase and aggregate to form linear strands that organize into a scaffold-like network. We now examine the process by which this structure forms as the surfactant-water-particle composite is cooled from the high temperature isotropic phase to room temperature.

2.3.5. Reversibility of particle aggregation at $T > T_{HI}$:

In the isotropic region (50^{o}C), SAXS from the surfactant-water-S15 (47.5%-47.5%-5%, by weight) system indicates a micellar phase with a broad peak at q = 0.105 Å^{-1} (average micellar spacing ≈ 6 nm, Figure 2.7). At low q (< 0.09 Å^{-1}), the form of the SAXS is similar to the dilute aqueous solution particle form factor (Figure 2.7, compare top two curves). Thus, in the isotropic micellar solution, scattering from the particle phase is dominated by the particle form factor and the structure factor from particle-particle correlations, $S(q) \approx 1$.

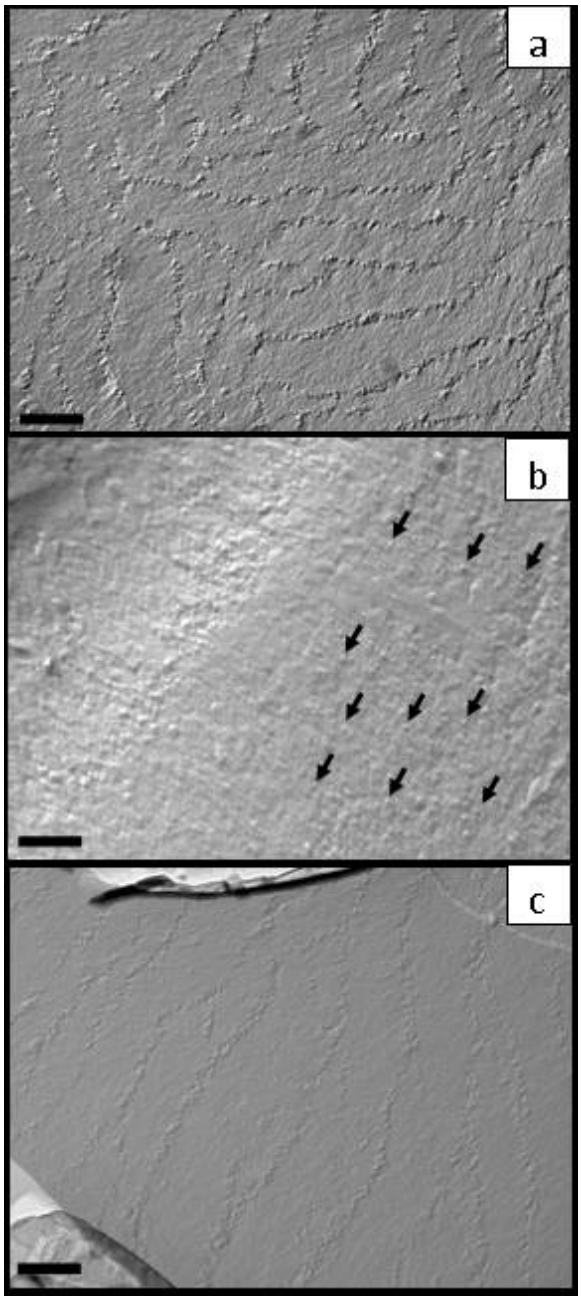

Figure 2.6. Freeze Fracture TEM images of composites of the H_1 phase with 5% (by weight) of (a) S15, (b) S11 and (c) S26. The arrows in (b) indicate some of the isolated particles in the S11-H_1 composite, while a diagonal strand-like aggregate is visible on the left. The scale bar in all images corresponds to 500 nm.

On cooling the mixture at 5°C/min, we observe the appearance of the pseudo structure factor peak at 0.04 $Å^{-1}$ at around 44°C, correlated with the appearance of the H_1 phase peaks ($q_2/q_1 \approx \sqrt{3}$, Figure 2.7). We have already seen that the "structure factor" peak arises from the strand-like aggregation of particles, with a spacing comparable to wavelength of visible light (Figure 2.6). Thus, formation of this structure leads to intense light scattering and the composite transitions from a transparent low-viscosity high temperature phase to an opaque gel as compared to transparent neat H_1 phase.

The shape of the SAXS curve is essentially unchanged from 40°C to room temperature. We have repeatedly cycled the system between isotropic and hexagonal phases and find that the transition between the high temperature clear phase where the particles are dispersed, and the opaque gel phase with the particle strands, is fully reversible. On heating at 5°C/min into the isotropic phase, the peaks corresponding to the hexagonal phase and to particle aggregation both disappear, and both re-appear on cooling into the hexagonal phase (Figure 2.7). This thermoreversible particle aggregation is intriguing, since aggregation of silica nanoparticles is typically irreversible. This behaviour is explored in detail in a subsequent chapter (Chapter 3).

Interestingly, the data in Figure 2.7 indicates an isotropic-H_1 transition temperature of around 44°C, significantly higher than the transition temperature of around 40°C for the neat H_1 phase. We confirm this using both SAXS and POM and note that transition temperatures obtained from POM are about 1°C lower than from SAXS. This *increase* in the transition temperature on addition of the particles is rather unusual – previous investigations of particle-doped thermotropics[12,13] and lyotropics[3] have reported a *decrease* in the isotropization temperature with increased particle

loading and have attributed this mesophase destabilization to the cost of accommodating the added particles. It is worth noting that recent investigations[13] on PMMA particle-doped nematics suggest that the decrease in transition temperature might arise from contamination by residual solvent present in the particles rather than from the incorporation of the particles themselves in the liquid crystal.

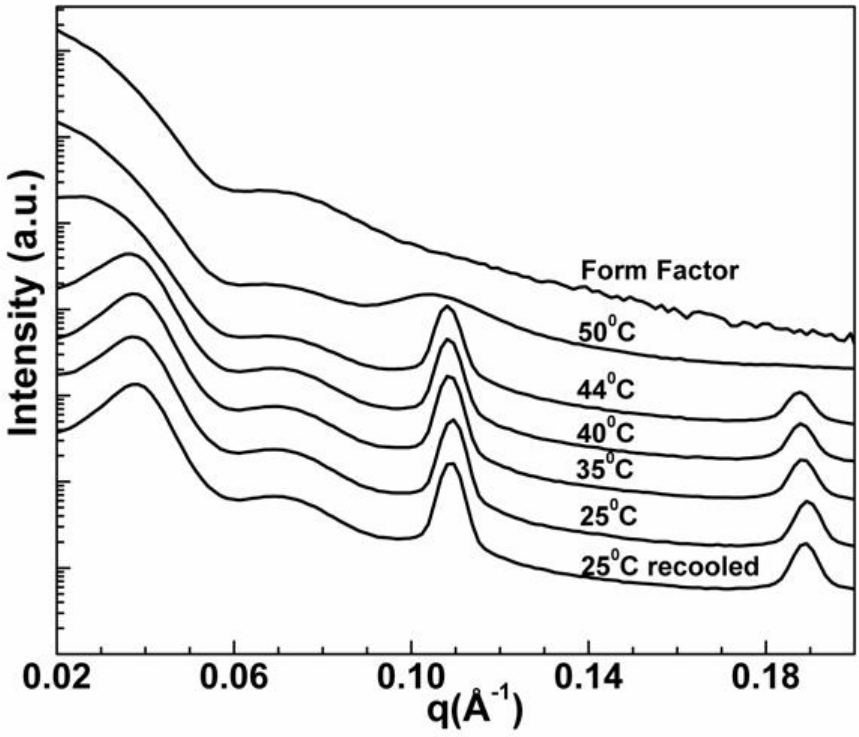

Figure 2.7. SAXS from a 5% (by weight) S15-H_1 composite as a function of temperature, as it is heated from 25°C to 50°C, and on cooling back to 25°C, as indicated. The dilute solution form factor from the S15 particles is shown for comparison. Data is plotted on the same scale and shifted vertically for clarity.

To understand the unusual increase in the H_1-isotropic transition for the composites, we use POM of slowly heated/cooled (0.1°C/min) samples. The "neat" H_1 phase shows a transition at about 40°C, and does not exhibit hysteresis. For composites containing S15, the transition temperature increases to 40.2°C for a loading of 0.25% (by weight) to 42.4°C for 1% and saturates at 42.8°C for particle loadings above 1%. Thus, the transition temperature increases with particle concentration, saturating at a loading of around 1% suggesting that the addition of the silica nanoparticles might facilitate nucleation to form the H_1 phase. The stabilization of ordered lyotropic phases in the vicinity of surfaces, leading to an increase in phase transition temperatures has been reported in the literature.[29] It is possible that the initial increase and subsequent saturation in transition temperature that we observe in our system might result from nucleation of the H_1 phase at the surface of the dispersed silica particles.[30]

2.3.6. Mechanism of Particle Aggregation:

To investigate the formation of the particles network on cooling into the H_1 phase, we use SAXS to observe structure development in a 5% S15 composite quenched from the isotropic phase (50°C) and held isothermal at the isotropic-mesophase transition point (44°C), where mesophase formation happens over a long time scale. Immediately after quenching, we observe a broad SAXS peak at 0.105 $Å^{-1}$, characteristic of the micellar phase and no evidence for particle aggregation (Figure 2.8, compare with particle form factor). With time, the H_1 phase develops. After 4 hours, we observe the appearance of a peak corresponding to the H_1 phase at q_1, that overlaps with the broad micellar peak, indicating that both phases are present. After 12 hours, the broad peak characteristic of the micellar phase totally disappears while the H_1 peaks grow indicating complete transformation of the isotropic micellar sample to

the H_1 phase. We quantify the time-dependent particle aggregation by monitoring the evolution of an apparent particle structure factor, $S_A(q)$, obtained by normalizing the SAXS at longer times with that at t = 0 (Figure 2.8, inset). $S_A(q)$ arises from the ordering of the particles relative to their initial dispersed state at t = 0. We model $S_A(q)$ as arising from liquid-like correlations and use the Ornstein-Zernike relation with the Percus-Yevick closure, assuming hard-sphere particle-particle interactions.[31] With time, $S_A(q \rightarrow 0)$ decreases and $S_A(q)$ develops a peak that moves to higher q. We obtained reasonable fits to $S_A(q)$ with a particle diameter of around 16 nm and with increasing particle volume fractions of 10.7% at 4 hours to ≈ 28% at 24 hours. We do not observe any further change in structure beyond 24 hours, suggesting that the particles have jammed to form the strands by 24 hours. The volume fraction obtained from our fits (28%) is much smaller than that expected for jammed colloidal hard spheres in bulk. We believe that this might be due to the particles jamming into an open network-like scaffold of particulate strands. Remarkably, the "effective hard-sphere" particle size obtained from fitting $S_A(q)$ has approximately the same value at all times, and is approximately equal to the particle size from the dilute solution form factor. This suggests that long -range electrostatic interactions between particles in the surfactant-water medium are not significant in this system and that our assumption of hard-sphere interactions is thus reasonable. We return to this theme and explore inter-particle interactions in more detail in a subsequent chapter (Chapter 3).

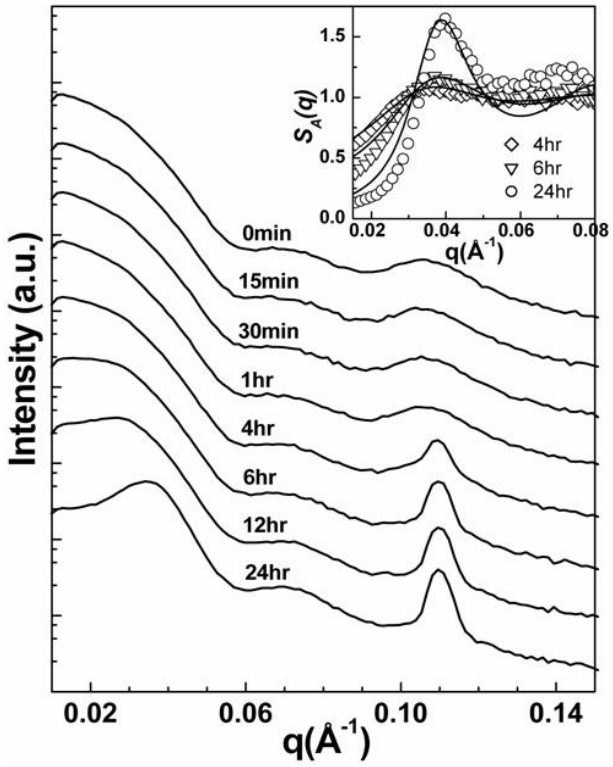

Figure 2.8. Evolution of SAXS from a 5% (by weight) S15-H_1 composite with time, on cooling from the isotropic phase to 44ºC. The inset shows the apparent structure factor, $S_A(q)$, obtained as discussed in the text, and the fits to the hard sphere model (in solid lines).

Our data suggests that, with time, the H_1 phase grows at the expense of the isotropic, and correspondingly, the apparent particle volume fraction increases. This suggests that the silica particles are expelled from the H_1 phase and are confined to the isotropic regions. As the H_1 domains grow, the particles are concentrated in the isotropic phase until they impinge to form the networks observed with FFTEM.

Finally, we note that when H_1-particle composites are heated to 50^{o}C, viz., well above the isotropization temperature, POM observations show that the birefringent domains characterizing the hexagonal phase disappear almost instantly and the

particle networks break up subsequently. Particulate networks of S8, S11, S15 and S26 are clearly observed under the microscope and we see that these disappear in about 10 s after heating to 50^{o}C, while networks of S500 disappear in about 7 to 8 minutes. The particles disperse and a transparent micellar solution containing dispersed particles is obtained again. If particles diffusivity leads to the break-up of the particle networks, the time for break-up ought to scale with particle size. This is broadly consistent with the around 45-times slower breakup of the S500 networks relative to networks of S8, S11, S15 and S26. However, our visual observations are unable to resolve the differences between break-up times for networks of the smaller particles.

2.4. Discussion

In the H_1-particle composites examined here, the smallest inherent length scale of interest is the characteristic spacing between cylindrical micelles (5.7 nm). This length scale is much larger than the corresponding length scale for thermotropic nematics (viz. the molecular mesogen size), and is comparable to the size of the smallest particles used to prepare our composites. Our work indicates that the characteristic H_1 length scale delineates different regimes of particle organization in a natural way. Particles smaller than the characteristic size (viz. Sil), behave like solvents and swell the space between surfactant cylinders while probably changing the cylinder curvature. Particles comparable to the characteristic size are partitioned - they are partly accommodated in the H_1 phase and partly expelled to form aggregated strands. Larger particles are expelled to isotropic regions, and jam into strands that organize into a network phase as isotropic regions transform into the H_1 phase. A schematic summarizing this trend in particle/mesophase organization with particle size is shown in Figure 2.9.

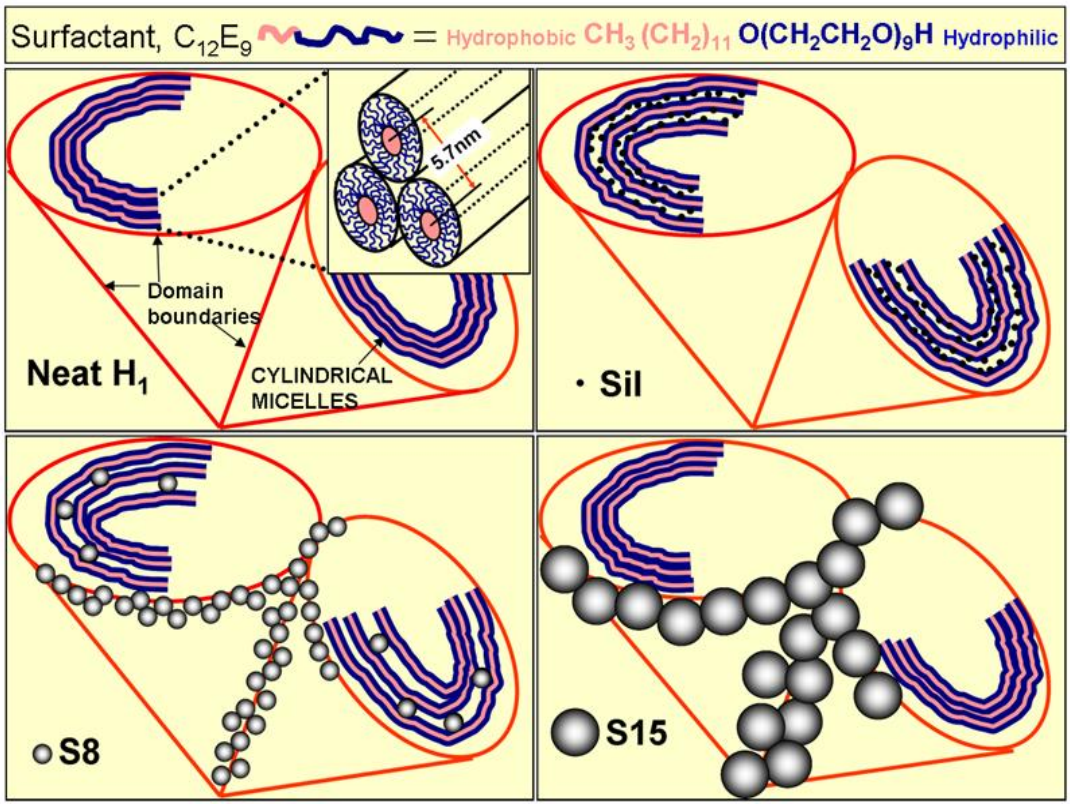

Figure 2.9. Cartoon schematic that shows the spatial localization of particles of increasing sizes in the H_1 phase. The surfactant cylinders curve around the "fans" to form the domain structure observed in the polarized optical micrographs. The particles (black filled circles) in the schematic are drawn so as to maintain the correct relative (average) size with respect to the mesophase cylinder spacing.

The formation of particulate networks by phase separation from nematics has been reported[12-14] previously. West et. al.[14] suggest that network formation is possible only when the moving isotropic-nematic interface is slower than a critical speed, $v_c = W.(\rho K)^{-1/2} \approx 1mm.s^{-1}$ (where ρ is the particle density) for the nematic-particle composites. Recent work[13] indicates that particle networks form by the generic mechanism proposed by West et. al.[14] only when the particle surface is wetted by the nematic. It is

now believed[13] that the presence of solvent impurities released from the brush layer of polymeric particles that have been widely used in such studies reduce the isotropic-nematic interface speed to below v_c, thus enabling the particles to be swept up by the moving isotropic-nematic front to form networks. At the same time, these solvent impurities decrease the clearing temperature of the nematic. For the nonionic surfactant–silica systems used in our work, there are no experimentally available estimates for W. If, similar to Poulin et al.,[32] we assume that the anchoring of surface micelles is governed by entropy, we obtain $W \sim k_BT/a^2 \approx 96\ \mu J/m^2$, where a = 5.7 nm, is the characteristic size of the H_1 phase. Thus, in our system, $v_c \approx 2\ m.s^{-1}$, significantly larger than in thermotropic nematics. It is not clear that a continuum description using W is relevant in our system for small particles such as S8, where the particle size is comparable to a. However, particulate strands organize into networks for particles as small as S8 and as large as S500, suggesting that the interface speed is always smaller than v_c. Further, unlike previous reports, the H_1-isotropic temperature *increases* in our systems.

2.5. Summary

In this chapter, we use a combination of techniques – SAXS, optical microscopy under crossed polarizers and FFTEM to examine microstructural evolution when silica nanoparticles are dispersed in a nonionic surfactant hexagonal phase. Our work indicates that the characteristic H_1 length scale delineates different regimes of particle organization. Particles smaller than the characteristic size (viz. Sil), behave like solvents and swell the space between surfactant cylinders while probably changing the cylinder curvature. Particles comparable to the characteristic size are partitioned - they

are partly accommodated in the H_1 phase and partly expelled to form aggregated strands. Larger particles are expelled to isotropic regions, and jam into strands that organize into a network phase as isotropic regions transform into the H_1 phase. The network formation is reversible as the aggregated particulate network disperse above hexagonal-isotropic transition temperature and again aggregate below it. The mechanism of network formation is explained in terms of nucleation and growth of H_1 phase, with the simultaneous expulsion of silica particles so as to concentrate in the isotropic phase and finally aggregate at domain boundaries.

2.6. References

1. (a) Balazs, A. C.; Emrick, T.; Russell, T. P. *Science* **2006**, *314*, 1107. (b) Thompson, R. B.; Ginzburg, V. V.; Matsen, M. W.; Balazs, A. C. *Science*, **2001**, *292*, 2469.
2. Bockstaller, M. R.; Mickiewicz, R. A.; Thomas, E. L. *Adv. Mater*. **2005**, *17*, 1331.
3. Khoo, I. C.; Werner, D. H.; Liang, X.; Diaz, A. *Optics Letters* **2006**, *31*, 2592.
4. (a) Poulin, P.; Raghunathan, V. A.; Richetti, P.; Roux, D. *J. Phys. II France* **1994**, *4*, 1557. (b) Poulin, P.; Stark, H.; Lubensky, T. C.; Weitz, D. A. *Science* **1997**, *275*, 1770. (c) Poulin, P.; Weitz, D.A. *Phys. Rev. E* **1998**, *57*, 626. (d) Mondain-Monval, O.; Dedieu, J. C.; Gulik-Krzywicki, T.; Poulin, P. *Eur. Phys. J. B* **1999**, *12*, 167.
5. Ramaswamy, S.; Nityananda, R.; Raghunathan, V. A.; Prost, J. *Mol. Cryst. Liq. Cryst.* **1998**, *288*, 175.
6. Voeltz, C.; Maeda, Y.; Tabe, Y.; Yokoyama, H. *Phys. Rev. Lett.* **2006**, *97*, 227801.
7. (a) Loudet, J. C.; Barois, P.; Poulin, P. *Nature* **2000**, *407*, 611. (b) Loudet, J. C.; Barois, P.; Auroy, P.; Keller, P.; Richard, H.; Poulin, P. *Langmuir* **2004**, *20*, 11336.
8. Musevic, I.; Skarabot, M.; Tkalec, U.; Ravnik, M.; Zumer, S. *Science* **2006**, *313*, 954.
9. Zapotocky, M.; Ramos, L.; Poulin, P.; Lubensky, T. C.; Weitz. D. A. *Science* **1999**, *283*, 209.
10. Basappa, G.; Suneel; Kumaran, V.; Nott, P. R.; Ramaswamy, S.; Naik, V. M.; Rout, D. *Eur. Phys. J. B* **1999**, *12*, 269.

11. Shouche, S. V.; Chokappa, D. K.; Naik, V. M.; Khakhar, D. V. *J. Rheol*. **1994**, *38*, 1871.

12. (a) Meeker, S. P.; Poon, W. C. K.; Crain, J.; Terentjev, E. M. *Phys. Rev. E* **2000**, *61*, R6093. (b) Anderson, V. J.; Terentjev, E. M.; Meeker, S. P.; Crain, J.; Poon, W. C. K. *Eur. Phys. J. E* **2001**, *4*, 11; (c) Petrov, P. G.; Terentjev, E. M. *Langmuir* **2001**, *17*, 2942.

13. (a) Cleaver, J.; Vollmer, D.; Crain, J.; Poon, W. C. K. *Mol. Cryst. Liq. Cryst.* **2004**, *409*, 59. (b) Vollmer, D.; Hinze, G.; Poon, W. C. K.; Cleaver, J.; Cates, M. E. *J. Phys. Cond. Matt.* **2004**, *16*, L227.

14. West, J. L.; Glushchenko A. ; Liao G.; Reznikov Y.; Andrienko D.; Allen M. P. *Phys. Rev. E* **2002**, *66*, 012702.

15. Tanaka, H.; Isobe M.; Yamamoto J. *Phys. Rev. Lett.* **2002**, *89*, 168303-1.

16. Maldonado, A.; Nicot C.; Waks M.; Ober R.; Urbarch W.; Langevin D. *J. Phys. Chem. B* **2004**, *108*, 2893.

17. (a) Koehler, R. D.; Kaler, E. W. *Langmuir* **1997**, *13*, 2463. (b) Jayalakshmi, Y.; Kaler, E. W. *Phys. Rev. Lett.* **1997**, *78*, 1379.

18. (a) Ramos, L.; Fabre, P.; Nallet, F.; Lu, C.-Y.D. *Eur. Phys. J. E* **2000**, *1*, 285. (b) Sallen, L.; Oswald, P. *J. Phys. II (France)* **1995**, *5*, 937.

19. (a) Fabre, P.; Cassagrande, C.; Veyssie, M.; Cabuil, V. ; Massart, R. *Phys. Rev. Lett.* **1990**, *64*, 539. (b) Quilliet, C.; Ponsinet. V.; Cabuil, V. *J. Phys. Chem.* **1994**, *98*, 3566-3569.

20. (a) Eiser, E.; Bouchama, F.; Thathagar, M. B.; Rothenberg, G. *Chem. Phys. Chem.* **2003**, *4*, 526; (b) Bouchama, F.; Thathagar, M. B.; Rothenberg, G., Turkenburg, D. H,; Eiser, E. *Langmuir* **2004**, *20*, 477-483.

21. Alexeev, V. L.; Ilekti, P.; Persello, J.; Lambard, J.; Gulik, T.; Cabane, B. *Langmuir* **1996**, *12*, 2392.

22. Adhikari, R. *Eur. Phys. J. E*, **2002**, *9*, 127.

23. Wadekar, M. N.; Pasricha, R.; Gaikwad, A. B.; Kumaraswamy, G. *Chem. Mate*r. **2005**, *17*, 2460.

24. Glatter, O.; Kratky, O. "*Small Angle X-ray scattering*" Academic Press **1982**, NY.

25. Qiu, D.; Cosgrove, T.; Howe, A. M.; Dreiss, C. A. *Langmuir* **2006**, *22*, 546.

26. Mitchell, J. D.; Tiddy, G. J. T.; Waring, L.; Bostock, T.; McDonald, M. P. *J. Chem. Soc., Faraday Trans. 1* **1983**, *79*, 975-1000.

27. Kunieda, H.; Ozawa, K.; Huang, K.-L. *J. Phys. Chem. B* **1998,** *102*, 831.

28. Ramazanoglu M. K.; Clegg, P. S.; Birgeneau R. J. *Phys. Rev. E* **2004**, *69*, 061706.

29. (a) Braun, C.; Lang, P.; Findenegg, G. H. *Langmuir* **1995**, 11, 764. (b) Lang, P.; Steitz, R.; Braun, C. *Coll. Surf. A.* **2000**, *163*, 91.

30. Knight, P.; Wyn-Jones, E.; Tiddy, G. J. T. *J. Phys. Chem.* **1985**, *89*, 3447.

31. Kaler, E. W. *Small Angle Scattering from Complex Fluids in Modern Aspects of Small Angle X-ray Scattering*, Brumberger, H. (ed) Kluwer Academic Publishers (Dordrecht), **1995**.

32. Poulin, P.; Francès, N.; Mondain-Monval, O. *Phys. Rev. E* **1999**, *59*, 4384.

Chapter 3

Surfactant Structure and Interparticle Interactions for Dispersion of Silica Nanospheres in H_1 Phase

3.1. Introduction

In the second chapter we demonstrated that electrostatically stabilized silica nanoparticles aggregate and form networks[1] when a surfactant/water system containing these particles is cooled into the hexagonal (H_1) phase. Our work extended understanding from previous studies of particle assembly in surfactant H_1 phases by systematically mapping the influence of particle size. Specifically, we showed that particles over a wide size range (diameter, d, greater than 10 nm and up to about 500 nm; $d > a$, characteristic length scale of the H_1 phase; a = 5.7 nm, in our case) form particulate networks in surfactant-water systems. This particle-particle aggregation into strands, and into networks is driven by phase separation of the particles from the ordered H_1 phase. On cooling from the isotropic micellar phase, H_1 domains nucleate and grow, and expel the particles to the isotropic regions. Thus, as the isotropic regions shrink, the particles get concentrated, and eventually get jammed at the domain boundaries as the H_1 domains impinge. An intriguing aspect of this particle aggregation in the surfactant/water system is its thermoreversibility: On heating the particle-H_1 composite to above 44^{o}C, viz. above the H_1-isotropic transition temperature, the particulate network breaks up and redisperses into individual particles in the low viscosity micellar phase. Thus, the nanoparticles aggregate and disperse reversibly on cooling into the H_1 phase and, on heating into the isotropic micellar phase, respectively. In contrast to this thermoreversibility in the surfactant micellar system, aggregation of charge stabilized silica particles from aqueous dispersions (for example, due to destabilization by increasing the ionic strength or changing the pH) was irreversible. Typically, for particle aggregation in aqueous dispersions, even vigorous sonication is unable to break up the aggregated particulate flocs. Thus, when particle aggregation in aqueous dispersions is

irreversible, what is the origin of the thermoreversibility of aggregation of the same particles in surfactant solutions?

In this chapter, we use SAXS and contrast matching SANS experiments to probe the change in nature of interparticle interactions for dispersions in water and in micellar solutions. We also investigate the microstructure of micelle-particle solutions to understand the origin of the interparticle interactions, and finally examine how coating the nanoparticles with polymers can alter this microstructure. Our results form the basis of our scheme to prepare self standing nanoparticulate scaffolds that will be described in the next chapter. We begin by briefly summarizing the relevant literature in the area of surfactant adsorption on colloids, before we describe our experimental system and our results.

Adsorption of surfactants; and the role of surfactants in stabilizing colloidal dispersions has been studied extensively, as these phenomena are relevant to a range of industrial applications ranging from processing of minerals, cleaning and detergency, cosmetics and personal care applications, food products, pharmaceuticals, etc.[3] Specifically, nonionic surfactants find extensive use in the aforementioned applications, and there is a wealth of literature that describes their interactions with flat,[4-8] porous[9-12] and colloidal surfaces.[5,13-15] Dispersion of colloids in surfactant solutions can dramatically influence colloidal stability since surfactants interact strongly with colloidal surfaces. Therefore, a wide range of experimental techniques, including, ellipsometry,[6] fluorescence decay spectroscopy,[9,16] atomic force microscopy,[17-20] dynamic light scattering,[5] small angle neutron scattering[13,15,21] and neutron reflectivity,[4,5,7,22] etc., have been brought to bear on studies of surfactant adsorption on surfaces. Specifically, it is now understood that oligooxyethylene-based nonionic surfac-

tants interact with silica surfaces by hydrogen bonding with the surface silanol groups. Nonionic surfactants with short hydrophilic oligooxyethylene headgroups, relative to the size of the hydrophobic tail, are believed to form bilayers on adsorption on surfaces.[4] However, several groups have also reported that, rather than forming bilayers, the nonionic surfactants adsorb on surfaces in the form of micellar structures.[9,15,16,23-25] The group of Levitz has suggested that the formation of the adsorbed micellar structures on surfaces proceeds via the initial adsorption of surfactant molecules on the surfaces, and their subsequent reorganization into micellar structures. Alexeev et. al.[25] suggest that the stability of silica nanoparticles in nonionic surfactant solutions depends on the extent of surface coverage by surfactant micelles – they claim that nanoparticle dispersions are stable so long as there is at least one layer of surfactant micelles that separates the nanoparticles.

Thus, it is clear that surfactant-nanoparticle interactions, and the structures that form as a consequences of these interactions critically determine the phase behavior of nanoparticle dispersions in surfactant solutions. In this chapter, we focus on interparticle interactions in surfactant solutions, and relate these to the surfactant/particle microstructure.

3.2. Experimental Details

Non-ionic surfactant, nonaethylene glycol dodecyl ether ($C_{12}E_9$), was obtained from Sigma Aldrich and was used as received (HPLC previously reported[26]). Distilled deionized water (resistivity = 18.2 MΩ·cm) from a Millipore MilliQ unit was used to prepare all samples. Polyethylene-imine (PEI) was obtained from Aldrich as a 50% (by weight) solution with a weight average molecular weight of 2000 $g.mol^{-1}$. All the chemicals were used as received.

Electrostatically stabilized 30% (by weight) colloidal suspension of silica particles, Ludox, LS30, was obtained from Sigma Aldrich. We have thoroughly characterized the Ludox LS30 particles using DLS, SAXS and TEM. As before, we refer to these particles as S15 (viz., silica particles with an average diameter of 15 nm).

The surface of S15 was coated with PEI according to a procedure reported in the literature.[27] We maintain pH = 5 when S15 is coated with PEI to enable protonation of the amine groups on the PEI, since PEI-S15 interactions are believed to be driven by electrostatics. The ratio of PEI to S15 was chosen so as to have a surface coverage of 0.1 mg/m^2 (calculated assuming the manufacturer specified surface area of 220 m^2/g for S15). PEI coated S15 particles are referred to as PEI-S15 and are characterized using SAXS (to determine the size) and using zeta potential measurements (on a Brookhaven Zetasizer, to determine the surface charge).

SAXS measurements were performed on a Bruker Nanostar, as described in Chapter 2. SANS measurements were done at the beam line in the Dhruva Nuclear Reactor at the Bhabha Atomic Research Centre, Mumbai. The wavelength of the neutron beam was 5.2 Å and the *q*-range of scattering was 0.017 to 0.34 Å^{-1}. Samples were contrast matched by tuning the ratio of H_2O and D_2O in the solvent so as to match the scattering length densities of the solvent with either the silica particle or, with the surfactant, $C_{12}E_9$. All samples were equilibrated for at least 12 hours before measurements. Measurements were performed with 2 mm thick quartz cuvette. All the data sets were normalized with the beam monitor and the sample volume and were background corrected to obtain the scattering cross section. The scattering data was reduced to an absolute cross section (in cm^{-1}) by reference to scattering from a standard sample. Fits to the SANS are convoluted with the resolution function obtained

previously[28] to account for the wavelength spread ($\Delta\lambda/\lambda$) and the neutron beam angular resolution.

Data analysis was performed using codes written in our laboratory, and the results were compared, in some cases, with analysis using SASfit.[29] As the results were comparable, here, we report only the analysis based on our routines.

3.3. Results and Discussion

Our results are divided into three parts. (1) We begin with SAXS and SANS investigations of particle-particle interactions in water, and in isotropic micellar solutions. (2) We then investigate structure in the micelle-particle system using SANS and finally, (3) we describe the structure observed in micellar solutions containing PEI coated silica nanoparticles.

3.3.1 Studies on interactions between silica particles in:

(a) Water

S15 particles are electrostatically stabilized. At dilute concentrations (1% by weight, viz. approximately 0.5% by volume), in solutions containing salt (25 mM sodium chloride, added to screen the range of electrostatic interparticle interactions), we obtain the SAXS form factor, $F^2(q)$, for S15 (Figure 3.2, inset). We have verified that scattering profiles from solutions at lower particle concentrations can be superposed with the form factor in Figure 3.2, inset, after normalization with particle volume fraction. We can fit the form factor for S15 assuming that the particles are spherical (this is a reasonable assumption based on TEM results[1]), and follow a log-normal distribution of sizes with a mean radius (R_{S15}) of 74.5 Å and a standard deviation of 14%. Thus, the S15 particles are not monodisperse (but have a *unimodal* size distribution),

and the form factor obtained experimentally, $F^2(q)$, is an *average* over the S15 particle size distribution.

As the particle volume fraction is increased, to 5%, 10%, 15% and 30% (by weight), inter particle interference increases resulting in a structure factor, $S(q)$, that becomes increasingly prominent with increase in particle concentration (Figure 3.2; Note that no salt is added to prepare these dispersions). For an isotropic dispersion of monodisperse particles, $S(q)$ is given by the Fourier transform of the particle radial distribution function. In this case, $S(q)$ can be calculated from the Ornstein-Zernicke equation, with an appropriate closure relation, and by assuming a suitable form for the interparticle interaction. An excellent review of this analysis and the commonly made assumptions, especially in the context of polydisperse colloidal and micellar systems, is given in the chapter by Kaler.[30] Thus, we write the scattered intensity, I as:

$$I = \Delta\rho^2 \phi V_s \hat{S}(q) F^2(q) \qquad (1)$$

where $\Delta\rho$ is the contrast between the scatterer and the matrix (electron density difference, in the case of SAXS, and scattering length density difference in the case of SANS), ϕ is the volume fraction of the scatterer, V_s is the scattering volume and $\hat{S}(q)$ is the "apparent" structure factor that averages over the interactions between the polydisperse S15 particles, viz. $\hat{S}(q)F^2(q) = \sum_i \sum_j F_i F_j S_{ij}$, where the indices, i and j are summed over all S15 particles and S_{ij} is the structure factor. Thus, we model the experimental scattered intensity with the average form factor for polydisperse spherical particles and with an apparent structure factor that assumes monodisperse spherical scatterers. Assuming a hard sphere interparticle interaction potential yields an analytical expression for the apparent structure factor.[31] We observe a reasonable fit to our data, with the experimentally obtained form factor and with a structure factor based on

an effective hard sphere model for the interparticle potential (Figure 3.1). The particle radius predicted by the effective hard sphere model is larger than the experimental value since it accounts for the electrostatic repulsion between the charged particles, and accordingly the predicted volume fraction is also larger than the experimental value. However, the values of the best fit hard sphere radius and volume fraction are not physically realistic (Table 3.1) since, for example, the discrepancy between the fitted volume fractions and hard sphere radii, and the experimental values increases with the concentration of nanoparticles in the dispersion, while one would expect the opposite trend for the effective hard sphere model.[32a,b] Therefore, we are unable to model the scattering from our system using an effective hard sphere potential to represent interparticle interactions.

For electrostatically stabilized particles dispersed in a buffer, one might imagine that particles interact via a soft exponentially decaying potential of the form, $U \sim r^{-1} e^{-\kappa r}$, where κ is the inverse Debye screening length set by the ionic strength of the solution.[33] Therefore, we fit our data using an apparent structure factor from the Hayter-Penfold model[34] that assumes that the silica nanoparticles interact via a screened Coulombic interaction potential. The form of the potential is similar to the Yukawa model and is given by:

$$U(r) = 2\pi\varepsilon_0\varepsilon r_{HPY}{}^2\psi_0^2 \exp[-\kappa(r - 2r_{HPY})]/r \qquad (2)$$

where ε_o is the permittivity of free space, ε is the dielectric constant of water, r_{HPY} is the particle radius and ψ_o is the electrostatic potential of the silica nanoparticles. This model fits the data reasonably well (Figure 3.2) at low q, and the fit parameters are summarized in Table 3.2.

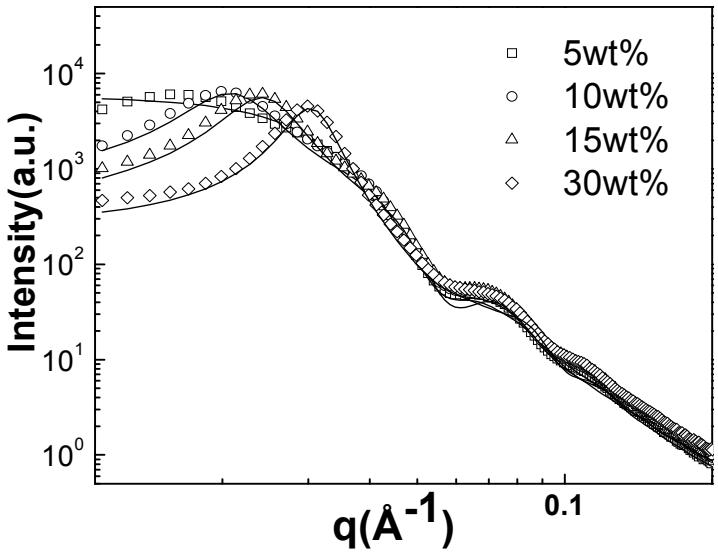

Figure 3.1. SAXS data at different concentrations of S15 (5, 10, 15 and 30%, by weight) in water at 50°C. The data was fitted (solid lines) assuming hard sphere interactions between the charged particles, as described in the text. The fit through the data is shown as a solid line.

Sample (S15, % by weight)	ϕ_e	Parameters from fitting Structure Factor, *S(q)*	
		ϕ_f	R_{HS} (?)
5	0.023	0.059	88.3
10	0.049	0.30	146.1
15	0.074	0.34	129.4
30	0.164	0.42	108.37

Table 3.1. Parameters from fitting a structure factor based on hard sphere inter-particle interactions. We use a form factor based on fitting data to a 1% (by weight) dispersion of S15 in 25 mM aqueous solution, that gives an average particle radius of 74.5Å, and a lognormal distribution of radii with σ = 0.14 .

At high q, near the first oscillation in the structure factor, the fit to the data is not perfect. We attribute this to two possible reasons: (a) limitations in modeling the data using an *effective* structure factor, and accounting for the effect of the polydispersity only in the form factor, especially for higher particle volume fractions and, (b) problems associated with subtracting the background intensity from the acquired data, prior to normalization with particle concentration. We note that the samples are prepared by diluting the 30% S15 dispersions with distilled, deionized water. We observe a decrease in conductivity on diluting the S15 dispersion (reported in Table 3.2). The trends in the fitted parameters with concentration broadly accord with previous findings.[35]

(b) In micellar solutions containing 50% surfactant, at 50^{o}C

We now consider scattering from silica particles in a matrix comprising equal weight fractions of nonionic surfactant, $C_{12}E_9$, and water. We have previously shown[1] that S15 particles form transparent dispersions in 1:1 $C_{12}E_9$/water at high temperature (50^{o}C) indicating that the particles are well dispersed. For example, SAXS from a 1% dispersion of S15 in 1:1 $C_{12}E_9$/water at 50^{o}C shows the form factor for the S15 and a micellar correlation peak.[1] On cooling, the surfactant goes from a low viscosity solution to a gel, due to the formation of a hexagonal (H_1) mesophase (the phase behavior of $C_{12}E_9$/water[36] and also for other surfactants of the C_nE_m type has been described previously[6,37]). When the H_1 phase forms, the particles are expelled from the H_1 domains and aggregate at the domain boundaries, giving rise to a pronounced structure factor in SAXS.[1] On heating back into the isotropic micellar phase, the particles redisperse and we recover the form factor.

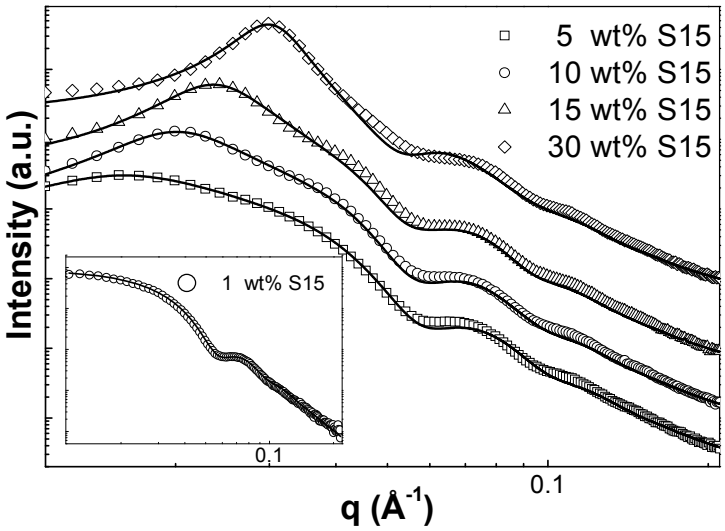

Figure 3.2. SAXS data at different concentrations of S15 (5, 10, 15 and 30%, by weight) in water at 50°C. The data was fitted (solid lines) assuming screened Coulombic interactions between the charged particles using a Hayter-Penfold model, as described in the text. For ease of viewing, the data plots have been vertically offset by multiplying with 1, 4, 20 and 200 for 5, 10, 15 and 30% respectively. The inset shows the scattering from a dilute solution (1% by weight) of S15 in a 25mM solution of sodium chloride. The fit through the data is shown as a solid line.

Sample (S15, % by weight)	*Measured Ionic strength (μS/cm)*	ϕ_e	*Parameters from Fitting Structure Factor, S(q)*				
			ϕ_f	r_{HPY} *(Å)*	κ^{-1} *(Å)*	*Potential* ψ_o *(mV)*	*Particle charge (in e.u.)*
5	201	0.023	0.024	78.5	154.8	46.7	31.1
10	388	0.049	0.055	80.6	96.0	46.0	37.4
15	601	0.074	0.10	82.8	66.8	45.6	46.3
30	1357	0.164	0.22	84.5	41.5	41.4	58.1

Table 3.2. Parameters from fitting a structure factor for screened Coulombic interactions (based on the Hayter-Penfold model). We use a form factor based on fitting data to a 1% (by weight) dispersion of S15 in 25 mM aqueous solution, that gives an average particle radius of 74.5Å, and a lognormal distribution of radii with σ = 0.14 and ionic conductance of 62.8μS/cm.

This is very unlike the aggregation of S15 particles in water, where destabilization, for example, by increasing the ionic strength or by changing the pH, leads to irreversible particle aggregation. Therefore, clearly, there is a change in particle-particle interactions in the surfactant micellar phase, resulting from the structure of the $C_{12}E_9$/water/particle system. Therefore, we now investigate the surfactant/water/particle system at high temperature (50^{o}C), in the low viscosity, isotropic micellar phase.

In the micellar phase, $C_{12}E_9$ aggregates to form a hydrophobic core of C_{12} segments and a solvated shell of the E_9 segments. Therefore, for our SANS studies, we adjust the water/D_2O composition in our surfactant formulation so as to contrast match the aliphatic C_{12} micellar core (97.5% H_2O, 2.5% D_2O; scattering length density = -3.86 x 10^{-7}Å^{-2}). We confirm that the micelles are, indeed, contrast matched at this water/D_2O concentration – SANS from these micellar solutions yields a very low scattered intensity, arising mainly from the incoherent background (Figure 3.4). SANS data from dispersions of S15 particles (at concentrations of 1%, 5%, 10% and 15%, by weight) in contrast matched 1:1 $C_{12}E_9$:(97.5% H_2O- 2.5% D_2O) micellar solutions is shown in Figure 3.3. We first fit the SANS data (Figure 3.3) for 1% S15 dispersions using a spherical form factor averaged over a polydisperse size distribution, and note that the average particle size and polydispersity obtained from our fit (Table 3.3) accord very well with that obtained from the SAXS for S15 in water (compare with Table 3.2). We fit the SANS data at higher S15 concentations (5%, and higher) with the obtained form factor, and assuming an apparent structure factor for monodisperse particles. Interestingly, the SANS data is fitted very well assuming hard sphere interparticle interactions. The volume fraction, ϕ_f obtained by fitting the apparent structure fac-

tor accords reasonably well with the experimental values, ϕ_e. At the highest particle concentration, the fitted value (ϕ_f = 0.087) is higher than the experimental value (ϕ_e = 0.074) by about 17.6%. We believe that this difference may be attributed to the error from averaging the interparticle interactions into an apparent structure factor. The hard sphere radius obtained by fitting the apparent structure factor (viz. the length scale over which particles interact) is similar at all particle concentrations, and is within 10% of the particle radius from the form factor, as expected for particles interacting through a hard sphere potential (Table 3.3). At the high surfactant concentrations investigated here (50% by weight), "crowding" effects[38] due to the large number density of surfactant micelles that surround the silica particles influence interparticle interactions. Further, we expect that the effective dielectric properties of the surfactant/water matrix is considerably different from that of pure water, and influences the interparticle electrostatic interactions. Finally, we anticipate surfactant-particle interactions in our system based on the surfactant chemistry and the particle surface chemistry. Interestingly, we observe that, taken together, these effects result in an effective hard sphere interaction between the silica particles.

3.3.2. Structure of the adsorbed surfactant on the particle surface:

To understand the structural underpinning of the change in interparticle interaction between the silica particles on addition of surfactant, we investigate surfactant organization in the dispersion. We anticipate that surface silanol groups on the S15 particles would interact with the ethylene oxide segments of $C_{12}E_9$.

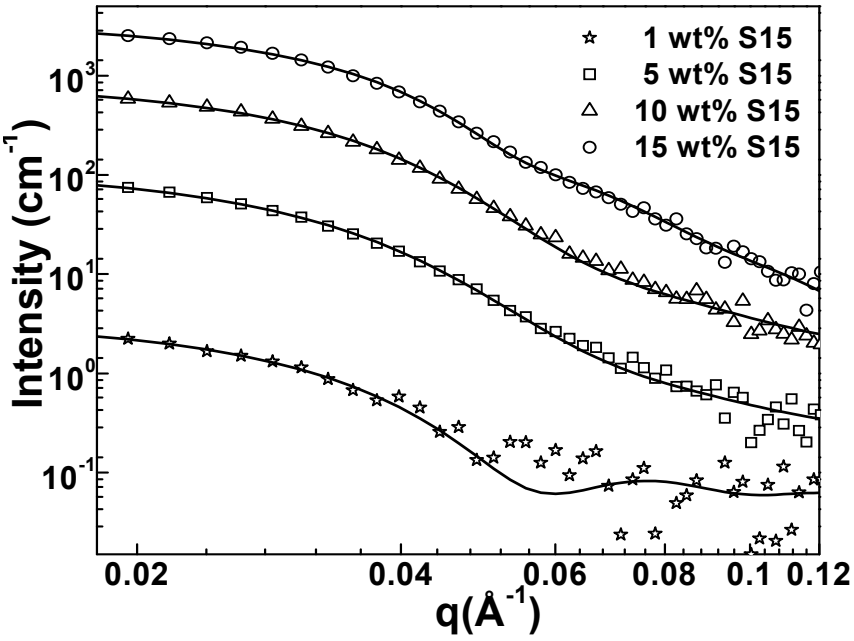

Figure 3.3. SANS data from dispersions of S15 particles at concentrations of 1%, 5%, 10% and 15%, by weight) in contrast matched 1:1 $C_{12}E_9$:(97.5% H_2O- 2.5% D_2O) micellar solutions, at 50°C. The data sets for 1wt%, 5wt%, 10wt% and 15% have been vertically offset by multiplying with 0.5, 3, 12 and 40 respectively, for ease of viewing. Since the particles are supplied in a 30% by weight solution, the highest concentration possible in 1:1 surfactant solution is about 15% by weight.

Sample (S15, % by weight)	ϕ_e	*Parameters from fitting Structure Factor, S(q)*	
		ϕ_f	R_{HS} (Å)
5	0.023	0.025	81.4
10	0.049	0.048	78.7
15	0.074	0.087	77.5

Table 3.3. Parameters from fitting a structure factor based on hard sphere inter-particle interactions. We use a form factor based on fitting data to a 1% (by weight) dispersion of S15 in 25 mM aqueous solution, that gives an average particle radius of 74.5Å, and a lognormal distribution of radii with σ = 0.14.

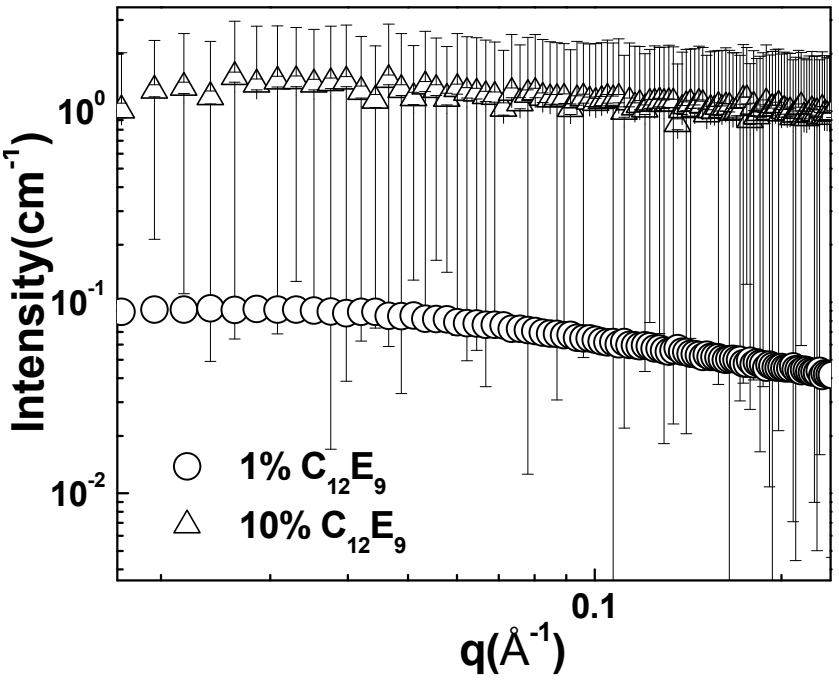

Figure 3.4. SANS spectra for $C_{12}E_9$ Surfactant matched in 97.5:2.5 H_2O:D_2O. There is no scattering from the system indicating that the surfactant is matched.

(a) Core-shell model

Intuitively, one might imagine the formation of a surfactant bilayer on the S15 surface, with a hydrophobic shell comprising of C_{12} segments sandwiched between layers of ethylene oxide segments, the inner layer adsorbed on the S15 surface and the solvated outer layer in contact with water (see Schematic in Figure 3.6). If we contrast match the silica particle (scattering length density = 3.59 x 10^{-6} Å^{-2}) by working in a 40/60 mixture of water and D_2O, we obtain the scattered intensity as[31]:

$$I = \Delta\rho^2 \nu_m \hat{S}_{mm}(q) F_m^2(q) + \Delta\rho^2 \nu_s \hat{S}_{ss}(q) F_s^2(q) + 2 \Delta\rho^2 (\nu_s \nu_m)^{0.5} \hat{S}_{sm}(q) F_s(q) F_m(q) \quad (3)$$

Where the subscripts, *m* and *s*, refer to the micelle and the surfactant shell, respectively, ν_x is the number density of the scattering species, *x*, and $\hat{S}_{xy}$ are the apparent partial structure factors (averaged over the polydisperse size distribution) for interference between scattering species, *x* and *y*. The scattered intensity has contributions from surfactant micelles and the intermicellar apparent structure factor, $\hat{S}_{mm}$; from the surfactant "shells" around S15 particles and from shell-shell interference, $\hat{S}_{ss}$; and from interference between micelles and shells, $\hat{S}_{sm}$. As the silica is contrast matched with water/D_2O, and since the ethylene oxide segments are solvated, the neutron scattering in our experiments is primarily from the structures formed by the hydrophobic C_{12} segments (viz. the micellar cores and the hydrophobic part of the shells). Typically, determining partial structure factors in multi-component systems requires contrast variation experiments on the same sample to generate multiple data sets that are fitted simultaneously.[31] However, in our experiments, the different scattering entities (viz. the micelles and the surfactant shells) have the same scattering length density difference, $\Delta\rho$, with respect to the solvent (see Equation 3). Thus, it is not possible to extract partial structure factors for our system, even with contrast variation experiments. Therefore, to extract meaningful information about our experimental system, we design our samples such that $\hat{S}_{mm}$ is close to 1, and $\hat{S}_{sm}$ is close to 0.

Concentrated surfactant solutions, for example, the 1:1 $C_{12}E_9$:(water/D_2O) system that we have described earlier, have a large number density of micelles and therefore, in such systems, S_{mm} is not expected to be close to 1. SANS from 1%, 5% and 10% (by weight) $C_{12}E_9$ solutions (not containing S15) show that the scattering can be described by the form factor of the micellar core for 1% and 5% solution (viz. $\hat{S}_{mm}(q) = 1$; Figure 3.5, size of hydrophobic core of micelle = 19.1 Å). For the 10% solution,

the scattering can be modeled only if we consider a micelle-micelle apparent structure factor based on a hard-sphere interaction between the micelles (viz. we cannot assume that $\hat{S}_{mm}(q) = 1$; Figure 3.5). Therefore, we only consider scattering for systems where the surfactant concentration does not exceed 5%. Further, we assume that, at these surfactant concentrations, where $\hat{S}_{mm}(q) = 1$, we can also neglect the micelle-shell term, viz $(\nu_s \nu_m)^{0.5} F_s(q) F_m(q) \hat{S}_{sm}(q) = 0$. We return to this point and justify our assumption later.

We initially examine scattering from a 1% (by weight) dispersion of S15 in a solution containing 1% (by weight) surfactant (that we term a "1%1%" sample) in water/D_2O (with scattering length density matched to silica). At these particle and surfactant concentrations, we assume that there is no contribution from the apparent partial structure factors (viz. $\hat{S}_{ss}(q) = \hat{S}_{mm}(q) = 1$ and $\hat{S}_{sm}(q) = 0$), and the scattering comes only from the micellar and shell form factors (averaged over their size distributions, respectively). Thus, the 1%1% sample comprises of a *dilute* solution of micelles and shells and there is no interference between the scattering from these. The SANS data from the 1%1% sample is fitted well (Figure 3.7 a), and the fit parameters are summarized in Table 3.5. When fitting the experimental data, we fix the inner size of the shell as R_o = 74.5 Å, based on the average particle size from the form factor, R_{S15}. Our fit yields an average shell thickness R_s of 36.1 Å and an average micellar radius, R_m = 18.4 Å.

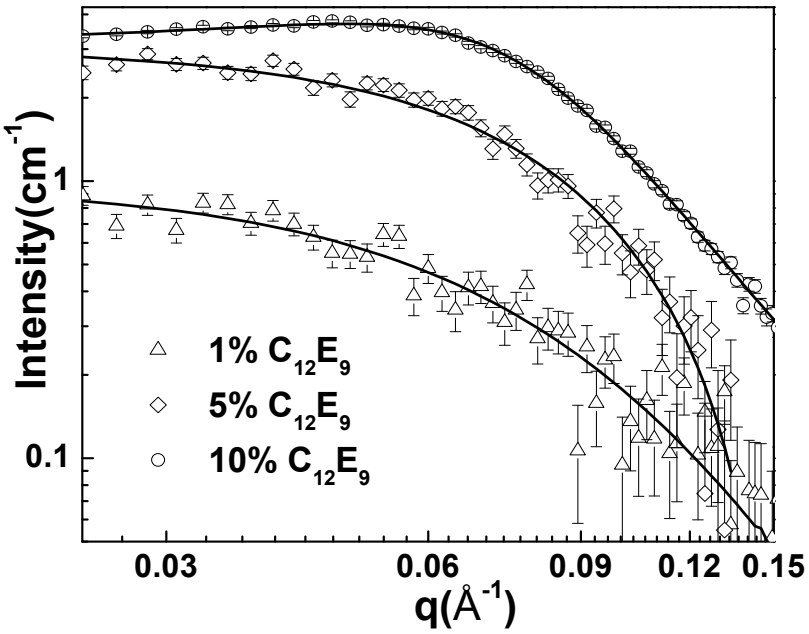

Figure 3.5. SANS data for 1wt%, 5wt% and 10wt%$C_{12}E_9$ in 40:60 H_2O:D_2O matrix.

Sample($C_{12}E_9$ by wt%)	R_m *(Å)*/σ	ν_m (cm^{-3})	R_{HS} *shell-shell interaction (Å)*	ϕ_f
1	19.1/0.28	1.93E+17	-	
5	19.1/0.24	9.8E+17	-	
10	18.8/0.27	1.85E+18	32.9	0.089

Table 3.4. Parameters obtained from fitting for data in Figure 3.5.

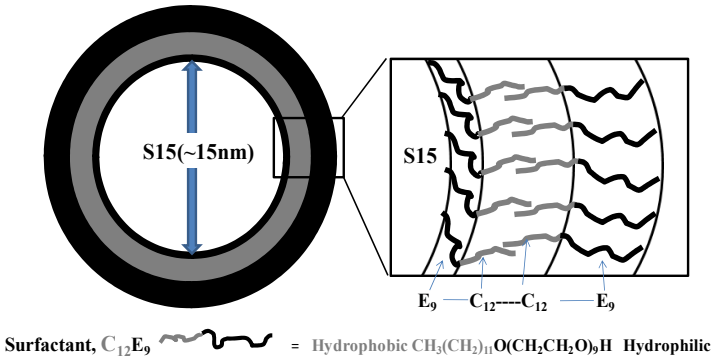

Figure 3.6. Schematic of surfactant adsorbed as a bilayer "shell" on a nanoparticle surface. The ethylene oxide segments are shown in dark, while the hydrophobic segments are indicated in light lines.

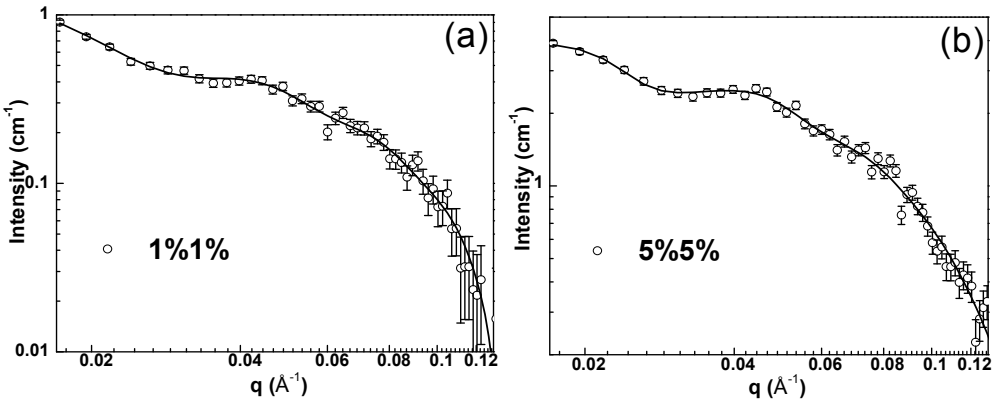

Figure 3.7. SANS from (a) 1%1% sample and (b) 5%5% sample (see text) at room temperature. Fits through the data using the core-shell model for adsorbed surfactant are given as solid lines.

Sample	R_m (Å)/σ	ν_m (cm^{-3})	R_s(Å)	ν_s (cm^{-3})	R_{HS} (shell-shell interaction) (Å)	ϕ_f
1%1%	18.4/0.24	3.15E+17	36.1	4.55E+13	-	-
5%5%	18.7/0.30	2.1E+18	36.8	2.9E+14	121.6	0.23

Table 3.5. Fit parameters for the core-shell model of surfactant adsorption on S15 (Data presented in Figures 3.7 a and 3.7 b).

For scattering from a 5% dispersion of S15 in a 5% surfactant solution (a "5%5%" sample), we are unable to fit the SANS data with just the micelle and shell form factors. As the micelle-micelle apparent structure factor for a 5% surfactant solution in water is equal to 1 (Figure 3.5), we assume that the apparent partial structure factor, $\hat{S}_{mm}(q)$, is also equal to 1. We note that the size of the surfactant bilayer "shell" is large compared to a micelle (see Table 3.5; the shell forms around the S15 particle with diameter ≈ 15 nm). Therefore, we attempt to fit the 5%5% data assuming interference between the scattering from shells, and by modeling an apparent partial structure factor, $\hat{S}_{ss}(q)$, assuming that the potential of mean force between the shells is a hard sphere potential. Our data is fitted well, with an average R_s = 36.8 Å and an average R_m = 18.7 Å, in good accord with the fit to the 1%1% data (Figure 3.7 b). The fitted structure factor gives a hard sphere radius (R_{HS}) of 121.6 Å for the shells, a value that is slightly larger than 111.3 Å (= $R_o + R_s$) – this is reasonable since the shells interact through the hydrated ethylene oxide segments.

Since our SANS data is normalized to absolute intensity, we can calculate the surfactant concentration that is required to form the shells and micelles in our model structure. We assume a density, ρ, of 750 kg.m^{-3} (= the density of dodecane) for the density of the condensed hydrocarbon phase for the aliphatic chains in the shell and in the micellar core, and calculate the surfactant concentration as $[\nu_m\ (4/3)\pi R_m^3\ \rho + \nu_s\ 4\pi R_o^2\ R_s\ \rho] M_s/M_{HC}$, where M_s is the molecular mass of $C_{12}E_9$ (582 g.mol^{-1}), and M_{HC} (169 g.mol^{-1}) is the molecular mass of the aliphatic C_{12} chain. For the 1%1% system, this yields a calculated surfactant concentration of 2.17%, while for the 5%5% system, this yields a calculated surfactant concentration of 15%, well in excess of the experimental quantities (details of calculation in *Appendix*). Therefore, it appears that our

model of the surfactant adsorbing onto the silica particles to form a bilayer shell does not describe our system accurately. This conclusion accords with recent work by Oberdisse et. al.[15,23,24] who have examined a variety of surfactant – silica nanoparticle systems and have shown that these systems are best described as micelles that are adsorbed onto the nanoparticle surface (rather than an adsorbed bilayer surfactant shell). In the work of Oberdisse et. al.,[24] the scattering data at high q (> 0.08 $Å^{-1}$) are not described by a model of surfactants adsorbing to form a shell. We note that our model of scattering from individual micelles and adsorbed surfactant shells fits our experimental SANS data over the entire range of q. However, the large discrepancy between the surfactant concentration calculated from our model fits and the experimental values clearly indicate that the adsorbed surfactant shell model provides an inaccurate description. We also contrast the surface coverage of the surfactant calculated from our model fit to data from adsorption isotherms. Data for adsorption of $C_{12}E_9$ on silica is not available in the literature – however, adsorption isotherm data for $C_{12}E_8$ and for a family of $C_{12}E_m$ have been previously reported.[5,6,24] Based on this data, we estimate that saturation surface coverage of $C_{12}E_9$ adsorbed on our particles surface is between 1 and 2 $\mu mol.m^{-2}$ (viz. ≈ 0.6 – 1.2 $mg.m^{-2}$) and, that the particle surface is saturated at a bulk surfactant concentration of about 0.1 $mmol.l^{-1}$ (viz. ≈ 0.06%). Thus, at the surfactant bulk concentrations that we use in our work, we expect saturation surface coverage. Our fit, using the bilayer model, indicate that a surfactant surface coverage of 14.6 $mg.m^{-2}$, vastly higher than the value expected from the adsorption isotherms (see calculations in *Appendix*). Therefore, we now model our data using an alternate model, the adsorbed micelles picture suggested by Oberdisse et. al.[15]

(b) Adsorbed micelle model

In the adsorbed micelle model, we assume that n_a micelles are adsorbed on average on each silica particle. It is to be noted that we do not imply that the surfactants assemble into micelles in solution, and subsequently adsorb on the particle surface as discussed in pioneering work by Levitz.[9,39] We refer only to the final structure of the surfactant-particle system. Thus, the scattered intensity arises from free micelles in solution and from adsorbed micelles, and we also account for the interference between these (see Schematic, Figure 3.8). The scattered intensity can, thus, be written as:

$$I = \Delta\rho^2 \nu_m \hat{S}_{mm}(q) F_m^2(q) + \Delta\rho^2 \nu_p \hat{S}_{pp}(q) n_a \hat{S}_{aa}(q) F_a^2(q) + 2 \Delta\rho^2 (\nu_p n_p \nu_m)^{0.5} \hat{S}_{am}(q) F_a(q) F_m(q) \quad (4)$$

where ν_p is the number of silica particles, $F_a^2(q)$ is the form factor of the adsorbed micelles, $\hat{S}_{aa}(q)$ accounts for the interference from micelles adsorbed on a single particle, and $\hat{S}_{pp}(q)$ accounts for interference between micelles adsorbed on different particles. $\hat{S}_{am}(q)$ is an apparent partial structure factor that accounts for interference between free micelles and adsorbed micelles. The other symbols have the same meaning as defined earlier. To fit our data, we simplify our model by assuming that the adsorbed micelles have the same structure as the free micelles, viz. $F_a^2(q) = F_m^2(q)$. Further, recalling that in solutions of up to 5% surfactant in water, we can model the scattering with only the micellar form factor (viz. without recourse to a structure factor), it is reasonable that $\hat{S}_{mm}(q) = 1$ and $\hat{S}_{am}(q) = 0$ at the relatively dilute concentrations of surfactant and silica particles in our experiments. We model $\hat{S}_{aa}(q)$ as suggested by Oberdisse et. al. Briefly, we randomly place n_a micelles on the surface of a silica particle and calculate the structure factor as in equation 5 (viz. by assuming that the vec-

tor, $\boldsymbol{r}_i$-$\boldsymbol{r}_j$, is isotropically distributed), and simulate $\hat{S}_{aa}(q)$ by averaging over 10000 realizations.

$$\hat{S}_{aa}(q) = 1 + \frac{1}{n_a} \sum_{i=1}^{n_a} \sum_{j>i}^{n_a} \frac{Sin(q(r_i - r_j))}{q(r_i - r_j)} \tag{5}$$

Thus, the scattering from our dispersion simplifies to:

$$I = \Delta\rho^2 F_m^2(q) [\nu_m + \nu_p \hat{S}_{pp}(q) n_a \hat{S}_{aa}(q)] \tag{6}$$

For a particle radius of ≈ 75 Å, and a micellar radius of ≈ 20 Å, we can accommodate a maximum of ~ O($4R_o^2/R_m^2$ = 56) micelles. Therefore, we have simulated $\hat{S}_{aa}(q)$ for different number of adsorbed micelles, n_a (= 2, 10, 14, 20, 50), and have fitted the scattering data for each guess value of n_a (simulated $\hat{S}_{aa}(q)$shown in Figure 3.9).

For the 1%1% system, we assume that $\hat{S}_{pp}(q)$ = 1 as the nanoparticle concentration is dilute, and present fits to the data for n_a = 2, 10, 14, 20 and 50 (Figure 3.10). We constrain the average particle size, R_o, to the value obtained by fitting the form factor for the particles (R_{S15}, see Tables 3.2, 3.3) and fit the data to equation (6) for various values of n_a. We see that the data is not fitted well for n_a = 2 – however, for the other values of n_a the quality of the fit is good and the dip around q = 0.04 Å^{-1} is reproduced (Figure 3.10). Our data is fitted well with an average micellar radius of 19 to 20 Å. We calculate the surfactant concentration based on our fits for different values of n_a and observe that our experimental values are most closely reproduced for n_a = 14 (Table 3.6; for details of calculation, see *Appendix*). Further, we observe that the number density of particles, ν_p, from our fit, closely matches the average number of silica particles for a 1% dispersion of particles (Table 3.6). In addition, the surfactant surface coverage estimated from this model is 1.5 mg.m^{-2}, in reasonable agreement

from the value expected from adsorption isotherm data (see *Appendix*). Thus, we believe that the structure of the surfactant/silica nanoparticle dispersion is most accurately described by an adsorbed micelle model, with an average of 14 surfactant micelles adsorbed on the surface of each nanoparticle. Within the accuracy of our scattering data, we believe that the adsorbed micelles are similar to those in solution.

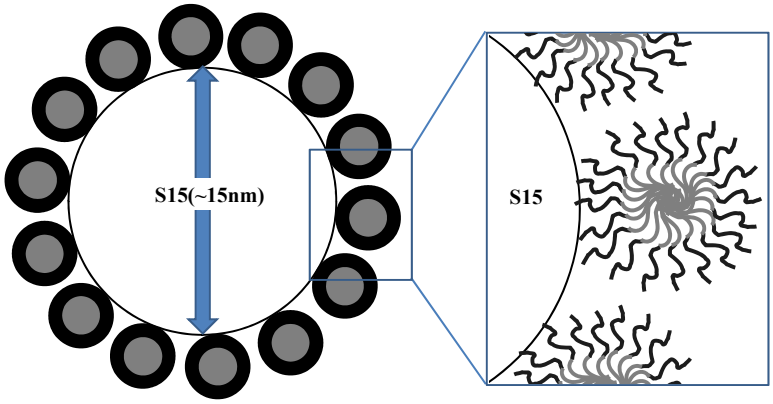

Figure 3.8. Schematic of surfactant adsorbed as a micelle on a nanoparticle surface. The ethylene oxide segments are shown in dark, while the hydrophobic segments are indicated in light lines.

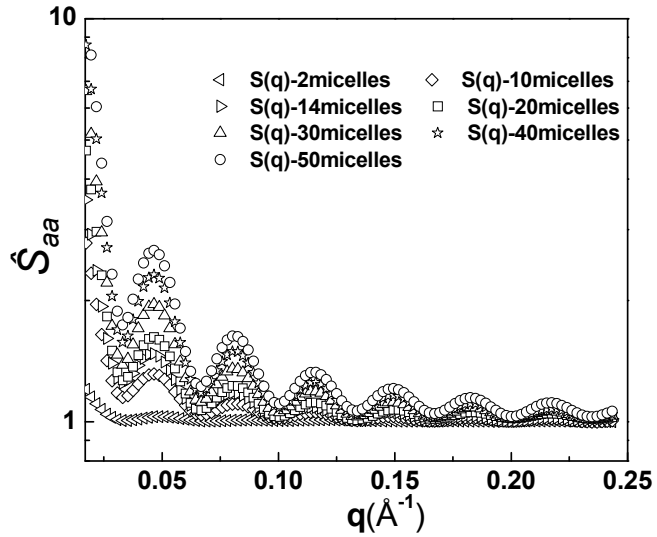

Figure 3.9. Simulated $\hat{S}_{aa}(q)$ data for different number of adsorbed micelles of radius of ≈ 20 Å, n_a (= 2, 10, 14, 20, 30, 40, 50) on a silica particle of radius ≈ 75 Å.

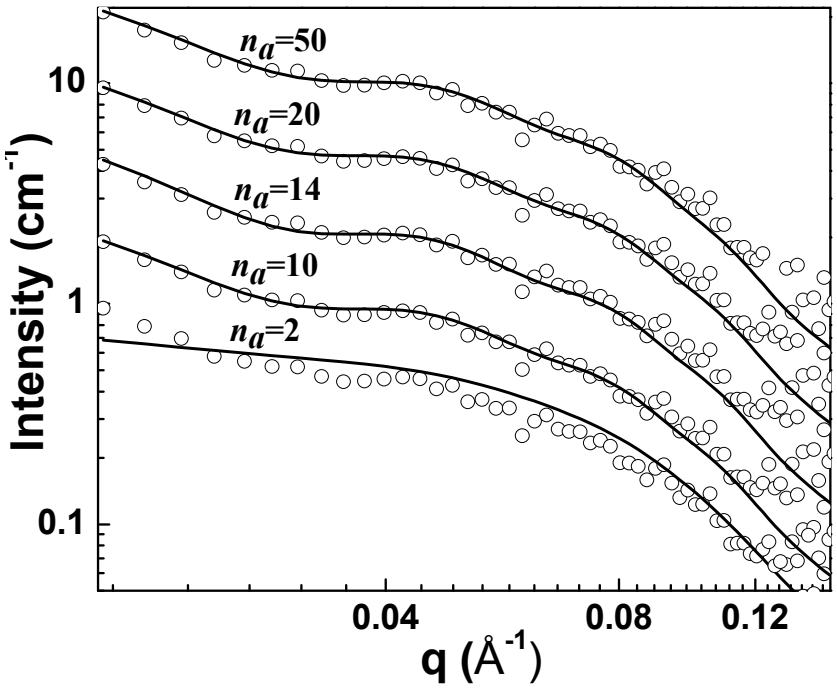

Figure 3.10. SANS from 1%1% sample at room temperature, and fits corresponding to the adsorbed micelle model for n_a= 2, 10, 14, 20 and 50 micelles. The data (and fits) for different n_a are vertically shifted for clarity.

n_a (1%/1%sample)	*ν_m (cm^{-3})*	*ν_p (cm^{-3})*	*Calculated Surfactant concentration (mg/ml)*	*Under (+) / Over (-) estimation of surfactant concentration (%)*	*Under (+) / Over (-) estimation of silica particles (%)*
2	1.71E+16	6.75E+16	11.45	-14.54	-2473.67
10	9.12E+16	4.40E+15	10.18	-1.77	-67.66
14	**9.63E+16**	**2.61E+15**	**9.99**	**0.10**	**0.68**
20	1.04E+17	1.36E+15	9.88	1.21	47.11
50	1.25E+17	1.96E+14	10.16	-1.61	92.73

Table 3.6. Fit parameters for the adsorbed micelle model (Figure 3.10), for different values of n_a. In the model, the radius of the free micelles (= radius of adsorbed micelles) is taken as 19.1 Å (radii follow a lognormal distribution with σ = 0.28). The error in surfactant concentration and number density of particles for the fit parameters relative to the experimental values are also indicated.

We now examine the 5%5% sample and fit the adsorbed micelle model, represented by equation (6) to the scattering data. When we assume $\hat{S}_{pp}(q) = 1$, we are unable to fit the data for any value of n_a. As the nanoparticles, with micelles adsorbed on them are large ($=2R_o+2R_m$), and at a relatively high concentration (5% by weight of the nanoparticles in the dispersion), it is reasonable that we have to account for the interference between the scattering from these structures. We assume the simplest model to account for the interaction between the micelle covered nanoparticles, viz. a hard sphere potential and calculate $\hat{S}_{pp}(q)$ accordingly. Again, for $n_a = 14$, the scattering data fits well (Figure 3.11), the surfactant concentration calculated from the fit matches closely with the experimental value and, the number density of silica nanoparticles closely matches that expected for a 5% dispersion of particles (Table 3.7, and see *Appendix* for detailed calculations). The fit to $\hat{S}_{pp}(q)$ yields reasonable values (Table 3.7) for the hard sphere radius of the surfactant micelle adsorbed silica particles (119.6 Å $\approx R_o + 2R_m$) and for the volume fraction [$0.27 \approx \phi\,(R_o + 2\acute{R}_m)^3/R_o^3$, where $\phi = 0.023$ is the volume fraction of the silica nanoparticles, and $\acute{R}_m$ is the radius of the adsorbed surfactant micelle (estimated ≈ 47 Å); $\acute{R}_m$ includes the hydrophobic core (R_m) and, the solvated ethylene oxide segments].

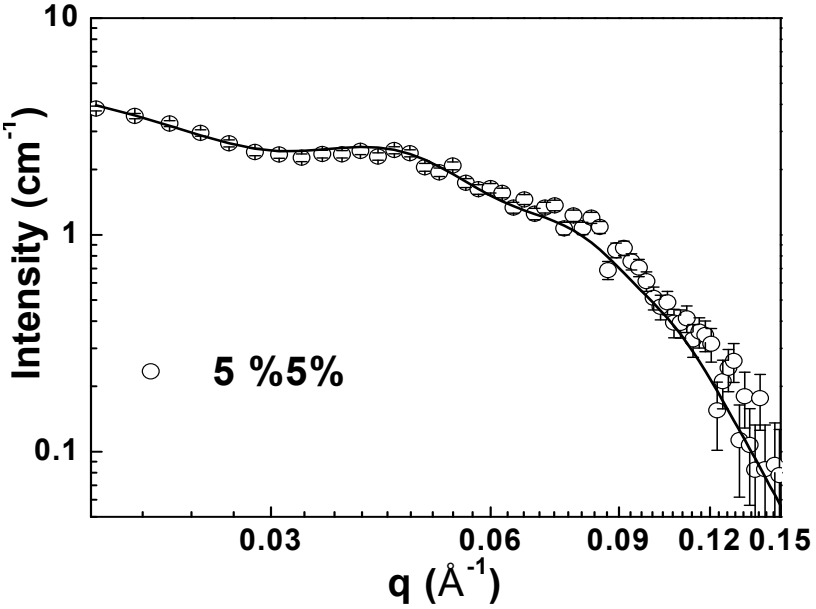

Figure 3.11. SANS for 5%5% sample (room temperature), showing the fit (solid line) to the adsorbed micelle model for n_a=14.

n_a (5%5% sample)	*R_m=R_a(Å)/ σ*	*ν_m (cm^{-3})*	*ν_p (cm^{-3})*	*R_{HS} (Å)*	*ϕ*	*Calculated surfactant concentration (mg/ml)*	*Under (+) / Over (-) estimation of surfactant concentration (%)*	*Under (+) / Over (-) estimation of silica particles (%)*
14	19.1/0.28	4.65E+17	1.33E+16	119.6	0.27	49.05	+1.91	-1.73

Table 3.7. Fit parameters for 5%5% sample using the adsorbed micelle model (Figure 3.11), for n_a = 14. The errors in surfactant concentration and number density of particles for the fit parameters relative to the experimental values are also indicated.

3.3.3. Scattering from PEI coated silica particles:

Now, we examine the structure of polyethyleneimine (PEI) coated silica particles in surfactant solutions. We show in the next chapter that PEI with a molecular weight of 2000 g.mol^{-1} adsorbs on the surface of S15, and that zeta potential measurements indicate a reversal in the mean zeta potential from -33.5 mV for the S15 to +8 mV for the PEI-S15. From SAXS of 1% (by weight) PEI-S15, we obtained a particle radius/standard deviation of 81 Å /0.15 (marginally higher than for the S15, 74.5 Å /0.14, Figure 3.12). Thus, our data indicates that the PEI coats the S15, forming a monolayer on the surface of the silica nanoparticle. SANS from 5% (by weight) PEI-S15 in 5% (by weight) $C_{12}E_9$ (that we call the PEI-5%5% sample) in a water/D_2O 40/60 mixture, that contrast matches the silica is presented in Figure 3.13 a. A comparison between scattering profiles from 5%5% (Figure 3.11) and PEI-5%5% (Figure 3.13 a) and from a 5% surfactant solution (Figure 3.13 b) clearly indicates that the scattering profiles look similar for the 5% surfactant solution and PEI-5%5%, and that there is a qualitative difference in the shape of the scattering profile for the 5%5% sample. Specifically, the dip in the scattered intensity near q = 0.04 Å^{-1} observed for the 5%5% sample is absent for PEI-5%5%. This suggests that adsorption of the PEI on S15 prevents adsorption of the surfactant micelles. We model the scattered data from the PEI-5%5% solution using the form factor for dilute polydisperse spheres and obtain a mean radius of 20.3 Å, and a standard deviation of 0.3 (Figure 3.13 a, Table 3.8). This compares well with the values from fitting the scattering from 5% surfactant solution (mean radius = 19.5 Å, standard deviation = 0.24; Figure 3.13 b, Table 3.8). Thus, scattering from PEI-5%5% in solvent contrast matched to silica, is dominated by the scattering from surfactant micelles and the PEI-S15 particles do not appear to

contribute much to the scattering. We have shown in Chapter 4 that nanoparticulate networks, formed by PEI-S15 particles that phase separate from $C_{12}E_9$ solutions, can be crosslinked using agents that create bonds that link PEI molecules and, that these crosslinked PEI-S15 scaffolds are self standing, even after removal of the surfactant. In contrast, particulate networks of the S15 are thermoreversible, and redisperse on surfactant removal, or on heating the surfactant into the isotropic micellar phase. Our SANS data provide us with an understanding of the mechanism for this behavior. $C_{12}E_9$ micelles adsorb on the surface of S15 particles, and stabilize the particles against aggregation. The micelle adsorbed particle structures interact with each other through a hard sphere potential. In contrast, PEI coating the S15 particles prevents micellar adsorption, and provides a crosslinkable polymer coat to the S15 particles – thus, allowing the formation of crosslinked and self standing PEI-S15 nanoparticulate scaffolds.

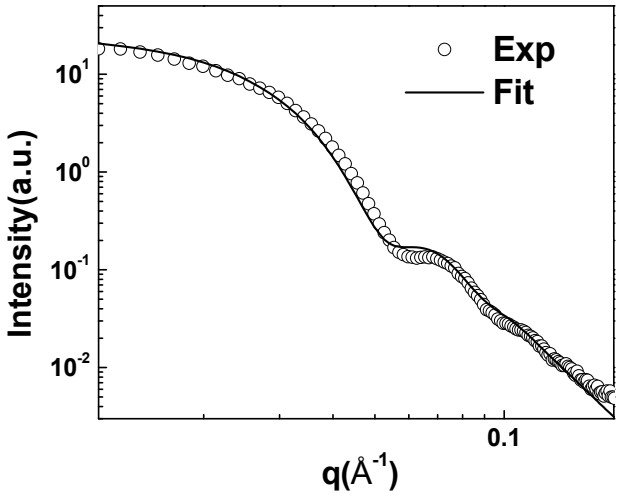

Figure 3.12. SAXS data at for 5% PEI coated S15 particles in water at 25°C. The data was fitted (solid lines) assuming screened spherical form factor yielding radius of 81Å and std. deviation of 0.15.

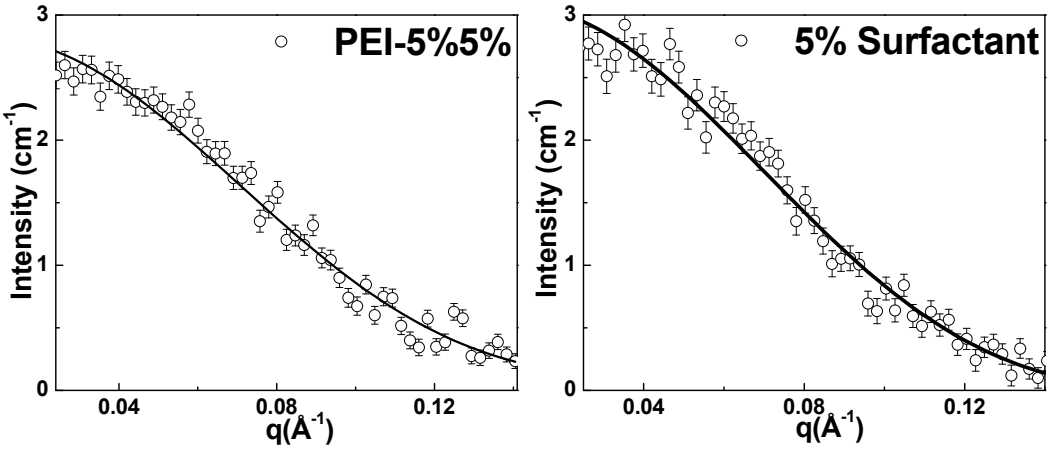

Figure 3.13. SANS (at room temperature) for (a) PEI-5%5% and (b) 5% surfactant samples in 40:60 H_2O:D_2O matrix, contrast matched to the scattering length density of silica.

Sample	R_m *(Å)*	σ	ν_m *(cm^{-3})*
PEI-5%5%	20.3	0.3	8.7E+17
5% $C_{12}E_9$	19.1	0.24	9.8E+17

Table 3.8. Parameters from fitting SANS data from PEI-5%5% (Figure 3.13 a) and 5% surfactant (Figure 3.13 b).

3.4. Summary

Charge stabilized silica particles, disperse readily in a 1:1 $C_{12}E_9$:water solution when mixed at high temperature (50^{o}C), in the isotropic micellar phase. An aqueous dispersion of the silica particles aggregates irreversibly when it is destabilized, for example, by increasing the ionic strength. However, interestingly, a dispersion of the same particles in 1:1 $C_{12}E_9$:water is stable even in brine, and over a range of pH. SANS on particle dispersions in 1:1 $C_{12}E_9$:water, where the surfactant is contrast matched, reveals that the interparticle interaction can be modeled by a hard sphere interaction. Thus, the mean potential of interparticle interaction changes from a screened Coulombic potential in water to a hard sphere potential in 1:1 $C_{12}E_9$:water. SANS on dilute particle/surfactant solution reveals that the structure can be modeled as surfactant micelles adsorbed on the particle surface, with 14 micelles adsorbed on each particle, on average. We believe that these adsorbed micelles provide a steric repulsion between the particles that stabilizes them against irreversible aggregation, and gives rise to the hard sphere interparticle potential. The adsorbed micelles appear to be strongly associated with the silica particles. In particle dispersions in concentrated (viz., 1:1) $C_{12}E_9$:water solutions, cooling from 50^{o}C to room temperature results in formation of a hexagonal (H_1) gel phase. H_1 domains exclude the silica particles, and these nanoparticles phase separate to form scaffolds. This particle aggregation to form scaffolds is thermoreversible, and the particles redisperse on heating into the micellar phase. This suggests that, even when the particles phase aggregate at the H_1 domain boundaries, surfactant micelles remain associated with the particles, rendering the aggregation thermoreversible. Coating the silica particles by adsorbing an oppositely charged polyelectrolyte, PEI, prevents surfactant adsorption on the particle surface.

3.5. Appendix

Calculations for structure of the adsorbed surfactant on the particle surface from both the models:

MODEL 1: Calculations of surfactant amount from core-shell (bilayer) model parameters:

(a) For 1%1% sample

Average radius of micelles (R_m) = 18.2 Å

Number of micelles, ν_m = 3.15E+17 cm^{-3}

Number of shells, ν_s = 4.55E+13 cm^{-3}

Thickness of shell, R_s = 36.1 Å.

Mol. Wt of $C_{12}E_9$= 582g.mol^{-1} ; Mass of C_{12}- chain

= 169 g.mol^{-1}

Inner radius of shell (R_0)= Radius of silica particle (R_{S15})

= 74.5 Å

Therefore volume of 1 shell = $(4/3)* \pi*[(R_o+ R_s)^3-(R_o)^3]$

= 3.94E-18 cm^3

Mass of 1 shell (density=0.75g/cm^3) = 2.95E-18 g

This is the mass of the C_{12} segment.

Therefore mass of 1 shell (considering the entire surfactant, rather than just the C_{12} part) = 2.95E-18 * (582/169)

= 1.02E-14 mg

Thus, surfactant surface coverage = 1.02E-14/[4π (74.5E-10)^2]

$= 14.6 \text{ mg.m}^{-2}$

Therefore mass of ν_s=4.55E+13 shells (M_{shells})

$= 0.46$ mg

Mass of 1 micelle of R_m= 18.2 Å

$=(4/3)*(22/7)*(18.2)^3*1E\text{-}24(\text{cm}^3)*0.75(\text{g/cm}^3)*(582/169)$

$= 6.74E\text{-}17$ mg

Therefore mass of, ν_m =3.15E+17 number of micelles ($M_{micelle}$)

$= 21.2$ mg

Therefore total amount of surfactant utilized in free micelles and shell formation

$= M_{shells} + M_{micelle} = 21.7$mg

Actual amount of surfactant used = 10 mg (1% surfactant)

Therefore amount of surfactant calculated by core shell model

= 21.7 mg (2.17% surfactant)

(b) For 5%5% sample

Average radius of micelles (R_m) = 18.7 Å.

Number of micelles, ν_m = 2.1E+18 cm^{-3}

Number of shells, ν_s = 2.9E+14 cm^{-3}

Thickness of shell, R_s = 36.8 Å

Inner radius of shell (R_0)= Radius of silica particle (R_{S15})

= 74.5 Å

Therefore volume of 1 shell $= (4/3)* \pi*[(R_o + R_s)^3 - (R_o)^3]$

$= 4.04E\text{-}18 \text{ cm}^3$

Mass of 1 shell (density=0.75g/cm^3) = 3.03E-18 g

This is the mass of the C_{12} segment.

Therefore mass of 1 shell (considering the entire surfactant, rather than just the C_{12} part) = 3.03E-18* (582/169)

= 1.04E-14 mg

Therefore mass of ν_s=2.9E+14 shells (M_{shells})

= 3.0 mg

Mass of 1 micelle of R_m = 18.7 Å

= 7.1E-17 mg

Therefore mass of, ν_m =2.1E+18 number of micelles ($M_{micelle}$)

= 147 mg

Therefore total amount of surfactant utilized in free micelles and shell formation

= M_{shells}+ $M_{micelle}$= 147 + 3= 150 mg

Actual amount of surfactant used = 50 mg (5% surfactant)

Therefore amount of surfactant calculated by core shell model

= 150 mg (15% surfactant)

MODEL 2: Calculations of surfactant amount from adsorbed micelles model parameters: Under (+) / Over (-) estimation of surfactant concentration (%)

(a) 1%1% sample

$$I = \Delta\rho^2 F_m^2(q) [\nu_m + \nu_p \hat{S}_{pp}(q) n_a \hat{S}_{aa}(q)]$$

For a 1%1% sample F_m^2 gives a radius of R_m

= 19.1Å.

Also 1%1% system corresponds to 10mg surfactant and 10mg silica per milliliter of sample.

ν_m= 9.63E+16 cm^{-3}, ν_p =2.61E+15 cm^{-3} and n_a=14

Mol. Wt of $C_{12}E_9$= 582g.mol^{-1} ; Mass of C_{12}- chain=169 g.mol^{-1}

The volume of 1 micelle (C_{12} core) is equal to

$= (4/3)*\pi*(R_m)^3$

$= 2.9E\text{-}20\ cm^3$

Mass of 1 micelle (Assuming density as 0.75 g/cm^3)

= 2.18E-20 g

This mass is for the C_{12} chain

Therefore mass of 1 micelle (considering the entire surfactant, rather than just the C_{12} part)

= 2.18E-20* (582/169)

= 7.5E-17 mg

Thus, surfactant surface coverage = [7.5E-17*14]/[4π (74.5E-10)^2] = 1.5 mg/m^2

Therefore total surfactant mass calculated (*Surf.$_{calc}$*)

` $= M_{micelle}*[\nu_m + (\nu_p * n_a)]$

= 9.99 mg

Surfactant actually taken for the experiments (*Surf.$_{exp}$*)

= 10 mg

Therefore % error in surfactant calculation

$= [(Surf._{exp} - Surf._{calc})/ Surf._{exp}]*100$

= [(10-9.99)/10]*100

= +0.1%

Calculations for Under (+) / Over (-) estimation of silica particles (%) (ν_p)

Radius of silica particle as determined by SAXS and SANS by form factor

= 74.5 Å

Volume of 1 silica particle = (4/3)*(22/7)*(74.5)^3*(1E-24) cm^3

= 1.7E-18 cm^3

Mass of 1 silica particle (density of 2.2 g/cm^3)

= 1.7E-18cm^3*2.2(g/cm^3)= 3.8E-18 g

= 3.8E-15 mg

Therefore number of silica particles in 10mg of silica taken in the experiment ($\nu_{p\text{-}exp}$)

= 10/3.8E-15

= 2.62E+15

Therefore %error in calculated silica particles

= [($\nu_{p\,exp} - \nu_p$)/ $\nu_{p\,exp}$]*100

= [(2.62E+15-2.61E+15)/ 2.62E+15]*100

= +0.68%

Similarly one can calculate the %surfactant error and %silica particles error for different values of adsorbed micelles viz. n_a= 2, 10, 20, 50 and by using the corresponding values of ν_a and ν_p respectively.

(b) 5%5% sample

$$I = \Delta\rho^2 F_m^2(q) [\nu_m + \nu_p \hat{S}_{pp}(q)\, n_a \hat{S}_{aa}(q)]$$

For a 5%5% sample F_m^2 gives a radius of R_m=19.1 Å.

Also 5%5% system corresponds to 50mg surfactant and 50mg silica per milliliter of sample.

ν_m= 4.65E+17 cm^{-3} , ν_p = 1.33E+16 cm^{-3} and n_a=14

Mol. Wt. of $C_{12}E_9$= 582 $g.mol^{-1}$; Mass of C_{12}- chain=169 $g.mol^{-1}$

The volume of 1 micelle seen by the neutrons is equal to

$$= (4/3)*\pi*(R_m)^3$$

$$= 2.9E\text{-}20\ cm^3$$

Mass of 1 micelle (Assuming density as 0.75 g/cm^3)

$$= 2.9E\text{-}20cm^3*0.75(g/cm^3)$$

$$= 2.18E\text{-}20\ g$$

This mass is for the C_{12} chain

Therefore mass of 1 micelle (considering the entire surfactant, rather than just the C_{12} part)

$$= 2.18E\text{-}20* (582/169)$$

$$= 7.5E\text{-}17\ mg$$

Therefore total surfactant mass calculated ($Surf._{calc}$)

$$= M_{micelle}*[\nu_{m+} (\nu_p *n_a)]$$

$$= 49.05\ mg$$

Surfactant actually taken for the experiments ($Surf._{exp}$)

$$= 50\ mg$$

Therefore % error in surfactant calculation

$$= [(Surf._{exp} - Surf._{calc})/ Surf._{exp}]*100$$

$$= [(50\text{-}49.05)/50]*100$$

$$= +1.91\%$$

Calculations for Under (+) / Over (-) estimation of silica particles (%) (ν_p)

Radius of silica particle as determined by SAXS and SANS by form factor

$= 74.5$ Å

Volume of silica particle $= (4/3)*(22/7)*(74.5)^3*(1E\text{-}24)$ cm^3

$= 1.7E\text{-}18$ cm^3

Mass of 1 silica particle (density of 2.2 g/cm^3)

$= 1.7E\text{-}18$cm^3*2.2(g/cm^3)

$= 3.8E\text{-}18$ g

$= 3.81E\text{-}15$ mg

Therefore number of silica particles in 50mg of silica taken in the experiment ($\nu_{p\text{-}exp}$)

$= 50/3.8E\text{-}15$

$= 1.31E+16$

Therefore %error in calculated silica particles

$= [(\nu_{p\,exp} - \nu_p)/\nu_{p\,exp}]*100$

$= -1.73\%$

3.6. References

1. Sharma, K. P.; Kumaraswamy, G.; Ly. I.; Mondain-Monval, O. *J. Phys. Chem. B* **2009** *113*, 11, 3423-3430.
2. (a) Fabre, P.; Cassagrande, C.; Veyssie, M.; Cabuil, V.; Massart, R. *Phys. Re*V. *Lett.* **1990** *64*, 539. (b) Quilliet, C.; Ponsinet, V.; Cabuil, V. *J. Phys. Chem.* **1994** *98*, 3566–3569. (c) Eiser, E.; Bouchama, F.; Thathagar, M. B.; Rothenberg, G. *Chem. Phys. Chem.* **2003** *4*, 526. (d) Bouchama, F.; Thathagar, M. B.; Rothenberg, G.; Turkenburg, D. H; Eiser, E. *Langmuir* **2004** *20*, 477–483. (e) Wadekar, M. N.; Pasricha, R.; Gaikwad, A. B.; Kumaraswamy, G. *Chem. Mater.* **2005** *17*, 2460.
3. Holmberg, K.; Shah, D. O.; Schwuger, M. J.(eds) *Handbook of Applied Surface and Colloid Chemistry* **2002**, John Wiley (NY).
4. McDermott, D. C.; Lu, J. R.; Lee, E. M.; Thomas, R. K.; Rennie, A. R. *Langmuir* **1992** *8*, 4, 1204-1210.
5. Bohmer, M. R.; Koopal, L. K.; Janssen, R.; Lee, E. M.; Thomas, R. K.; Rennie, A. R. *Langmuir* **1992,** *8*, 9, 2228-2239.
6. Tiberg, F.; Jonsson, B.; Tang, J.; Lindmann, B. *Langmuir* **1994**, *10*, 7, 2294-2300.
7. Howse, J. R.; Steitz, R.; Pannek, M.; Simon, P.; Schubert, D. W.; Findenegg, G. H. *Phys. Chem. Chem. Phys.* **2001**, *3*, 4044-4051.
8. Matsson, M. K.; Kronberg, B.; Claesson, P. M. *Langmuir* **2004**, *20*, 10, 4051-4058.
9. (a) Levitz, P.; Damme H. V.; Keravis, D. *J. Phys. Chem.* **1984**, *88*, 11, 2228-2235. (b) Levitz, P.; Damme H. V. *J. Phys. Chem.* **1986**, *90*, 7, 1302-1310. (c) Levitz, P.; Damme H.V. *J. Phys. Chem.* **1986**, *90*, 7, 1302-1310.
10. Qiao, Y.; Schönhoff, M.; Findenegg, G. H. *Langmuir* **2003**, *19*, 15, 6160-6167.

11. Findenegg, G. H.; Eltekov, A. Y. *J. Chromatogr. A* **2007**, *1150*, 236-240.

12. Dietsch, O.; Eltekov, A. Y.; Bock, H.; Gubbins, K. E.; Findenegg, G. H. *J. Phys. Chem. C* **2007**, *111*, 43, 16045-16054.

13. (a) Cummins, P. G.; Staples, E.; Penfold, J. *J. Phys. Chem.* **1990**, *94*, 9, 3740-3745. (b) Cummins, P. G.; Penfold, J.; Staples, E. *Langmuir* **1992** *8*, 1, 31-35. (c) Penfold, J. *J. Phys. Chem.* **1996**, *100*, 46, 18133-18137.

14. Giordano-Palmino, F.; Denoyel, R.; Rouquerol, J. *J. Colloid Interface Sci.* **1994**, *165*, 82-90.

15. Despert, G.; Oberdisse, J. *Langmuir* **2003**, *19*, 18, 7604-7610.

16. Levitz, P.; Miri, A. E.; Keravis, D.; Damme, H. V. *J. Colloid Interface Sci.* **1984** *99*, 2, 484-492.

17. Dong, J.; Mao, G. *Langmuir* **2000**, *16*, 16, 6641-6647.

18. Patrick, H. N.; Warr, G. G.; Manne, S.; Aksay, I. A. *Langmuir* **1997**, *13*, 16, 4349-4356.

19. Grant, L. M.; Tiberg, F.; Ducker, W. A. *J. Phys. Chem. B* **1998**, *102*, 22, 4288-4294.

20. Tiberg, F.; Brinck, J.; Grant, L. *Curr. Opin. Colloid Interface Sci.* **1999**, *4*, 411-419. (b) Warr, G. G. *Curr. Opin. Colloid Interface Sci.* **2000**, *5*, 88-94.

21. Duits, M. H. G.; May, R. P.; Vrij, A.; de Kruif, C. G. *J. Chem. Phys.* **1991**, *94*, 6, 4521-4531.

22. Lee, E. M.; Thomas, R. K.; Cummins, P. G.; Staples, E.; Penfold, J.; Rennie, A. R. *Chem. Phys. Lett.* **1989**, *162*, 3, 196-202.

23. Oberdisse, J. *Phys. Chem. Chem. Phys.* **2004**, *6*, 1557-1561.

24. Lugo, D.; Oberdisse, J.; Karg, M.; Schweins, R.; Findenegg, H. *Soft Matter* **2009**, *5*, 2928-2936.

25. Alexeev, V. L; Ilekti, P.; Persello, J.; Lambard, J.; Gulik, T.; Cabane, B. *Langmuir* **1996**, *12*, 2392-2401.

26. Wadekar, M. N.; Pasricha, R.; Gaikwad, A. B.; Kumaraswamy, G. *Chem. Mater.* **2005**, *17*, 2460.

27. Bringley, J. F.; Wunder, A.; Howe, A. M.; Wesley, R. D.; Qiao, T. A.; Liebert, N. B.; Kelley, B.; Minter, J.; Antalek, B.; Hewitt, J. M. *Langmuir* **2006**, *22*, 4198-4207.

28. Aswal, V. K.; Goyal, P. S. *Curr. Sci.* **2000**, *79*, 7, 947-953.

29. *SASfit vers. 0.90.1* software by Joachim Kohlbrecher, Laboratory for Neutron Scattering, PSI, Switzerland. http://kur.web.psi.ch/sans1/SANSSoft/sasfit.html

30. Kaler, E. W. in Book chapter *Small-Angle Scattering from Complex Fluids* from Modern Aspects of Small-Angle Scattering Brumberger, H. (ed.), Kluwer Academic Publishers, Dordrecht, The Netherlands, **1993**, pp. 329-353.

31. Kline, S. R.; Kaler, E. W. *J. Chem. Phys.* **1996**, *105*, 9, 3813-3822.

32. (a) Qiu, D.; Cosgrove, T.; Howe, A. M.; Dreiss, C. A. *Langmuir* **2006**, *22*, 546-552. (b) Ramsay, J. D. F.; Avery, R. G.; Benest, L. *Faraday Discuss. Chem.* Soc. **1983**, *76*, 53-63.

33. Israelachvili, J. N. *Intermolecular and Surface Forces* **1992** 2nd ed., Academic Press Limited, London.

34. Hayter, J. B.; Penfold, J. *Mol. Phys.* **1981**, *42*, 109.

35. Penfold, J.; Ramsay, J. D. F. *J. Chem. Soc., Faraday Trans. 1* **1985**, *81*, 117-125.

36. Jijo, V. J.; Sharma, K. P.; Mathew, R.; Kamble, S.; Rajamohanan, P. R.; Ajithkumar, T. G.; Badiger, M. V.; Kumaraswamy, G. *Macromolecules* **2010**, *43*, 4782–4790 .

37. (a) Mitchell D. J.; Tiddy, G. J. T.; Waring, L.; Bostock, T.; McDonald, M. P. *J. Chem. Soc.***,** *Faraday Trans. I* **1983**, 79**,** 975-1000. (b) Kunieda, H.; Ozawa, K.; Huang, K.-L. *J. Phys. Chem. B* **1998**, *102*, 831.

38. Vrij, A. *Pure Appl. Chem.* **1976**, *48*, 471.

39. Levitz, P. *Langmuir* **1991**, *7,* 1595-1608.

40. Thwala, J. M.; Goodwin, J. W.; Mills, P. D. *Langmuir* **2009**, *25*, 12926–12936.

Chapter 4

Tunable Macroporous Scaffolds of Nanoparticles by Dynamic Templating of H_1 Domains

4.1. Introduction

Assembly of nanoparticles into free-standing macroporous materials has implications for a wide range of technologically important applications, such as separation, chromatography, catalysis, filtration, insulation and, biomedical scaffolds. A variety of approaches have been demonstrated for nanoparticle assembly into macroporous materials,[1] including, spray drying,[2] polymer-induced aggregation,[3] controlled destabilization of nanoparticle dispersions,[4] and sol-gel assembly.[5] In these techniques, control over pore morphology is possible by optimization of processing parameters, but is challenging. On the other hand, three dimensional writing with nanoparticle inks[6] affords precise control over structure formation, but is relatively complicated to implement.

An elegant strategy to create macroporous materials is to combine nanotectonics[7] (assembly of preformed nanoparticles), with templating of larger length scale structures,[8] including static templates, such as, colloidal crystals,[9] membranes,[10] gels,[11] polymer foams,[12] and biological organisms.[13] Nanoparticles can also be assembled around dynamic templates such as solvent drops in breath figures,[14] or in dynamic processing operations such as foaming.[15] In these methodologies, control over pore morphology remains a challenge, and requires either preassembly of precisely defined templates, or exquisite control over experimental protocols (viz. solvent condensation or foaming conditions). Recently, particles with specially tailored surface chemistry have been shown to segregate to interphases,[16] and jam, thus arresting structural evolution in phase separating blends[17] to produce a percolated particulate assembly. There has also been renewed interest in dynamic templating of ice crystals by polymer-nanoparticle dispersions.[18] Ice templating allows control over pore size, shape and

orientation.[18] While ice templating is a powerful technique,[18] it involves freezing temperatures, and employs freeze drying to remove the ice template. Thus, it would be advantageous to have a simpler technique to prepare macroporous materials using a wide variety of materials that retains the elegance of ice templating, but employs milder conditions and involves easier template removal.

Templating of nematic domains, by particles expelled to domain boundaries, results in the formation of particulate networks.[19] This network formation is reversible, and the particles redisperse on heating above the liquid crystal clearing temperature[19]– thus, free-standing porous materials have not been prepared using this route. Further, the particles need to be hydrophobic for dispersion in the liquid crystal, and network formation is observed only when impurities in the liquid crystal constrain the isotropic-nematic interface to propagate slowly.[19] In liquid crystal colloids with strong director anchoring, interactions between topological defects formed around dispersed particles result in particle organization.[20] Particles dispersed in lamellar phases segregate to defect nodes to stabilize "oily streak" networks.[21] However, none of the aforementioned techniques have been exploited to prepare macroporous materials.

In chapter 2 we reported,[22] for the first time, a systematic study of the effect of particle size on their organization in a nonionic surfactant hexagonal (H_1) mesophase. Our results, in accord with previous literature,[23] demonstrated that particles smaller than the characteristic H_1 spacing, (spacing between surfactant assemblies, $a \approx 5$ nm), template the surfactant structure, while larger particles ($> \approx 10$ nm) are expelled to form a network. For assembly of silica particles, network formation is rendered reversible[22] due to formation of micellar structures on the particle surface. However, interestingly, when the silica particles are coated with polyethyleneimine (PEI), it is observed

that, micelle-covered particle structures do not form.[24] Thus, PEI-coated particles can come into true physical contact, and crosslinking the PEI coat layer might enable us to stabilize the particulate networks.

Here, we demonstrate that dynamic templating of surfactant hexagonal domains is a facile technique to organize inorganic, organic and biological nanoparticles into a network of particulate strands. This technique involves near ambient temperatures, and a benign water wash for template removal. The network mesh size can be varied from the sub-micron to tens of microns by controlling the cooling rate and networks can be flow-oriented.

4.2. Experimental

4.2.1. Materials:

Ludox LS-30 silica particles (Sigma Aldrich) were used as received. Nonionic surfactant, nonaethylene glycol monododecyl ether, $C_{12}E_9$ (characterized earlier[25]); tetraethylorthosilicate; triethanolamine; cetyl ammonium chloride (CTAC); aminopropyltriethoxysilane; fluorescein isothiocyanate (FITC); 3-[2-(2-Aminoethylamino) ethylamino]propyltrimethoxysilane; Biotin-NHS; Streptavidin-phycoerythrin; polyethylene imine (PEI; 2000 $g.mol^{-1}$); and horse spleen ferritin (5-15 wt%) were obtained from Sigma Aldrich and used as received. Hydroxyapatite particles (HAP) were obtained as 10 wt% dispersion in water from Aldrich, and were sonicated using a probe sonicator immediately prior to coating with PEI. Fluorescent polystyrene latices were obtained from Microparticles GmbH, Germany.

Silica particles (90 nm diameter) were synthesized using a standard Stöber method. Amine groups were grafted onto these silica particles using a procedure reported earlier,[26] and finally, the particles were tagged with a fluorescent dye (FITC). The par-

ticles were characterized by TEM, TGA and IR. Preparation of PNIPAM microgels, [27] positively charged Fe_3O_4[28] and CeO_2[29] was done according to the procedure reported in literature.

4.2.2 Coating of particles with polymers:

(a) PEI coating on Ludox silica particles

Ludox silica particles (S15 (15nm); detailed characterization of S15 particles in Chapter 2) were coated with PEI using a modification of the process described in literature[30] (also shown in Figure 4.1). The pH of 1mg/ml PEI solutions was adjusted to 5.0 prior to coating on the silica particles. During coating, we ensured that the pH of the mixture remained between 5 and 6. PEI solution (5ml; 10 mg/ml) was added drop wise while continuous stirring to 1 ml of 15 wt% silica to get a PEI coating on the silica particles. PEI coated silica particles were characterized using TGA (Figure 4.2), SAXS[24] and by measuring their zeta potential (Figure 4.3). The manufacturer specified surface area for the silica particles is 220 m^2/g. For layer-by-layer coating of polyelectrolytes from aqueous solutions at moderate ionic strength, the typical mass adsorbed per layer[31] is around 1 mg/m^2. Thus, we expect that about 220 mg of PEI will be adsorbed per gram of the silica particles. Therefore, the calculated organic content = (0.22/1+0.22)*100 ≈ 18%. This is comparable to the organic fraction from our TGA measurements i.e. ~13% of PEI.

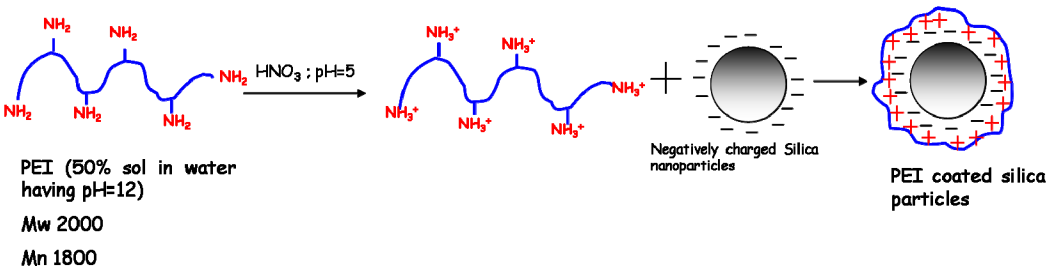

Figure 4.1. Schematic showing the procedure for PEI coating on the 15nm silica particles.

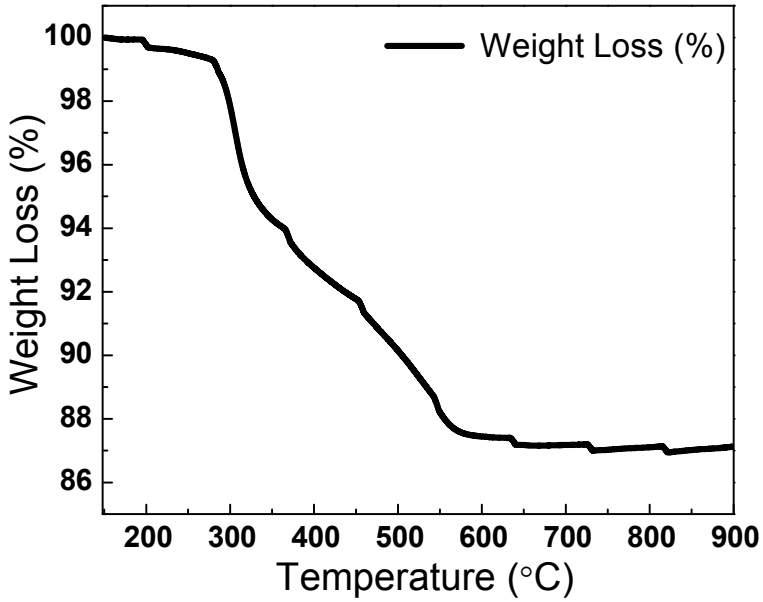

Figure 4.2. Thermogravimetric analysis for scaffold prepared from PEI coated 15 nm silica particles (PEI-S15).

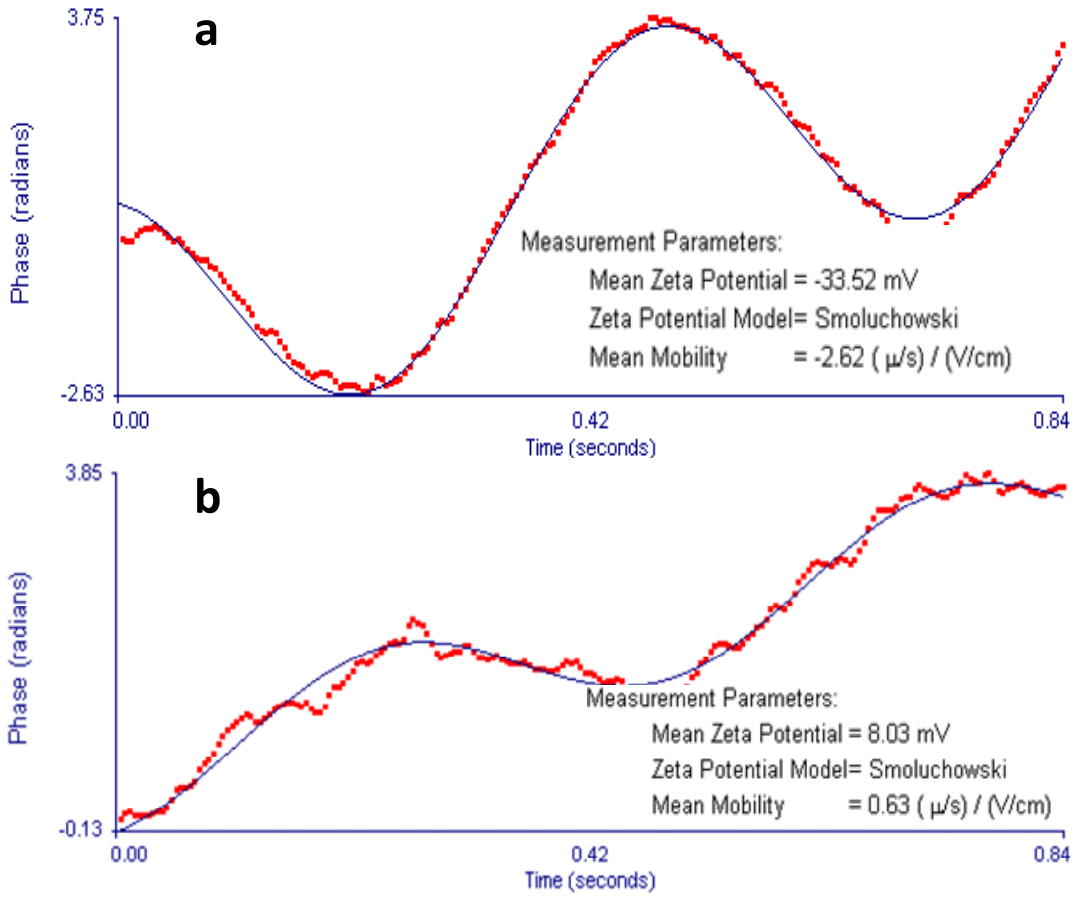

Figure 4.3. Zeta potential for the 15 nm S15 (Ludox silica particles). (a) Bare S15 particles, (b) PEI coated S15. Figures show the fits to the phase change using the Smoluchowski model while measuring the zeta potential for a 0.5 wt% dispersion of particles. (a) The mobility of the bare particles obtained is -2.62 µm/s/(V/cm) and the zeta potential is -33.52 mV. (b) The mobility of the particles obtained is 0.63 µm/s/(V/cm) and the zeta potential is +8.03 mV. The zeta potential changes sign, from negative to positive on PEI coating.

(b) PEI coating on polystyrene (PS) particles

Fluorescent 978 nm red PS latex dispersion (500 mg; 2.5% w/v) was diluted to 5 ml with Milli-Q water. To this dispersion, PEI solution (1 ml, 10 mg/ml, pH = 5) was added drop wise with continuous stirring. The PEI coated PS particle dispersion was then centrifuged at 6000 rpm for 30 minutes at 10°C, and washed to remove excess PEI.[32] The final concentration of the PEI-PS particles was adjusted in such a way so as to have 10% (w/v) particles. These particles were characterized using zeta potential for PEI adsorption. The zeta potential showed a reversal of charge from -32.2 mV for the uncoated PS to +27.2 mV for the PEI coated particles.

(c) PEI coating on Hydroxyapatite (HAP)

HAP was obtained as a 10% (by weight) suspension in water from Aldrich. The manufacturer specified particle size, based on BET measurements, was < 200 nm. However, the particles were aggregated and therefore needed to be sonicated before use. 1 ml of a 10 wt% HAP solution was diluted to 10 ml in a 30 ml glass bottle and was sonicated for 5 minutes at 5°C, using a tapererd microtop (3 mm diameter) with the Ultrasonic Processor GEX 400, operating at 40% amplitude. When the particle size was significantly reduced (viz. the particles stayed suspended and did not sediment on storing for several hours), PEI solution (5 ml, 1 mg/ml, pH= 5) was added drop wise with continuous stirring. The sample was then centrifuged and washed thrice at 6000 rpm at 10°C to remove excess PEI and finally the volume was reduced to 1 ml. The PEI coated hydroxyapatite particles were characterized by zeta potential measurements for checking the charge reversal. The zeta potential of the particles changed from -19.0 mV to +11.2 mV after coating with PEI.

(d) PEI coating on positively charged particles

Positively charged 16 nm Fe_3O_4 particles, were first coated with polystyrene sulphonate (sodium salt form, PSS-Na) and later with PEI before assembly in the hexagonal phase.[33] A suspension of Fe_3O_4 particles (1 ml; 10 wt%) were diluted to 10 ml with Milli-Q water and were sonicated in a bath sonicator for 30 minutes. To this, PSS-Na solution (1 ml; 10 mg/ml) was added drop wise with continuous stirring. Then, the mixture was equilibrated for 30 minutes and later centrifuged and washed multiple times at 5000 rpm for 30 minutes to remove excess PSS-Na. PSS coating was confirmed since zeta potential measurements indicated reversal of charge from +22.79 mV to -10.2 mV. PSS coated Fe_3O_4 particles (1 ml; 10 wt%) were diluted to 10 ml with Milli-Q water. To this PEI solution (1 ml; 10 mg/ml; pH = 5) was added drop wise with continuous stirring. After mixing and equilibrating for 30 min the sample was centrifuged multiple times at 5000 rpm for 30 minutes, and washed to remove excess PEI. The final volume of the sample was then made to 1 ml by adding Milli-Q water to obtain a 10% (by weight) particle dispersion. Zeta potential measurements after PEI coating the PSS coated Fe_3O_4 particles showed a change from -10.2 mV to +13.6 mV.[33] A similar layer by layer protocol was used to coat CeO_2 particles.

4.2.3. Methodology for assembly of nanoparticles for making a self-standing scaffold:

Typically, a 10% (by weight) dispersion of nanoparticles was added to surfactant $C_{12}E_9$ at 50°C, such that the surfactant to water ratio was 1:1. To this, glutaraldehyde was added and then the solution was cooled to room temperature. Subsequently, sodium cyanoborohydride was added to the gel to reduce the imine groups formed upon crosslinking of PEI and glutaraldehyde. Finally, the scaffold was washed repeatedly with ethanol and water to remove the surfactant and prepare the free standing macroporous material.

For example, to form a macroporous solid from S15-PEI nanoparticles, the following procedure was followed. To 1000 mg of 10% (by weight) S15-PEI, 900 mg of $C_{12}E_9$ was added and homogenized in a water bath at 50^{o}C. At this temperature, 20 mg of glutaraldehyde (25 wt% solution) was added. The sample was then cooled to room temperature at the desired cooling rate in a feedback controlled convective oven. The particle concentration in the overall composite is ≈5 wt%. The sample was then allowed to stand at room temperature for a week, during which its color changes from opaque white to opaque yellow, indicating the progress of the crosslinking reaction (Schiff's base reaction) between the primary amine groups on the PEI and the glutaraldehyde (Figure 4.4). The sample was observed over a period of time using an optical microscope, as the reaction took place. The network structure formed by the particles remained intact as the PEI coated particles crosslinked. The sample was reacted with 0.1M $NaCNBH_3$ solution and then (4-5 times) with water and ethanol to remove the surfactant. The silica scaffold was then dried in a vacuum oven at 120^{o}C before characterization. Samples for optical microscopy were prepared by taking a small

amount of sample on a glass slide, immediately after glutaraldehye addition. The sample was sandwiched between the glass slide and a cover slip to obtain a sample thickness of 10-20 μm. The sample was then heated to 55°C and cooled to 25°C at a desired cooling rate, to allow the particulate composite structure to form. The sample was sealed with adhesive and allowed to crosslink over a period of a week. All the other particles were assembled and crosslinked using a similar procedure as that mentioned here. Horse spleen ferritin did not require coating of PEI since the protein possesses primary amine group functionalities. Thus, the ferritin was uses as obtained from the supplier, for assembly in the H_1 phase.

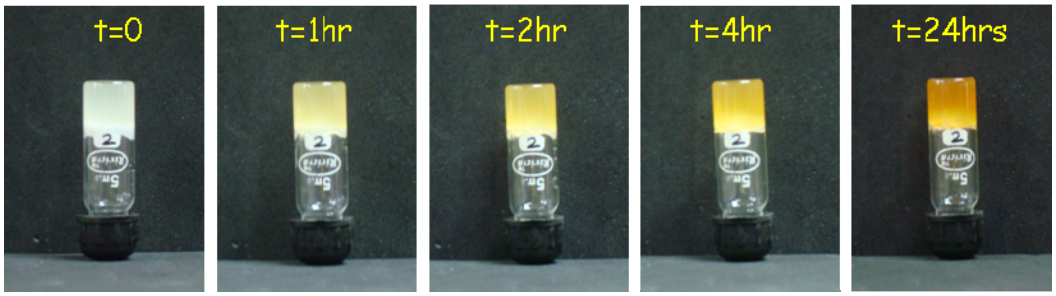

Figure 4.4. Photographs of a 5 wt% S15-PEI/glutaraldehyde sample in the H_1 phase as a function of time, starting from the time when sample is prepared by cooling to ambient temperature. The sample is prepared in a vial, and forms a gel that does not flow, even on inverting the vial. As the glutaraldehyde starts crosslinking the PEI, the colour changes from white to yellow. The colour change is significant within first 24 hrs of sample preparation at room temperature.

4.2.4. Two step assembly of Red and Green Fluorescent PS particles:

In a 5 ml glass vial, 125 mg of 10% (w/v) red fluorescent 978 nm PS particles, coated with PEI, were added to 110 mg of $C_{12}E_9$. Before mixing for homogenization, the solution was heated to 55°C in a water bath for 2 minutes and then vortexed thoroughly. 5 mg of glutaraldehyde solution (25 wt%) was then added to the above mixture maintained at 55°C. The sample was then cooled at 0.5°C/min cooling rate in a feedback controlled convective oven. The sample was then allowed to stand at room temperature for a week, for cross linking the PEI using glutaraldehyde before reduction of imine to amine groups using 0.1 M $NaCNBH_3$. The sample was then finally washed with water and ethanol (4-5 times) to remove the surfactant from the sample. The PS-red-PEI scaffold was then dried in a vacuum before characterization using confocal microscopy. A thin piece of this self standing scaffold formed by PS-red particles was taken and placed in the cavity of a confocal laser scanning glass slide. In another experiment 2.5% (w/v) of 490 nm PS-green fluorescent particles were centrifuged to and concentrated to 10% (w/v). 200 mg of this PS-green particle dispersion was taken in a 2 ml tube and, to it, 180 mg of non-ionic surfactant, $C_{12}E_9$, was added. Before mixing, for homogenization, the solution was heated to 55°C in a water bath for 2 minutes and then vortexed thoroughly. The mixture containing PS-green/water/$C_{12}E_9$ was then poured on the PS-red scaffold previously placed on the confocal slide. The slide was then heated to 55°C and cooled to room temperature at 5°C/min in a feedback controlled convective oven. The confocal slide was then imaged using a confocal microscope.

4.2.5. Materials Characterization:

Characterization of the particles/scaffolds was done using SAXS (Bruker Nanostar equipped with rotating anode and 2-D wire detector over a q-range of 0.01-0.20 $Å^{-1}$). Samples were imaged using a Quanta 200 3D SEM. In the high vacuum mode, we operated at 30kV and used an Everhardt Thornley detector (ETD) while in the low vacuum mode (0-200Pa), we operated at 20kV and used the Large field detector (LFD). Prior to SEM imaging, the sample was sputter coated using a Polaron SC 6420 sputter coater giving an Au thickness of 5 nm on the sample. Zeta potential measurements were performed on 90 Plus Particle Size Analyzer (Brookhaven Instruments, USA). TEM measurements were done at 100kV on an FEI Technai F30. Optical microscopy was performed using an Olympus-BX 50 equipped with a crossed polarizer setup and images were obtained using a Lookman CCTV camera. LSM 710 Carl Zeiss Laser Scanning Confocal Microscope (LSCM) was used to image the fluorescent samples. We used a He-Ne laser (543 nm) and Argon-ion laser (488 nm and 514 nm) for our experiments.

(b) Tagging of FITC to S15-PEI scaffold

S15-PEI scaffold (25 mg) was incubated with 50 µl of 0.0026M fluorescein isothiocyanate (FITC) in ethanol for 3 hours in the dark. It was then washed 5 times with EtOH. Thereafter a thin piece of this sample was place on a confocal slide and sandwiched with a glass cover slip such that it was properly sealed. This slide was imaged using confocal microscope using a 488 nm green laser.

(c) Tagging of fluorescent streptavidin-phycoerythrin to HAP scaffold

HAP network (5mg) was added to a 1 ml solution of Biotin-NHS ester (3 mg) in pH 7.4 PBS buffer and incubated overnight at room temperature. After completion

of the reaction, this suspension was washed with buffer solution (3 times) followed by washing with Millipore water (3 times). The labeled HAP network was then resuspended in phycoerythrin-streptavidin (1ml, 20 μg) conjugate in PBS buffer and the suspension was incubated at 4˚C for 2 hrs. The sample was then washed extensively with PBS buffer multiple times to remove the unreacted phycoerythrin-streptavidin conjugate. Control samples using HAP network which was not conjugated with biotin but was incubated with phycoerythrin-streptavidin conjugate was prepared using the same methodology described above. The confocal microscopy image of this control sample is given in supporting information. Millipore Milli-Q water was used to prepare the particle-surfactant samples.

4.3. Results and Discussion

Network formation by PEI-coated silica particles proceeds in the same manner as previously described for the uncoated silica particles.[22] Above the H_1-isotropic transition temperature, $T_{HI} \approx 45^oC$, 15 nm PEI-coated silica nanoparticles (S15-PEI, 5%, by weight) are well dispersed in the isotropic micellar phase of a 50% aqueous solution of nonionic surfactant, $C_{12}E_9$. On cooling below T_{HI} (at 5^oC/min), the particles are expelled by growing H_1 domains.[22] Once the H_1 domains (observed as birefringent bright regions between crossed polarizers, Figure 4.5 a) grow to impingement, the particles jam to form a network. A comparison of optical micrographs of this sample viewed between crossed (Figure 4.5 a) and parallel polarizers (Figure 4.5 b) shows that the H_1 phase boundaries are optically dense. In contrast, for an H_1 phase not containing silica particles, domain boundaries are not visible between parallel polarizers. Thus, segregation of silica particles to the H_1 domain boundaries results in the optical contrast observed in Figure 4.5 b.

The bulk three-dimensional structure of the particle network formed can be visualized using confocal microscopy to image the structure formed by assembly of fluorescently-tagged 90 nm silica particles in the H_1 phase (Figure 4.6 a). Confocal microscopy confirms that a three dimensional connected network is formed as the particles self assemble into *linear* aggregates. A two-dimensional projection of the structure is shown in Figure 4.5 c. The formation of linear aggregates suggests that particles are localized specifically where multiple H_1 domains meet. A 2D slice of network structure (Figure 4.6 b) shows that the particle organization is similar to that observed in optical micrographs on thinner samples (compare with Figure 4.5 a).

Networks form for particles larger than about 10 nm (viz., > characteristic H_1 spacing, a = 5.6 nm, in these experiments). In practice, an upper bound for the size of particles that we can use to form networks is determined by particle sedimentation – we are unable to form networks from particles that are too large to stay dispersed as the surfactant solution is cooled ($\approx$ 1 μm for silica particles, ~O(10 μm) for polystyrene particles). The nonionic surfactant H_1 phase in our experiments is characterized by an elastic constant, K ~ O(1 pN), and we estimate that the anchoring strength of surfactant micelles on the particle surface is given by $W = k_BT/a^2 \approx 100$ μJ/m^2. For silica particles whose size, R, varies from 10 nm to 1 μm, the nondimensional ratio of anchoring and elastic energies, WR/K varies from ~O(1) to ~O(100). Thus, in our experiments, the director is strongly anchored to the particles and we expect deformation of the director field to govern long range particle-particle interactions.[19,20] However, in our system, particle assembly appears to be governed primarily by expulsion of particles from the mesophase.

To stabilize the particulate network against dispersion after H_1 template removal, the PEI coated silica particles were crosslinked with glutaraldehyde upon network formation. Subsequent to crosslinking, the surfactant could be readily removed by washing with water, to yield a free standing particulate macroporous solid (Figure 4.5 d). Scanning electron microscopy reveals a network structure (Figure 4.5 d) comprised of a dense mesh of strands, with strand thickness varying from about 100 nm to a micron as seen at higher magnification (Figure 4.5 e). Typically, scaffolds prepared using PEI coated silica particles had an organic content of 12-13% (by weight). While mm to cm size samples of the macroporous materials were readily prepared (Figure 4.7), these materials are fragile.

On cooling below T_{HI}, H_1 domains nucleate and grow[34] to impingement. Thus, by varying the nucleation density of H_1 domains, it is possible to vary the size of the domains, and therefore, the characteristic spacing of the particulate network. Fast cooling, for example at 10^oC/min (Figure 4.8 a), results in particulate networks with smaller "strut" spacing as compared to cooling at 5^oC/min (Figure 4.8 b and Figure 4.5 a,b). As the sample is cooled at even slower cooling rates of 0.5^oC/min, the "strut" spacing increases (Figure 4.8 c). Optical micrographs of networks formed by crosslinking S15-PEI reveal that the average mesh spacing can be varied from $\approx 3.1\pm0.7$ μm to $\approx 26.4\pm5.6$ μm, on decreasing the cooling rate from 40^oC/min to 0.5^oC/min (Figure 4.8 a-c and Figure 4.8 f, spacings obtained by averaging over at least 150 domains from optical micrographs taken at more than 10 separate locations; Optical micrographs for samples cooled at 20^oC/min and 40^oC/min are shown in Figure 4.9. The SEM of sample cooled at 40^oC/min shows very small pores as seen in Figure 4.10.

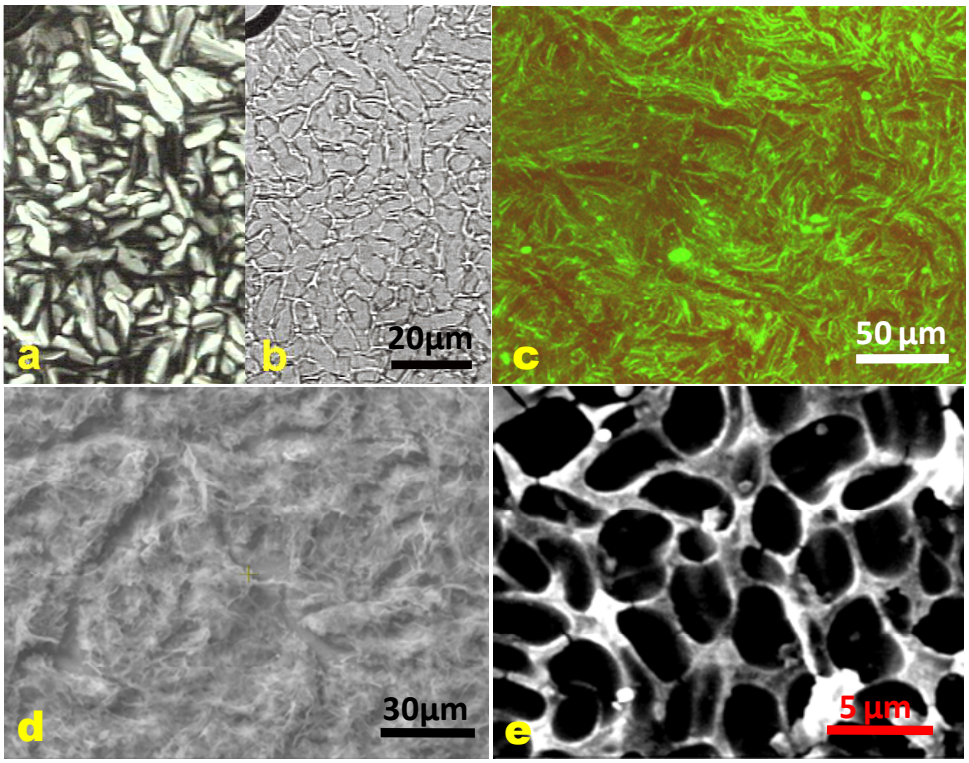

Figure 4.5. Optical microscopy of 5% (by weight) PEI-coated 15 nm silica particles (S15) in H_1 phase at room temperature (sample thickness ≈ 10 µm). The sample was cooled from isotropic phase at 50°C to room temperature at 5°C/min. (a) Between crossed polarizers, we observe birefringent H_1 domains grown to impingement. (b) The same sample as (a), viewed between parallel polarizers shows that the boundaries of the H_1 domains are optically dense due to aggregation of silica particles. (c) Confocal microscope 2D-projection image of 90 nm FITC-tagged Stöber silica particles in H_1 phase. The sample is prepared by cooling the particle-surfactant-water system from 50°C to room temperature at 5°C/min. A red dye (DCM) is dispersed in the H_1 phase. Thus, we observe a network of fluorescent green silica particles in the red H_1 matrix. (d) SEM of a free-standing 3-D scaffold prepared by crosslinking a network of PEI-coated 15 nm silica in the H_1 phase, (5 weight %) using glutaraldehyde. SEM is performed on a dry sample, after removal of the surfactant by washing. (e) A magnified section of the crosslinked scaffold.

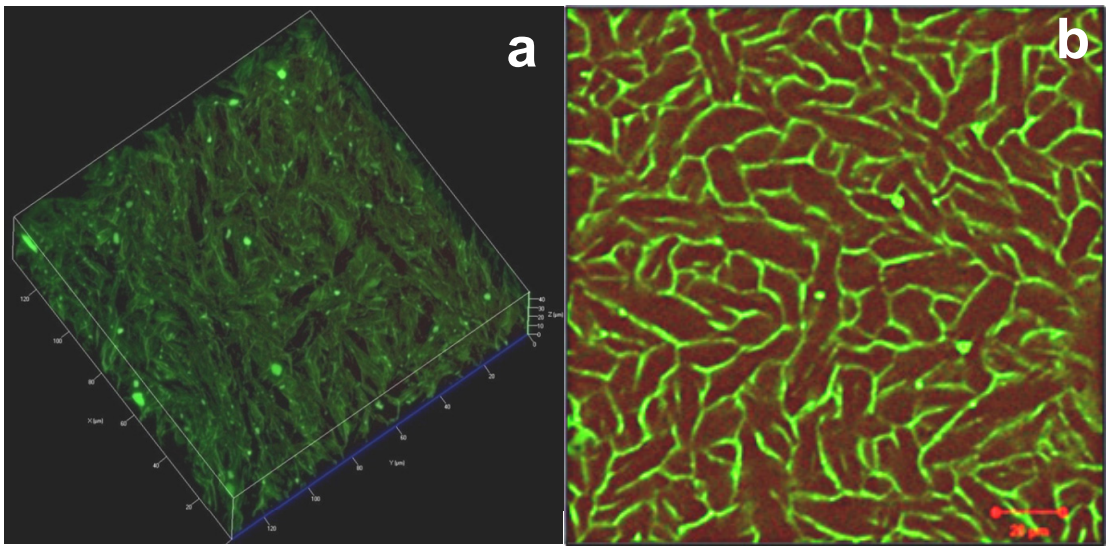

Figure 4.6. (a) 3D confocal image of 5 wt% 90 nm fluorescent silica particles in H_1 phase. The image represents a sample of dimensions 125 μm x 125 μm x 40 μm (thickness) (b) Confocal image represents a 2D slice of the same sample. The scale bar in (b) represents 20 μm.

Figure 4.7. Photographs of samples of self-standing scaffolds of S15-PEI. (Left): Typical samples of S15-PEI scaffolds that we prepare are several mm in size. SEM images for this particular scaffold have been shown in Figure 4.6 d,e. (Right): Image of S15-PEI scaffold obtained by extruding the composite mixture (S15-PEI/glutaraldehyde/H_1) through a syringe at 10 ml/min followed by crosslinking and washing of the sample.

Freeze fracture TEM of rapidly cooled (> 300^{o}C/min) samples indicate a mesh size of about 0.45±0.12 μm (Chapter 2, see Figure 2.6).[22] Thus, the mesh spacing can be varied by ≈ 50-fold, by simply controlling the cooling rate. The anisotropic shape of the particle-templated regions reflects the geometry of growing H_1 domains – in hexagonal mesophases, domains develop as elongated "bâtonnets",[35] (Figure 4.11) before they grow into characteristic fan-shaped domains. For rapid cooling rates (> 5^{o}C/min), where dense nucleation precludes extensive domain growth before impingement, the final domain morphology (and therefore, particle organization in the particle-H_1 composite) is determined by the elongated shapes of the initially developed bâtonnets.

We observe that the elongated shape of the particle assembly is not retained after crosslinking and surfactant removal, when the final macroporous solid is imaged using SEM (Figure 4.5 d, e; Figure 4.8 d;) and confocal microscopy (Figure 4.8 e). While the anisotropic shape of the pores in the network are not retained after surfactant removal, the decrease in average pore size in the free-standing macroporous solid with cooling rate, is preserved and correlates with the decrease in mesh width in the particle-surfactant composite (Figure 4.8 f). Thus, while the crosslinked particulate mesh of coated silica particles has sufficient mechanical stability to retain macroporosity after surfactant removal, and even on drying, it is unable to retain the elongated domain shapes observed in the particle-surfactant composite.

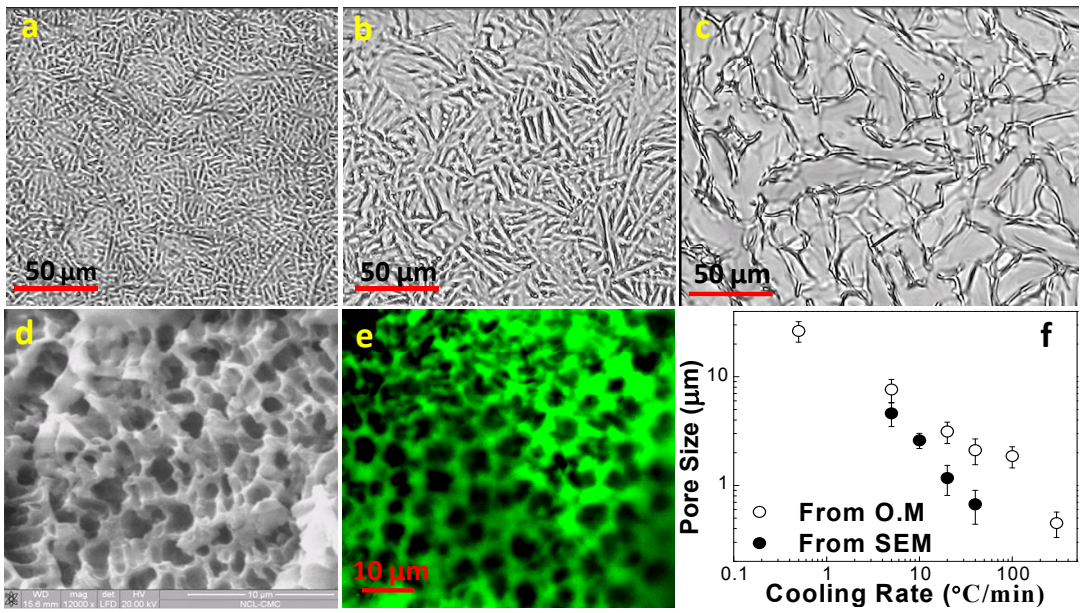

Figure 4.8. Optical micrographs of crosslinked network structures formed from assembly of 15nm S15-PEI particles (5 weight %), at the domain boundaries of the H_1 phase at cooling rates of (a) 10°C/min (b) 5°C/min and (c) 0.5°C/min. As the cooling rate is increased, we observe a decrease in the domain size. (d) SEM micrograph of self standing scaffold prepared at a cooling rate of 10°C/min. (e) Confocal micrograph image of crosslinked self standing scaffold, tagged with a green dye, fluorescein isothiocyanate (FITC), after removal of the surfactant template and imaged using an argon laser at an excitation wavelength of 488 nm). The scaffold was formed by cooling 15 nm S15-PEI particles in the H_1 phase at 5°C/min. (f) Decrease in pore size (from optical micrographs and SEM) observed as a function of cooling rate. The error bars represent the standard deviation over multiple measurements.

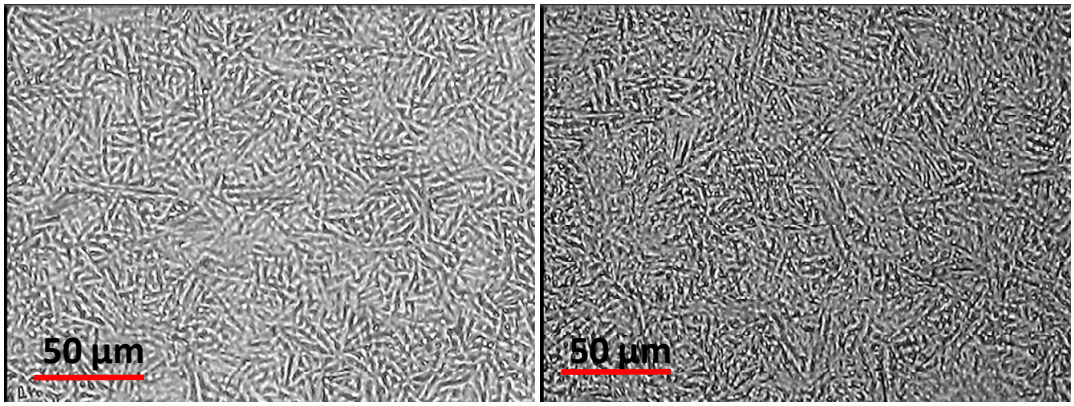

Figure 4.9. Optical micrographs of S15-PEI network formed in H_1 phase, The 5% (by weight) S15-PEI/$C_{12}E_9$/H_2O/glutaraldehyde mixture was made at 50ºC and subsequently cooled at (a) 20ºC/min, and (b) 40ºC/min.

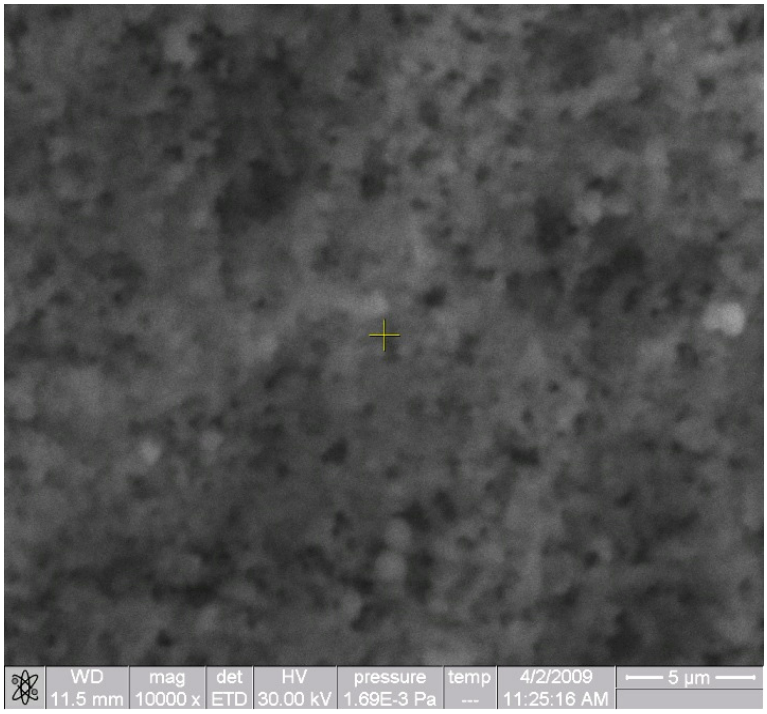

Figure 4.10. SEM image of scaffold formed by assembly of S15-PEI particles (5% by weight) in the H_1 phase, followed by crosslinking with glutaraldehyde. The sample was cooled at 40°C/min, from the isotropic dispersion to the particle-H_1 composite.

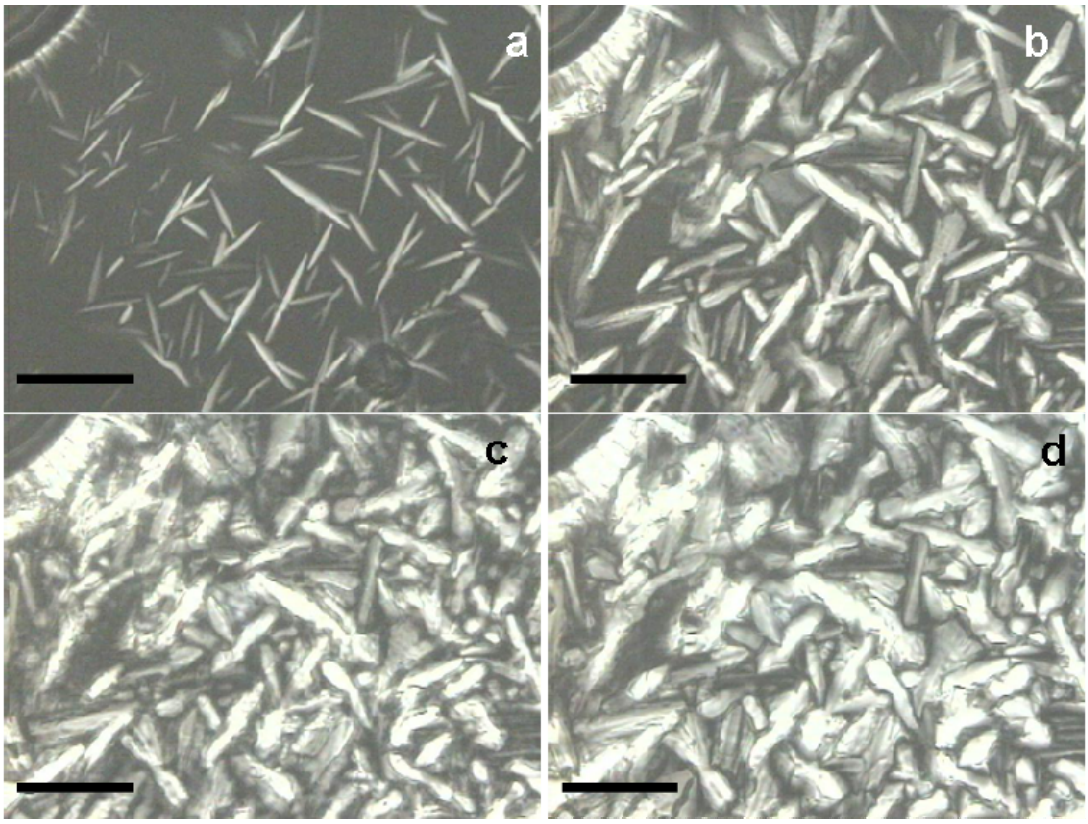

Figure 4.11. Optical micrographs, under crossed polarizers, of structural evolution when a 1:1 surfactant-water mixture containing a 5% dispersion of PEI coated silica particles is cooled at 5°C/min from 50°C to room temperature. (a) At 45°C, elongated bâtonnet structures are formed as the H_1 phase nucleates and starts growing. On further cooling to (b) 42°C, (c) 40°C and (d) 35°C, birefringent H_1 domains grow and eventually impinge. The scale bar corresponds to 20 µm. As the H_1 domains grow, the particles are expelled to the isotropic domains,[22] and eventually, they jam at the domain boundaries (as indicated in Figure 4.5).

The particulate network/H_1 system is a gel that can be readily restructured and oriented by application of shear (Figure 4.12). Shearing of H_1 gels results in orientation of the surfactant cylinders along the flow direction at low shear rates, and in shear melting at higher rates.[36] In polydomain samples, there is yielding as shear aligns the various domains, and eventually a monodomain forms. In our S15-PEI/H_1 systems, shearing at a rate of 0.01 s^{-1} results in progressive flow-direction alignment of the particulate strands and a concomitant decrease in the strand-strand spacing with increasing strain units (Figure 4.12). Fourier transforms of the optical micrographs (4.12, insets) clearly indicate an increase in flow direction alignment, with increasing strain. We note that extensional flow, imposed, for example, by squeezing the particle/H_1 gel through a syringe with a tapered exit, also efficiently orients the particle networks. In all flow orientation experiments, the glutaraldehyde crosslinker concentrations are adjusted so that the orientation is complete at time scales significantly shorter than that required for extensive crosslinking.

Network formation by segregation of nanoparticles is observed to be independent of particle chemistry. Here, we describe preparation of self supporting macroporous solids from dispersions of other inorganic nanoparticles. For example, PEI-coated hydroxyapatite particles (HAP), in $C_{12}E_9$-water assembled into a network by cooling at 5^{o}C/min, and by subsequent crosslinking using glutaraldehyde as seen in the optical micrograph in Figure 4.13 a. This material showed a mesh spacing of 20 μm, comparable to the minimum dimensions required for mammalian cell growth.[37] Materials with larger pore sizes can be prepared by slower cooling. Interestingly, as not all amine groups in the PEI react with glutaraldehyde, the strands of the macroporous solid are amenable to chemical modification.

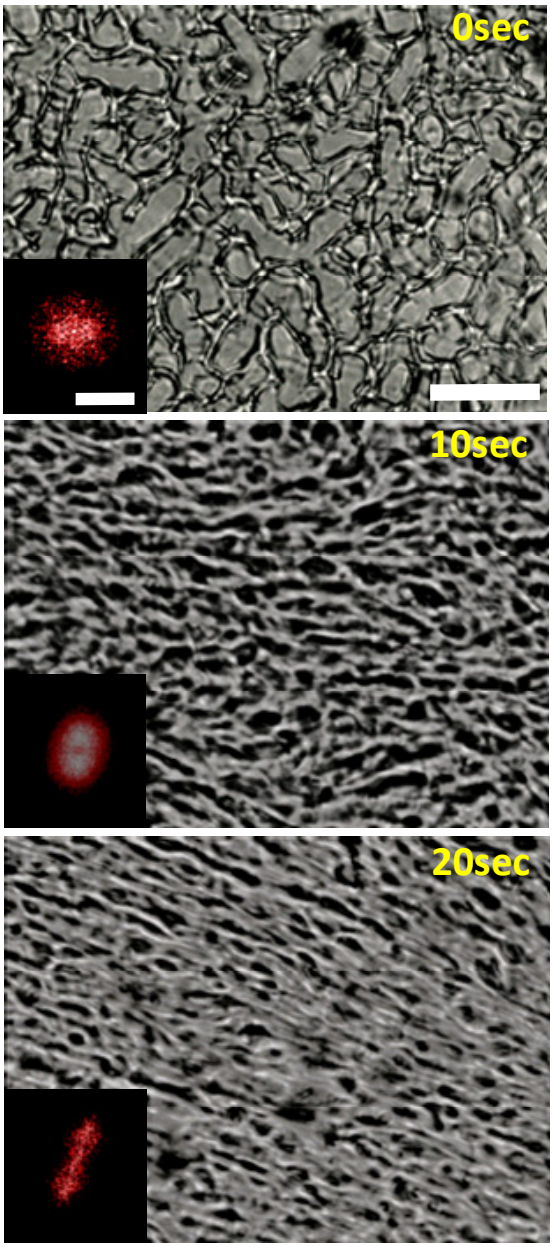

Figure 4.12. Optical micrographs of crosslinked networks of PEI-coated 15 nm silica particles (5 weight %) assembled by cooling at 0.5°C/min from the isotropic dispersed phase to room temperature and, then sheared at 0.01 s^{-1} for (a) 0 s; (b) 10 s and (c) 20 s. The scale bar indicated represents 50 μm. The inset shows the Fourier transform of the optical microscopy images, and the scale bar corresponds to 2.6 μm^{-1}.

Such modification would be advantageous, for example, to graft cell adhesion promoters in scaffolds for cell growth. To demonstrate the possibility of chemical modification, the amine groups of PEI were further reacted with a biotin-NHS. The presence of the biotin on the scaffold was then probed using fluorescently labeled streptavidin, a tetrameric protein, which has a very high binding affinity for biotin. The biotin modified macroporous scaffold upon incubation with streptavidin-phycoerythrin turned fluorescent and could be imaged using confocal microscopy (Figure 4.13 b). Control samples of scaffolds not treated with biotin-NHS did not show significant fluorescence. Thus, these macroporous materials allow diffusion of reactants through them and allow on-demand surface functionalization through the amine groups.

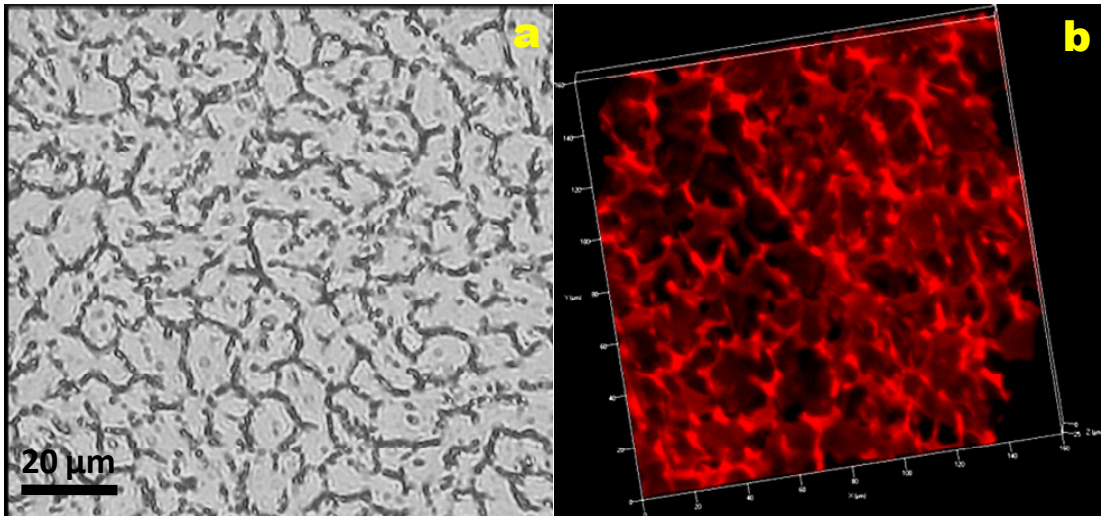

Figure 4.13. (a) Optical micrograph of a network of PEI-coated hydroxyapatite particles (HAP). (b) Laser scanning confocal micrograph (514 nm filter) showing 3D image of 120x120x25 µm self standing HAP scaffold. The scaffold is functionalized with biotin, and biotin functionalized network is incubated with fluorescent streptavidin-phycoerythrin and imaged using confocal.

Inorganic nanoparticles with a positive surface charge can also be assembled into macroporous materials in the H_1 phase – in this case, we adopt the layer-by-layer technique to initially coat the nanoparticles with a polyanion (sodium salt of polystyrene sulphonate), followed by PEI. We have assembled crosslinked macroporous materials from positively charged 16 nm Fe_3O_4 magnetite particles, to demonstrate this (Figure 4.14 a). Similarly, positively charged ceria particles were coated with PSS and PEI, and were also observed to assemble to form a network of strands in the surfactant H_1 phase (Figure 4.14 b).

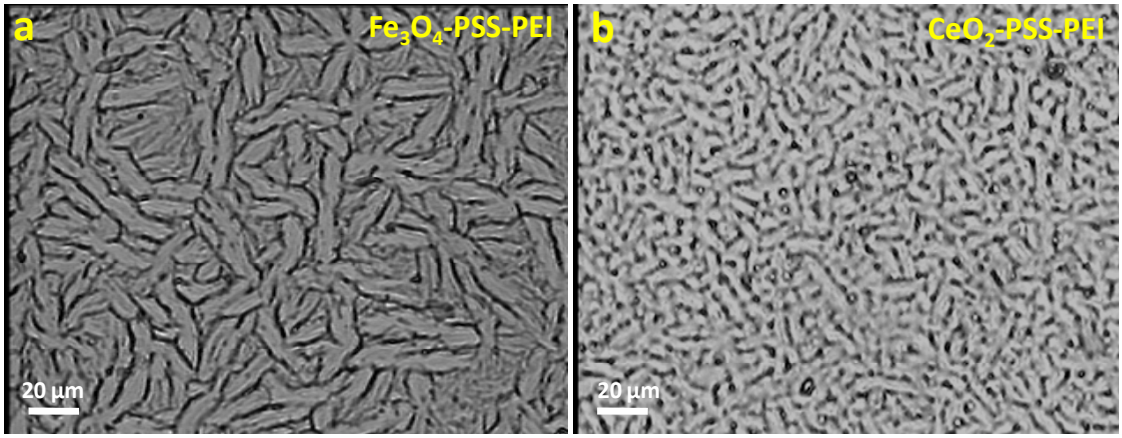

Figure 4.14. Optical Micrographs of self assembled networks formed by positively charged particles. (a) Fe_3O_4 particles and (b) Ceria particles. The particles were first coated with negatively charge polymer poly(styrene-sulphonate) and later with positively charged polyethyleneimine.

This methodology was also extended to form crosslinked three-dimensional networks from soft organic microparticles, such as polymer latices and proteins. We demonstrate assembly of 220 nm microgel particles of a temperature responsive po-

lymer, PNIPAM in H_1 phase. PEI coated PNIPAM particles were cooled in aqueous surfactant solutions at 5°C, and were observed to assemble into networks as the surfactant H_1 phase formed. Interconnected strands of crosslinked PNIPAM microgel particles are seen in optical microscopy (Figure 4.15 a). The PNIPAM microgel networks are self standing after removal of the surfactant template and could be imaged using confocal microscopy after incubation with 10 ppm of rhodamine red dye for 24 hours (Figure 4.15 b). Such PNIPAM microgel networks are anticipated to have applications where relatively rapid volume transition kinetics are important,[38] as well as in sensing[39] and for drug delivery.[39] We note here, that we have also previously reported[40] the phase separation of PNIPAM linear chains to H_1 domain boundaries.

Interpenetrating particle networks can also be formed using a two-step variation of this technique. We have assembled red fluorescently labeled 978 nm PS particles into a network on cooling at 0.5°C/min. Subsequently, networks of a green fluorescently labeled 490 nm polystyrene (PS) particle were assembled from dispersions in the H_1 phase, by cooling at 5°C/min, within the previously assembled network of red fluorescent particles (4.16 a). In the pre-formed network of red particles (formed by cooling at 0.5°C/min), 490 nm green particles are incorporated with the $C_{12}E_9/H_2O$ (and cooled from isotropic phase at 5°C/min to form H_1 phase), and the sample is imaged using confocal microscopy. The structure indicates that each of the red and green fluorescent PS particles form an interconnected network (Figures 4.16 a, b). The composite image can be seen in Figure 4.16 c, wherein the green particles form interpenetrating structures within the preformed red particle network.

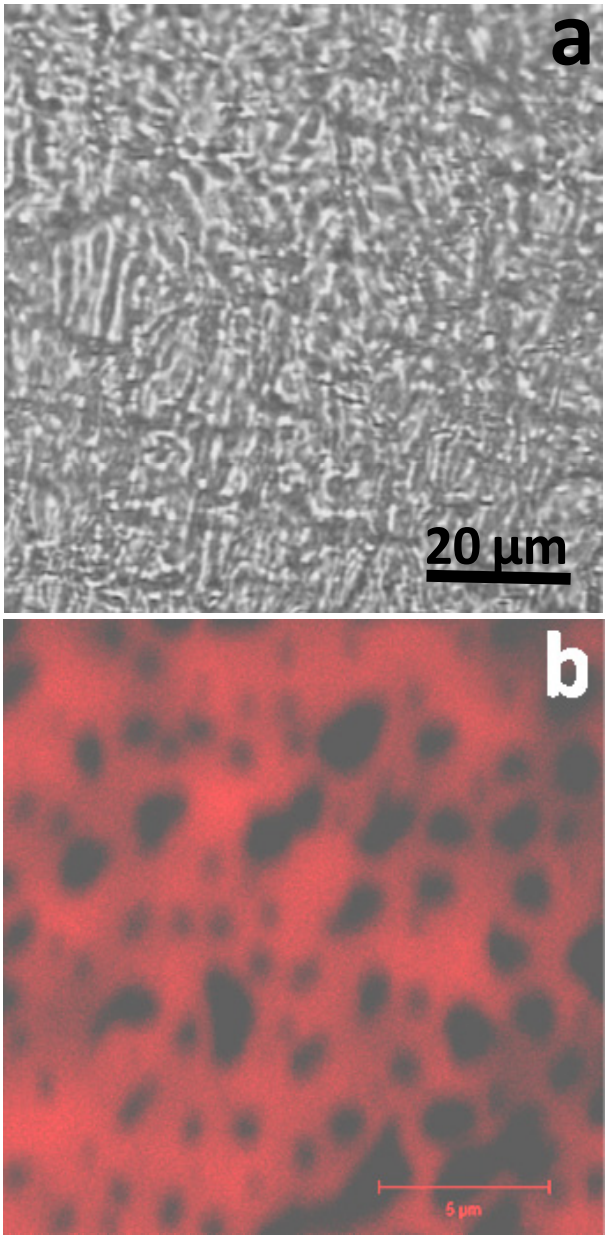

Figure 4.15. Self standing network of 220 nm PEI coated PNIPAM microgel particles crosslinked with glutaraldehyde. (a) Optical micrograph of the self standing scaffold of PNIPAM in water, after the removal of surfactant. (b) 2-D confocal micrograph of rhodamine tagged PNIPAM-PEI microgel network.

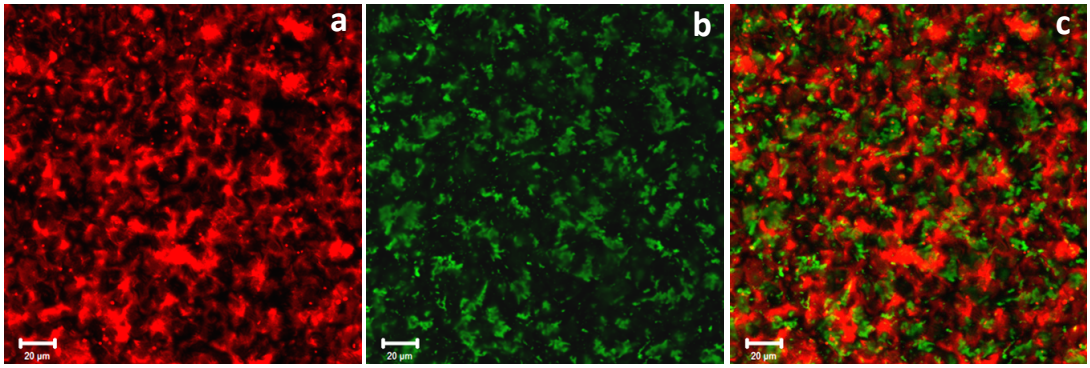

Figure 4.16. Confocal microscopy images of the interpenetrating structure formed by two different fluorescent PS particles (978 nm PS-Red and 490 nm PS-Green). (a) Structure formed by PS-Red on cooling at 0.5°C in the H_1 phase (b) Structure formed by PS-Green within the initially formed red particle structure. (c) Composite interpenetrating structure of PS-Green network within the PS-Red network. The scale bar in all images is 20 µm.

Finally, we demonstrate the use of this methodology to synthesize macroporous materials from a 450 kDa globular protein, ferritin. This bionanoparticle contains an iron oxide core within an assembly of 24 protein subunits. Assembly of such bionanoparticles into three dimensional networks is still very challenging[41] and, chemical modification of the ferritin surface is typically necessary for assembly into networks. We demonstrate that native horse spleen ferritin can be organized into networks by dispersion in the surfactant H_1 phase. We crosslinked surface amine groups on the ferritin with glutaraldehyde to form a network that is stable in water, after template removal (Figure 4.17). Since different inorganic materials can be incorporated by using biomineralization into the core of ferritin from which the iron oxide core has been removed, this offers a route to develop macroporous scaffolds with unique functionalities.

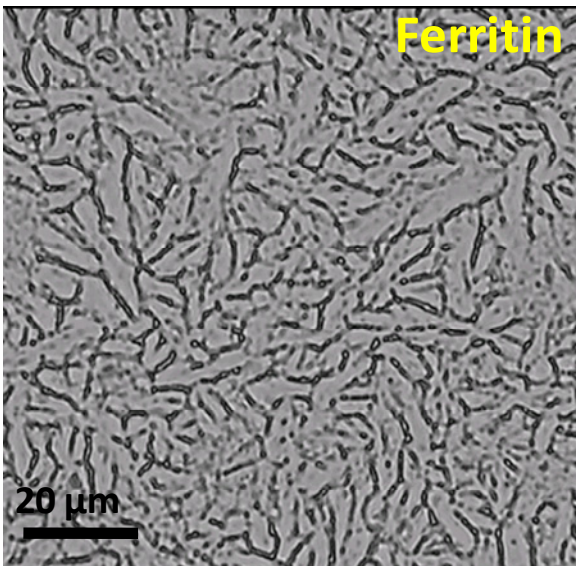

Figure 4.17. Optical micrograph of a network of ferritin, after crosslinking with glutaraldehyde.

4.4. Summary

In this chapter we demonstrate that dynamic phase separation of nonionic surfactant hexagonal domains is a generic technique for assembly of three dimensional nanoparticulate networks. Inorganic, organic, and protein particles can be assembled into networks. The large surfactant content in solution renders the matrix amphiphilic and therefore, hydrophobic nanoparticles can also be dispersed in such matrices.[23d] Dynamic templating of H_1 mesophases involves mild conditions – near ambient temperatures and a facile water wash for template removal. Thus, we demonstrate that it is possible to employ our technique to prepare networks of even relatively delicate bionanoparticles, such as ferritin protein, that would aggregate irreversibly on freezing. We believe that materials prepared using this technique have potential for application in a wide variety of technologically important areas.

4.5. References

1. Mann, S. *Nature Mater.* **2009**, *8*, 781-792.
2. (a) Iskandar, F.; Mikrajuddin; Okuyama, K. *Nano Lett.* **2001**, *1*, 231-234. (b) Vanbever, R.; Mintzes, J. D.; Wang, J.; Nice, J.; Chen, D.; Batycky, R.; Langer, R.; Edwards, D. A. *Pharmaceutical Research* **1999**, *16*, 1735-1742.
3. Boal, A. K.; Ilhan, F.; DeRouchey, J. E.; Thurn-Albrecht, T.; Russell, T. P.; Rotello, V. M. *Nature* **2000**, *404*, 746-748.
4. Lin, S.; Li, M.; Dujardin, E.; Girard, C.; Mann, S. *Adv. Mater.* **2005**, *17*, 2553-2559.
5. Arachchige, I. U.; Brock, S. L. *Acc. Chem. Res.* **2007**, *40*, 801-810.
6. Michna, S.; Wu, W.; Lewis, J. A. *Biomaterials* **2005**, *26*, 5632-5639.
7. Davis, S. A.; Breulmann, M.; Rhodes, K. H.; Zhang, B.; Mann, S. *Chem. Mater.* **2001**, *13*, 3218-3226.
8. Nie, Z.; Petukhova, A.; Kumacheva, E. *Nature Nanotech.* **2009**, *5*, 15-25.
9. (a) Vlasov, Y. A.; Yao, N.; Norris, D. J. *Adv. Mater.* **1999**, *11*, 165-169. (b) Velev, O. D.; Kaler, E. W. *Adv. Mater.* **2000**, *12*, 531-534. (c) Rhodes, K. H.; Davis, S. A.; Caruso, F.; Zhang, B.; Mann, S. *Chem. Mater.* **2000**, *12*, 2832-2834. (d) Stein, A.; Li, F.; Denny, N. R. *Chem. Mater.* **2007**, *20*, 649-666.
10. (a) Caruso, R. A.; Antonietti, M. *Chem. Mater.* **2001**, *13*, 3272-3282. (b) Wang, Y.; Tang, Y.; Dong, A.; Wang, X.; Ren, N.; Shan, W.; Gao, Z. *Adv. Mater.* **2002**, *14*, 994-997.
11. (a) Breulmann, M.; Davis, S. A.; Mann, S.; Hentze, H. P.; Antonietti, M. Adv. Mater. 2000, *12*, 502-507. (b) Caruso, R. A.; Giersig, M.; Willig, F.; Antonietti, M. *Langmuir* **1998**, *14*, 6333-6336.

12. (a) Huerta, L.; Guillem, C.; Latorre, J.; Beltrán, A.; Beltrán, D.; Amorós, P. *Chem. Commun.* **2003**, 1448-1449. (b) Zhang, Y.; Zha, S.; Liu, M. *Adv. Mater.* **2005**, *17*, 487-491.

13. Davis, S. A.; Patel, H. M.; Mayes, E. L.; Mendelson, N. H.; Franco, G.; Mann, S. *Chem. Mater.* **1998**, *10*, 2516-2524.

14. (a) Böker, A.; Lin, Y.; Chiapperini, K.; Horowitz, R.; Thompson, M.; Carreon, V.; Xu, T.; Abetz, C.; Skaff, H.; Dinsmore, A. D.; Emrick, T.; Russell, T. P. *Nature Mater.* **2004**, *3*, 302-306. (b) Bunz, U. H. F. *Adv. Mater.* **2006**, *18*, 973-989. (c) Sakatani, Y.; Boissière, C.; Grosso, D.; Nicole, L.; Soler-Illia, G. J. A. A.; Sanchez, C. *Chem. Mater.* **2007**, *20*, 1049-1056. (d) Shah, P. S.; Sigman, M. B. Jr.; Stowell, C. A.; Lim, K. T.; Johnston, K. P.; Korgel, B. A. *Adv. Mater.* **2003**, *15*, 971-974.

15. (a) Walsh, D.; Arcelli, L.; Ikoma, T.; Tanaka, J.; Mann, S. *Nature Mater.* **2003**, *2*, 386-390. (b) Wu, M.; Fujiu, T.; Messing, G. L. *Journal of Non-Crystalline Solids* **1990**, *121*, 407-412. (c) Walsh, D.; Kulak, A.; Aoki, K.; Ikoma, T.; Tanaka, J.; Mann, S. *Angew. Chem., Int. Ed.* **2004**, *43*, 6691-6695.

16. Lin, Y.; Skaff, H.; Emrick, T.; Dinsmore, A. D.; Russell, T. P. *Science* **2003**, *299*, 226-229.

17. (a) Herzig, E. M.; White, K. A.; Schofield, A. B.; Poon, W. C. K.; Clegg, P. S. *Nature Mater.* **2007**, *6*, 966-971. (b) Stratford, K.; Adhikari, R.; Pagonabarraga, I.; Desplat, J.-C.; Cates, M. E. *Science* **2005**, *309*, 2198-2201.

18. (a) Zhang, H.; Hussain, I.; Brust, M.; Butler, M. F.; Rannard, S. P.; Cooper, A. I. *Nature Mater.* **2005**, *4*, 787-793. (b) Munch, E.; Launey, M. E.; Alsem, D. H.; Saiz, E.; Tomsia, A. P.; Ritchie, R. O. *Science* **2008**, *322*, 1516-1520. (c) Deville,

S.; Saiz, E.; Nalla, R. K.; Tomsia, A. P. *Science* **2006**, *311*, 515-518. (d) Vickery, J. L.; Patil, A. J.; Mann, S. *Adv. Mater.* **2009**, *21*, 2180-2184.

19. (a) Anderson, V. J.; Terentjev, E. M.; Meeker, S. P.; Crain, J.; Poon, W. C. K. *Eur. Phys. J. E.* **2001**, *4*, 11-20. (b) Meeker, S. P.; Poon, W. C. K.; Crain, J.; Terentjev, E. M. *Phys. Rev. E* **2000**, *61*, R6083. (c) Petrov, P. G.; Terentjev, E. M. *Langmuir* **2001**, *17*, 2942-2949. (d) West, J. L.; Glushchenko, A.; Liao, G.; Reznikov, Y.; Andrienko, D.; Allen, M. P. *Phys. Rev. E* **2002**, *66*, 012702. (e) Vollmer, D.; Hinze, G.; Poon, W. C. K.; Cleaver, J.; Cates, M. E. *J. Phys. Condens. Matter* **2004**, *16*, L227-L233.

20. (a) Poulin, P.; Raghunathan, V. A.; Richetti, P.; Roux, D. *J. Phys. II France* **1994**, *4*, 1557-1569. (b) Ramaswamy, S.; Nityananda, R.; Raghunathan, V. A.; Prost, *J. Mol. Cryst. Liq. Cryst.* **1998**, *288*, 175-180. (c) Poulin, P.; Francès, N.; Mondain-Monval, O. *Phys. Rev. E* **1999**, *59*, 4384-4387. (d) Loudet, J. C., Barois, P.; Auroy, P.; Keller, P.; Richard, H.; Poulin, P. *Langmuir* **2004**, *20*, 11336-11347. (e) Muševič, I.; Škarabot, M.; Tkalec, U.; Ravnik, M.; Žumer, S. *Science* **2006**, *313*, 954-958.

21. (a) Basappa, G.; Suneel; Kumaran, V.; Nott, P. R.; Ramaswamy, S.; Naik, V. M.; Rout, D. *Eur. Phys. J. B* **1999**, *12*, 269-276. (b) Zapotocky, M.; Ramos, L.; Poulin, P.; Lubensky, T. C.; Weitz, D. A. *Science* **1999**, *283*, 209-212.

22. Sharma, K. P.; Kumaraswamy, G.; Ly, I.; Mondain-Monval, O. *J. Phys. Chem. B* **2009**, *113*, 3423-3430.

23. (a) Fabre, P.; Casagrande, C.; Veyssie, M.; Cabuil, V.; Massart, R. *Phys. Rev. Lett.* **1990**, *64*, 539-542. (b) Quilliet, C.; Ponsinet, V.; Cabuil, V. *J. Phys. Chem.* **1994**, *98*, 3566-3569. (c) Alexeev, V. L.; Ilekti, P.; Persello, J.; Lambard, J.; Gulik, T.;

Cabane, B. *Langmuir* **1996**, *12*, 2392-2401. (d) Eiser, E.; Bouchama, F.; Thathagar, M. B.; Rothenberg, G. *ChemPhysChem* **2003**, *4*, 526-528. (e) Ramos, L., Fabre, P.; Nallet, F.; Lu,C.-Y. D *Eur. Phys. J. E.* **2000**, *1*, 285-299. (f) Bouchama, F.; Thathagar, M. B.; Rothenberg,G.; Turkenburg, D. H.; Eiser, E. *Langmuir* **2004**, *20*, 477-483.

24. Sharma, K. P., Aswal, V. K.; Kumaraswamy, G. *J. Phys. Chem. B* **2010**, *114*, 10986-10994.
25. Wadekar, M. N.; Pasricha, R.; Gaikwad, A. B.; Kumaraswamy, G. *Chem. Mate*r. 2005, *17*, 2460.
26. Chandran, S. P.; Hotha, S.; Prasad, B. L. V. *Current Science* **2008,** *95***,** 1327.
27. Senff, H.; Richtering, W. *Colloid Polym. Sci.* **2000**, *278*, 830.
28. Iida, H.; Takayanagi, K.; Nakanishi, T.; Osaka, T. *J. Coll. Inter. Sci.* 2007, *314*, 274.
29. Yuan, Z,-Y; Idakiev, V.; Vantomme, A.; Tabakova, T.; Ren, T.,-Z.; Su, B.,-L. *Catalysis Today* 2008, *131*, 203.
30. Bringley, J. F.; Wunder, A.; Howe, A. M.; Wesley, R. D.; Qiao, T. A.; Liebert, N. B.; Kelley, B.; Minter, J.; Antalek, B.; Hewitt, J. M. *Langmuir* **2006,** *22*, 4198-4207.
31. (a) Baba, A.; Kaneko, F; Advincula, R. C. *Colloids Surfaces A*. **2000**, *173*, 39-49. (b) Caruso, F.; Niikura, K.; Furlong, D. N.; Okahata, Y. *Langmuir* **1997**, *13*, 3422-3426.
32. (a) Decher, G. *Science* **1997**, *277*, 1232-1237. (b) Caruso, F.; Caruso, R. A.; Moehwald, H. *Science* **1998**, *282*, 1111-1114.

33. Sharma, K. P.; Ganai, A. K.; Sengupta, S. S.; Kumaraswamy, G. *Chem. Mater.* **2011.** (DOI: 10.1021/cm102945x)

34. Knight, P., Wyn-Jones, E.; Tiddy, G. J. T. *J. Phys. Chem.* **1985**, *89*, 3447-3449.

35. Textures of Liquid Crystals; Dierking, I., Ed.; *Wiley-VCH*, **2003**.

36. (a) Ramos, L.; Molino, F.; Porte, G. *Langmuir* **2000**, *16*, 5846-5848. (b) Schmidt, G.; Muller, S.; Lindner, P.; Schmidt, C.; Richtering, W. *J. Phys. Chem. B* **1998**, *102*, 507-513.

37. Freyman, T. M.; Yannas, I. V.; Gibson, L. J. *Progress in Materials Science* **2001**, *46*, 273-282.

38. Cho, E. C.; Kim, J.-W.; Fernandez-Nieves, A.; Weitz, D. A. *Nano Lett.* **2007,** *8*, (1), 168-172.

39. (a) Zhang, Y.; Guan, Y.; Zhou, S. *Biomacromolecules* **2007**, *7*, 3196-3201. (b) Hu, Z.; Huang, G. *Angew. Chem., Int. Ed.* **2003**, *42*, 4799 -4802. (c) Kim, J.; Nayak, S.; Lyon, L. A. *J. Am. Chem. Soc.* **2005**, *127*, 9588-9592.

40. Jijo, V. J.; Sharma, K. P.; Kamble, S.; Rajamohanan, P. R.; Ajithkumar, T. G.; Badiger, M. V.; Kumaraswamy, G. *Macromolecules* **2010,** *43*, 4782–4790.

41. (a) Broomell, C. C.; Birkedal, H.; Oliveira, C. L. P.; Pedersen, J. S.; Gertenbach, J. A.; Young, M.; Douglas, T. *Soft Matter* **2010**, *6*, 3167-3171. (b) Hu, Y.; Chen, D.; Park, S.; Emrick, T.; Russell, T. P.; *Adv. Mater.* **2010**, *22*, 2583-2587.

Chapter 5

Organization of Polyethyleneimine in the H_1 Phase

5.1. Introduction

Organized surfactant mesophases are increasingly finding applications as matrices for sustained release of therapeutic molecules[1] and, in the foods and cosmetics industry.[2] Often, the active compounds to be delivered are complexed with polymers, that either stabilize the compound or that play a role in targeted delivery. For example, polyethylene imine (PEI) finds application to prepare polymer complexes for pharmaceutical formulations, in gene transfection, drug delivery, etc.[3-6] When polymer complexes need to be incorporated in a surfactant mesophase matrix, it is important to understand the nature of the interactions between the polymer and the surfactant. Such interactions might be influenced by the external environment, viz. pH, temperature, etc. In this Chapter, we investigate the microstructure, and interactions when a pH responsive polymer, PEI, is dispersed in non-ionic surfactant, $C_{12}E_9$/water system that can form a hexagonal mesophase (H_1).

In recent work from our group, we have investigated the volume phase transition of a weakly interacting, thermoresponsive poly(N-isopropylacrylamide), PNIPAM, in the hexagonal mesophase (H_1) of non-ionic surfactant, $C_{12}E_9$, and water.[7] Nonionic surfactants, such as $C_{12}E_9$ are known to interact weakly with PNIPAM. Accordingly, we have shown that there is only a small change in the volume transition temperature/LCST for the PNIPAM in *isotropic micellar solutions* of $C_{12}E_9$, even for relatively high concentrations of $C_{12}E_9$. Interestingly, once the surfactant forms an H_1 phase, there is a dramatic decrease in the coil-globule transition onset temperature i.e. from 34^{o}C in water to 13^{o}C in the H_1 phase. We believe that this behavior results from a competition between $C_{12}E_9$ in the H_1 phase, and PNIPAM to associate with water. Thus, we show that for PNIPAM in a weakly interacting surfactant matrix, it is the

phase behavior of the matrix rather than the matrix chemistry that governs the coil-globule transition. Interestingly, we have observed that a PNIPAM/acrylamide copolymer with a higher LCST, shows an interesting sequence of transitions in the surfactant phase. On cooling from a high temperature free flowing turbid globular state (~75^{o}C), we enter a free flowing translucent coil phase (~47^{o}C), then a turbid gel (~ 25^{o}C) where the copolymer is collapsed in the H_1 phase, and finally a low temperature clear gel (~5^{o}C) where the copolymer is in the expanded coil state.[7]

There is extensive literature on investigations of colloidal mixtures of polymers and surfactants, due to the technological importance of such systems in industrial and biological applications.[8] Charged polymers associate strongly with oppositely charged surfactants through electrostatic interactions.[9] Interactions between like-charged polymers and surfactants are repulsive; however, even in such systems, the surfactants might associate with the polymer through hydrophobic interactions, especially if the polymer has long alkyl side chains.[10] Interactions between a charged polymer and nonionic surfactants are typically weak relative to charged polymer-charged surfactant interactions. Charged polymers can associate with nonionic surfactants through H-bonding or through hydrophobic interactions.[11,12]

Most of the literature on PEI-surfactant complexes focus on interactions of sodium dodecyl sulphate (SDS), an anionic surfactant, with linear and branched PEI.[13-15] For example, Wang et. al.[15] reported the pH dependent association of linear and branched PEI, with SDS below its critical micellization concentration. At low pH, linear PEI is highly protonated and therefore interacts strongly with SDS. At higher pH (= 10), the PEI behaves as a neutral polymer and therefore SDS remains associated only as adsorbed spherical micelles. The PEI chain structure has also been shown to

play a role, with branched PEI associating more strongly at all pH values compared to linear chains. Gainanova et. al.[16] reported that modified PEI – non ionic surfactant complexes formed at very low surfactant concentrations in chloroform showed catalytic activity towards phosphorylation. This catalytic activity is inhibited as the surfactant concentration is increased above the critical association concentration.

Research on polymers in surfactant mesophases[17] has focused mainly on lamellar surfactant phases, due to their morphological similarity with biological membranes. As the interactions between lipid membranes and their associated membrane proteins are known to modulate protein structure and function, it is interesting to investigate the structural changes in polymer chains associated with lamellar phases, as simple model systems. Polymer-surfactant interactions determine the polymer chain localization – for example, the polymer chain might be localized in the water region,[18] within the membrane,[19] partitioned between the aqueous phase and the membrane,[20] or might stay adsorbed on the surface of the membrane due to hydrophobic interactions.[21] Polymer localization is also a function of the size of the polymer chain, relative to the interlamellar spacing. For polymers in lamellar bilayer phases, low molecular weight polymers are accommodated in and, swell the lamellar phase while, high molecular weight polymers are excluded from the lamellar phase.[24] Typically, surfactant lyotropic lamellar mesophases have a repeat distance ranging from 2-10 nm, and polymers having a coil size in this range are typically accommodated in the surfactant mesophase. Pacios et. al.[22,23] investigated dispersions of a non-interacting polymer, poly(dimethylacrylamide), in the lamellar mesophase of anionic surfactant, AOT. Their work suggests that the lamellar mesophase acts as a "*sieve*" that can "dissolve" polymer chains with a chain size smaller than or similar to the dimensions of the water

channel, *d*, and that the mesophase expels larger chains. Therefore, the authors suggest that the confinement of the non-interacting polymer in the lyotropic liquid crystal solely depends on the size/geometry of the polymer chain. Similarly, it has been observed[24] that high molecular weight carbohydrates are expelled from the lamellar phase of a zwitterionic phospholipid, lecithin, and remain dispersed in the isotropic phase. However, Ligoure et. al.[25] have reported confinement of a high molecular weight non-interacting poly(vinylpyrollidone) having dimensions much larger than the lamellar phase repeat spacing. They suggested that confinement of the high molecular weight polymer was a result of intermembrane repulsive interactions that could be controlled by changing the ionic strength. We also mention in passing that there is considerable literature on dispersion of colloidal particles in lamellar surfactant phases.[26] However, the conformational entropy of solvated polymer chains results in qualitatively different behavior as compared to particles, on confinement in a surfactant mesophase.

Association of non-ionic surfactants with hydrophobically modified polymers has also been reported. Iliopoulos and Olsson[27] used a combination of viscosity and self-diffusion measurements to report the association of hydrophobically modified poly(sodium acrylate) with the micelles and lamellar phase of $C_{12}E_5$ and of $C_{12}E_8$. They report polymer-surfactant association as a result of hydrophobic interactions between the alkyl side chains of the polymer and the alkyl tails of the surfactants and suggest that the polymer chains adsorb on the surface of the surfactant lamellae. Similar results were shown by Yang et. al.[28] for hydrophobically modified poly(sodiumacrylate) in the lamellar and sponge phases of $C_{12}E_5$. Interactions between a random heteropolymer poly(styrene- sodium styrene sulphonate) of 25,000 $g.mol^{-1}$

molecular weight, and nonionic lamellar phase have also been studied as a function of charge content on the polymer.[29,30] A lamellar phase formed as a result of high surfactant to water ratio, exists till high concentration of polymer, independent of the extent of charge from the sulphonated groups. An increase in water content leads to a first order phase transition to a cubic phase.

In this work, we use a combination of experimental techniques and molecular simulations to probe the effect of pH on PEI-nonionic surfactant interactions, and therefore, on the isotropic-H_1 phase transition. We begin with a detailed description of the experimental system and then present experimental results, followed by simulation data.

5.2. Experimental

5.2.1. Materials:

PEI was obtained from Sigma Aldrich and was used as received. (M_w = 2000 g.mol^{-1} and M_n = 1800 g.mol^{-1}, as reported by the manufacturer). Nitric acid, HNO_3, used to adjust the pH of the sample was obtained from Merck as a 70 % (w/v) solution. Hydrochloric acid, HCl was obtained as 35-38% aqueous solution from SD-Fine chemicals. Nona ethyleneglycol dodecyl ether, $C_{12}E_9$, non-ionic surfactant was obtained from Sigma and used as obtained.

Samples were prepared by mixing surfactant, PEI and water at 50^{o}C, in the low viscosity isotropic micellar phase, and then cooling down to room temperature. The 50% PEI solution from the manufacturer was directly used to prepare samples at pH = 12.8. For lower pH samples, the stock solution of PEI was diluted with water and the pH was adjusted by adding 70 % (w/v) HNO_3. Samples were prepared such that the ratio of surfactant to water in the final sample was always 1:1, by weight. The pH of

the samples was checked using a Mettler Toledo instrument (SevenMulti), calibrated with standards.

5.2.2. Sample preparation for NMR:

The samples for NMR with D_2O as the solvent were prepared using the following procedure. A known amount of stock solution (50% by weight) of PEI was first rota-vaporized at 70^oC for 1 hour. After this, the sample was frozen using liquid N_2 and then lyophilized (Heto PowerDry LL3000) at -55^oC for 24 hrs. This procedure resulted in a PEI sample with a concentration of 99 weight %. We were unable to dry the sample any further, even after repetition of the above procedure. The sample at pH 12.8 was directly prepared by diluting the concentrated PEI solution to 5 wt% using D_2O as the solvent. For lower pH samples, the concentrated PEI solution was first diluted with D_2O till the concentration reached 15 wt% and then it was subjected to change in pH by adding required amount of concentrated, 70% (w/v) HNO_3. Finally, the concentration was made to 5 wt% with D_2O. Thus, all the samples prepared for NMR studies contained a minimal amount of H_2O that could not be removed during the concentration of PEI. Samples containing 25 wt% surfactant and 5 wt% PEI for 2D ROESY experiments were prepared in a similar manner as mentioned above.

5.2.3. Characterization tools:

NMR studies were done on (1) aqueous solution of PEI at different pH and (2) mixtures of PEI/$C_{12}E_9$/H_2O at different pH. All NMR measurements were performed on a Bruker AV400 MHz spectrometer operating at 400 and 100 MHz, respectively for ^1H and ^{13}C using a 5mm BBFO probe. For 2D ROESY measurements, a standard 2D pulse sequence with a spin lock (CW) time of 200 ms was used.[31] 2D data containing 256 increments were collected by adding 16 transients with a repetition delay

of 3 s using 1K data points. NMR studies were performed in collaboration with the group of Dr. Rajamohanan at NCL.

Small angle X-ray scattering (SAXS) was used to obtain the phase behavior of 1:1 $C_{12}E_9/H_2O$ mixture in the presence of PEI. The scattering experiments were carried out on a three pinhole collimated Bruker Nanostar machine equipped with rotating copper anode, operating at 45 kV and 100mA and providing characteristic K_α radiation of wavelength 1.54 Å. The experiments were performed in the normal resolution mode having q-range of 0.011-0.2 $Å^{-1}$. The samples were filled in a 2 mm (outer diameter) glass capillary having wall thickness of ~10μm and scanned at temperatures from 10°C to 50°C. The temperature was controlled using a Peltier stage controlled by a MCU-temperature controller. The scattered data was collected using a 2-D Histar® detector and was later converted from 2-D to 1-D by azimuthal averaging using the Bruker software. Optical Microscopy was performed on an Olympus BX-50 microscope equipped with a Lookman camera. Viscosity measurements were performed on a Ubbelohde viscometer having diameter of 0.53 mm mounted on a Schott instrument.

5.3. Computational Procedure

Molecular dynamics simulations were performed in collaboration with the group of Dr. Sudip Roy, NCL. We report an all atomistic molecular dynamics simulation of (a) a linear 20-mer and 50-mer polyethyleneimine (PEI, $–(CH_2-CH_2-NH)-$) in water and (b) 10 linear 20-mer PEI chains with 49 surfactant molecules and water. We note that the 50-mer PEI has approximately similar molecular weight when compared with the polymer used for the experimental study. Results from the simulation of 20-mer PEI were compared with the results of Ziebarth *et. al.*,[32] to validate our simulations. As in Ziebarth et. al.,[32] each 20-mer and 50-mer system had three sub-systems

on the basis of different levels of protonation, viz., no-protonation (representative of behaviour at high pH, basic medium), protonation on every alternate nitrogen atom along the chain (representative of intermediate pH) and complete protonation (representative of very low pH, acidic medium). For the PEI-surfactant systems, we simulated only the non-protonated and all-protonated PEI. Protonation was done at the secondary nitrogen atoms present in the polymer chain. The protonated nitrogen atoms were neutralized using chloride ions. We compare the simulation results with the experimental systems that were acidified using nitric acid (viz. a nitrate counterion). We have confirmed that the concentration dependence of the viscosity of PEI solutions at different values of pH does not depend on whether nitric or hydrochloric acid is used to adjust the pH. Therefore, we believe that the trends from the simulation data (obtained using a chloride counterion) are comparable to the experimental data. The details of the computational method employed are mentioned elsewhere.[33]

5.4. Experimental Results

Our results are organized as follows: we first describe the effect of pH on the aqueous solution of PEI and on the surfactant/water system. We then examine the influence of adding PEI to the surfactant/water system, and use a combination of visual observations, microscopy, SAXS and NMR to understand the pH dependent changes in surfactant-PEI interactions. Finally, we present simulation results that provide a molecular understanding of our experimental observations.

5.4.1. Aqueous solutions of PEI:

There is a qualitative change in the ^1H-NMR of a dilute (5%, weight/weight) solution of PEI (in D_2O) with change in pH (Figure 5.1 a-c). At pH 12.8 (Figure 5.1 a), there are multiple peaks between δ=2.45-2.70, that can be attributed to the $–CH_2–$

protons adjacent to nitrogen atoms. Protons on nitrogen atoms are rapidly exchanged with deuterium from the solvent, D_2O, and are therefore, not detected. Multiple peaks are observed for $–CH_2–$ protons due to the heterogeneity in the environment experienced by the nuclei of these protons. In PEI, this heterogeneity can result either from partial protonation of the chain (viz. protonation of only some amine groups), or from branching along the chain.[34] As the pK_a values for the primary, secondary and tertiary amines range from 8.2-9.5,[32] it is unlikely that any of the amine groups will be protonated at a pH = 12.8. However, the presence of primary, secondary and tertiary amines due to branching along the PEI chain, results in a heterogeneous environment for the non-nitrogen atoms. For example, protons on carbon atoms in α-position to a nitrogen from a tertiary amine are more deshielded relative to a secondary, and to a primary amine.[34] Thus, we believe that it is branching along the PEI chain that results in multiple peaks for the $–CH_2–$ protons at pH = 12.8 (Figure 1 a). Our results are in accord with studies reported in the literature.[35]

As the pH of the PEI is reduced to 5, the $-CH_2-$ protons show peaks between δ=2.55-3.50, viz. down-field relative to those observed for pH 12.8 (compare Figure 5.1 b with Figure 5.1 a). At this pH, we expect that the amine groups along the PEI chain get protonated, thus deshielding the protons on carbons that are α and β to the nitrogen atoms. We observe a larger number of peaks at pH = 5 relative to pH = 12.8, suggesting a greater inhomogeneity in the environments for the protons. We attribute this to partial protonation of the amine groups at this pH, resulting in a distribution of charge along the PEI chain. At the lowest pH (= 1, Figure 5.1 c), we anticipate further protonation of the amine groups on the PEI. This results in a shift of the methylene proton signals to δ=2.55- 3.60, downfield relative to that at pH = 5. Interestingly, there

are fewer –CH_2– proton peaks relative to pH= 5, suggesting that almost all the amines are protonated at this low pH, and consequently, there is less heterogeneity in the proton environments. We note that, at pH = 1, there are a larger number of –CH_2– proton peaks relative to pH 12.8, suggesting that, even at this low pH, the amine groups on the PEI are not completely protonated. This is in agreement with the literature, where it has been reported only ~70% amines in PEI can be protonated due to conformational effects.[36]

The effect of protonation is more clearly visible in the ^{13}C spectra (Figure 5.1 d-f). At pH 12.8, we observe eight signals that we classify into three categories (Figure 1 d). The more deshielded signals (δ = 57-52 ppm) correspond to the methylene carbon attached to the tertiary nitrogen. The three signals following them (δ = 51.5-46 ppm) represent methylenes attached to secondary amine group (-NH-). The remaining (most shielded) signals (δ = 41-38 ppm) are attributed to the methylene carbon bonded to the terminal primary amino groups.[34] The spectrum at pH 5 exhibits shielding of all the resonances indicating a random ionization of the amine functionalities present in PEI (Figure 5.1 e). Reducing the pH further to 1 (Figure 5.1 f) did not induce any further shielding, but led to broadening of signals, especially in the 52-48 ppm region (associated with the protonated secondary amine functionalities and protonated/non protonated tertiary amine functionalities).

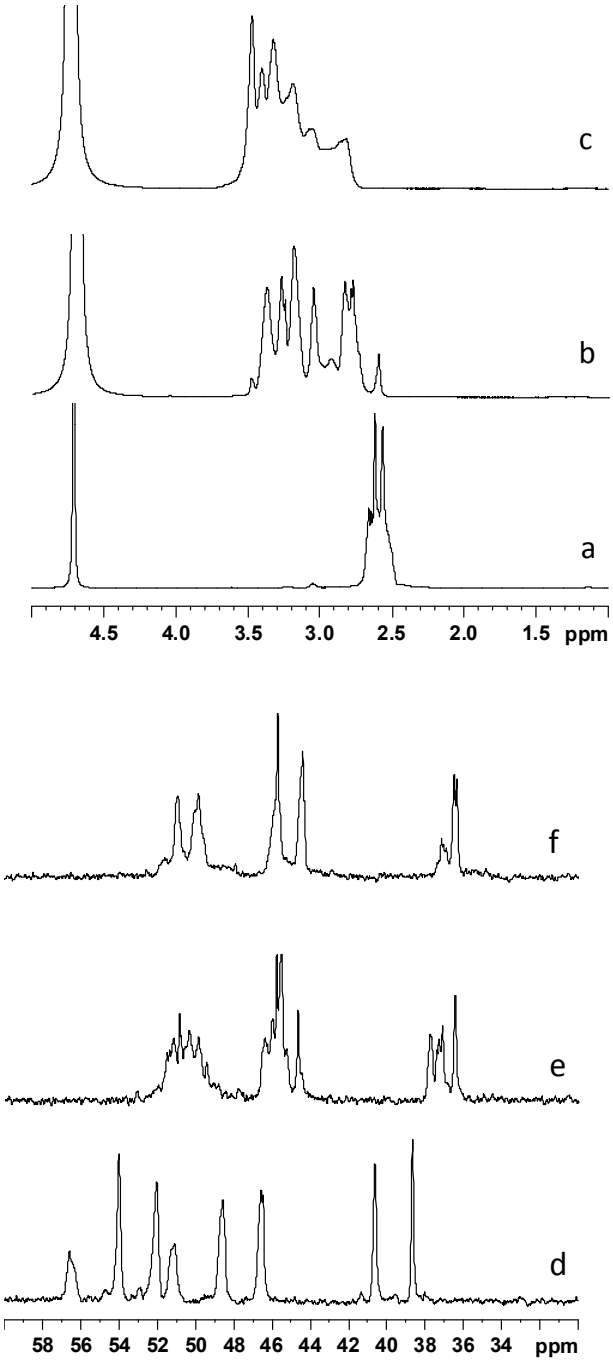

Figure 5.1. ^{1}H-NMR of 5 wt% PEI in D_2O at (a) pH 12.8, (b) pH 5 and (c) pH 1. ^{13}C-NMR of the same sample at (d) pH 12.8, (e) pH 5 and (e) pH 1.

5.4.2. PEI in $C_{12}E_9/H_2O$:

There is no effect of pH on the isotropic-H_1 phase transition of the 50/50 $C_{12}E_9/H_2O$ system (Figure 5.2). This is as expected, since $C_{12}E_9$ is a nonionic surfactant. For this system, the H_1 phase forms a transparent gel below the isotropic-H_1 transition temperature, T_{HI}, ≈ 50-51°C at all pH values between 1 and 12.8. We note here that there is a significant variation in T_{HI} for the $C_{12}E_9/H_2O$ system due to bottle-to-bottle variations in the surfactant (compare with the value of T_{HI}, ≈ 40°C in Chapter 2). This is not unexpected, since the surfactant is synthesized by ethoxylation, and there is polydispersity in the number of ethylene oxide units in the surfactant molecules. Therefore, we use the same bottle of surfactant for each *set* of experiments – for example, all experiments reported in this Chapter were performed using the same bottle of surfactant. The fan-like texture and domain size observed using optical microscopy is also independent of pH in this range. However, on addition of PEI, we see a dramatic influence of pH on the behavior of the 5% PEI–47.5% $C_{12}E_9$–47.5% water, that we examine in detail in this section. We report our results at pH = 12.8, 5, and 1.

(a) Visual Observations:

At high temperature, viz. above 45°C, a 5 wt% PEI sample in 47.5/47.5 wt% of $C_{12}E_9/H_2O$ is a transparent solution of low viscosity for all three pH values examined (Figure 5.3, bottom row), similar to the neat $C_{12}E_9/H_2O$ system. However, samples containing PEI were not observed to gel on cooling to just below T_{HI} for the neat $C_{12}E_9/H_2O$ system, (≈ 50°C). For pH = 12.8, the PEI/$C_{12}E_9/H_2O$ sample was a transparent, low viscosity solution even at room temperature (≈ 28°C, Figure 5.3, 1st column, middle).

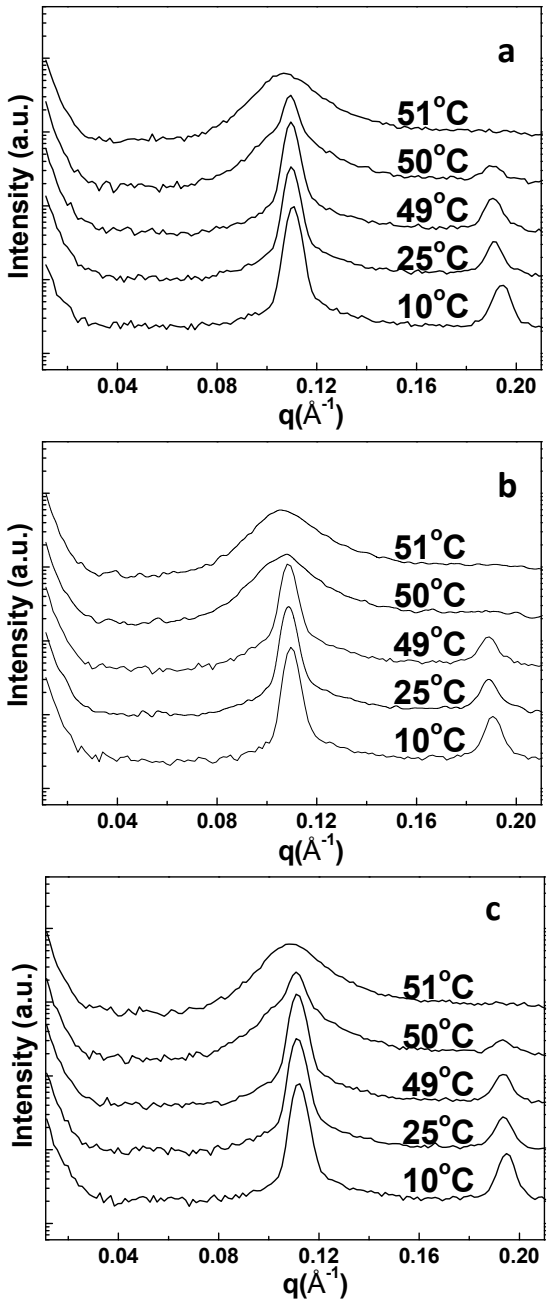

Figure 5.2. SAXS spectra for neat H_1 phase at (a) pH 12.8, (b) pH 5 and (c) pH 1.

We observed a noticeable increase in viscosity only on cooling to ~16^{o}C, and the sample became a self-standing clear gel at ~13^{o}C. At 10^{o}C (Figure 5.3, 1st row, top), the PEI/$C_{12}E_9$/H_2O sample at pH = 12.8 was a transparent gel. We now examine the behavior of the PEI/$C_{12}E_9$/H_2O sample at pH = 5. At pH = 5, the sample was a clear low viscosity solution on cooling to room temperature (~28^{o}C, Figure 5.3, 2nd column, 2nd row). However, on cooling to ~25^{o}C (Figure 5.4 a), the sample formed a transparent gel. On further cooling to ≈ 17^{o}C, this gel turned turbid (Figure 5.4 b) and we observed a progressive increase in opacity of the sample till 13^{o}C. We could observe no further change on cooling to 10^{o}C (Figure 5.3, 1st row, middle). In contrast to the higher pH sample, at pH = 1, the sample containing 5% PEI turned turbid, but did not gel at room temperature ~28^{o}C (Figure 5.3, 3rd column, 2nd row) and then transformed into an opaque gel on cooling to ~25^{o}C (Figure 5.5). The sample showed no further change to the eye, on cooling to 10^{o}C (Figure 5.3, 3rd column, top row). We now relate our visual observations to the sample microstructure probed using SAXS and optical microscopy.

(b) Small angle X-ray scattering studies:

Small Angle X-ray scattering (SAXS) was performed on PEI/ $C_{12}E_9$/H_2O samples at all three values of pH, as a function of temperature (Figure 5.6), and can be compared with measurements on the neat $C_{12}E_9$/H_2O sample (Figure 5.2). In the neat $C_{12}E_9$/H_2O sample, hexagonal order in the H_1 phase is characterized by peaks in the SAXS scattering at q~0.11 Å^{-1} and 0.18 Å^{-1} (≈ 0.11 x √3) at temperatures below T_{HI}.[37] On heating above T_{HI} (say, to 50^{o}C – presumably not at pH 1) a broad peak is observed at q~0.105 Å^{-1} that characterizes the isotropic micellar phase.

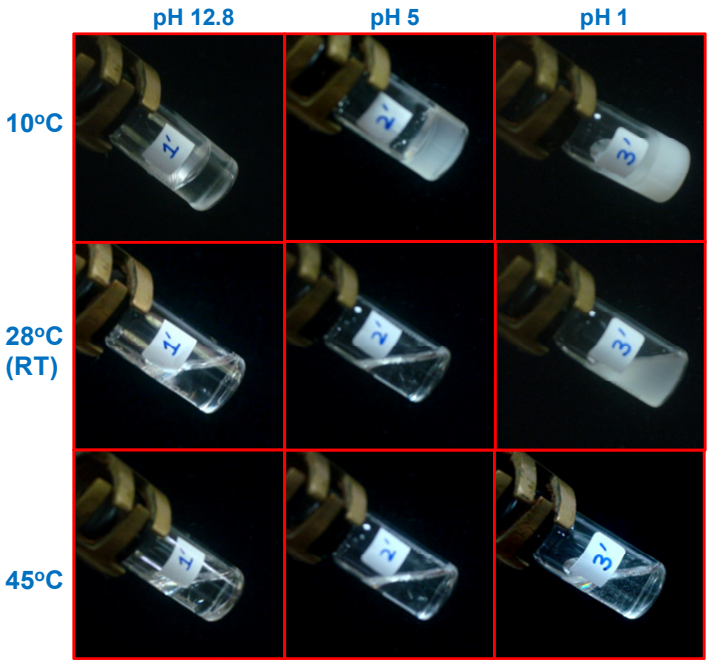

Figure 5.3. Temperature dependent visual observations for 5 wt% PEI in 47.5%/ 47.5% (by weight) $C_{12}E_9/H_2O$ at pH values of 12.8, 5 and 1.

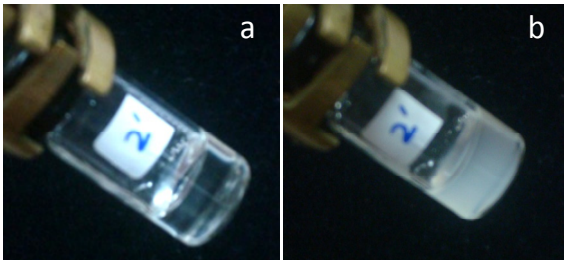

Figure 5.4. Snapshots of sample of 5 wt% PEI in 47.5%/47.5% (by weight) of $C_{12}E_9/H_2O$ at pH 5 from (a) 25°C and (b) at 17°C.

Figure 5.5. Snapshot of sample of 5% PEI in 47.5%/47.5% (by weight) $C_{12}E_9/H_2O$ at 25°C at pH 1.

At pH = 12.8, for the 5% PEI sample, we observe a broad micellar peak at q~0.1Å^{-1} at 50^{o}C (Figure 5.6 a), that shifts to higher q values when the temperature is decreased. Sharp Bragg peaks characterizing the H_1 phase appear at 15^{o}C (primary peak position ≈ 0.11 Å^{-1}; second order peak ≈ 0.19 Å^{-1}), viz. in accord with the temperature at which a self-standing gel is observed to form. However, the H_1 Bragg peak at 15^{o}C exhibits a shoulder on the low q side, suggesting coexistence of the H_1 and isotropic micellar phases. On decreasing the temperature to 10^{o}C, we observe that the H_1 peaks become more pronounced, suggesting an increase in the fraction of and/or improved ordering in the H_1 phase.

At pH = 5 (Figure 5.6 b), SAXS from the sample shows the broad isotropic micellar peak at 50^{o}Cand the H_1 peaks are observed on cooling to 25^{o}C (primary peak q~0.11Å^{-1} with second order peak at q~ 0.18Å^{-1}). Thus, in accord with our visual observations, T_{HI} for the PEI/ $C_{12}E_9/H_2O$ sample at pH = 5, is between 30^{o}C and 25^{o}C. With further decrease in temperature below T_{HI}, the H_1 peaks grow more prominent, as for the sample at pH = 12.8. Similarly, for the PEI/ $C_{12}E_9/H_2O$ sample at pH = 1 (Figure 5.6 c), we can observe a transition from an isotropic micellar state (characterized by a broad peak q~ 0.09 Å^{-1}) on cooling from 50^{o}C to 25^{o}C, where peaks from the H_1 phase appear (at q≈ 0.11Å^{-1}and ≈ 0.19Å^{-1}). The H_1 peaks grow more prominent on cooling, and we cannot observe the broad peak from the isotropic micellar phase below 25^{o}C. Our SAXS measurements accord with the visual observations: the T_{HI} from SAXS match the gelation temperatures from our visual observations. For PEI/ $C_{12}E_9/H_2O$ samples, formation of an H_1 phase appears to be inhibited at higher pH: T_{HI} decreases with increase in pH, and when the H_1 phase forms, the SAXS peaks that characterize it are significantly broadened at higher pH.

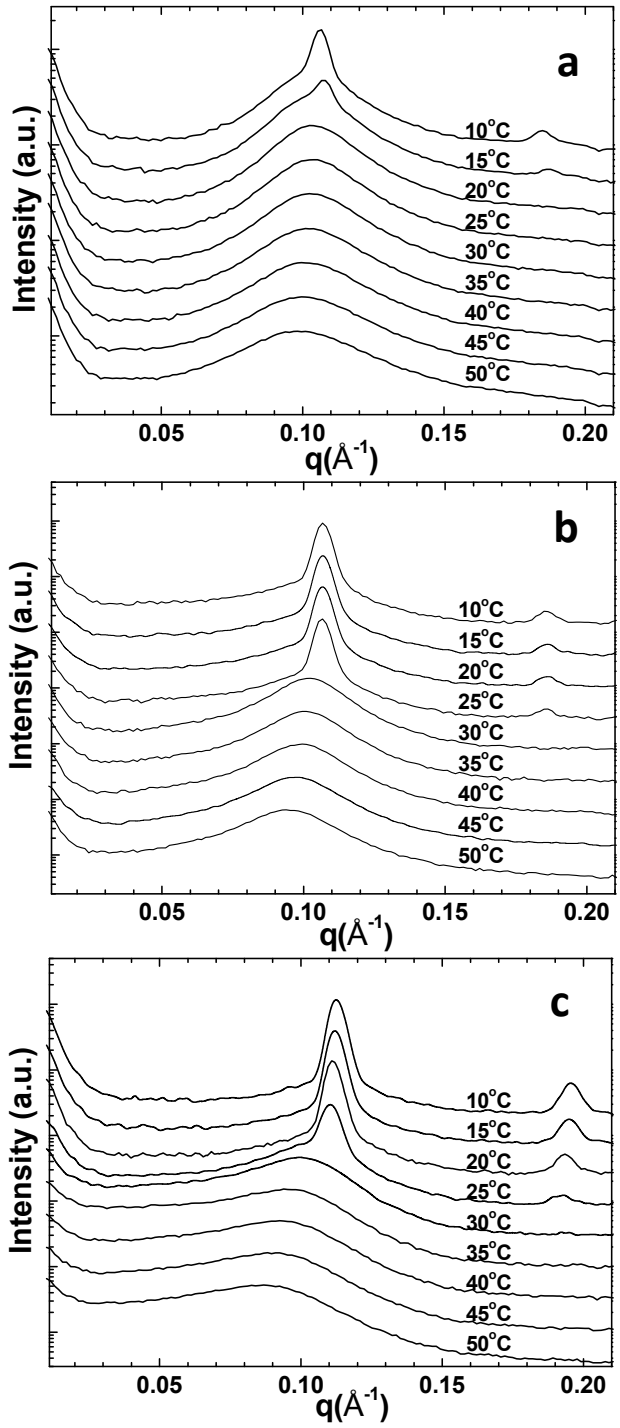

Figure 5.6. Temperature dependent SAXS spectra of 5% PEI in 47.5/47.5 wt% of $C_{12}E_9/H_2O$ system at (a) pH 12.8, (b) pH 5 and (c) pH 1.

(c) Optical microscopy studies:

We now present optical microscopy images of our samples observed between parallel, as well as, crossed polarizers, as a function of pH and temperature (Figure 5.7). A neat H_1 phase (viz. not containing PEI) shows a fan-like texture that is characteristic of the hexagonal phase, when observed between crossed polarizers (see, for example, images in ref. 7 and 37). At 45°C, the PEI/ $C_{12}E_9/H_2O$ samples are transparent at pH between 1 and 12.8, and are in the isotropic micellar phase. Therefore, optical microscopy of these samples does not yield any information – a uniform, featureless image is observed between parallel polarizers and no light is transmitted through crossed polarizers.[33] At pH = 12.8, the H_1 phase does not form at 25°C and, therefore, we can obtain no information from optical microscopy, as in the case of the samples at 45°C (Figure 5.7 a). However, on cooling to 15°C, a birefringent fan-like texture, characteristic of the H_1 phase, is observed between crossed polarizers (the image at 10°C, is shown in Figure 5.7 c). The corresponding image between parallel polarizers (Figure 5.7 b) is uniform, suggesting that there is no aggregation of PEI. In contrast to the sample at pH = 12.8, the behaviour is different at lower pH.

At pH = 5, the H_1 phase forms at around 26°C and the characteristic fan like texture is visible in the image between crossed polarizers (data at 25°C in Figure 5.7 e). The corresponding image, between parallel polarizers (Figure 5.7 d), has no features. These images accord with our visual observation (Figure 5.3, 2nd row, 2nd column and Figure 5.4 a) that the sample remains transparent at 25°C, after the formation of the H_1 phase. However, on cooling, the sample turned turbid at around 17°C (Figure 5.4 b). When viewed under the microscope at 10°C, we observe optically dense structures that are a few microns in size (Figure 5.7 f), and that are localized at the bounda-

ries of the H_1 phase domains. The formation of these structures, that we expect will scatter visible light, correlates with the onset of turbidity in the sample. We also note that the domain structure of the H_1 phase (Figure 5.7 g) formed at 25°C does not change with the formation of these structures. We had previously reported[7] that for poly(N-isopropylacrylamide) (PNIPAM) chains in the $C_{12}E_9/H_2O$ system, we observe the precipitation of PNIPAM from the surfactant/water phase once an H_1 phase forms. Further, the PNIPAM was observed to be localized at the domain boundaries of the H_1 domain. Similarly, in the PEI/$C_{12}E_9/H_2O$ system investigated here, we believe that the structures that are observed in the optical microscopy are formed by precipitation of PEI chains that phase separate from the $C_{12}E_9/H_2O$ to form micron sized aggregates. These polymer aggregates cannot be accommodated in the H_1 phase and are expelled to the boundaries of the H_1 domains.

At lower pH, viz. for the sample at pH = 1, we observe the formation of droplets that phase separate from the isotropic micellar phase, at about 28°C (image between parallel polarizers, Figure 5.8). These droplets scatter light rendering the sample opaque. On cooling the sample to around 26°C, the fan like texture characteristic of the H_1 phase is observed between crossed polarizers. This fan like texture is clearly visible at 25°C (Figure 5.7 i). Between parallel polarizers, we observe that the droplets that phase separate at 28°C form anisotropic polymer aggregates on cooling the sample into the H_1 phase (see, for example, Figure 5.7 h at 25°C). The H_1 texture observed is much finer, when compared with the sample at pH = 5, suggesting smaller domain dimensions at pH = 1. On further cooling the pH = 1 sample to 10°C, we observe that there is no qualitative change in the structure of the anisotropic PEI precipitates – however, there is higher optical contrast relative to that at 25°C Figure 5.7 j, k).

We summarize the results from our visual observations, SAXS and optical microscopy on a pH-temperature "state diagram" (Figure 5.9). Clearly, the H_1 phase forms at lower temperatures as we increase pH from 1 to 12.8. For the samples at pH = 12.8, the samples are always clear, and we always see a coexistence of isotropic micellar and H_1 phases, even at the lowest temperature (10°C). At pH = 5, the sample gels to form the H_1 phase, and then turns opaque as the PEI chains phase separate and aggregate at the H_1 domain boundaries. Finally, at pH = 1, there is phase separation of the PEI chains from the isotropic micellar solution at about 28°C, resulting in turbidity, followed by formation of the H_1 phase on cooling to about 26°C. We also indicate the temperature at which the gel can support its own weight in a 5 ml vial (viz. when the yield stress exceeds ½ $\rho g r \approx 3.5$ kPa, where ρ is the density of the sample, g is the acceleration due to gravity and r is the radius of the vial). We observe that the sample forms a gel stiff enough to support its weight with the onset of the formation of the H_1 phase. Thus, PEI decreases the T_{HI} of the surfactant/H_2O system at all pH values, relative to the neat H_1 phase, and this decrease is more pronounced at higher pH. Our data clearly points to pH-dependent interactions between the PEI and the nonionic surfactant, with stronger interactions at higher pH, that suppress the formation of the H_1 phase to lower temperatures compared with the neat $C_{12}E_9/H_2O$ system. We now describe NMR experiments that probe these interactions in detail.

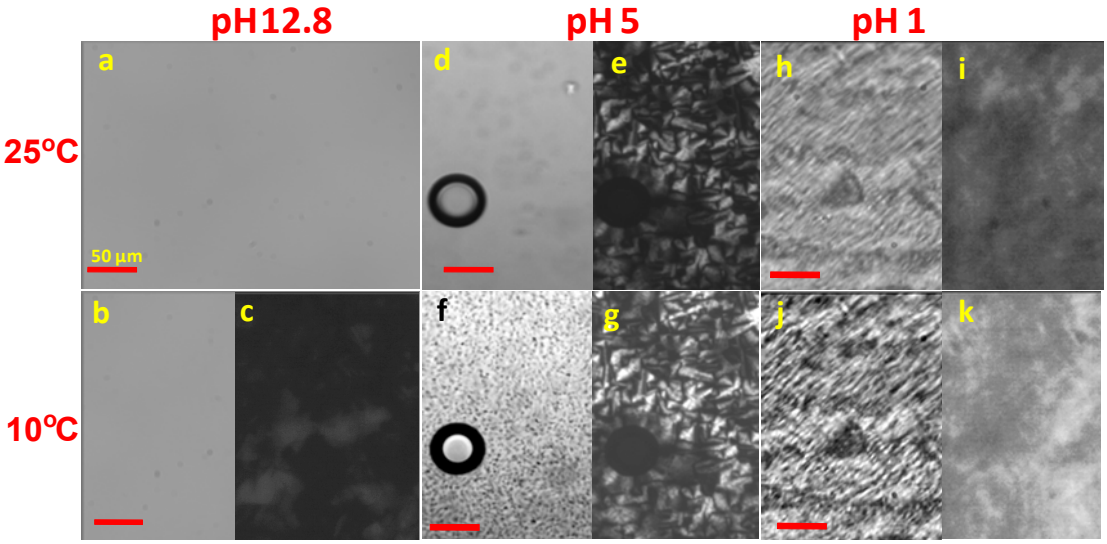

Figure 5.7. Optical micrographs of 5 wt% PEI in 47.5%/47.5% (by weight) $C_{12}E_9$/ H_2O system. Scale bar in all images is 50µm.

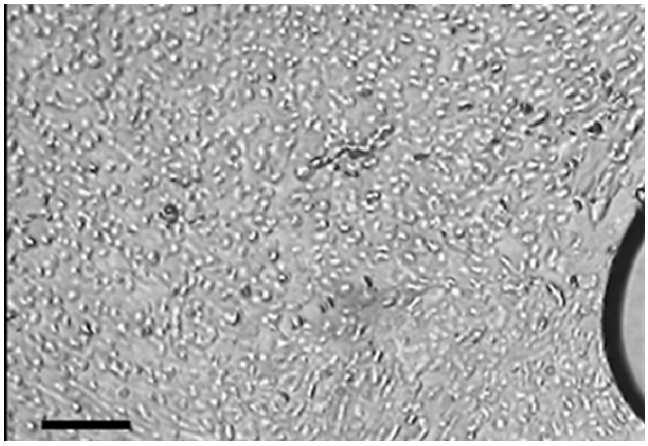

Figure 5.8. Optical micrograph of polymer rich droplets formed at room temperature i.e. ~28°C in a 5 wt% PEI in 47.5%/47.5% (by weight) $C_{12}E_9/H_2O$ system at pH 1. Scale bar refers to 50 µm.

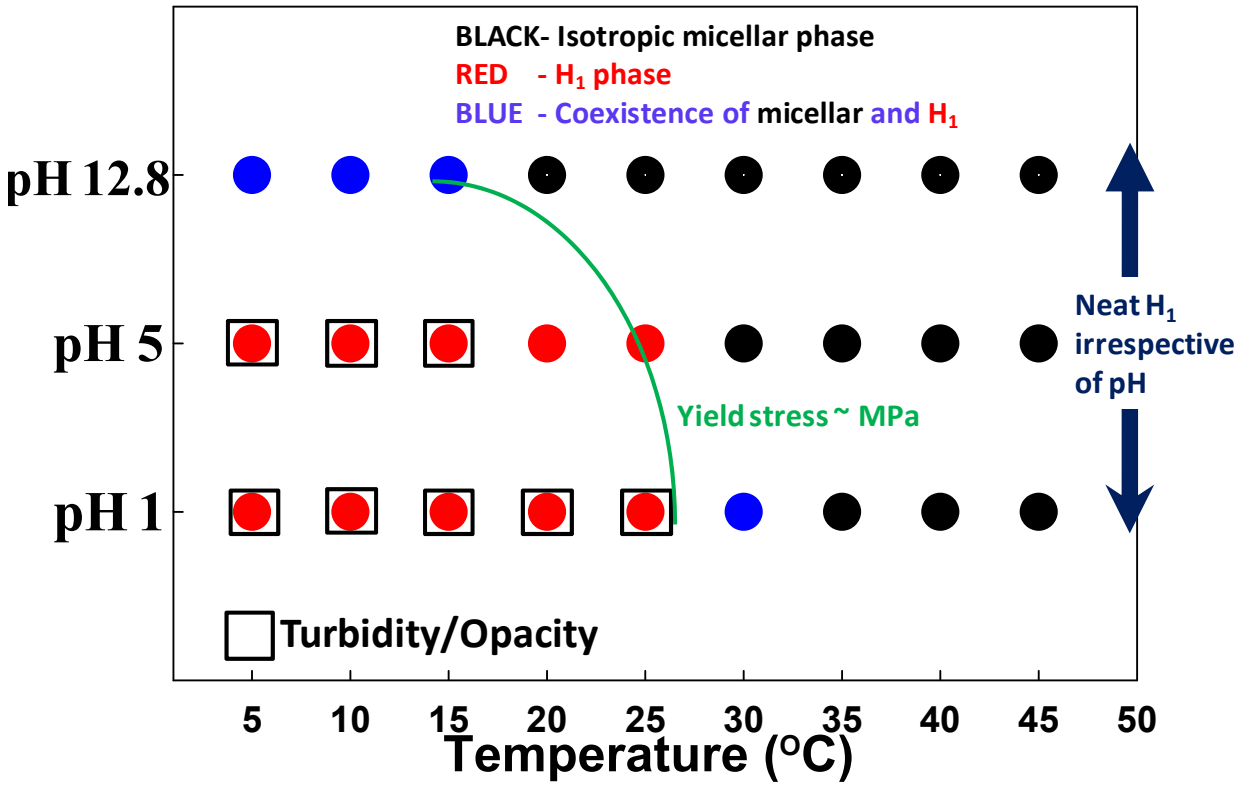

Figure 5.9: State diagram based on visual, SAXS and optical microscopy studies. The green line represents the temperatures above which the samples yield.

(d) NMR studies:

(1) ^{1}H-NMR:

We obtained proton NMR of samples containing 5% PEI and 25 wt% $C_{12}E_9$ in D_2O (Figure 5.10). At these surfactant concentrations, we do not observe the formation of an H_1 phase at room temperature, where NMR was performed. Thus, the samples are in a low viscosity isotropic micellar phase for all the NMR experiments reported here. We observe that there is no change in the position of the peaks from methylene protons in PEI at different pH, in the presence of the nonionic surfactant (compare Figure 5.10 with Figure 5.1). In addition to the peaks from the PEI, we observe peaks at δ= 3.3-3.75 ppm corresponding to protons in the ethylene oxide, –(OCH_2-CH_2-O)- units in the surfactant and, at δ = 0.75-1.5 ppm corresponding the methyl, CH_3, and methylene protons, -CH_2- in the hydrophobic surfactant tail. At pH = 12.8 the –CH_2– protons from PEI and the ethylene oxide proton peaks are well separated and can be easily distinguished (Figure 5.10 a). However for pH = 5 and pH = 1, as the PEI –CH_2– peaks shift downfield (Figure 1, Figure 5.10 b, c), they overlap with the peaks from the ethylene oxide units in the surfactant and are difficult to distinguish (especially for pH = 1, Figure 5.10 b, c).

(2) 2-D NMR (ROESY experiments):

We employ 2D ROESY to probe surfactant-PEI-water interactions. This experiment uses Nuclear Overhausser Enhancement (nOe) to probe the spatial proximity of protons, for systems in the long correlation limit. ROESY data for the PEI/$C_{12}E_9$/H_2O systems at pH = 1, 5 and 12.8 is shown in Figure 5.11. In all the cases, cross-peaks within the surfactant system i.e. between the ethylene glycol moieties and aliphatic protons of the C_{12} moieties could be clearly seen indicating its micellar na-

ture. Since $C_{12}E_9$ remains in the micellar form at all experimental pH values, their cross peak intensities are similar, to a first approximation. At pH 12.8 (Figure 5.11 a), we can clearly observe cross peaks between the methylene protons, $-CH_2-$, of the PEI (δ =2.6-2.7) and protons in the $-OCH_2-$ groups (δ = 3.6) of the surfactant, suggesting spatial proximity between the PEI and hydrophilic units of the surfactant. At pH = 12.8, we also observe cross peaks that suggest spatial proximity between water (δ = 4.7) and the $-OCH_2-$ groups of the surfactant and the $-CH_2-$ group of PEI. As the pH is decreased, we observe a decrease in the intensity of the cross peaks from the surfactant $-OCH_2-$ protons and the PEI protons, indicating a decrease in the surfactant-PEI interactions. At pH = 5 and pH = 1, ROESY cross peaks are either very weak relative to those at pH = 12.8, or are absent (Figure 5.11 b and c).

Thus, the NMR data confirms that there are interactions between the PEI and surfactant, that results in their spatial proximity, and in accord with our other data, indicates that the magnitude of PEI-surfactant interactions decreases with decrease in pH. We now, use molecular dynamics simulations to understand the influence of pH on the chain conformations of the PEI and, to probe PEI-surfactant interactions. We begin by modeling the behavior of PEI chains in water, at various levels of protonation, to understand the effect of changing pH. Subsequently, we examine a system containing PEI (at different levels of protonation) and surfactant molecules in water, to compare with the experimental data.

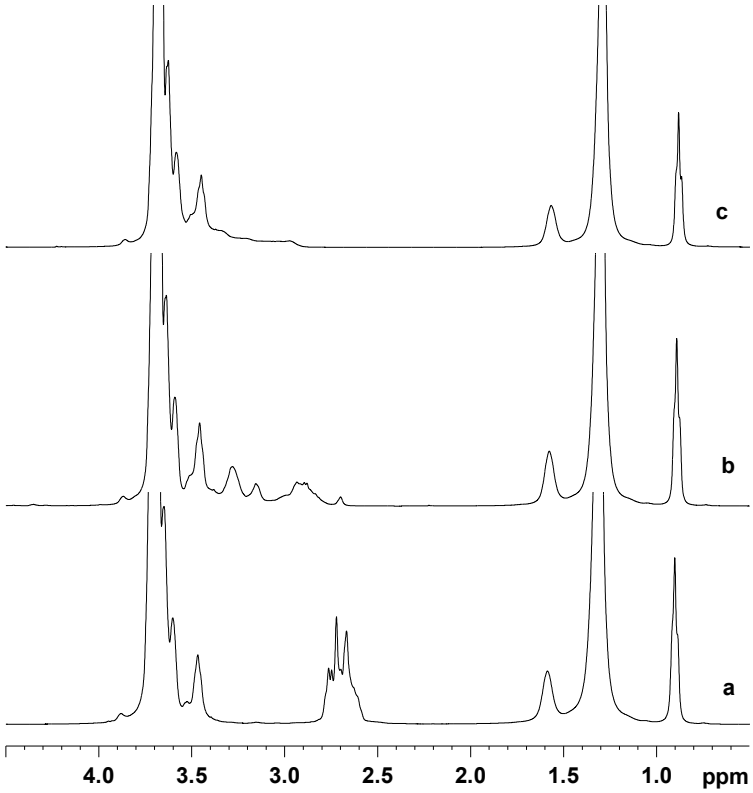

Figure 5.10. ^{1}H-NMR of 5 wt% PEI in 25 wt% $C_{12}E_9$ and remaining D_2O at (a) pH 12.8, (b) pH 5 and (c) pH 1.

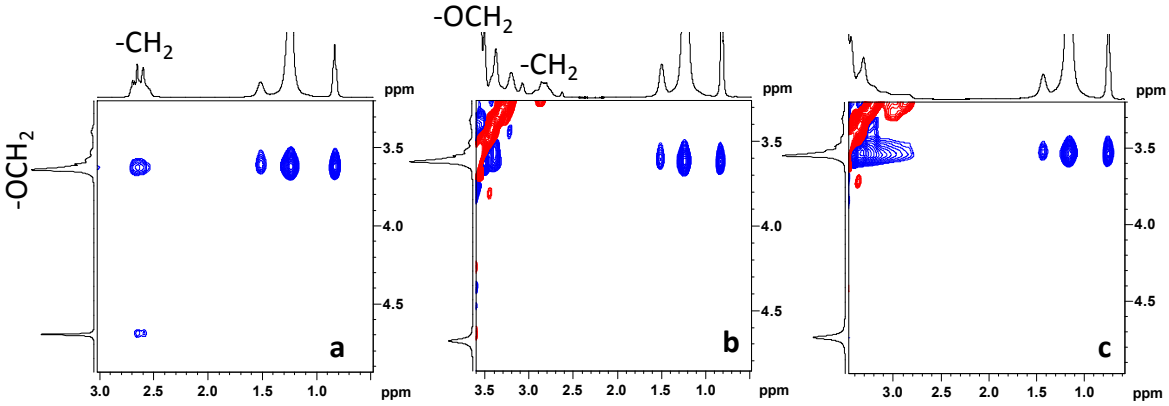

Figure 5.11. 2-D ROESY spectrum for 5% PEI in 25 wt% $C_{12}E_9$ in D_2O at (a) pH 12.8, (b) pH 5 and (c) pH 1.

5.5. Computer Simulations

5.5.1. Single linear PEI chain (20-mer and 50-mer) in water:

To investigate the size of PEI chain as a function of ionization along the chain, our collaborators in the group of Dr. Sudip Roy, NCL, performed all atom molecular dynamic simulations for a single chain in water. Simulations were carried out on a linear PEI chain containing 20 and 50 monomer units of -(CH_2-CH_2-NH)- (In comparison, the number of monomer units for the 2000 g.mol^{-1} PEI used in the experiments is ~43, and our NMR data indicates the presence of chain branching). The single 20-mer and 50-mer PEI chains in water were simulated for 50 ns and the trajectory was recorded. Last 10 ns of the trajectory were used for the analysis of the end-to-end distance and the radius of gyration (R_g) to understand the effect of protonation on the size and the shape of the polymer chain. For the all-protonated system, the end-to-end distance and the radius of gyration (R_g) are greater than that of the alternate-protonated and unprotonated systems (details can be found in reference 33). It is observed that the PEI chain expands due to repulsion between the charged amine groups as the pH is reduced. These observations are consistent with the calculations reported by Zakharova et. al.[38]

5.5.2. PEI chains with surfactant molecules:

Simulations of the non-ionic surfactant H_1 mesophase are computationally very expensive. Therefore, we examine results of simulations that mimic a part of this phase by having 10 PEI chains and 49 surfactant molecules that were solvated with TIP3P water molecules. Simulations were performed for 100 ns, for both the non-protonated PEI and all protonated PEI systems with surfactants, and the trajectory for the last 10 ns has been analyzed. Figure 5.12 (a, b) clearly depicts the differences in

interaction of the all protonated (Figure 5.12 b) and unprotonated (Figure 5.12 a) PEI chains with the surfactant. In Figure 10, the water molecules are not shown for clarity. The surfactant self assembles with its non-polar tail buried inside, shielded from the water molecules by the polar head groups. To check the interaction between the surfactant molecules and the PEI chains, we plotted the pair distribution between the oxygen atoms of the surfactants and nitrogen atoms of the PEI chains (Figure 5.13). The minima for the first peak for both the fully protonated, and unprotonated cases are at 0.36 nm. We find a higher value of the peak minimum for the unprotonated system, indicating that this system has higher attractive interactions between the PEI and the surfactant molecules, as compared to the all protonated system. We observe that integrating the first peak for the unprotonated system yields a ten-fold higher peak area compared with the all protonated system. This result is in good accord with the experimental observations.

5.6. Comparison of experimental data with simulations

Nonionic surfactants, such as $C_{12}E_9$ used in our work, typically interact weakly with water soluble polymers, when compared with ionic surfactants. In previous work on PNIPAM in a $C_{12}E_9/H_2O$ system, we observed very little influence of the polymer on the surfactant phase behavior. However, for the system investigated here, we observe that the presence of PEI strongly influences the $C_{12}E_9/H_2O$ phase transition temperatures, and further, that this effect of PEI is a strong function of pH. Since pH does not significantly affect the phase behavior of the neat $C_{12}E_9/H_2O$ phase, it is clear that the change in PEI-surfactant interactions with pH influences the isotropic-H_1 transition in the $C_{12}E_9/H_2O$ system.

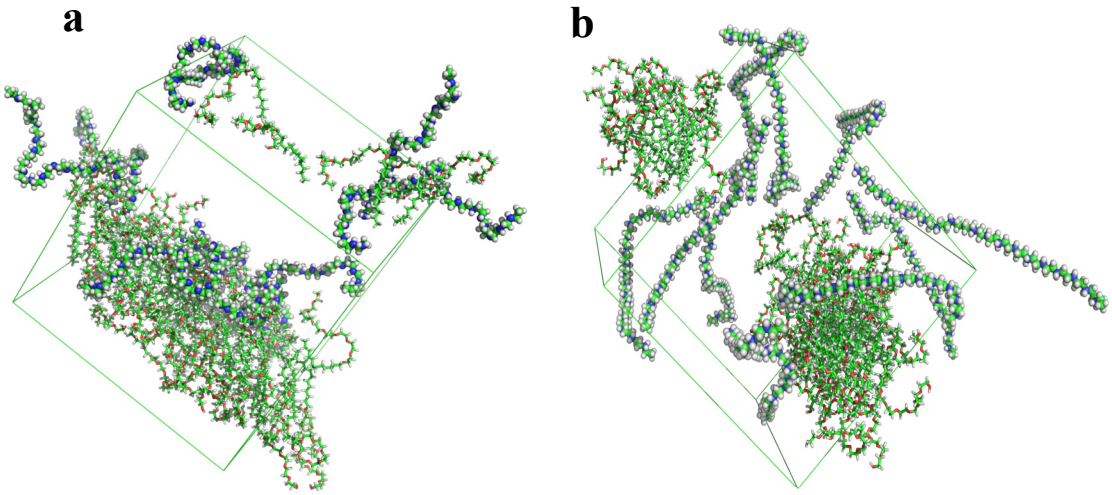

Figure 5.12. PEI-water-surfactant system containing 10 PEI chain and 49 surfactant molecules (a) non-protonated (b) all protonated. It can be clearly seen that the PEI chains do not interact with the surfactant in the all protonated case. The surfactant molecules are shown as lines and the PEI is presented as ball and stick model.

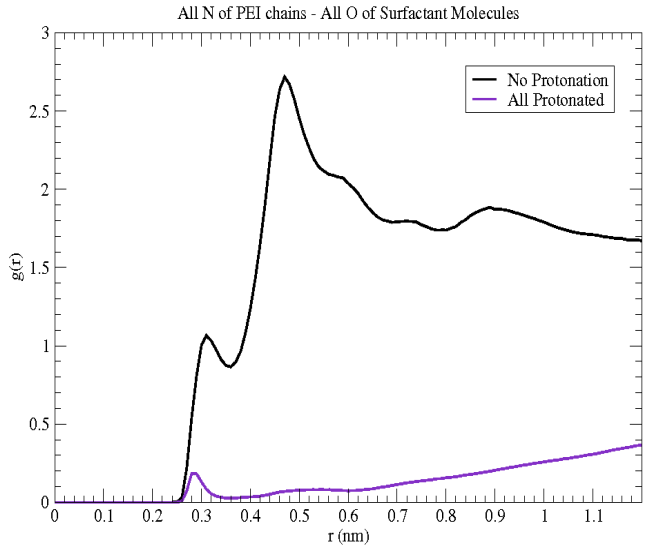

Figure 5.13. Pair distribution between the all nitrogen atoms present in the PEI chain– all protonated and no-protonated system and the all oxygen atoms present in the surfactant molecules.

Our NMR data and simulations point to a change in the PEI-surfactant microstructure with change in pH. We observe higher spatial proximity between the PEI and the hydrophilic units of the surfactant at pH = 12.8, as compared to lower pH (= 5, 1). With decrease in pH, we expect higher protonation of the PEI, as indicated by NMR (Figure 5.1). With increase in protonation, our simulations reveal an increase in the end-to-end distance of the PEI chain, as expected. Our simulations also accord with the NMR data on the aqueous PEI/surfactant systems, and indicate that the PEI-surfactant interactions are higher, when the PEI is not protonated. This interaction between the PEI and the surfactant inhibits formation of the H_1 phase.

At pH = 12.8, the strong PEI-surfactant interaction results in coexistence of the H_1 phase with isotropic micellar phase, even when the sample is cooled to 10^oC. In fact, even when this sample is cooled to lower temperatures, $\approx 5^oC$, the sample remains a clear gel and there is a coexistence of the H_1 and isotropic micellar phases. For pH = 5, the formation of the H_1 phase on cooling results in the expulsion of PEI to aggregated particles. As in the case of the PNIPAM,[7] the phase separation of PEI is a result of the H_1 phase formation. At surfactant concentrations (< 35%) where the H_1 phase does not form, the PEI stays in solution in the isotropic micellar phase, even on cooling to lower temperature (10^oC). Thus, the H_1 phase forms at higher temperatures relative to pH = 12.8, due to the decrease in PEI-surfactant interactions, and once the H_1 phase forms, the PEI chains cannot be localized within the H_1 domains and are expelled to the domain boundaries. On decreasing the temperature further (to 10^oC), the fraction of the isotropic micellar phase decreases relative to the H_1 phase, and the PEI aggregates are dehydrated, forming increasingly optically dense structures at the H_1 domain boundaries. At the lowest pH (= 1), a further decrease in PEI-surfactant inter-

actions relative to pH = 5 results in expulsion of the PEI into polymer rich droplets, even while the surfactant is in the isotropic micellar phase. After the PEI is expelled, the surfactant/water system forms an H_1 phase, and anisotropic PEI aggregates are observed. At this low pH, we expect that the PEI is in an extended conformation relative to pH =12.8, and that the PEI chains are protonated. It is interesting that the formation of the H_1 phase by the surfactant/water system results in aggregation of protonated PEI chains by expulsion to the H_1 domain phase boundaries. It is not currently clear how anisotropic aggregates form from PEI chains that are protonated and that show an increase in the chain end-to-end distance. It is possible that correlations between the charges on the protonated chains, and in the counterions in solution results in the observed anisotropic aggregates.

5.7. Summary

We demonstrate the pH dependence of structuration in a PEI/$C_{12}E_9$/H_2O system. The $C_{12}E_9$/H_2O system is not influenced by pH. However, on addition of PEI, pH dependent PEI-surfactant interactions influence the transition from the isotropic to H_1 phase. At high pH (=12.8), the transition to the H_1 phase is significantly suppressed to lower temperatures, from 45^{o}C for the neat $C_{12}E_9$/H_2O system to 13^{o}C for the system containing 5% PEI. Even at low temperatures, when the H_1 phase forms, strong PEI-H_1 interactions result in a coexistence of the H_1 phase with an isotropic micellar phase. Thus, a clear gel is obtained for the PEI/$C_{12}E_9$/H_2O system at high pH, even at low temperatures. In contrast, for lower pH (=5, 1), we observe higher T_{HI} relative to pH = 12.8. On cooling, the $C_{12}E_9$/H_2O system organizes into the H_1 phase, and the formation of the organized mesophase expels the PEI to the mesophase domain boundaries. Competition to complex with water results in dehydration of the PEI be-

low T_{HI}, and therefore, the PEI aggregates at the H_1 domain boundaries form structures that are observed as optically dense structures that scatter light, and render the gel turbid. Molecular dynamics simulations confirm that protonatedlinear PEI chains (representative of the low pH state) interact less strongly with the nonionic surfactant, when compared with unprotonated chains (representative of the high pH state). The protonated chains are extended relative to the unprotonated chains, thus, possibly explaining the formation of anisotropic PEI aggregates below T_{HI} for pH = 1.

5.8. References

1. (a) Drummond, C. J.; Fong, C. *Current Opinion in Colloid & Interface Science* **2000**, *4*, 449-456. (b) Farkas, E.; Zelkó, R.; Németh, Z.; Pálinkás, J.; Marton, S.; Rácz, I. *International Journal of Pharmaceutics* **2000**, *193*, 239-245 (c) Clogston, J.; Caffrey, M. *J. Control. Release* **2005**, *107*, 97–111. (d) Mohammady, S. Z.; Pouzot, M,; Mezzenga, R. *Biophys. J.* **2009**, *96*, 1537–1546. (e) Shah, J. C.; Sadhale, Y.; Chilukuri, D. M. *Adv. Drug Deliv. Rev.* **2001**, *47*, 229-250.(f) Koltover, I.; Salditt, T.; Radler, J. O.; Safinya, C. R. *Science* **1998,** *281*, (5373), 78-81. (g) Radler, J. O.; Koltover, I.; Salditt, T.; Safinya, C. R. *Science* **1997,** *275*, (5301), 810-814. (h) Safinya, C. R.; Ewert, K.; Ahmad, A.; Evans, H. M.; Raviv, U.; Needleman, D. J.; Lin, A. J.; Slack, N. L.; George, C.; Samuel, C. E., *Philosophical Transactions of the Royal Society A: Mathematical, Physical and Engineering Sciences* **2006,** *364*, (1847), 2573-2596.
2. (a) Mezzenga, R.; Schurtenberger, P.; Burbidge, A.; Michel, M. *Nat. Mater.* **2005**, *4*, 729–740 (b) Ubbink, J.; Burbidge, A.; Mezzenga, R. *Soft Matter* **2008**, *4*, 1569–1581.
3. Park, I.-K.; Singha, K.; Arote, R. B.; *Choi, Y.***-J.;** K*im,* W. J.; Cho, C.-S., *Macromolecular Rapid Communications* **2010**, *31*, (13), 1122-1133.
4. Sethuraman, V. A.; Na, K.; Bae, Y. H. *Biomacromolecules **2005,** 7, (1),* 64-70.
6. Werth, S.; Urban-Klein, B.; Dai, L.; Höbel, S.; Grzelinski, M.; Bakowsky, U.; Czubayko, F.; Aigner, A. *J. Control. Release* **2006,** *112*, (2), 257-270.
7. Jijo, V. J.; Sharma, K. P.; Mathew, R.; Kamble, S. B.; Rajamohanan, P. R.; Ajithkumar, T. G.; Badiger, M. V.; Kumaraswamy, G. *Macromolecules* **2010**, *43*, 4782–4790 .

8. Holmberg, K.; Jönsson, B.; Kronberg, B.; Lindman, B.; *Surfactants and Polymers in Aqueous Solution*; 2nd ed. John Wiley & Sons: West Sussex, U.K., **2003**.
9. (a) Goddard, E. D. *Colloids Surf.* **1986**, 19, 301. (b) Antonietti, M.; Conrad, J.; Thuenemann, A. *Macromolecules* **1994,** *27*, (21), 6007-6011. (c) Faul, C.; Antonietti, M.; Sanderson, R.; Hentze, H.-P. *Langmuir* **2001**, *17*, (6), 2031-2035. (d) von Ferber, C.; Lowen, H. *Faraday Discuss.* **2005**, *128*, 389–405. (e) Hentze, H.-P., *Dekker Encyclopedia of Nanoscience and Nanotechnology, 2nd Edition* **2009**, 3403 – 3408. (f) Thünemann, A. F. *Progress in Polymer Science* **2002,** *27*, (8), 1473-1572.
10. Iliopoulos, I.; Wang, T. K.; Audebert, R. *Langmuir* **1991,** *7*, (4), 617-619.
11. Saito, S. in *Nonionic Surfactants: Physical Chemistry;* Schick, M. J., Ed.; *Marcel Dekker*: New York**, 1987**; 881-926.
12. Magny, B.; Iliopoulos, I.; Audebert, R.; Piculell, L.; Lindman, B. *Prog. Colloid Polym. Sci.* **1992**, *89*, 118.
13. Bystryak, S. M.; Winnik, M. A.; Siddiqui, J. *Langmuir* **1999,** *15*, (11), 3748-3751.
14. Winnik, M. A.; Bystryak, S. M.; Chassenieux, C.; Strashko, V.; Macdonald, P. M.; Siddiqui, J. *Langmuir* **2000,** *16*, (10), 4495-4510.
15. Wang, H.; Wang, Y.; Yan, H.; Zhang, J.; Thomas, R. K. *Langmuir* **2006,** *22*, (4), 1526-1533.
16. Gainanova, G.; Zhil'tsova, E.; Kudryavtseva, L.; Lukashenko, S.; Timosheva, A.; Kataev, V.; Konovalov, A. *Colloid Journal* **2006,** *68*, (5), 533-540.
17. Kotz, J.; Kosmella, S. Current Opinion in Colloid & Interface Science **1999**, *4*, 348-353.

18. (a) Ligoure, C.; Bouglet, G.; Porte, G. *Phys. Rev. Lett.* **1993,** *71*, (21), 3600. (b) Singh, M.; Ober, R.; Kleman, M. *J. Phys. Chem.* **1993,** *97*, (42), 11108-11114. (c) Ligoure, C.; Bouglet, G.; Porte, G.; Diat, O. *J. Phys. II* **1997**, *7*, 473. (d) Zang, K.; Linse, P. *J. Phys. Chem*. **1995**, *99*, 9130.

19. (a) Radlinska, E. Z.; Gulik-Krzywicki, T.; Lafuma, F.; Langevin, D.; Urbach, W.; Williams, C. E.; Ober, R. *Phys. Rev. Lett.* **1995,** *74*, (21), 4237. (b) Radlinska, E. Z.; Gulik-Krzywicki, T.; Lafuma, F.; Langevin, D.; Urbach, W.; Williams, C. E. *J. Phys. II* **1997**, *7*, 1393.

20. Kekicheff, P.; Cabane, B.; Rawiso, M. *Journal of Colloid and Interface Science* **1984,** 102, (1), 51-70.

21. (a) Iliopoulos, I.; Olsson, U. *J. Phys. Chem.* **1994**, *98*, 1500. (b) Ficheux, M.-F.; Bellocq, A.-M.; Nallet, F. *J. Phys. II* **1995**, *5*, 823. (c) Ficheux, M.-F.; Bellocq, A.-M.; Nallet, F. *Colloid Surf., A* **1997**,*123*, 253.

22. Pacios, I. E.; Renamayor, C. S.; Horta, A.; Lindman, B.; Thuresson, K. *J. Phys. Chem. B* **2005,** *109*, (50), 23896-23904.

23. Pacios, I. E.; Renamayor, C. S.; Horta, A.; Thuresson, K.; Lindman, B. *Macromolecules* **2005,** 38, (5), 1949-1957.

24. Deme, B.; Dubois, M.; Zemb, T.; Cabane, B. *J. Phys. Chem.* **1996,** *100*, (9), 3828-3838.

25. Ligoure, C.; Bouglet, G.; Porte, G. *Phys. Rev. Lett.* **1993,** *71*, (21), 3600.

26. Yamamoto, J.; Tanaka, H. *Nat. Mater.* **2005**, *4*, 75-80.

27. Iliopoulos, I.; Olsson, U. *J. Phys. Chem.* **1994**, *98*, 1500.

28. Yang, Y.; Prud'homme, R.; Richetti, P.; Marques, C. M. *Supramolecular Structure in Confined Geometries*, American Chemical Society: **1999**, *736*, 169-179.

29. Radlinska, E. Z.; Gulik-Krzywicki, T.; Lafuma, F.; Langevin, D.; Urbach, W.; Williams, C. E.; Ober, R. *Phys. Rev. Lett.* **1995**, *74*, (21), 4237.

30. Radlinska, E. Z.; Gulik-Krzywicki, T.; Lafuma, F.; Langevin, D.; Urbach, W.; Williams, C. E. *J. Phys. II* **1997**, *7*, 1393.

31. Bax, A.; Davis, D.G. *J. Magn. Reson*. **1985**, *63*, 207-213.

32. Ziebarth, J. D.; Wang, Y. *Biomacromolecules* **2010**, *11*, 29-38.

33. Sharma, K. P.; Choudhary, C. K.; Roy, Sudip, S.; Kumaraswamy, G. in Assembly of Polyethylenimine in the Hexagonal mesophase of Non-Ionic surfactant: Effect of pH and Temperature. *J. Phys. Chem. B* **2011** (submitted).

34. (a) Axelson, D. E.; Blake, S. L. *Journal of Polymer Science: Polymer Chemistry Edition*, **1985,** *23*, 2507-2525; Lukovkin, G. M.; (b) Pshezhetsky, V. S.; Murtazaeva, G. A. *European Polymer Journal*, **1973**, *9*, 559-565.

35. (a) Idris, S. A.; Mkhatresh, O. A.; Heatley, F. *Polymer International* **2006,** *55*, (9), 1040-1048. (b) Lukovkin, G. M.; Pshezhetsky, V. S.; Murtazaeva, G. A. *European Polymer Journal* **1973**, *9*, (6), 559-565.

36. Li, Y.; Ghoreishi, J.; Warr, J.; Bloor, D. M.; Holzwarth, J. F.; Wyn-Jones, E. *Langmuir* **2000**, *16*, 3093.

37. Sharma, K. P.; Kumaraswamy, G.; Ly. I.; Mondain-Monval, O. *J. Phys. Chem. B* **2009**, *113*, 11, 3423-3430.

38. Zakharova, L. Y.; Ibragimova, A. R.; Valeeva, F. G.; Zakharova, A. V.; Mustafina, A. R.; Kudryavtseva, L. A.; Harlampidi, H. E.; Konovalov A. I. *Langmuir* **2007**, *23*, 3214.

Chapter 6

Assembly of Anisotropic Particles in the H_1 Phase

6.1. Introduction

Assembly of anisotropic metallic nanoparticles results in the formation of interesting materials that find a variety of applications in electronics,[1,2] catalysis,[3] sensors,[4-6] tagging and imaging of biological specimens,[7-9] and optical devices.[10,11] Gold nanorods (Au NRs), in particular, have been investigated extensively since they show remarkable optical properties, and since methods for their preparation in bulk solutions have been reported. While drying of Au NR dispersions yield aggregates that are characterized by some degree of local order,[12] it is not possible to control the aggregate structure by controlling the drying process. However, the use of molecular species that exhibit controllable association enables "programmable" assembly[13] of Au NRs. The anisotropic shape of Au NRs can be exploited to assemble them in either end-to-end or side-by-side manner and thus the optical properties can be varied depending on the type of assembly done.[14] It is known that Au NRs have different crystallographic facets at the end and side surfaces.[15] As the side facets have a higher surface energy, surfactants used during Au NR synthesis (for example, cetyltrimethylammonium bromide, CTAB), adsorb preferentially on the sides of the Au NR as compared to on the end facets.[16,17] This attribute of Au NRs has been used to selectively bind chemical moieties on a particular facet.[23] Such chemistry has been used to guide assembly of the Au NRs in either side-by-side or end-to-end fashion.[23] Side-by-side assemblies have been achieved by introducing active sites on the sides of the rods and subsequently connecting via DNA, electrostatic interactions,[18-21] or click chemistry.[22] Arrangement of NRs in an end-to-end orientation to form one-dimensional chains or branched structures, requires specific functionalization near the ends. This has been achieved by using groups such as thiol (–SH) or disulphide (–SS) at the end faces that

subsequently form bonds that align the Au NRs.[5,23-26] End-to-end assembly of Au NRs have been achieved using hydrogen bonding between ligands having terminal carboxylic or amino groups,[24,25,27] biocompatible streptavidin-mediated linkage with disulfide-modified biotin on the ends of Au NRs,[4] surface linking by small-molecular weight dithiol molecules[23] and antibody–antigen interactions between disulphide (-SS-) modified linkers.[5] Mann and coworkers have shown the assembly of Au NRs using –SH bound DNA[18] to form reversible structures by the decomposition of the DNA on changing temperature. However, side-by-side assembly of the Au NRs was found to be irreversible. Recently, it has been shown that polymer-functionalized Au NRs can be assembled end-to-end to form rings. Such rings form either by templating water droplets[28] or by changing the solvent quality for the amphiphilic polymer grafted on the ends of the Au NRs.[29] In the latter, assembly into rings was claimed to be reversible, when poor-solvent is present near the end faces of the Au NRs. Thiols are known to preferentially bind to the ends of Au NRs and it has been shown that above a critical concentration of thiols, the Au NRs couple end-to-end.[23] Recently longitudinal coupling as a result of dithiol linkages in acetonitrile-water mixture results in the formation of dimers and has been used to study the effect of flexibility of the linker.[34] Some recent reports form Kumacheva's group has also shown end-to-end assembly of Au NRs grafted with synthetic polymers which are either sensitive to solvent quality or heat.[35,36]

However all the aforementioned methods of controlled assembly of Au NRS require complicated chemical functionalization of specific facets of the rods. Here, we report a simple procedure wherein end-to-end alignment of AuNRs is effected by simply mixing the nanoparticles with a non-ionic surfactant, $C_{12}E_9$ and H_2O. We also

show that this strategy of aligning the particles in an end-to-end fashion is not specific to the type of particle and can be employed even for micron sized polymeric ellipsoids.

6.2. Experimental

6.2.1. Materials

The precursor salt for Au NR synthesis, $HAuCl_4$ was purchased from SRL Ltd. (India). Cetyltrimethylammonium bromide, CTAB, ascorbic acid, octadecyltrimethoxy silane and hydrogen peroxide (H_2O_2; 30% w/v) were purchased from Sigma-Aldrich. $AgNO_3$ and poly(vinyl alcohol), PVA, having mol. wt. 1,25,000, were both obtained from Merck India Ltd. Fluorescent polystyrene latices of diameter 2.8 μm with polydispersity of 0.1% in size were purchased as 2.5% (w/v) suspension from Microparticles, GmbH, Germany. All the chemicals were used as obtained from the manufacturer.

6.2.2. Synthesis of Au Nanorods:

Gold nanorods (Au NRs) were synthesized using a slight variation of a reported procedure for seed mediated growth.[37] In a typical procedure, the growth solution was first prepared as follows. CTAB (25 ml, 0.20 M) was added to 0.75 ml of 0.0040 M $AgNO_3$ solution at 25 °C. To this solution, 25.0 ml of 1 mM $HAuCl_4$ was added, and after gentle mixing of the solution, 350 mL of 0.08 M ascorbic acid was added. Ascorbic acid is a mild reducing agent, and changes the growth solution from dark yellow to colorless. To prepare the seed solution, a CTAB solution (5 ml, 0.20 M) was mixed with 5.0 ml of 0.50 mM $HAuCl_4$. To this stirred solution, 0.60 ml of ice-cold 0.010 M $NaBH_4$ was added, which resulted in the formation of a brownish yellow solution. Vigorous stirring of the seed solution was continued for 2 min and

then, kept at 25°C. The final step was the addition of 65 mL of the seed solution to the growth solution at 27-30 °C. While Au NRs of aspect ratio ~4 were synthesized by us, the rods with aspect ratio ~3 were generously synthesized specifically for our experiments by Virginia D'Britto and Dr. B. L. V. Prasad (NCL, Pune).

6.2.3. Preparation of Polystyrene ellipsoids:

Micron sized polystyrene ellipsoids were prepared by uniaxial stretching of polystyrene microspheres using a modification of the procedure mentioned in the literature.[38] Monodisperse fluorescent iso-thiocyanate tagged polystyrene (PS) spherical particles (diameter = 2.8 μm), were dispersed in 7-10 wt% poly(vinyl alcohol), PVA, solution in water. The overall concentration of polystyrene particles in the PVA solution was 0.5 wt%. The homogenized PVA solution containing PS particles was poured in a flat bottom petri-dish (diameter 12 cm) and then dried in an oven at 60^{o}C for 8 hours. The dry film was removed and cut into rectangular strips of dimensions 1cm x 3cm. These strips were clamped between metal plates and stretched to a desired draw ratio (either 3 or 7) at a temperature of 115^{o}C, i.e. above the T_g of PVA and PS. A schematic of this procedure is shown in Figure 6.1. Temperature control during stretching was achieved using a feedback controlled convective oven. After stretching, the temperature was reduced to 60^{o}C before the strips were unloaded from the metal plates. The edges of the strips that remained unstretched were cut and discarded and only the centre portion of the strips was used for obtaining deformed particles. The stretched films were dissolved in water by continuous stirring at 60^{o}C for 24 hrs. The deformed PS particle dispersion was then centrifuged at 8000 r.p.m for 30 minutes and the supernatant solution was discarded and fresh water was added. This procedure was repeated 3 times to ensure maximum removal of PVA.

(a) Preparation of glass slides for confocal and optical microscopy:

The glass slides and cover slips used for imaging the samples under optical or confocal microscope were first hydrophobized, as follows. Glass slides were first cleaned for 30 minutes by dipping in acidic piranha solution (H_2SO_4 and 30 % w/v H_2O_2 in a ratio of 3:1 by weight). This removed all the organic impurities on the surface of the glass. The slides were then removed, washed multiple times with acetone and then dried in an oven for 1 hr at 100^{o}C. They were now taken in a round bottom flask containing 100 ml dry toluene. The flask was flushed with N_2 to remove moisture or air and 150 µl of octadecyltrimethoxy silane was then added. Surface grafting was allowed to proceed for 16 hrs at 70^{o}C. After the reaction, the glass slides were removed, washed with $CHCl_3$ and dried. To check for hydrophobicity, water was poured on the glass slide and we observed that the glass slide was not wet by the drops.

(b) Preparation of samples for optical and confocal microscopy:

A concentrated dispersion of PSe was prepared in a 1:1 water/$C_{12}E_9$ system at 50^{o}C. This composite sample was then placed on the hydrophobic glass slides and pressed with a cover slip to obtain a sample thickness of ~20 µm. The sample was heated to 50^{o}C in a convective oven and allowed to cool to 35^{o}C at 1^{o}C per minute. The glass slides for confocal microscopy were then sealed on the edges to prevent any water loss from the sample.

6.2.4. Characterization Tools:

UV-Vis spectroscopy was performed using a Shimadzu UV-1601PC spectrophotometer. The spectrum of absorption was obtained in a wavelength range of 300-1000 nm. Optical microscopy was performed using an Olympus-BX 50 equipped with

a crossed polarizer setup and images were obtained using a Lookman CCTV camera. LSM 710 Carl Zeiss Laser Scanning Confocal Microscope (LSCM) with an inverted stage was used to image the fluorescent samples. We used an Argon-ion laser (488 nm and 514 nm) for our experiments.

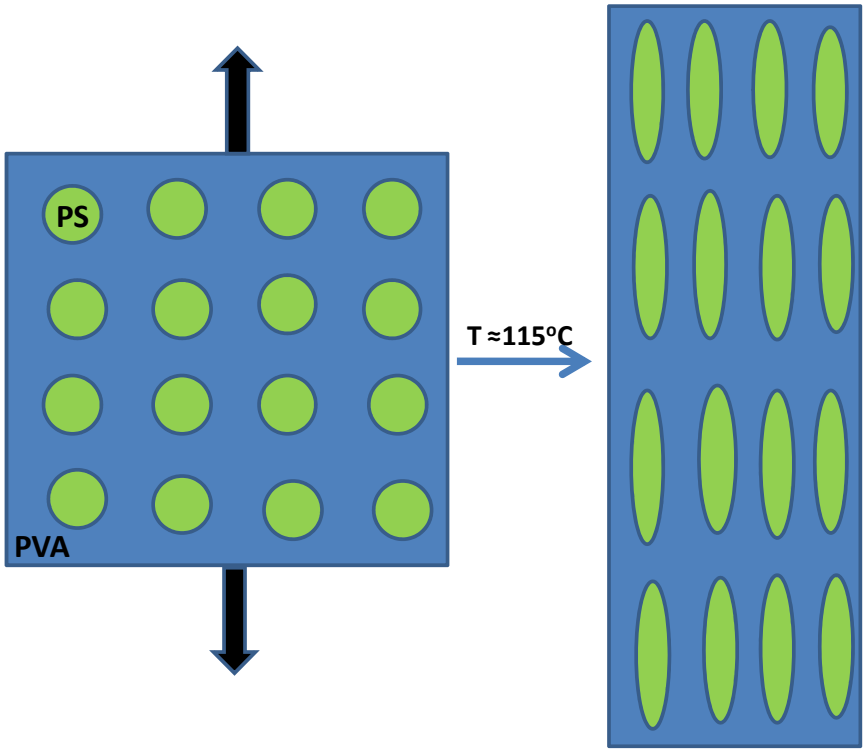

Figure 6.1. Fluorescent tagged polystyrene latices of 2.8 µm diameter are dispersed in PVA films and then stretched uniaxially at 115°C to a desired draw ratio to obtain polystyrene ellipsoids.

Scattering experiments were performed on two different machines that provided information at different range of length scales. Small angle X-ray scattering experiments were performed on Bruker Nanostar equipped with rotating copper anode operating at 45 kV and 100 mA and generating X-rays of wavelength 1.54 Å. Ultra small-angle neutron scattering (USANS) were performed on the medium resolution double crystal instrument at the guide laboratory of Dhruva reactor, Bhabha Atomic

Research Centre Mumbai. The instrument consists of a non-dispersive (1, –1) setting of 111 reflections of silicon single crystals with the sample between the two crystals. The neutron wavelength used was 0.312 nm and the instrument had a resolution function of $\Delta\lambda/\lambda \approx 1\%$. . The neutron beam was circular and had a diameter of 1.5 cm. The distance between the monochromator centre and the sample mount centre is 128 cm. The analyser crystal, placed 100.5 cm away from the sample, is set on a precise goniometer with smallest control step size of 0.0012°. Neutrons are detected by a BF_3 counter of 3.81 cm diameter, placed 55 cm away from the centre of the analyser crystal. At 65 MW of reactor power, the peak count rate of the blank rocking curve is about 55 counts per second at the detector position with sintered alumina. The accessible range of scattering wave vector transfer q is 0.003–0.173 nm^{-1}, which corresponds to a range of resolvable real-space dimension of 2000–40 nm.

6.3. Results and Discussion

Our results are divided in three parts: We first describe the UV-Visible analysis of Au nanorods of aspect ratio 3 at three different number densities in the H_1 phase. Then, we discuss our USANS results for the composite sample containing highest number density of Au nanorods in the H_1 phase. The observations for aspect ratio ~3 are then confirmed with Au nanorods of aspect ratio ~4 at various number densities in the H_1 phase with the help of UV-Visible spectrophotometry. We then present preliminary results on the assembly of micron sized polystyrene ellipsoids of aspect ratio 3 and 7 in the H_1 phase using confocal and optical microscopy.

6.3.1 Au nanorods in H_1 phase:

The Au nanorods were imaged using transmission electron microscopy and the size of the rods was calculated by ImageJ analysis on 150 nanorods in 5 different electron micrographs. The gold nanorods had an average radius and length of 16.4 ± 4.8 nm and 51 ± 9.2 nm, respectively. Thus, the average aspect ratio of the Au NRs was ~3. A representative electron micrograph of the synthesized Au nanorods is shown in Figure 6.2. A dilute aqueous solution (containing ~10^{10} Au nanorods per ml, sol) was then investigated using UV-Vis spectrophotometry.

(a) UV-Vis studies

As seen in UV-Vis spectra in Figure 6.4, there are two surface plasmon peaks corresponding to transverse and longitudinal dimensions of the Au NRs. The plasmon peaks corresponding to excitation in the transverse and longitudinal directions appear at 521.4 nm and 623.5 nm (obtained using PeakFit v4.12 software), respectively. This corresponds to an average aspect ratio of ~2.1-2.5 according to the simulations of Link et. al.[39] The discrepancy between our experimental data (aspect ratio from TEM ~ 3) and the simulation results might be attributed to the presence of the CTAB that caps the Au NRs. While the simulations are for Au NRs in water, the position of the surface plasmon strongly depends on the dielectric constant of the medium, and might appear might be influenced by the presence of CTAB.[40]

We now investigate three different concentrations of Au nanorods in the H_1 phase using UV-Vis. Samples are prepared, as in previous chapters, by dispersing the Au NRs in a 1:1 $C_{12}E_9$ and H_2O mixture at 50^oC, and subsequent cooling to room temperature. As before, we observe the formation of a gel phase, that shows fan shaped domains between crossed polarizers, characteristic of the H_1 phase (Figure 6.3

b). We anticipate that the Au NRs will not be incorporated within the H_1 phase, since both the rod diameter and the rod length exceed 10 nm (compare with characteristic H_1 spacing ~ 5.6 nm). Therefore, we anticipate exclusion of these rods to the domain boundaries of the H_1 phase. At the low concentrations of Au NRs examined here, optical micrographs of the samples, between crossed polarizers, reveal that an H_1 phase forms and that no large aggregates of Au NRs are observed (Figure 6.3 a). No further microstructural information on the assembly of Au NRs can be obtained from optical microscopy.

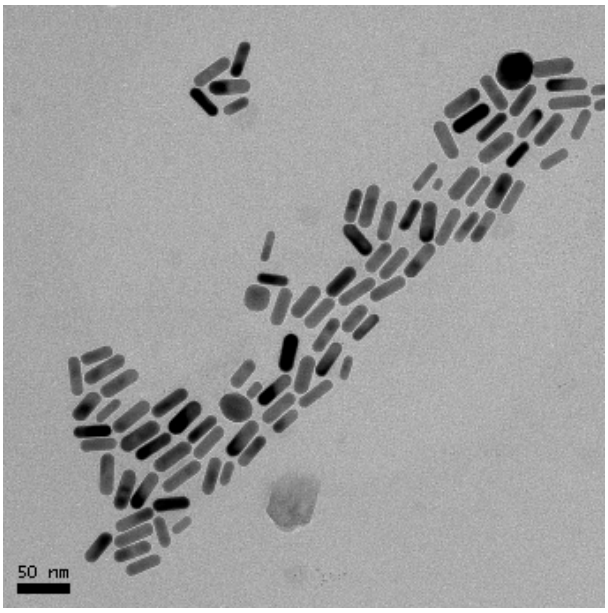

Figure 6.2. Transmission electron micrograph of Au nanorods (Au NRs) of average aspect ratio 3.

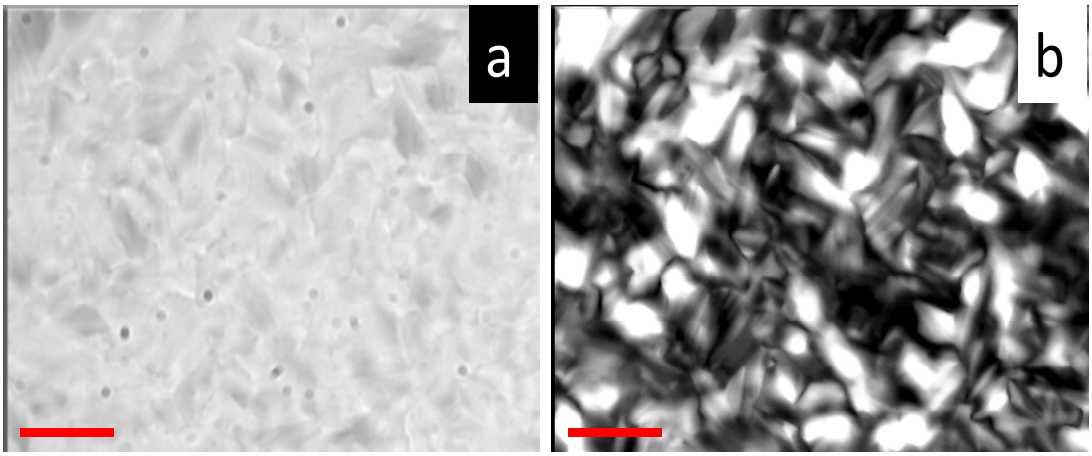

Figure 6.3. Optical micrographs of 2.9x10^{11} AuNRs (aspect ratio ~3) per ml sample as seen under (a) parallel polarizers and (b) under crossed polarizers. With crossed polarizers birefringence due to H_1 phase is observed but there is no aggregation of Au NRs is not seen at the boundaries in Figure 6.3 a. The scale bar in both the images corresponds to 50 µm.

When we use UV-Vis to examine a sample containing 5.9 x 10^{10} Au NRs, (Figure 6.4), we observe absorption at 527.1 nm, characteristic of a transverse surface plasmon. This absorption is slightly shifted to higher wavelength, as compared to the corresponding peak for an aqueous Au NR dispersion (521.4 nm). The full width at half maximum (FWHM) also increased slightly from 27.8 nm to 36.2 nm. However, in comparison, we observe that the second absorption, i.e. longitudinal plasmon, at higher wavelengths, is significantly broadened and shifted to much higher wavelength compared with the aqueous dispersion. For example, at an Au NR concentration of 5.9 x 10^{10} /ml, we observe a broad peak centered at ~ 657 nm (compare with the peak at 623.5 nm for the aqueous dispersion). We note that the neat H_1 phase shows no UV-Vis absorption in the wavelength range under investigation.

When the number density of Au rods was increased to ~1.5 x 10^{11} particles/ml, the transverse surface plasmon is observed at the same wavelength as earlier, but the longitudinal peak shifts further to ~684 nm. At the highest concentration of ~2.9 x 10^{11} particles/ml, the transverse peak is still observed at ~527 nm while the longitudinal surface plasmon peak position shifts even further to ~728.1 nm. Our data suggests that the Au NRs do not aggregate laterally, since there is no significant change in the transverse plasmon absorption. However, the longitudinal plasmon position shifts to higher wavelengths at higher Au NR concentrations, suggesting that the rods line up, resulting in a coupling of the longitudinal plasmons.[25,34] Thus, our data indicate that the Au NRs phase separate to the boundaries of the H_1 phase, where they assemble largely in end to end fashion. Further, the broadening of the longitudinal plasmon peaks for the Au nanorods in the H_1 phase, suggest that the end-end aggregates of Au rods are characterized by polydispersity in the number of aggregated gold rods. Pramod *et. al.*[34] have reported UV-Vis studies on dimers of Au nanorods of similar aspect ratio (~2.7), linked end to end using dithiol (-SS-) linkers. They suggest that the plasmon coupling mainly depends on the interparticle distance and relative orientation of the coupled nanorods. They have demonstrated that the red shift in the longitudinal plasmon is higher when the coupling linker molecule is rigid, when compared to a flexible linker. Specifically, they observed that the longitudinal surface plasmon peak shifted from ~630 nm (for dispersed single rods) to ~830 nm (for dimers coupled using a rigid molecule, so that the axes of the rods in the dimer are parallel) and to ~730 nm, when the rods coupled through flexible linkers (viz. when the rods were not aligned end-to-end). In our experiments, we observe a no change in the position of the transverse plasmon peak, but a shift in the longitudinal plasmon peak to higher wave-

length, as the Au NRs aggregate at the domain boundaries of the H_1 phase. We observe the longitudinal surface plasmon peak at ~ 623.5 nm for a dilute dispersion of Au NRs, that, in the H_1 phase, shifts from ~657 nm, to ~ 684 nm and ~728.1 nm as the number density of particles is increased. For Au NRs with an aspect ratio ~3, the data of Pramod *et. al.* suggests that the longitudinal plasmon absorption for end-to-end dimers would be observed a ~830 nm. The shift observed in our data is more modest and further, the longitudinal plasmon absorption that we observe in the H_1 phase is significantly broader, relative to the dilute dispersion. We believe that, in the H_1 phase, there is a coexistence of isolated Au NRs, dimers and oligomers that contribute to the broad longitudinal plasmon peak that we observe. With increase in Au NR concentration, the fraction of Au NR dimer and oligomer aggregates increases, relative to the isolated nanorods resulting in a systematic red shift of the longitudinal plasmon absorption.

We have repeated UV-Vis experiments with Au NRs of higher aspect ratio (~3.9, as obtained from TEM image analysis of ~100 particles), obtained over a wide concentration range in the H_1 phase. As before, a dilute dispersion (1.4×10^{10} particles/ml) of these Au NRs shows a transverse plasmon at 521 nm, while the longitudinal plasmon is observed at ~750 nm, in accord with the higher aspect ratio (Figure 6.5). In the H_1 phase, when the number density of the Au rods was varied from ~3.5×10^9 per ml to ~7×10^{10} per ml, the transverse peak did not show any significant change from its position of ~521 nm (Figure 6.5). However, the longitudinal plasmon peak was broadened relative to that for the dilute dispersion and a shoulder is seen at ~950 nm (for ~3.5×10^9particles/ml). On increasing the Au NR loading to 7.0×10^9 per ml, the shoulder at ~ 950 nm becomes more prominent.

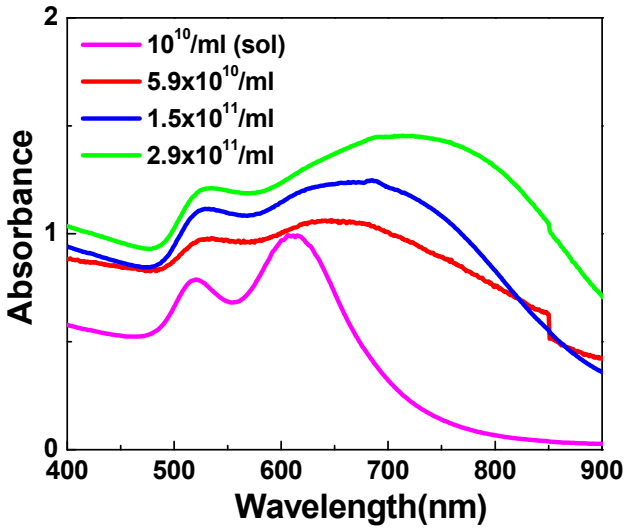

Figure 6.4. UV-Vis spectra for Au NRs (aspect ratio ~3) at concentrations of (a) 10^{10} per ml in water and (b) 5.9 x 10^{10} (c) 1.5 x 10^{11} and (d) 2.9 x 10^{11} per ml in the H_1 phase. The data has been vertically shifted for clarity purpose.

At a concentration of 1.05 x 10^{10} per ml, the longitudinal plasmon is even more prominent and additionally, two broad peaks are observed at ~890 nm and ~ 975 nm. For an Au NR concentration = 1.4 x 10^{10} particles/ml, the longitudinal peak becomes even broader, and we observe a plateau in the absorption for higher concentrations of Au NRs (3.5 x 10^{10} and 7 x 10^{10} particles/ml). For samples of higher concentrations of ~2.8 x 10^{11} particles/ ml, the absorption spectrum is qualitatively different from that at lower concentrations (Figure 6.6). Our data is indicative of the presence of oligomers of Au NRs that coexist with isolated particles, and suggests that the oligomer concentration increases with increasing loading of the Au NRs. At the highest concentration (2.8 x 10^{11} particles/ml), the Au NRs no longer aggregate as linear oligomers, but form irregular aggregates. Our data is consistent with the results of Thomas et. al.,[25] who have demonstrated the shift of the longitudinal plasmon to higher wavelengths in the infra-red region for the formation of 6-7 mer linear chains of Au nanorods.

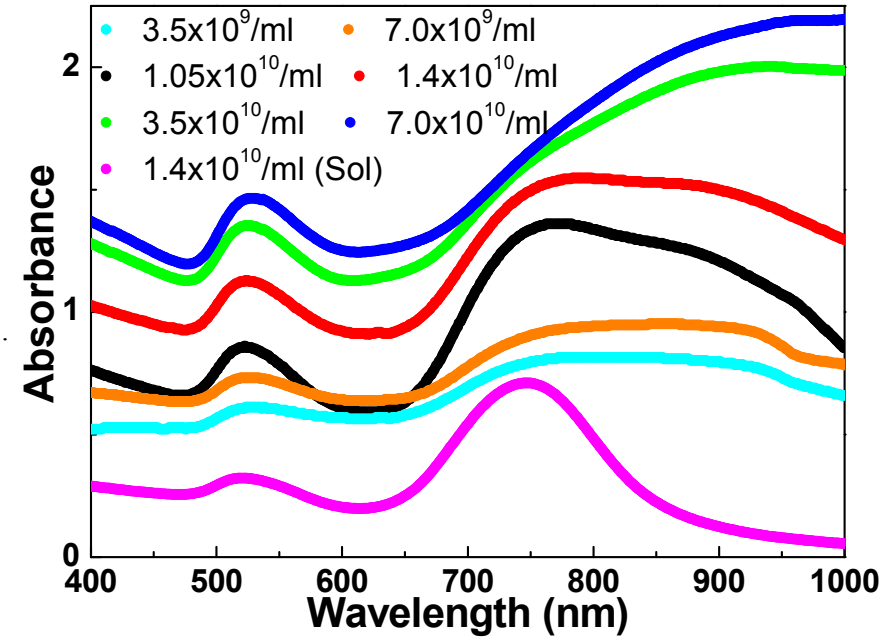

Figure 6.5. UV-Vis spectra for Au NRs (aspect ratio ~3) at concentrations of (a) $1.4x10^{10}$ per ml in water and (b) $3.5x10^9$, (c) $7x10^9$, (d) $1.05x\ 10^{10}$, (e) $1.4x10^{10}$, (f) $3.5x10^{10}$, and (g) $7x10^{10}$ per ml in the H_1 phase. The data has been vertically shifted for clarity purpose.

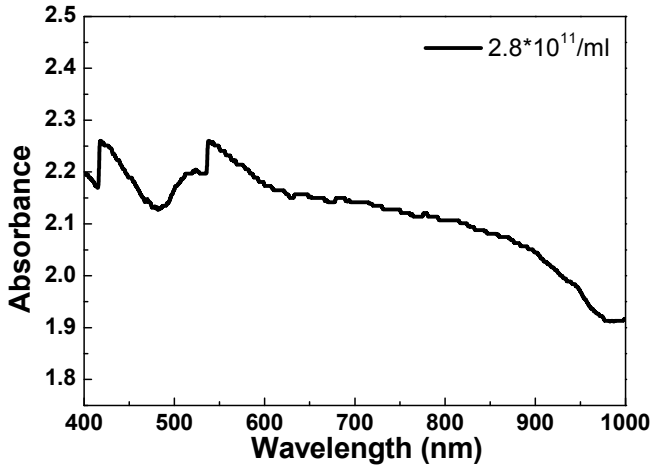

Figure 6.6. UV-Vis spectra for 2.8 x 10^{11} Au NRs (aspect ratio ~3) per ml in H_1 phase.

(b) Ultra SANS studies:

We now investigate the particle-particle correlations for Au NRs of aspect ratio 3, using ultra small angle neutron scattering (SANS) measurements. Figure 6.7 shows merged SAXS and SANS data for the sample containing 2.9 x 10^{11} particles/ml in the H_1 phase. We observe peaks for the H_1 phase at scattering vector, q ~ 1.1 nm^{-1} and 1.8 nm^{-1}, as expected. However, in the ultra-SANS data, we observe a peak at 0.09 nm^{-1}, corresponding to a correlation length of ~65 nm (= $2\pi/0.09$). This value is higher than the TEM average length of the Au NR (~51 nm ± 9.2 nm). The SANS data accord with the UV-Vis data and suggest end-to-end coupling of the Au NRs.

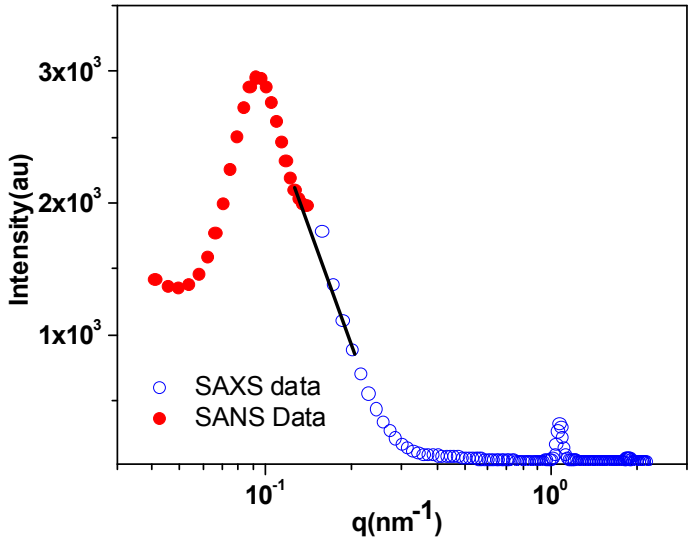

Figure 6.7. SAXS and SANS data for 2.9 x 10^{11} per ml Au nanorods (aspect ratio ~3) in the H_1 phase. Correlation peak at 0.09 nm^{-1} suggests particle-particle aggregation.

As imaging the assemblies of a dilute dispersion of Au NRs in the H_1 phase is not straightforward, we examined the dispersion of ellipsoidal particles of fluorescent polystyrene that can be readily imaged using confocal microscopy. We present this data in the next section.

6.3.2 Assembly of Polystyrene Ellipsoids in H_1 phase:

PS ellipsoids of aspect ratio 3 and 7 were dispersed in the surfactant/water system using the previously described protocol, and were cooled to room temperature to prepare the samples used for optical microscopy and for confocal experiments.

(a) Optical microscopy studies:

At very low concentrations = 5 x 10^4 particles/ml in H_1 phase, most of the PSe particles were isolated and only a few aggregates could be observed. At a few places on the slide, we could see PSe aggregating in a linear fashion to form dimers and oligomers. At higher particle number density = 8 x 10^6 particles/ml (Figure 6.8), the ellipsoids were homogenously distributed throughout the sample. Under parallel polarizers (Figure 6.8 a), we observe several isolated PSe particles, and note that the PSe aggregates are predominantly end-to-end linear aggregates. The linear aggregates of the PSe particles are indicated by the circles in Figure 6.8 a. The aggregates were mainly dimers and a few trimers were also observed. At some places, we observe multiple dimers align themselves to form a linear structure over a larger length scale (as shown by elliptically marked area). We also observe aggregates with randomly aligned PSe at a few places and one instance of two particles in a perpendicular (cross) orientation. To identify where the PSe particles are located relative to the H_1 domains, we image the sample at an angle of 15^o between the polarizer and analyzer. As expected, PSe particles are observed to localize at the H_1 domain boundaries (Figure 6.8 b and c). Interestingly, at some places the PSe aggregates are arranged in a linear end-to-end manner to form trimers or even hexamers and are observed to follow the shape of the domain boundaries (marked by elliptical area in Figure 6.8 b and c) at regions where multiple domains impinge. Individual particles also seem to follow the bounda-

ries of the H_1 phase. At some places, we also observe three ellipsoids coming together in a triangular assembly at the junction where three domains meet. However at higher concentrations investigated, for example 2.5 x10^7 particles per ml, we could mainly see random aggregates and very few linear aggregates (data not shown).

Similar experiments were performed with PSe of aspect ratio 7. Figure 6.9 shows the parallel polarized optical micrographs of these ellipsoids at a number density of 2 x 10^6 particles per ml in the H_1 phase, taken at different places in the sample. The optical micrographs on the left column (Figure 6.9 a and c) are taken with parallel polarizers while the corresponding crossed polarized micrographs are shown in the second column (Figure 6.9 b and d). As compared to the data for PSe of aspect ratio 3 (8 x 10^6 particles/ml; see Figure 6.8), here we could observe the particles mainly in the form of linear aggregates (see Figures 6.9 a and c) with very few isolated particles. There were also very few instances of random aggregates. The particles that were isolated were also observed to be aligned along the H_1 domain boundaries (see, for example, the organization of particles along the curved H_1 domain in the middle part of Figure 6.9 c). As the particles cannot be clearly imaged between crossed polarizers (Figure 6.9 b and d), we performed optical microscopy with polarizer and analyzer at an angle of 15^o (Figure 6. 10). Here, the ellipsoidal particles and the H_1 domain boundaries were visible in the same image. It is clear that the particles form linear aggregates that are localized at the domain boundaries, as observed for the PSe particles of aspect ratio 3.

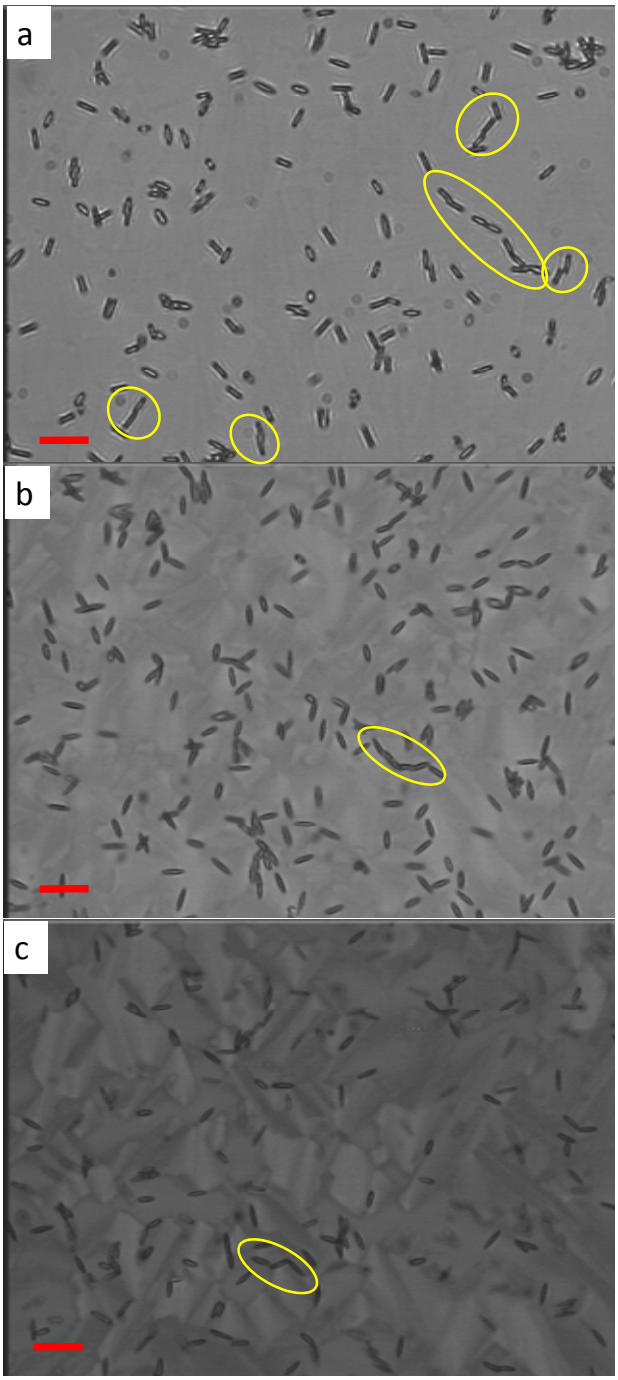

Figure 6.8: Optical micrographs of 8 x 10^6 per ml PSe (aspect ratio ~3) in the H_1 phase with (a) parallel polarizers and (b), (c) with polarizer and analyzer at an angle of 15^o. The scale bar represents 20 µm.

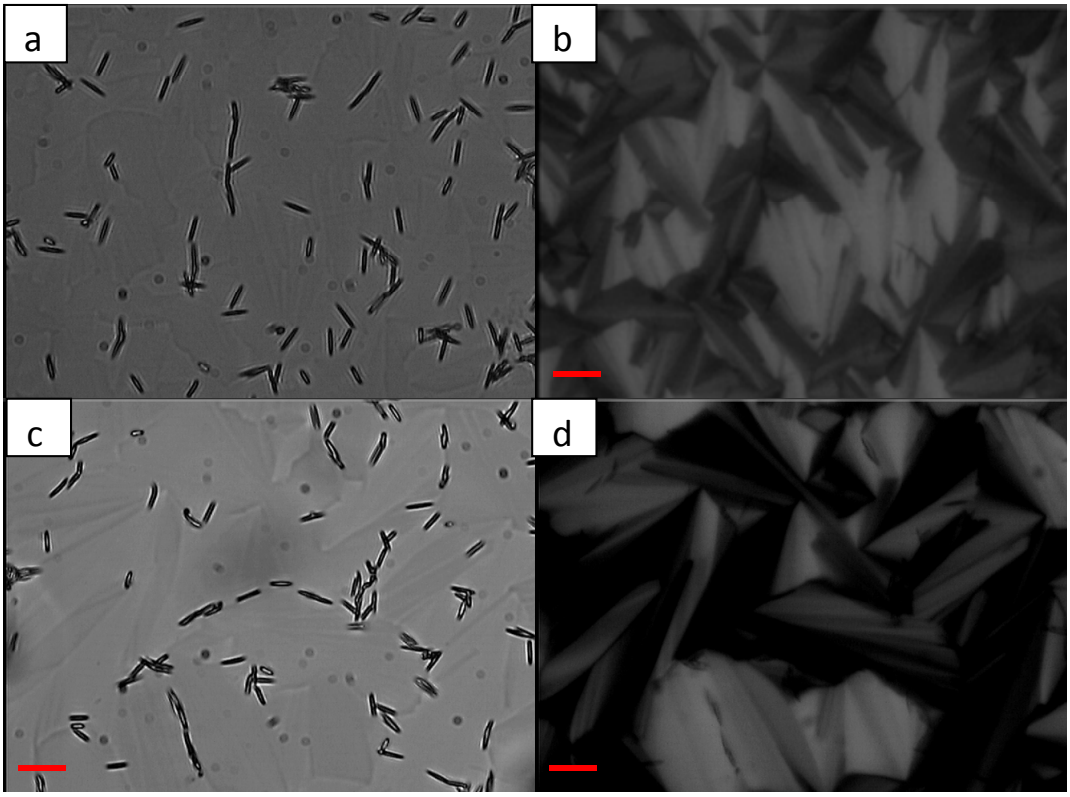

Figure 6.9. Optical micrographs of 2 x 10^6 per ml PSe (aspect ratio ~7) in the H_1 phase. Figure (a and c) are under parallel polarizers and the corresponding micrographs under crossed polarizers are seen in (b and d). The scale bar represents 20 µm.

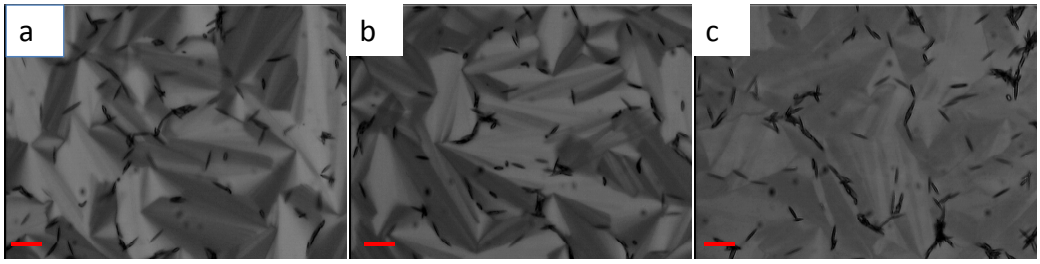

Figure 6.10. Optical micrographs of 2 x 10^6 per ml PSe (aspect ratio ~7) in the H_1 phase observed at an angle of 15^o between the polarizer and analyzer. The particles either isolated or linearly aggregated are clearly seen to follow the boundaries of the H_1 phase. The scale bar represents 20 µm.

(b) Laser scanning confocal microscopy studies:

Since the PSe were fluorescent, we used laser scanning confocal microscopy to image the three dimensional assembly of these particles in the H_1 phase. Figure 6.11 shows several 2D slices of confocal micrographs of the 8 x 10^6 /ml PSe (aspect ratio 3) in the H_1 phase. These images are representative of the structures observed throughout the sample. The images confirm the formation of linear oligomers of PSe ellipsoids which range in length from 3 particles (Figure 6.11 a, c) in a chain to 5 or 6 ellipsoids particles at some places (Figure 6.11 b, d). The samples used for confocal were made on a glass slide having a ~100 μm deep wedge. Therefore, we could also see some linear chains containing ellipsoidal particles which appear to come from the bulk of the sample i.e. their tips pointing towards the viewer (Figure 6.11 b). We note that the particles in an end-to-end aggregate are not always in actual contact, and are separated by a small distance (Figure 6.11 c).

At some places within the sample we could also observe two linear chains connecting at the junction of the domain boundaries as seen in Figure 6.11 d. Confocal microscopy from PSe of aspect ratio 7 showed qualitatively similar results.

The results from PSe particles indicate the formation of linear 1D structures by the aggregation of particles at the domain boundaries. At very low concentrations of PSe (aspect ratio 3) for e.g. at a number density of 5 x 10^4 particles/ml, almost all the particles are dispersed in the H_1 phase and the oligomers are seen only at very few places. Aggregation of particles into linear end-to-end structures is consistently seen at higher concentration, for e.g. at 8 x 10^6 per ml. However, at very high particle concentrations (~10^8 particles/ml), we do not observe localization of the particles to the domain boundaries, but a "complete" phase separation of the particles that then aggre-

gate in random fashion. These random aggregates include side-by-side aggregated structures, that are observed only rarely for low concentrations dispersions in the H_1 phase, where the particles are localized to the H_1 domain boundaries.

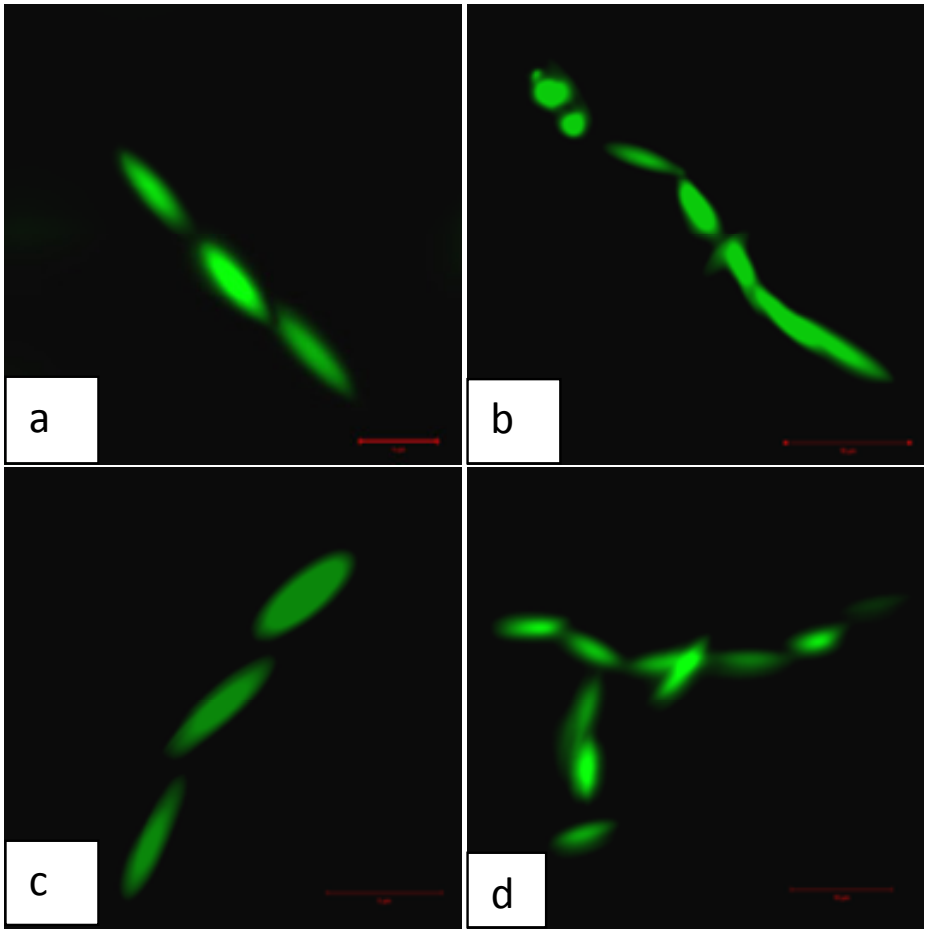

Figure 6.11. Laser scanning confocal micrographs of 8 x 10^6 per ml PSe (aspect ratio ~3) in the H_1 phase. Scale bars in image in the left and right columns are 5 and 10 µm respectively.

We note, that our data on PSe correlates well with the data on Au NRs, even though the size of the PSe particles is about two orders of magnitude larger than the Au NRs. At low An NR concentrations, isolated nanorods exist in the H_1 phase. However, with increasing Au NR concentration, we observe the formation of oligomers that align in end-to-end manner, at the H_1 domain boundaries. Finally, at very high concentrations of the Au NRs, we observe large aggregates (large enough to be observed in optical microscopy) comprised of irregularly oriented nanorods.

6.4. Summary

We have demonstrated matrix mediated interactions of anisotropic particles resulting in the formation of linear aggregates. Au NRs of two different aspect ratios in a certain concentration range seem to aggregate in an end-to-end fashion at the domain boundaries resulting in a red shift of longitudinal surface plasmon. Interestingly, there is minimal change in the width or the position of transverse surface plasma which suggests the formation of linear chains that are ~1 particle thick. As the concentration is increase the plasmons shifts to higher wavelength and ultimately plateaus. The analysis of these broad peaks suggests the presence of distribution of oligomers of different chain length. As the concentration is further increased there is random aggregation of particles. Micron sized ellipsoidal particles also aggregate linearly at the domain boundaries over a particular range of particle concentration. These particles clearly appear to follow the domain boundaries whether in the isolated or the aggregated form. Similar to Au NRs, after a particular concentration these ellipsoids are completely phase separated and aggregate randomly.

6.5. References

1. Peter, A. S.; Christopher, D. N.; Thomas, N. J.; Theresa, S. M.; Benjamin, R. M.; Jeremiah, M.; Thomas, E. M. *Appl. Phys. Lett.* **2000**, *77*, 1399-1401.
2. Melosh, N. A.; Boukai, A.; Diana, F.; Gerardot, B.; Badolato, A.; Petroff, P. M.; Heath, J. R. *Science* **2003**, *300*, 112-115.
3. Chen, M. S.; Goodman, D. W. *Science* **2004**, *306*, 252-255.
4. Caswell, K. K.; Wilson, J. N.; Bunz, U. H. F.; Murphy, C. J. *J. Am. Chem. Soc.* **2003**, *125*, 13914-13915.
5. Chang, J.-Y.; Wu, H.; Chen, H.; Ling, Y.-C.; Tan, W. *Chem. Commun.* **2005**, 1092-1094.
6. Rex, M.; Hernandez, F. E.; Campiglia, A. D. *Analy. Chem.* **2005**, *78*, 445-451.
7. Durr, N. J.; Larson, T.; Smith, D. K.; Korgel, B. A.; Sokolov, K.; Ben-Yakar, A. *Nano Lett.* **2007**, *7*, 941-945.
8. Agarwal, A.; Huang, S. W.; Donnell, M. O.; Day, K. C.; Day, M.; Kotov, N.; Ashkenazi, S. *J. Appl. Phys.* **2007**, *102*, 064701.
9. Murphy, C. J.; Gole, A. M.; Hunyadi, S. E.; Stone, J. W.; Sisco, P. N.; Alkilany, A.; Kinard, B. E.; Hankins, P. *Chem. Commun.* **2008**, 544-557.
10. Maier, S. A.; Kik, P. G.; Atwater, H. A.; Meltzer, S.; Harel, E.; Koel, B. E.; Requicha, A. A. G. *Nat. Mater.* **2003**, *2*, 229-232.
11. Maier, S. A.; Brongersma, M. L.; Kik, P. G.; Atwater, H. A. *Phys. Rev. B* **2002**, *65*, 193408.
12. (a) Nikoobakht, B.; Wang, Z. L.; El-Sayed, M. A. *J. Phys. Chem. B* **2000**, *104*, 8635. (b) Sau, T. K.; Murphy, C. J. *Langmuir* **2005**, *21*, 2923. (c) Guerrero-

Martínez, A.; Pérez-Juste, J.; Carbó-Argibay, E.; Tardajos, G.; Liz-Marzán, L. M. *Angew. Chem., Int. Ed.* **2009**, *48*, 9484.

13. (a) Korgel, B. A.; Zaccheroni, N.; Fitzmaurice, D. *J. Am. Chem. Soc.* **1999**, *121*, 3533. (b) Murray, C. B.; Kagan, C. R.; Bawendi, M. G. *Science* **1995**, *270*, 1335. (c) Talapin, D. V.; Shevchenko, E. V.; Kornowski, A.; Gaponik, N.; Haase, M.; Rogach, A. L.; Weller, H. *Ad*V. *Mater.* **2001**, *13*, 1868. (d) Sun, S.; Murray, C. B.; Weller, D.; Folks, L.; Moser, A. *Science* **2000**, *287*, 1989. (e) Lin, Y.; Skaff, H.; Emrick, T.; Dinsmore, A. D.; Russell, T. P. *Science* **2003**, *299*, 226. (f) Cox, J. K.; Eisenberg, A.; Lennox, R. B. *Curr. Opin. Colloid Interface Sci.* **1999**, *4*, 52. (g) Lopes, W. A.; Jaeger, H. M. *Nature* **2001**, *414*, 735.
14. (a) Jain, P. K.; Eustis, S.; El-Sayed, M. A. *J. Phys. Chem. B* **2006**, *110*, 18243. (b) Draine, B. T.; Goodman, J. *Astrophys. J.* **1993**, *405*, 685.
15. Wang, Z. L.; Gao, R. P.; Nikoobakht, B.; El-Sayed, M. A. *J. Phys. Chem. B* **2000**, *104*, 5417-5420.
16. Gou, L.; Murphy, C. J. *Chem. Mater.* **2005**, *17*, 3668-3672.
17. Nikoobakht, B.; El-Sayed, M. A. *Langmuir* **2001**, *17*, 6368-6374.
18. Dujardin, E.; Hsin, L.-B.; Wang, C. R. C.; Mann, S. *Chem. Commun.* **2001**, 1264-1265.
19. Gole, A.; Murphy, C. J. *Langmuir* **2005**, *21*, 10756-10762.
20. Gole, A.; Orendorff, C. J.; Murphy, C. J. *Langmuir* **2004**, *20*, 7117-7122.
21. Orendorff, C. J.; Hankins, P. L.; Murphy, C. J. *Langmuir* **2005**, *21*, 2022-2026.
22. Gole, A.; Murphy, C. J. *Langmuir* **2007**, *24*, 266-272.
23. Joseph, S. T. S.; Ipe, B. I.; Pramod, P.; Thomas, K. G. *J. Phys. Chem. B* **2006**, *110*, 150-157.

24. Zhang, S.; Kou, X.; Yang, Z.; Shi, Q.; Stucky, G. D.; Sun, L.; Wang, J.; Yan, C. *Chem. Commun.* **2007**, 1816-1818.

25. Thomas, K. G.; Barazzouk, S.; Ipe, B. I.; Joseph, S. T. S.; Kamat, P. V. *J. Phys. Chem. B* **2004**, *108*, 13066-13068.

26. Murphy, C. J.; Sau, T. K.; Gole, A. M.; Orendorff, C. J.; Gao, J.; Gou, L.; Hunyadi, S. E.; Li, T. *J. Phys. Chem. B* **2005**, *109*, 13857-13870.

27. Sudeep, P. K.; Joseph, S. T. S.; Thomas, K. G. *J. Am. Chem. Soc.* **2005**, *127*, 6516-6517.

28. Khanal, B. P.; Zubarev, E. R. *Angew. Chem. Int. Ed.* **2007**, *46*, 2195-2198.

29. Nie, Z.; Fava, D.; Kumacheva, E.; Zou, S.; Walker, G. C.; Rubinstein, M. *Nat. Mater.* **2007**, *6*, 609-614.

30. Salem, A. K.; Chen, M.; Hayden, J.; Leong, K. W.; Searson, P. C. *Nano Lett.* **2004**, *4*, 1163-1165.

31. Chen, M.; Guo, L.; Ravi, R.; Searson, P. C. *J. Phys. Chem. B* **2005**, *110*, 211-217.

32. Salant, A.; Amitay-Sadovsky, E.; Banin, U. *J. Am. Chem. Soc.* **2006**, *128*, 10006-10007.

33. Wang, Y.; Li, Y. F.; Wang, J.; Sang, Y.; Huang, C. Z. *Chem. Commun.* **2010**, *46*, 1332-1334.

34. Pramod, P.; Thomas, K. G. *Adv. Mater.* **2008**, *20*, 4300-4305.

35. Fava, D.; Nie, Z.; Winnik, M. A.; Kumacheva, E. *Adv. Mater.* **2008**, *20*, 4318-4322.

36. Fava, D.; Winnik, M. A.; Kumacheva, E. *Chem. Commun.* **2009,** 2571-2573.

37. Nikoobakht, B.; El-Sayed, M. A. *Chem. Mater.* **2003**, *15*, 1957-1962.

38. (a) Nagy, M.; Keller, A. *Polymer Commun.* **1989,** *30*, 133. (b) Ho, C. C.; Keller, A.; Odell, J. A.; Ottewill, R. H. *Polymer International* **1993**, *30* 207-211.

39. Link, S.; Mohamed, M. B.; El-Sayed, M. A. *J. Phys. Chem. B* **1999**, *103*, 3073-3077.

40. Jun,T.; Yong-Hua, L.; Rong-Sheng, Z.; Kai-Qun, L.; Zhi-Guo, X.; Zhao-Feng, L.; Sheng-Li, L.; Pei, W.; Hai, M. *Chin. Phys. Lett.* **2008**, *25*, 4459.

Chapter 7

Conclusions and Future Work

This thesis presents a detailed investigation (a) into the mechanism of nanoparticle and polymer organization in a non-ionic surfactant hexagonal mesophase; (b) into how this can be exploited to prepare self-standing 3D macroporous materials with tunable microstructure and, (c) into the preparation of linear assemblies of gold nanorods that have implications for photonic applications. We summarize the salient results as follows:

The organization of nanoparticles in the H_1 phase is size dependent. Particles that are less than 10 nm in diameter template the H_1 phase and are incorporated in the hydrophilic regions of the H_1 phase. Particles larger than the characteristic H_1 spacing are always expelled from the surfactant mesophase and form a three dimensional network of particulate strands. Isothermal SAXS experiments at the isotropic-hexagonal transition temperature reveal that as domains of the H_1 phase are nucleated and grow, the dispersed particles are excluded from the mesophase domains and are concentrated in the isotropic regions. Eventually, as the H_1 domains impinge, the particles are localized at the domain boundaries. Interestingly, we observe that the aggregation of silica particles into the particulate network is thermoreversible, i.e. the aggregated particles reversibly disperse above the hexagonal-isotropic transition temperature and reaggregate below this. This is in contrast to the situation when an aqueous dispersion of electrostatically stabilized silica nanoparticles becomes irreversibly aggregated upon the addition of salt or changing pH. This observation motivated our investigations of surfactant-silica nanoparticle interactions and the resultant surfactant/particle structure. Using a combination of SAXS and SANS, we found a change in the form of the interparticle interactions, from a screened coulombic interaction for an aqueous dispersion of silica particles to a hard sphere interaction for the same particles in a

surfactant/water system. We confirmed that this change in interparticle potential resulted from the formation of an aggregated surfactant structure (represented as surfactant micelles asorbed on the silica particles) around the silica particles. Thus, micellar adsorption on silica particles stabilizes them against irreversible aggregation. Finally, we demonstrated that the surfactant did not adsorb on PEI coated silica particles.

We exploited this last observation to attempt a strategy to render particle aggregation irreversible using PEI coated particles. PEI coated silica particles phase separated from the H_1 phase just as the bare silica particles however, the PEI amine groups at the surface of the particles were crosslinked using glutaraldehyde to stabilize the particulate network. The crosslinking could be carried out using. The covalent imine bonds formed between the PEI and glutaraldehyde were reversible in presence of water, and were therefore reduced using cyanoborohydride, and finally the surfactant template was removed by washing with water and ethanol. Varying the cooling rate into the H_1 phase controls the nucleation rate for H_1 domains, and therefore, the domain size. Thus, the network spacing in the particulate macroporous solid could be controlled by varying the cooling rate and we have demonstrated self-standing 3D scaffolds of silica nanoparticles with pore sizes ranging from ~0.5 μm to ~30 μm. We also showed that this dynamic templating of the H_1 phase is independent of particle chemistry and can be employed for preparing self standing scaffolds of polystyrene latices, hydroxyapatite nanoparticles, positively charged iron and ceria nanoparticles, temperature sensitive PNIPAM microgels and bionanoparticle like ferritin. We also demonstrated that these scaffolds can be flow oriented, prior to crosslinking, to form self standing structures with oriented pores. Finally, using this methodology, interpenetrating networks of red and green polystyrene particles were formed.

We described the effect of incorporating environment-responsive polymers in the H_1 phase. We investigated pH responsive low molecular weight PEI in the H_1 phase. We have demonstrated the change in interactions of PEI chains with surfactant and its assembly within the H_1 phase at three different pH values. PEI shows significant interactions with surfactant and water at pH 12.8 and therefore does not allow the nucleation of the H_1 phase till 15^{o}C. Below this temperature there is always a coexistence of isotropic micellar and H_1 phases. At pH 5 the interactions between PEI and surfactant are significantly reduced and therefore mesophase formation happens at ~25^{o}C. However at this pH, PEI only shows aggregation at the domain boundaries at ~17^{o}C i.e. at a temperature much below T_{HI}. On decreasing the pH to 1, the interactions between and surfactant is greatly decreased. Therefore, the phase separation of PEI to the domain boundaries takes place along with the formation of the phase.

In the last part of the thesis, we have investigated the effect of incorporating anisotropic particles in the H_1 phase. Au nanorods when incorporated, at moderate concentrations, in the H_1 phase, show coupling of the longitudinal plasmons. We believe that the coupling of longitudinal plasmons arises due to the end-end assembly of Au nanorods at the domain boundaries of the H_1 phase. We also report exclusion of micron sized polystyrene ellipsoids from the H_1 phase, and their end-to-end aggregation into linear chains at the H_1 domain boundaries. Thus, for the first time we demonstrate the organization of rod shaped particles in a controlled end to end fashion without the use of any chemical functionality.

Scope of Future Work

The work outlined in this thesis opens up several interesting avenues for future investigation, some of which are listed below.

1. *Surfactant-silica interactions*:

The stability of nanoparticles in non-ionic surfactants is very important for many industrial applications like cosmetics, pharmaceuticals, food etc. It has been suggested[1] that silica particles aggregate in the presence of surfactant in the isotropic micellar phase, due to competition between particles and surfactant to associate water molecules. Such particle aggregation is observed at low concentration of surfactant where the surface coverage is incomplete. However, we show that a dispersion of silica particles is highly stable in the presence of 50 wt% surfactant (Chapter 3). It would be interesting to extend our investigation to explore the stability of silica/surfactant mixtures, and to investigate the microstructural underpinnings of this behaviour. Such studies will require construction of adsorption isotherms using surface tension measurements combined with external contrast matching neutron scattering experiments to investigate the surfactant geometry.

2. *Polymer behavior in H_1 phase*:

Confinement of polymers in lyotropic lamellar phases has been discussed in the literature[2] on protein-membrane interactions in biological cells. For e.g., a neutral polymer confined in a lamellar phase, induces attractive interlamellar interactions that destabilize the lamellar phase. This could result in the formation of coexisting polymer rich and surfactant rich lamellar phases. However there has been little understanding of how polymers behave in the H_1 phase, a situation that is relevant to novel delivery systems for conjugation and delivery of drugs. Thus, a systematic study of

the influence of polymer molecular weight on confinement in the hexagonal phase is necessary. Here, the chemistry of the polymer is important, since it will determine whether the polymer penetrates through the surfactant phase or if it interacts with the surfactant.

3. *Colloids in lamellar phases*:

Similar to the previous section, it is also proposed to incorporate colloidal particles in different liquid crystalline phases for e.g. in lamellar (L_α) phase formed by similar type of surfactants. There have been reports[3] that suggest the suppression of undulation of lamellae by the incorporation of neutral particles in the bilayers. This suppression results in repulsive interactions between the lamellar bilayers ultimately leading to deformation of surfactant structure and exclusion of the particles. However, there remains a lot of scope to understand the particle interactions by varying size, geometry as well as chemistry within the lamellar phase.

4. *Crystallization of proteins in lyotropic phases*:

There has been extensive study on crystallization of proteins using surfactant phases. Bicontinuous cubic phases and lamellar phases have been used to crystallize membrane proteins.[4,5] For e.g., it has been reported that membrane proteins are stabilized by surfactant cubic phases, and that proteins crystallized on addition of salt and the surfactant transforms into lamellar bilayer phase. It would be interesting to understand how the H_1 phase influences protein-protein interactions. While proteins such as the ferritin used in our studies are globular proteins that are robust to the surfactant environment and behave like particles, is it possible to engineer strategies for controlled protein aggregation, and perhaps, protein crystallization using surfactant mesophases? This is a potentially interesting area for future work.

5.*Tissue engineering materials*:

One of the goals in tissue engineering is to create three-dimensional scaffolds that are highly porous and, within which oxygen and nutrients can be readily transported to the growing cells. Clearly, such scaffolds should be bio-compatible. Scaffolds made up of bio-compatible materials for e.g. hydroxyapatite, polymers etc. can be used for cell-growth studies. The functions of these scaffolds include cell adhesion, proliferation and deposition of extracellular matrix to facilitate tissue growth. Macroporous scaffolds formed from hydroxyapatite/ calcium phosphate attracts lot of attention as tissue engineering materials. Although there are several reported routes to porous tissue engineering scaffolds, control over pore size and distribution always remain a challenge. The materials fabricated by our methodology can have very well defined pores sizes with narrow distribution. The 3D scaffolds formed using our methodology (for e.g. from hydroxyapatite nanoparticles) can be used for cell-growth studies. Since our scaffolds are formed by connected network of particulate strands, they can provide high surface area for the cells to grow. These macroporous scaffolds also provide several other advantages for e.g. (1) tunable macroporosity which can be used for growing cells of different sizes, (2) cell growth factors can be grafted using the amine functional groups on the PEI coated hydroxyapatite particles and (3) growing polymers off the surface for e.g., polylactide-co-glycolide, (PLGA) so as to form hybrid biomaterials which can utilize advantages of nanoparticle forming the scaffold and the bio-compatible polymer grown on them.

6. *Hierarchical structures*:

Hierarchical structures having mesoporosity and macropososity can be prepared by using our methodology from particles like for e.g. MCM or mesoporous sil-

ica. The hierarchical materials thus synthesized with bimodal meso–macroporous interconnected pores can provide high diffusion and high surface areas for adsorption and reaction, particularly for large molecules. Such hierarchical materials might find use in various applications for e.g. HPLC, catalysis, electrodes for fuel cell applications, drug delivery, and tissue engineering etc.[6]

References

1. Alexeev, V. L.; Ilekti, P.; Persello, J.; Lambard, J.; Gulik, T.; Cabane, B. *Langmuir* **1996**, 12, 2392.
2. Ligoure, C.; Bouglet, G.; Porte, G. *Phys. Rev. Lett.* **1993,** *71*, (21), 3600.
3. Suganuma, Y.; Urakami, N.; Mawatari, R.; Komura, S.; Nakaya-Yaegashi, K.; Imai, M. *J .Chem. Phys.* **2008**, *129*, 134903.
4. (a) Nollert, P.; Qiu, H.; Caffrey, M.; Rosenbusch, J. P.; Landau, E. M. *FEBS Lett.* **2001**, *504*, 179–186; (b) Rummel, G.; Hardmeyer, A.; Widmer, C.; Chiu, M. L.; Nollert, P.; Locher, K. P.; Pedruzzi, I.; Landau, E. M.; Rosenbusch, J. P. *J. Struct. Biol.* **1998**, *121*, 82–91.
5. Angelov, B.; Ollivon, M. L.; Angelova, A. *Langmuir* **1999**, *15*, 8225–8234.
6. Yuan, Z. –Y.; Su, B.,-L. *J. Mater. Chem.* **2006**, *16*, 663–677.

List of Research Credentials, Awards and Conferences

Publications and Patents

1) **Sharma, K. P.**; Kumaraswamy, G.; Ly, I.; Mondain-Monval, O. "*Self-Assembly of Silica Particles in a Nonionic Surfactant Hexagonal Mesophase*" ***J. Phys. Chem. B,*** 2009 *113*, 11, 3423-3430.

2) Jijo, V.J.; **Sharma, K.P**.; Kumaraswamy, G.; Mathew, R.; Rajamohanan, P.R.; Kamble, S. B. "*Volume Transition of PNIPAM in Non-Ionic surfactant Mesophase*" ***Macromolecules,*** 2010 *43*, 4782–4790.

3) **Sharma, K. P.**; Kumaraswamy, G.; Aswal, V.K. "*Adsorption of Nonionic Surfactant on Silica Nanoparticles: Structure and Resultant Interparticle Interactions*" ***J. Phys. Chem. B,*** 2010 *114*, 10986-10995.

4) **Sharma, K. P**.; Ganai, A.; Gupta, S. S.; Kumaraswamy, G. "*Self Standing Three Dimensional Networks of Nanoparticles, With Controllable Morphology by Dynamic Templating of Surfactant Hexagonal Domains*" ***Chem. Mater.*** 2011 **(**DOI: 10.1021/cm102945x)

5) **Sharma, K.P.**; Choudhary, C. K.; Srivastava, S.; Rajamohanan, P. R.; Roy, S.; Kumaraswamy, G. "*Effects of pH on the Self Assembly of Polyethylenimine in the Hexagonal Mesophase of Non-Ionic Surfactant*" (**submitted to *J. Phys. Chem.. B***).

6) **Patent** on "*Self standing nanoparticle networks/scaffolds with controllable void dimensions*" Guruswamy. K.; **Sharma, K.P**. WO/2010/070679.

7) Ganai, A.; **Sharma, K. P.;** Gupta, S. S.; Kumaraswamy, G. " *Hierarchical Porous Materials from Surfactant Mesophase Templating*" (manuscript in preparation for ***Chem. Comm.***).

8) **Sharma, K. P.;** Ganai, A.; Venugopal, E.; Kumaraswamy, G. "*Hydrodynamic driven end to end assembly of Au nanods in surfactant mesophase*" (manuscript in preparation for ***J. Phys. Chem. Lett.***)

Awards

1) **Keerthi Sangoram** award for "Best Research Thesis" for 2010 at National Science Day 2011 held in National Chemical Laboratory.
2) **Best Poster** Award at Science Day 2010 held in National Chemical Laboratory.
3) **Best Poster** Award at National Science Day 2009 held in National Chemical Laboratory.
4) Awarded prestigious **Indo-French Sandwich Ph.D. fellowship** for 4 months by the French Embassy in India to visit and work at CRPP, Bordeaux, France.
5) **Topper** in the coursework conducted for PhD students joining NCL Pune.
6) Awarded **Junior Research Fellowship** (**JRF**) by Council of Scientific and Industrial Research (CSIR) for pursuing Ph.D.
7) Awarded **Gold Medal** for being a top ranker in M.Sc.

Conferences

1) Attended the APS March meeting in Portland USA from 15th March-20th March 2010 and gave an oral and a poster presentation.
2) Attended the School and Symposium on "*Rheology of Complex Fluids*" organized in IIT Madras from 4th-9th January 2010. Work presented in the form a poster.
3) Attended the SANS workshop held in Bhabha Atomic Research CMntre, mumbai, India in October 2009.
4) Attended the Franco-Israeli Trends conference held in Biarritz, France in 2007 via French Embassy scholarship.
5) Presented Poster titled "*SAXS and SANS investigations of bare and polymer coated silica nanoparticles*" in International conference on Neutron Scattering on Mesoscopic Systems held in Goa 2009.
6) Presented "Poster" in International Conference on "*Multiscale Structures and Dynamics of Complex Systems"* held in Bangalore Sep 2008.